Characterization of the fluid-structure interaction on a vertical axis turbine with deformable blades

Stefan Hoerner

Characterization of the Fluid-Structure Interaction on a Vertical Axis Turbine with Deformable Blades

Dissertation for the award of the degree:

Doktor-Ingenieur der Otto-von-Guericke-Universität Magdeburg

and

Docteur de l'Université Grenoble-Alpes

in international supervision at:

The Faculty of Process and Systems Engineering
Otto-von-Guericke-University Magdeburg

and

The Laboratory of Geophysical and Industrial Flows
Doctoral School of Industrial, Material, Mechanical and Process Engineering
University Grenoble-Alpes

by Stefan J. Hoerner, M.Sc.
born 05.05.1975 in Landau in der Pfalz

Jury:

Prof. Dr.-Ing. Christian O. Paschereit, President & Reviewer
Technische Universität Berlin

Prof. Jacques André Astolfi, Reviewer
École Navale de Lanvéoc-Poulmic

Prof. Dr.-Ing. Dominique Thévenin, Reviewer & Director
Otto-von-Guericke-Universität Magdeburg

Maître de Conférences Thierry Maître, HDR, Reviewer & Director
LEGI, Grenoble-INP, Université Grenoble-Alpes

Prof. Dr.-Ing. Christian-Toralf Weber, Examiner
Hochschule Magdeburg-Stendal

Dr. Cyrille Bonamy, Invited Member of the Jury & Co-Supervisor
LEGI, CNRS, Université Grenoble-Alpes

Thesis submitted on 20th December 2019
Graduation Colloquium on 31th March 2020
Accepted version

This Dissertation was funded by means of the Rosa-Luxemburg–Foundation, the German–French University and the German Ministry of Education and Research (BMBF) through the project Wachstumskern Flussstrom Plus.

Declaration

I hereby declare that I prepared the submitted work without inadmissible assistance and without the use of any aids other than those indicated. Facts or ideas taken from other sources, either directly or indirectly, have been marked as such. In particular, I did not use the services of a commercial graduation consultation. Furthermore, I have not made payments to third parties either directly or indirectly for any work connected with the content of the submitted dissertation. This work has so far not been submitted either in Germany or abroad in same or similar form as a dissertation and has also not yet been published as a whole.

Magdeburg, April 14, 2020 Stefan J. Hoerner

Du bout de l'horizon accourt avec furie
Le plus terrible des enfants
Que le Nord eût porté jusque-là dans ses flancs.
L'Arbre tient bon ; le Roseau plie.
Le vent redouble ses efforts,
Et fait si bien qu'il déracine
Celui de qui la tête au ciel était voisine,
Et dont les pieds touchaient à l'empire des morts.

Am Horizont in schwarzer Wolke zeigt sich
und rast heran, ein Sturmessausen;
des Nordens schlimmsten Wind hört man da brausen.
Fest steht der Baum,
das Schilfrohr aber neigt sich,
Der Sturm verdoppelt seine Wut
und tobt, bis er den fällt,
des stolzes Haupt dem Himmel sich gesellt
und dessen Fuß ganz nah dem Reich der Toten ruht.

The North sent forth her fiercest child,
Dark, jagged, pitiless, and wild.
The oak, erect, endured the blow;
The reed bowed gracefully and low.
But, gathering up its strength once more,
In greater fury than before,
The savage blast
Overthrew, at last,
That proud, old, sky-encircled head,
Whose feet entwined the empire of the dead!

from Le chêne et le Roseau, Jean de la Fontaine

Abstract

In this thesis, the fluid-structure interaction (FSI) on a vertical-axis water turbine (VAWT) with flexible blades is investigated using both numerical and experimental investigations.

A numerical study is presented, after a short overview of the peculiarities of VAWT and the current state of the investigations in FSI on VAWT is given. This numerical approach is based on the open source toolbox foam-extend. The code is evaluated and its functionality is extended. The simulation of an oscillating profile with strong deformations, including two-way coupling, is carried out by way of example with simplified fluid properties and without consideration of the composite materials. Although the complexity of the setup could not be fully modeled, the investigations provide an outlook for the potential and the limitations of a numerical approach.

In the experimental investigations, the complex multi-physical interactions in the rotor of a VAWT are partly reproduced in a surrogate model consisting of a single oscillating blade in a water channel. It is shown that, through the variation of oscillation trajectory and frequency, multiple turbine designs can be investigated without changing the hardware configuration. An experimental setup based on existing hardware is developed. A highly-accurate position control is obtained for the forced rotational oscillations, and a data acquisition framework is set up. Force and torque measurements show that flexible blades bring significant benefits for a tip-speed ratio $\lambda = 2$ over a wide range of turbine designs. In order to get deeper insight over the FSI at the blade level, the instantaneous flow field was captured in a time-resolved manner with high-speed, two-dimensional, two-component (2D2C) particle image velocimetry (PIV). An adaptive masking algorithm was developed in order to mask dynamic deformations of the structure. Periodic flow separation with strong, chaotic components is visualized; and the influence of the structural deformations is shown.

The structural deformations of the flexible blades were measured synchronized with the hydrodynamic forces and the position feedback of the drive. The interdependency between, on the one hand, turbine design and operating point, and on the other hand, blade deformation and the associated forces, is characterized. Two independent methods for the deformation measurement were developed and applied. The first measures the deformation of a single cross-section, with usage of the masking technique in raw images of the PIV measurements and a surface-tracking method. The latter is based on a structured light pattern projection on the surface which allows to achieve a measurement of the surface deformation with highly temporal and spatial resolution.

In the last section of the thesis, a spatial spectral analysis for the deformations, as well as a temporal spectral analysis of deformation along with forces and motion, are carried out. This allows to distinguish the deformation and hydrodynamic forces which are directly linked to the forced motion, from those resulting from secondary effects of the FSI.

Kurzzusammenfassung

In der vorliegenden Dissertation wird die Fluid-Struktur-Interaktion (FSI) an einer Vertikalachsigen-Wasserturbine (VAWT) mit flexiblen Schaufeln untersucht. In der Studie werden in der Hauptsache experimentelle Verfahren eingesetzt.
Ein numerischer Ansatz wird, nach einem kurzen Überblick über VAWT und dem aktuellen Stand der Technik zur FSI an VAWT, vorgestellt. Er basiert auf der Open Source Toolbox Foam-Extend, deren FSI toolkit zunächst evaluiert und dessen Funktionalität erweitert wird. Die Simulation eines oszillierenden Profils mit starken Deformationen, inklusive zwei-Wege-Kopplung wird für vereinfachte Fluideigenschaften und ohne Berücksichtigung der Kompositmaterialien exemplarisch durchgeführt. Die numerischen Untersuchungen geben jedoch nur einen Ausblick, da der vorgegebene Aufbau nicht in der erforderlichen Komplexität modelliert werden konnte.

Für das Experiment werden die komplexen, multiphysikalischen Wechselwirkungen im Rotor einer VAWT durch ein Ersatzmodell, bestehend aus einer einzelnen, oszillierenden Schaufel, vereinfacht. Im Abschnitt Modellierung wird gezeigt, dass durch die Variation der Oszillationstrajektorie und ihrer Frequenz mehrere Turbinendesigns ohne jegliche Hardwarevariationen untersucht werden können. Ein experimenteller Aufbau, basierend auf vorhandener Hardware, wurde entwickelt. Eine hochgenaue Lageregelung für die erzwungenen Drehschwingungen sowie ein Datenerfassungs–Framework wurden erstellt.

Kraft– und Drehmomentmessungen zeigen einen signifikanten Vorteil flexibler Schaufeln für eine Schnellaufzahl von $\lambda = 2$ und eine Vielzahl von Turbinenkonstruktionen. Für einen tieferen Einblick in die FSI auf Schaufelebene wurde das momentane Strömungsfeld mittels Particle-Image-Velocimetry (PIV) zeitaufgelöst erfasst. Ein Algorithmus wurde entwickelt, um dynamische Deformationen der Struktur zu maskieren. Die periodische Strömungsablösung mit hohen chaotischen Anteilen wird visualisiert und der Einfluss der strukturellen Verformungen gezeigt. Die Strukturverformungen der flexiblen Schaufeln wurden synchron mit den hydrodynamischen Kräften und dem Lagefeedback des Antriebs gemessen. Die Wechselwirkung von Turbinenkonstruktion und Betriebspunkt zu Verformung und daraus resultierenden Kräften wird charakterisiert. Es wurden zwei unabhängige Methoden für die Deformationsmessungen entwickelt und angewendet: Eine Verfolgung des Querschnitts der Struktur basierend auf der PIV und eine Oberflächenverfolgungsmethode. Letztere gründet auf einer strukturierten Lichtmusterprojektion auf die Oberfläche, die eine zeitlich und räumlich hoch aufgelöste Messung der Oberflächendeformation ermöglicht.

Im letzten Teil wird eine räumliche Spektralanalyse für die Verformungen sowie eine zeitliche Analyse der Verformung zusammen mit Kräften und Oszillation durchgeführt. Diese ermöglicht die Unterscheidung zwischen Verformungen und hydrodynamischen Kräften, die direkt mit der erzwungenen Bewegung und solchen, die mit den Sekundäreffekten der FSI zusammenhängen.

Resumé

Dans cette thèse, l'interaction fluide-structure (FSI) au sein d'une hydrolienne à axe vertical (VAWT) munie de pales flexibles est étudiée, avec une approche numérique et une approche expérimentale. Après une courte présentation des particularités des VAWT et de l'état de l'art de la recherche en FSI dans ces turbines, une étude numérique est présentée. Cette approche numérique est basée sur le logiciel open source foam-extend. Le code est évalué et ses fonctionnalités sont étendues. Une simulation d'un profil oscillant avec de fortes déformations est réalisée, incluant un couplage bidirectionnel ; dans cette simulation, les propriétés du fluide et de la structure composite sont significativement simplifiées. Bien que la complexité du cas d'étude ne soit pas entièrement modélisée, ce résultat fournit une première perspective sur le potentiel et les limitations d'une approche numérique.

Au sein de l'étude expérimentale, les interactions multiphysiques complexes au sein du rotor d'une VAWT sont modelisées avec un profil oscillant en veine hydraulique. Il est montré que de très nombreuses configurations de turbine peuvent être reproduites par variation de la trajectoire et de la fréquence du profil oscillant, sans nécessiter de changement du matériel expérimental. Une manipulation expérimentale est mise au point. Un contrôle précis de la position du profil est obtenu pour les oscillations forcées, et une chaîne d'acquisition de données est mise au point. Les mesures de force et de couple montrent que les pales flexibles fournissent un avantage significatif par rapport aux pales rigides pour une vitesse spécifique $\lambda = 2$, sur une large plage de configurations de turbine. Pour approfondir la compréhension de la FSI au niveau de la pale, l'écoulement instantané est capturé au fil du temps avec une vélocimétrie par image de particules (PIV) à haute fréquence, deux composants, et en deux dimensions (2D2C). Un algorithme de masquage adaptatif est développé pour masquer les déformations dynamiques de la structure. La séparation périodique de l'écoulement, avec de forts composants chaotiques, est visualisée ; l'influence des déformations structurelles est mise en évidence.

Les déformations structurelles des pales flexibles sont mesurées de façon synchronisée avec les forces hydrodynamiques et la position du servomoteur de la pale. L'interdépendance entre, d'une part, la configuration et la vitesse de la turbine, et d'autre part, la déformation de la pale et les forces associées, est caractérisée. Deux méthodes indépendantes sont mises au point et appliquées pour mesurer la déformation du profil. La première mesure la position d'une coupe du profil avec une technique de masquage des images obtenues par PIV. La seconde est basée sur la projection et la capture vidéo d'un motif lumineux projeté sur le profil ; elle permet de mesurer la déformation de la surface entière avec une haute résolution spatiale et temporelle.

Dans la dernière partie, une analyse spectrale spatiale des déformations, ainsi qu'une analyse spectrale temporelle des déformations, des forces et du mouvement, sont effectuées. Ce travail permet de faire la distinction entre les déformations et forces hydrodynamiques qui sont directement liées aux oscillations forcées, et celles qui découlent des effets secondaires de la FSI.

Nomenclature

Notes, Norms and Conventions:

The thesis spans over multiple disciplines, in which the same symbols are used to designate different physical entities, e.g. u which traditionally represents displacement in solid mechanics, X-component of flow velocity in fluid mechanics, and unsteady tension in electrical engineering. Conseqently, in this thesis, the use of symbols for some physical entities may appear somewhat exotic to the reader; the author apologizes for this inconvenience. Vectors are noted with underline, e.g. $\underline{u}$, and their magnitude without underlining. Tensors and matrices are noted with double underline: e.g. $\underline{\underline{R}}_Z(\alpha)$

Abbreviations

2D2C	Two dimensional two components
ALE	Arbitrary-Lagrangian-Eulerian
API	Application Programming Interface
BEP	Best-Efficiency Point
CFD	Computational Fluid Dynamics
CNC	Computational Numerical Control
CNRS	French National Center for Scientific Research
CR	Chargé de Recherche (scientific assistant position in French laboratories)
CSM	Computational Solid Mechanics
DAC	Data Acquisition Card
DFT	Discrete-Fourier-Transformation
FE	FOAM-extend
FEM	Finite Element Method
FFT	Fast-Fourier-Transformation
FS	Error in % to full scale
FSI	Fluid-Structure Interaction
FVM	Finite Volume Method
GGI	General Grid Interface
GPLv3	General Public License, version three
GUI	Graphical User Interface
h5/hdf5	Hierachical Data Format v.5 (file format)
HAWT	Horizontal Axis Water Turbines
HPC	High-Performance Computing
IR	Research Engineer
JSON	JavaScript Object Notation file format
LAN	Low Area Network
LDV	Laser Doppler Velocimetry
LEGI	Laboratory of Geophysical and Technical Flows in Grenoble, France
LES	Large-Eddy-Simulation
LSS	Laboratory of Fluid Mechanics and Fluid Dynamics in Magdeburg, Germany
NACA	National Advisory Committee for Aeronautics (precursor of NASA)
PIV	Particle-Image Velocimetry
PTV	Particle-Tracking Velocimetry
R	Error in % to reading
RAM	Read Access Memory
RANS	Reynolds-Averaged Navier-Stokes
RBM	Rigid Body Motion
RGB	Color model based on red, green and blue light
RMS	Root Mean Square

SFT	Surface Tracking
SVG	Scalable Vector Graphics file format
TPS	Thin-Plate-Spline
VAWT	Vertical Axis Water Turbines
VTK	Visualization Toolkit (file format)

Coefficients

c_C	cross-talk coefficient [-]
c_L	drag force coefficient [-]
c_L	lift force coefficient [-]
c_M	motor torque coefficient [-]
c_N	normal force coefficient [-]
c_P	power coefficient [-]
c_T	thrust coefficient [-]

Dimensionless Numbers

Re	Reynolds number [-]
Sr	Strouhal number [-]

Greek symbols

α	angle of incidence [rad]
α'	pitched blade angle of incidence [rad]
Δ	difference, shift [-]
$\dot{\alpha}$	pitching foil angular velocity [rad/s]
ϵ	relative elongation [-]
ϵ_{small}	10^{-15} [-]
γ	pitch angle [rad]
ι	imaginary number [-]
λ	tip speed ratio $\lambda = \frac{u}{v_\infty}$ [-]
$\lambda_\sim$	wave length [m]
λ_{solid}	second Lamé coefficient [-]
μ_{solid}	first Lamé coefficient [-]
ν	dynamic viscosity [m^2s]
ν_{solid}	Poisson ratio [-]
ω	angular velocity [rad]
Φ	refraction angle [rad]
ϕ	phase angle [rad]
ρ	density [kg/m^3]
σ	solidity $\sigma = \frac{nC}{R}$ [-]
τ	thickness [m], relative thickness [-]
θ	azimuth (rotor) angle [rad]
ζ	deformation angle [rad]

Superscripts

$'$	shifted, apparent
$\bar{}$	average
$\dot{}$	time derivative $\frac{\mathrm{d}}{\mathrm{d}t}$
$\hat{}$	amplitude

Symbols

b	width [m]
d	displacement, deformation [m]
f	frequency [Hz]
f_{b}	mass-specific body force [N/kg]
h	height [m]
k	reduced frequency [-]
$k_\sim$	wave vector [1/m]
l	length [m]
n	number [-]
p	pressure [Pa]
pi	pivot [m]
px_{size}	pixel size [m]
q	line load [N/m]
r	uncertainty [%]
s	surface area [m^2]
s_{f}	safety factor [-]
t	time [s]
v	velocity [m/s]
C	chord of the profile [m]
D	distance [m]
E	Youngs modulus [N/m^2]

F	force [N]
I	geometrical moment of inertia [m^4]
I_e	electrical current [A]
K	stiffness [N/m]
M	moment [Nm]
N	cycles until material failure [-]
P	power [W]
R	radius [m]
S	stress [MPa]
T	oscillation period [s]

Subscripts

$_{ch}$	water channel
$_{max}$	maximum
$_{o}$	oscillation
$_{pos}$	position
$_{pro}$	projected
$_{px}$	pixel
$_{rec}$	recorded
$_{ana}$	analytic
$_{exp}$	experiment
$_{reatt}$	reattachment
$_{sim}$	simulation
$_{solid}$	variable used in solid mechanics
$_{stall}$	stall
$_{i}$	position in Y-axis on the pixel grid
$_{j}$	position in X-axis on the pixel grid
$_{n}$	node
$_{t}$	position in the time line of a recording
$_{x}$	in X-axis
$_{y}$	in Y-axis
$_{z}$	in Z-axis
$_{c}$	capturing
$_{D}$	Vertical-Axis (Darrieus) Turbine
$_{PC}$	between projector and camera
$_{BEP}$	best-efficiency-point

Vectors and Matrices

$\underline{\omega}$	angular velocity [rad/s]
$\underline{u}$	tangential velocity $\underline{\omega} \times \underline{R}$ [m/s]
$\underline{v_\infty}$	free-stream velocity [m/s]
$\underline{w}$	relative velocity $\underline{v_\infty} = \underline{u} + \underline{w}$ [m/s]
$\underline{\underline{D}}_{solid}$	damping matrix (solid mechanics)
$\underline{\underline{I}}_{id}$	identity matrix
$\underline{\underline{K}}_{solid}$	stiffness matrix (solid mechanics)
$\underline{\underline{M}}_{solid}$	mass matrix (solid mechanics)
$\underline{\underline{R}}_Z(\alpha)$	matrix for a rotation in Z-axis for angle α [rad]

Contents

Nomenclature ix
Table of Contents xii
List of Figures xvi
List of Tables xvii

1 Introduction **1**

2 VAWT **7**
2.1 Fluid mechanics 8
2.2 Optimization methods 13
2.2.1 Shape optimization 13
2.2.2 Blade pitch methods 14
2.2.3 Bioinspired methods 15
2.3 Research methodology 17
2.3.1 Experiments 17
2.3.2 Numerics 18

3 Numerics **21**
3.1 Computational fluid dynamics 21
3.2 Fluid-structure interaction 23
3.3 FSI modeling with *foam-extend* 26
3.4 Validation of the existing code 31
3.5 Code development 32
3.5.1 Solver adaptations regarding mesh motion 32
3.5.2 Integration of the body forces 34
3.6 Single material test case 34
3.7 Multi material test case 38
3.8 Conclusions and outlook 40

4 Experimental setup **42**
4.1 Modeling 43
4.2 Experimental design 44
4.2.1 Experimental facilities 45
4.2.2 Drive system 47
4.2.3 Measurement instrumentation and software 50
4.2.4 Measurement uncertainty 52

4.3 Flexible blades . . . 54
4.3.1 Design . . . 55
4.3.2 Determination of the material properties . . . 57
4.3.3 Manufacturing . . . 59

5 Measurements **62**
5.1 Active pitch . . . 63
5.1.1 Optimization method and experimental design . . . 63
5.1.2 Results . . . 66
5.2 Force and torque . . . 68
5.2.1 Setup and preliminary considerations . . . 69
5.2.2 Results of static force measurements . . . 70
5.2.3 Results of the dynamic force measurements . . . 71
5.2.3.1 The λ=2 case . . . 71
5.2.3.2 The λ=3 case . . . 76
5.2.4 Conclusions of the force and torque measurements . . . 80
5.3 Structural deformation - SFT . . . 81
5.3.1 Object distance and refraction . . . 83
5.3.2 Setup . . . 84
5.3.3 SFT: Methodology . . . 85
5.3.4 Software development . . . 88
5.3.5 SFT: Surface calibration . . . 89
5.3.6 Method validation . . . 91
5.3.7 Results and discussion . . . 93
5.3.7.1 Preliminary considerations . . . 93
5.3.7.2 The λ=2 case . . . 95
5.3.7.3 The λ=3 case: . . . 100
5.3.8 The influence of k_o and λ . . . 101
5.3.9 Conclusions of the SFT measurements . . . 103
5.4 Particle Image Velocimetry . . . 105
5.4.1 Methodology . . . 106
5.4.2 Setup . . . 107
5.4.3 Preprocessing and masking . . . 108
5.4.4 Processing . . . 109
5.4.5 Post-processing . . . 109
5.4.6 Software . . . 111
5.4.7 Uncertainty estimation . . . 111
5.4.8 Results and discussion . . . 113
5.4.9 Conclusions . . . 118
5.5 Structural deformation - CST . . . 119
5.5.1 Method . . . 119
5.5.2 Validation . . . 122
5.5.3 Conclusions of the CST measurements . . . 124

6 Post-processing **125**
6.1 Natural frequencies 126
6.2 Forces and oscillations 130
6.3 Deformation 132
6.4 Flow field 134
6.5 FSI – spectra 137
6.6 FSI – synopsis 141
6.7 Conclusions 148

7 Summary and outlook **149**

References **162**

List of Figures

1.1 Evolution of sea level and global temperature 1
1.2 Hydroquest - concept 2
1.3 Area-based power density of VAWT 4
1.4 Flexibility raises thrust efficiency 5

2.1 Speed triangles and turbine 7
2.2 Angle of incidence and relative speed 9
2.3 Influence of the solidity 11
2.4 Influence of tip-speed ratio and reduced frequency 12
2.5 2D Simulation of a VAWT 13
2.6 Optimization of the foil shape 13
2.7 Passive pitch methods 14
2.8 Influence of flexibility to the power 15
2.9 Influence of flexibility on the shape 16
2.10 Vorticity distribution in a VAWT 17
2.11 Stress distribution and deformation in a flexible blade 19
2.12 Frozen rotor setup 19

3.1 Three dimensional mesh and vorticity field for a VAWT 22
3.2 Two-dimensional simulations 22
3.3 FSI grid coupling 23
3.4 Two-way coupled segregated FSI 25
3.5 Setup of the numerical FSI case 29
3.6 foam-extend: deflection with grid and stress distribution 32
3.7 Detail of the FSI grid deformation 33
3.8 *fsiFoam* code validation: test case velocities 35
3.9 *fsiFoam* code validation: test case I solid detail 37
3.10 *fsiFoam* code validation: Combined FSI and RBM displacement . . . 37
3.11 *fsiFoam* code validation: Isolated FSI deformation 37
3.12 *fsiFoam* code validation: stress distribution 39
3.13 *fsiFoam* code validation: deformations,stress and velocity fields 40

4.1 α and $\dot{\alpha}$ on a turbine blade 43
4.2 Experimental test section 45
4.3 LEGI hydrodynamic tunnel 46
4.4 Workflow of the curve shape generation 48

4.5 Torque measurement via drive . . . 49
4.6 Bifurcal distribution . . . 50
4.7 Flow chart main experiment . . . 51
4.8 Error estimation F_X . . . 53
4.9 Static lift and drag measurement . . . 54
4.10 Design of the flexible foil . . . 55
4.11 Clamped beam . . . 55
4.12 Carbon composite Young's modulus . . . 57
4.13 Tensile test of the silicone . . . 59
4.14 Maximal elongation of the silicone . . . 59
4.15 Flexible hydrofoil in the casting mold . . . 60
4.16 The flexible hydrofoil mounted in the waterchannel . . . 60

5.1 Trajectory and pitch motion . . . 63
5.2 Experimental setup of the pitch angle optimization . . . 64
5.3 Generation of the knots for the base spline . . . 65
5.4 Flowchart hardware in the loop . . . 65
5.5 Optimal spline . . . 66
5.6 Thrust coefficient evolution during hardware-based optimization . . . 66
5.7 Lift and drag forces pitch optimization . . . 67
5.8 Variations of the reduced frequency . . . 69
5.9 Static lift plotted as a function of drag for all hydrofoils . . . 70
5.10 Forces at λ=2 for k_o=0.026 and k_o=0.277 . . . 71
5.11 Forces at λ=2 for k_o=0.45 and k_o=0.0.73 . . . 73
5.12 c_T at λ=2 . . . 74
5.13 $\hat{c}_N$ λ=2 . . . 74
5.14 Thrust-to-normal-force ratio η at λ=2 . . . 75
5.15 Forces at λ=3 for k_o=0.069 and k_o=0.130 . . . 76
5.16 Forces at λ=3 for k_o=0.241 and k_o=0.344 . . . 77
5.17 Forces at λ=3 for k_o=0.486 and k_o=0.653 . . . 78
5.18 c_T at λ=3 . . . 79
5.19 $\hat{c}_N$ at λ=3 . . . 79
5.20 Thrust-to-normal-force ratio η at λ=3 . . . 80
5.21 SFT fringe pattern detail . . . 82
5.22 Surface tracking setup . . . 83
5.23 SFT refraction magnification . . . 84
5.24 Resizing of the SFT result matrix . . . 86
5.25 Topology of the SFT algorithm . . . 88
5.26 SFT comparison of the surfaces . . . 90
5.27 SFT calibration . . . 91
5.28 Temporal point height and error . . . 92
5.29 SFT spatial error . . . 93
5.30 Deformation angle β . . . 94
5.31 Chordwise difference rigid to flex[03] over time . . . 95
5.32 Hydrodynamic forces and deformation . . . 96

5.33 Hydrodynamic forces and deformation, λ=2, k_o=0.06 97
5.34 Hydrodynamic forces and deformation, λ=2, k_o=0.16 97
5.35 Hydrodynamic forces and deformation, λ=2, k_o=0.28 98
5.36 Hydrodynamic forces and deformation, λ=2, k_o=0.33 98
5.37 Hydrodynamic forces and deformation, λ=2, k_o=0.45 99
5.38 Hydrodynamic forces and deformation, λ=2, k_o=0.71 99
5.39 Hydrodynamic forces and deformation, λ=3, k_o=0.13 101
5.40 Hydrodynamic forces and deformation, λ=3, k_o=0.24 102
5.41 Hydrodynamic forces and deformation, λ=3, k_o=0.65 102
5.42 Maximum relative deformation over reduced frequency 103
5.43 Light sheets of the measurements 105
5.44 Raw image of the PIV recordings 105
5.45 PIV hardware setup 106
5.46 Corrected PIV mask 108
5.47 PIV data processing 109
5.48 Low correlation vector treatment 110
5.49 PIV data post-processing 111
5.50 Comparison of the results from *DaVis* and *Fluidimage* 112
5.51 PIV: Confinement for rigid hydrofoils 114
5.52 PIV influence of k_o 115
5.53 PIV: stalling rigid at $k_o = 0.38$ 116
5.54 PIV: tail flapping $k_o = 0.38$ 117
5.55 PIV: tail flapping $k_o = 0.38$ 117
5.56 PIV raw data 119
5.57 Summed PIV images 120
5.58 CST method 120
5.59 Binarized neighbors and filtering 121
5.60 Structure from segmentation algorithm 121
5.61 Deformation measurements methods comparison k=0.14 & 0.16 . . . 122
5.62 Deformation measurements methods comparison k=0.28 & 0.28 . . . 123
5.63 Deformation measurements methods comparison k=0.38 & 0.33 . . . 123

6.1 Experimental setup natural frequencies 126
6.2 Excitation and DFT of the flexible hydrofoil 127
6.3 First and third normal mode, numerically and measured 128
6.4 Spring mass system 129
6.5 Spectra of the static measurements 130
6.6 Spectra of a stalled flexible hydrofoil at α=20° 130
6.7 Spectral analysis of the forces 132
6.8 Chordwise motion over time and 2D-FFT of the motion 133
6.9 Point spectra for the flow field at k_o=0.38, rigid hydrofoil 135
6.10 Two-dimensional spectra of the fluid velocity field 136
6.11 Summed point spectra of the flow field 137
6.12 Spectra of drive motion, loads, solid and fluid 138
6.13 Detail of the spectra of drive motion, loads, solid and fluid 140

6.14 FSI overview: k_o=0.06 142
6.15 FSI overview: k_o=0.14 144
6.16 FSI overview: k_o=0.28 145
6.17 FSI overview: k_o=0.36 147

List of Tables

3.1 3D simulation 21
3.2 2D simulation 21
3.3 Specifications of clamped single material beam case 31
3.4 Material properties for the multi-material case 31

4.1 "LEGI turbine" specifications 45
4.2 LEGI water tunnel 46
4.3 LEGI drive system specifications 47
4.4 Six-axis load cell specifications 50
4.5 Material specifications 57

5.1 SFT calibration matrix 90
5.2 Error determination I 94
5.3 Error determination II 94
5.4 Laser I specifications 107
5.5 Laser II specifications 107
5.6 Phantom V2511 High Speed Camera 107
5.7 *DaVis* and *Fluidimage* software settings 112
5.8 High speed videos 113
5.9 SFT/PIV couples 113

6.1 Natural frequencies of the hydrofoils (free vibration) 129
6.2 Natural frequencies of the hydrofoils (water tunnel) 131

Chapter 1

Introduction

Climate change (see fig.1.1), pollution, the resulting strictly negative effects on biota and humanity, as well as the catastrophes of Chernobyl and Fukushima, all force us to change our global energy provision strategies away from fossil and nuclear, towards renewable resources and low-risk technologies.

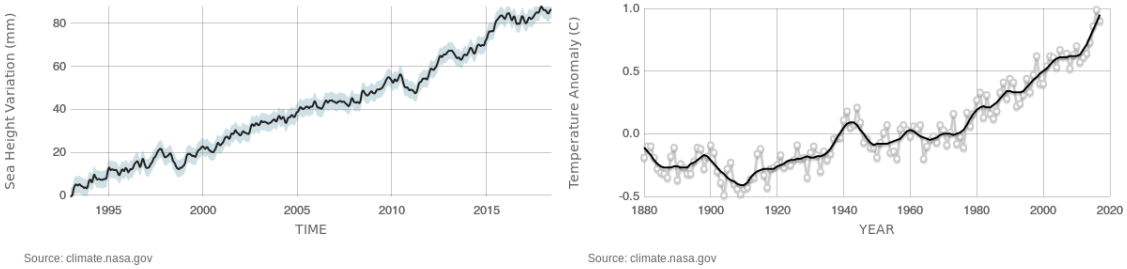

Figure 1.1: Evolution of sea level and global temperature, indicators for climate change from NASA Earth Science Communications Team (44)

As of the beginning of this millennium the strategies for a transition into renewable energy resource exploitation are mainly based on biomass, wind, hydro and solar energy conversion. Significant efficiency improvements and low prices for solar cells led to a bounce up in the installed power of factor 304 from 2000 to 2016, up to 304 GW. In the same time period, wind power has been growing by a factor 27 to 486 GW, while biomass increased up to 111 GW (110). Nevertheless, the unsteady character of wind and solar energy is a challenge for grid stability. In the last century, contributions to electrical power supply came essentially from a small number of thermal power plants. This structure was an advantage for the grid control strategies at the time - they were designed top-down with central governing system - but is nowadays a drawback for volatile renewable energies. Wind farms are regularly driven down to maintain grid stability while coal-fired or nuclear power stations remain operating at full load. The time those stations require to power down is larger than the duration of the fluctuations in wind and solar power. Besides innovative storage technologies, like power-to-gas or clustered battery storage in electric vehicles, the need for better power control for grid stabilization rises and is crucial for a successful change in the world's energy exploitation strategy.

Hydropower constitutes the oldest and largest share of renewable energies; this share is still growing - from 688 GW in 2000 to 1103 GW in 2016 (110). It is suitable to cover base load and has a high availability, which provides grid stability if it is used for grid control. This predestines hydropower to close the gap between the volatile renewable energies and the demand of a continuous power supply, in order to cover the worlds energy demand with 100% renewable low-carbon sources.

Unfortunately, in spite of this large advantage, conventional hydropower lacks sustainability. Classical turbines convert potential energy into mechanical and then (with a generator) into electrical energy. Three turbine families cover most of the hydropower market. They are classified according to hydraulic head - the potential energy resulting from the height difference from upstream to downstream - and mass flow. Pelton turbines operate under highest head with relative low mass flow; Francis turbines cover intermediate conditions, and Kaplan turbines operate under low head with high mass flow. All those systems provide highest efficiency in a fully canalized or ducted flow, but require a dam to generate hydraulic head and require in consequence a high constructional effort as well as high investments.

In Germany, most of the sites for classical hydropower facilities in large rivers are already exploited, taking into account political, social and environmental aspects, e.g. the EU Water Framework Directive. An increase in output of this resource can be mainly provided by upscaling or so-called repowering of existing power plants. The construction of new facilities is - according to this - less a technical than an environmental and political issue and plays no role in the scope of the national strategy for an energy transition (46). The main reasons for this fact is the negative social and environmental impact of dams as documented e.g. by Rosenberg et al. (112). For mega projects like the Three Gorges Dam in China, this impact is well known and nowadays indisputable, even if a detailed assessment of the full range is challenging due to the far-reaching consequences and its complexity (Tilt et al. (121)). But even small constructions obstruct rivers and hinder the migration of aquatic fauna. In consequence, the development of so-called "fish-friendly" solutions and new methods for their ethohydraulic evaluation is of recent research interest, see Baki et al. 2017 (13; 14) or Müller et al. 2019 (101). The significance of these studies becomes evident once one considers the more than 450 000 test animals deployed for the evaluation of mortality and harm of aquatic fauna due to migration of hydropower facilities in Germany in 2015 (54). Fishes mainly get injured either by a direct hit or crush, like in between turbine and guiding vanes, or through the enormous pressure drop in the

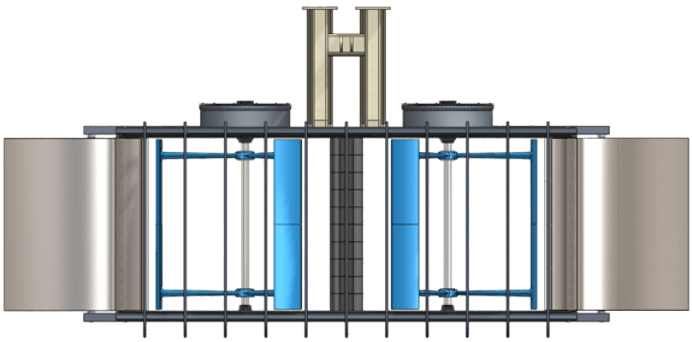

Figure 1.2: River turbine concept with two counter rotating rotors from Hydroquest - a start-up as spin-off of LEGI Grenoble (69)

runner which leads to internal organ damage as shown by Stephenson et al. 2010 (117) or Fu et al. 2016 (52).

Regarding the high restrictions for river oriented hydropower and the resulting small remaining potentials, the exploitation of marine energy resources, like tidal or marine currents, would provide a vast, nowadays almost unused renewable energy source. It is maybe one of the currently most promising and challenging tasks in renewable energy engineering: The technology must satisfy the rough conditions of a marine environment and saltwater but also the demand of sustainable technologies with low ecological impact. This, in combination with the need for high efficiency, results in contradicting requirements for a turbine design.

In this context, hydrokinetic turbines (see fig.1.2) could provide a simple and robust technology which would allow to overcome the drawbacks of conventional hydropower technology. They promise to be a low-risk and low ecological impact technology: No fish injury was reported in turbine assessments for marine current turbines operating with low rotational speed, performed by Amaral et al. 2011 (2) or Zhang et al. 2017 (134). Hydrokinetic water turbines mostly operate under low tip-speed ratio (λ, see later eq. (2.2)) conditions compared to wind turbines. This is due to their high solidity (σ, see eq. (2.8)), which is required by the higher density of water. Fish impact probability models, as those introduced by Turnpenny et al. 2000 (126) or Deng et al. 2007 (40), focus on the rotational speed of the rotor; the impact risk rises along with a rising rotor frequency. The pressure drop, which is the other main reason for the injury of fish in turbine passages (Stephenson et al. 2010 (117)) is negligible in hydro-kinetic turbines.

Nevertheless, both low pressure drop and low rotation speed reveal the system-immanent drawback of such facilities: According to Cleynen et al. 2017 (28), the available energy in a free-stream installation is significantly lower as for conventional systems, and their efficiency is much lower as well. The situation is similar as that of solar and wind power devices, which also suffer from a poor area-based energy density compared to thermal power plants.

All these renewable energy technologies need in consequence a lot of space to compensate this low power density. This is not always problematic for house roofs, but it is an important issue for large-scale wind farms. The resistance of local population against the development of new wind farms all over the planet shows that in developed countries, a saturation effect is reached in regions of highest potential. This is in particular true when the local population neither is included in the decision-making process, nor benefits from the installations, which is still often the case.

Ocean turbine farms could provide access to new energy resources with an enormous potential. Resistance from local population can be avoided by participation on the benefits and in the decision processes. Ecologist activists are not expected to protest if these farms are installed in a submarine park that exploits the marine currents in a proven sustainable way with low ecological impact. In this case, the low power density would not hinder their installation. However, the marine environment makes for harsh conditions, such as salt water or eddies, in a size of multiple times of the scale of the turbine. In consequence, the installed facilities should be very robust

and require low maintenance.

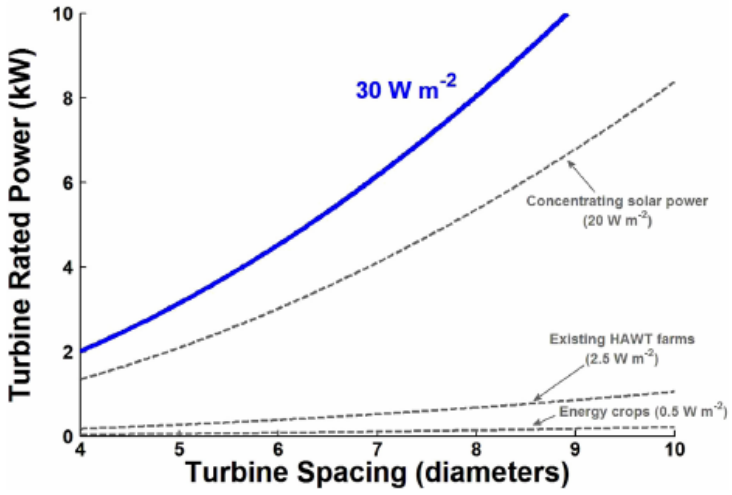

Figure 1.3: Area-based power density for VAWT (blue line) compared to several other renewable energy resources (30). The numbers in this diagram are for wind turbines. The power density of water turbines is an order of magnitude higher, because the density of water is 800 times that of air.

Vertical-axis water turbines (VAWT) are of special interest in the group of hydrokinetic turbines. One significant advantage is their simple design, without need for housing, guiding vanes or yaw control. This is also of interest from the ethohydraulic point of view, as there is less potential to harm the aquatic fauna. However, their most important feature is their order-of-magnitude higher area-based efficiency for array installations in farms (see fig.1.3), compared to other competing technologies as shown by Whittlesey et al. 2010 (130), Dabiri 2011 (30) and Brownstein et al. 2016 (21). This is an obvious advantage compared to horizontal-axis water turbines (HAWT) in farm installations, even if VAWT can nowadays not compete against them in terms of single turbine efficiency. Common magnitudes for maximum power coefficients found in literature are about $c_{p_{\max}}$=0.35, as experimentally measured by Maître et al. 2013 (91). In this context, farm installations for tidal and ocean currents would open vast potentials. The french start-up Hydroquest operates in this field and works intensively on a device for marine currents, after a first product for river currents in 2018 shown in fig.1.2 (69).

Although their design is simple, VAWT feature complex fluid flow. Because of the vertical axis, the flow streams crosswise through the rotor, passing the rotor blades twice, once in the upstream and once in the downstream part. The tangential speed of the blade with incoming free-stream velocity results in a relative velocity and an angle of incidence on the blade which both vary with the azimuth angle; this variation depends on the operating point of the turbine. For low-λ operating points (λ <3), the flow in the rotor region is dominated by highly unsteady hydrodynamics, such as dynamic stall as reported by Laneville & Vittecoq 1986 (77) and later shown with Particle-Image Velocimetry measurements such as Fujisawa & Shibuya (53), Ferreira et al. 2009 (48), Gorle et al. 2014 (55) and Buchner et al. 2018 (23). These conditions generate cyclic structural load peaks and can lead to material failure from fatigue, which is an important point in the design of a VAWT (23). Additionally, the efficiency in low-λ operating points is low for conventional VAWT designs as

Figure 1.4: The flexibility of flukes raises the thrust efficiency of bottlenose dolphins (Tursiops Truncatus) by approximately 20% (51). Bionical approaches investigate possibilities to improve VAWT by the use of flexible blades

experimentally shown by Shiono et al. 2000 (116).

According to Buchner et al. 2018 (23), the phenomenon of dynamic stall shows non-linear, chaotic characteristics with high instability: already small differences in the flow conditions can provoke massive changes in the resulting flow. The numerical modeling of these flow conditions and its impacts on the applications like turbomachinery or micro-aircrafts is challenging. Accurate results already on simplified geometries, like pitching plates, demand costly three dimensional simulations with high spatial and temporal resolution according to Zanotti et al. 2014 (132). Even if the loads, provided from integral forces of pressure and shear on a VAWT can successfully be reproduced with numerical methods like Large or Detached Eddy-Simulations, the underlying flow dynamics like vortex structure, the insetting of the leading edge vortex or the occurrence of the vortex shedding are still not reproducible with good accuracy as reported by Ferreira et al. 2007 (47). This leads to an ongoing interest in experimental research on dynamic stall and its influence on VAWT like Buchner et al. 2017 (22) or Miller et al. 2018 (96) or on a focus on simplified models like pitching plates or profiles, like Benton & Visbal 2019 (18) in order to provide deeper insights in the underlying mechanism or to develop control strategies for technical applications, like Müller et al. 2014 and 2016 (99; 98).

In summary, the study of VAWT is a challenging task in fluid dynamics and experimental investigations are of high interest.

In literature with application on the optimization of VAWT, three main approaches were mostly chosen for single-turbine efficiency improvements: 1) Based on the geometry, with optimization of the blade shape or housing; 2) based on smart control, active or passive pitch of the blade with respect to the azimuth angle; and 3) based on bioinspired methods.

A well known bioinspired approach - with overlap to the first method - is to control and improve the stall characteristics of a hydrofoil with the use of an optimized morphology, e.g. protuberances or tubercles on the leading edge as shown by Hansen et al. 2016 (58), or Pérez-Torro & Kim 2017 (109). The present work also focuses a bioinspired approach: Its aim is to characterize these complex turbine dynamics in interaction with highly flexible blades. In aquatic life, structures used for propulsion, like fins or membranes, are flexible. Fish showed in 1993 (51) that the flexibility in flukes significantly raises the propulsive efficiency of bottlenose dolphins (see fig.1.4).

Adjusted flexible structures can adapt to the flow by deformation. Artificial flexible composite structures can reproduce this effect with adapted stiffness which can be set by design.

The study at hand is focused on the benefit of flexible blades in a H-Darrieus turbine, considering both experimental and numerical methods. A second objective is the characterization of the underlying interactions of fluid and structure on blade level. As a consequence, the thesis is divided in seven parts. After this introduction, a short general overview of the fluid mechanical characteristics of VAWT is given (sec.2). The following chapter focuses on the numerical investigations: modelization, code development and testing (sec.3). It is followed by the experimental part (sec.4), which starts with the setup and the underlying experimental modeling. Measurement methodologies for forces, fluid and structure, relevant code development, as well as the corresponding results are presented in the subsequent chapter (sec.5). In the post-processing part (sec.6), the interaction between fluid and structure is analyzed with frequency spectra. In the last chapter, a synopsis of the experimental and numerical results is carried out (sec.7).

Chapter 2

Vertical-Axis Turbines

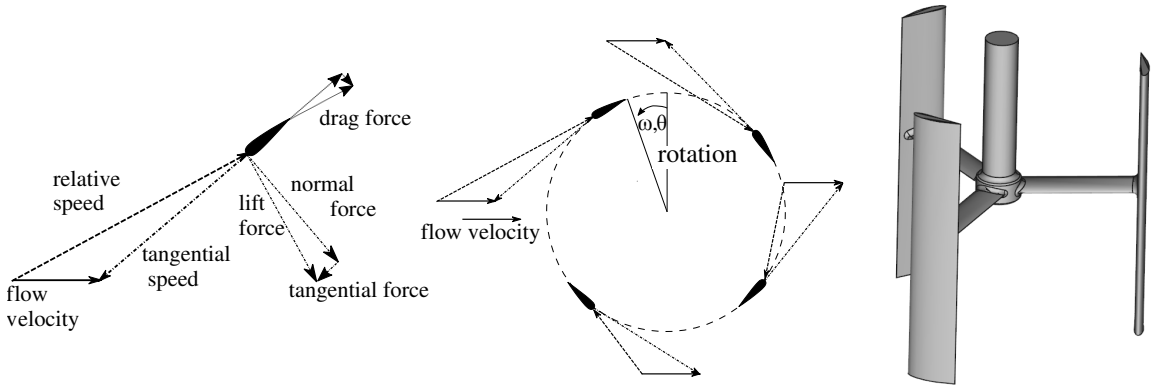

Figure 2.1: "Left and center: hydraulic forces and velocity triangles on a VAWT at $\lambda \approx 2.2$ for four azimuth angles: the angle of incidence varies with azimuth angle θ and tip-speed ratio. Only the tangential part (sinusoidal share) of the lift force generates thrust. Most of the hydrodynamic forces result in structural loads. Drag forces were scaled up for better readability. Right: Three-bladed H-Darrieus turbine rotor.", Reprinted from (65)

According to their name, hydrokinetic turbines convert the kinetic energy of the flow into mechanical energy. The contribution of potential energy and pressure gradients is negligible. They can be classified according to their axis of rotation, e.g. vertical-axis turbines and horizontal-axis turbine, like the commonly used wind turbines. But they can also be grouped according to their operating principle: a common classification is to distinguish between drag-driven devices, such as undershot waterwheels or Savonius turbines, and lift-driven devices, like modern wind turbines or Darrieus turbines. Drag-driven systems are robust and easier to construct, but suffer from poor single-turbine performance compared to lift-driven devices. In order to compare different turbines, the performance is made dimensionless by the relation of the power output to the available kinetic energy for the projected turbine area:

$$c_P = \frac{P}{0.5 \cdot \rho \cdot s \cdot v_\infty^3} \tag{2.1}$$

Current Savonius turbines have a best-efficiency point (BEP) with c_P=0.25 (Kerikous & Thévenin 2019 (71)) while commercial (lift-driven) wind turbines provide a c_P=0.5 (45). Darrieus turbines perform in the range in between with c_P=0.35 (Maître et al. 2013 (91)).

There is a maximum achievable power coefficient c_P for kinetic turbines. The so-called Lanchester-Betz-Joukowsky limit is set to 16/27 or 0.593 for horizontal turbines. For vertical-axis cross-flow turbines, a comparable limit a with slightly higher magnitude was formulated from momentum based models: Loth & McCoy 1983 implemented a model for a straight-bladed Darrieus turbine and received a physical limit of $c_{P_{max}}$=0.61 (85). Newman 1986 found $c_{P_{max}}$=0.64 (103). In all cases, the difference with horizontal-axis machine models is that the turbine is modeled with multiple (n>1) actuator discs, thus reaching beyond the model of Lanchester-Betz-Joukowsky because energy is extracted in multiple stages.

A deeper understanding of the flow in VAWT may allow to raise this c_P to values even higher than known these days for HAWT.

The first occurrence of Darrieus turbines is a French patent (79) dated to 1925. A later US patent (1931) named Georges Darrieus as patent holder (31) and led to the turbine's name. The three-bladed rotor was of troposkein shape, which allowed to reduce blade stress (Paraschiviou 2002 (104)). Another approach introduced by Gorlov 1995 are twisted blades (56), in order to reduce torque ripple.

Current development is mostly focused on straight-bladed turbines (see fig. 2.1 right). This allows to use low-cost extruded aluminum profiles for the blades, leads to simpler geometries, and is more efficient in the exploitation of the area facing the flow. Subsequently, the term VAWT is used in what follows as a synonym for a straight-bladed Darrieus water turbine. Drag-driven devices are not in the scope of the thesis.

2.1 Fluid mechanical peculiarities

The fluid mechanical characteristics of VAWT are governed by the effects of the vertical rotation axis and the absence of a guiding structure. The sum of the tangential speed $\underline{u}$ of a blade (which is the cross product of the rotor's angular velocity $\underline{\omega}$ and the radius $\underline{R}$) and the free-stream velocity $\underline{v_\infty}$ is the relative velocity $\underline{w}$ (with an angle of incidence α) in the local reference frame of the blade (see fig. 2.1). α and $\underline{w}$ vary with the rotor or azimuth angle θ. Here, the crucial parameter is the tip-speed ratio λ, the ratio of the tangential velocity to free-stream velocity (see fig. 2.2):

$$\lambda = \frac{\omega_\mathrm{D} R}{v_\infty} \tag{2.2}$$

Theoretically, both α and w can be found through geometrical dependence from λ and θ:

$$\alpha = \arctan\left(\frac{\sin\theta}{\lambda + \cos\theta}\right) \tag{2.3}$$

$$w = v_\infty \sqrt{1 + 2\lambda\cos\theta + \lambda^2} \tag{2.4}$$

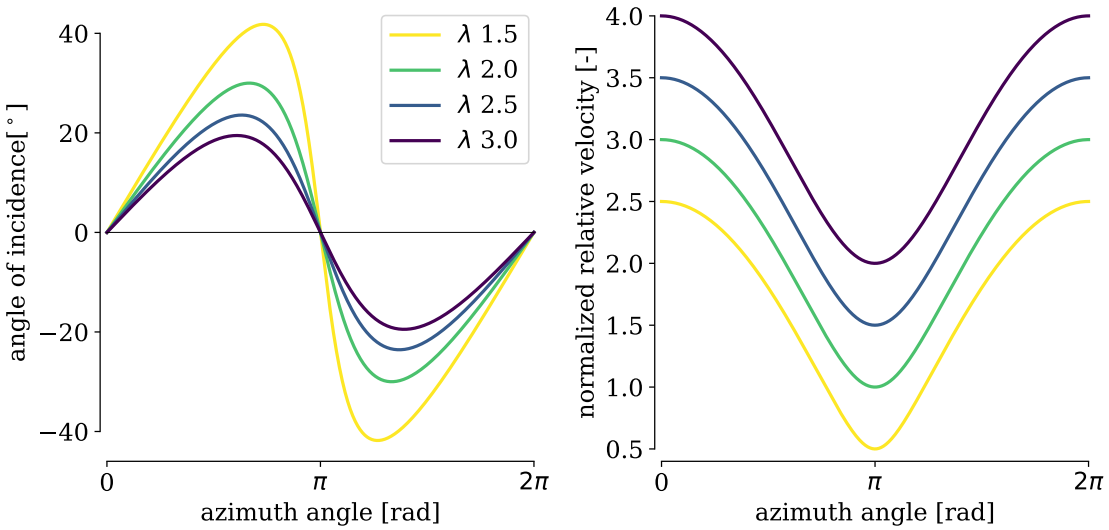

Figure 2.2: Left: α as a function of θ and λ. The maximum angle of incidence α_{max} reduces with increasing tip-speed ratio. Right: The relative speed $w_{norm} = w/v_\infty$ as a function of θ and λ. w_{max} for λ=3 is four times v_∞

The influence of both parameters can be found in fig. 2.2. In a real turbine the wake of the upstream section highly influences the flow of the downstream section. The resulting angles of incidence are reduced significantly by this effect, as reported by Delafin 2014 (39).

The trajectories in fig. 2.2 show that $\alpha_{\max}$ for λ <4 is higher than the static stall angle α_{stall} for commonly-used symmetric NACA profiles. A NACA0018 stalls at about 15° at Reynolds numbers of magnitudes of 10^5. According to Leishman 2002, stall always occurs if $\alpha > \alpha_{\text{stall}}$ (80), which is true for the case of static and quasi-static angles of incidence as they appear in HAWT. The flow characteristics in VAWT, however, are highly unsteady, and the blades operate under dynamic conditions.
Dynamic stall is a phenomenon that differs drastically from static stall, because the stall point and its characteristics not only depend on α but also on the time scale of the pitch motion in relation to the time scale of the vortex convection over the foil by the flow. According to McCroskey et al. 1976, the ratio between those factors is called reduced frequency k; together with the maximum angle of incidence $\alpha_{\max}$, it is the governing factor in dynamic stall (95). Dynamic stall is a phenomenon extensively studied for helicopter aerodynamics, which have some similarities to VAWT, due to the cross-flow rotation axis of their rotors.

The motion of a structure influences the surrounding flow and changes the stall characteristics compared to a static case. As consequence of the motion, the boundary layer separates from the surface and vortices at leading and trailing edge will appear (Buchner et al. 2017 (22)). These vortices will continuously grow and may cover the full surface of the structure until they shed. The leading edge vortex is known to induce higher lift forces and allow higher angles of incidence as for the static case. The vortex increases and gets convected continuously to the trailing edge. Reaching

the trailing edge, the vortex is shed, which results in a instantaneous breakdown of the lift and an overshoot of the drag. The interaction with a second vortex starting from the trailing edge itself can also effect in a rise of the lift acting on the structure (Laneville & Vittecoq 1986 (77)). It can be concluded that the full mechanisms of dynamic stall are still under ongoing research, as shown by recent studies such as Müller et al. 2016 (98), Buchner et al. 2017 (22), Patil et al. 2018 (106) or Benton & Visbal 2019 (18).

McCroskey 1981 defined k for a static reference frame (eq. (2.5 left) with respect to v_∞ (92)). According to McCroskey et al. 1976 (94), the dynamics can be divided into six phases (for a case of k=0.15 and $\alpha_{\max}$=25°):

1. At start the boundary layer flow reverses, after passing the static stall angle.
2. A vortex forms near the leading edge with rising angle of incidence.
3. A maximum lift is reached while the leading edge vortex grows, moving to the trailing edge.
4. By covering the whole surface a maximum negative pitch moment is reached along with sudden breakdown of the lift.
5. After a fully separated flow,
6. the boundary layer reattaches from front to the rear and finishes the period.

McCroskey's definition of k was extended to a rotating reference by Laneville & Vittecoq (eq. (2.5 right) (77)):

$$k = \frac{C \cdot \dot{\alpha}_{\max}}{2v_\infty \cdot \alpha_{\max}} = \frac{C \cdot \dot{\alpha}_{\max}}{2\omega \cdot R \cdot \alpha_{\max}} \tag{2.5}$$

The pitch velocity of a blade in a rotating VAWT, $\dot{\alpha}$, is derived from eq. (2.3) as a function of λ, θ and the angular velocity of the rotor ω_D:

$$\dot{\alpha} = \frac{\omega_{\mathrm{D}} \left(1 + \lambda \cdot \cos\theta\right)}{1 + 2\lambda \cdot \cos\theta + \lambda^2} \tag{2.6}$$

In a second step, Laneville & Vittecoq 1986 defined k_D for a VAWT (77). To this effect, eq. (2.3) and (2.6) are inserted in eq. (2.5 right). In this case the maximum of the absolute value of $\dot{\alpha}$ is of interest, since the maximum occurs in the descending branch of the non-sinusoidal motion (see slope of the trajectories in fig. 2.2 (left)):

$$k_D = \frac{C}{2 \cdot R \cdot (\lambda - 1) \cdot \arctan\left[(\lambda^2 - 1)^{-\frac{1}{2}}\right]} \tag{2.7}$$

Eq. (2.7) includes the ratio of chord length C to the turbine radius R, which is the solidity σ of a single-bladed VAWT. σ, the relation of the plan view area of the blades to half of the turbine's cross-section area, (see eq. (2.8)) is the second important parameter for the characteristics in a VAWT (n is the number of blades in the rotor).

$$\sigma = \frac{n \cdot C}{R} \tag{2.8}$$

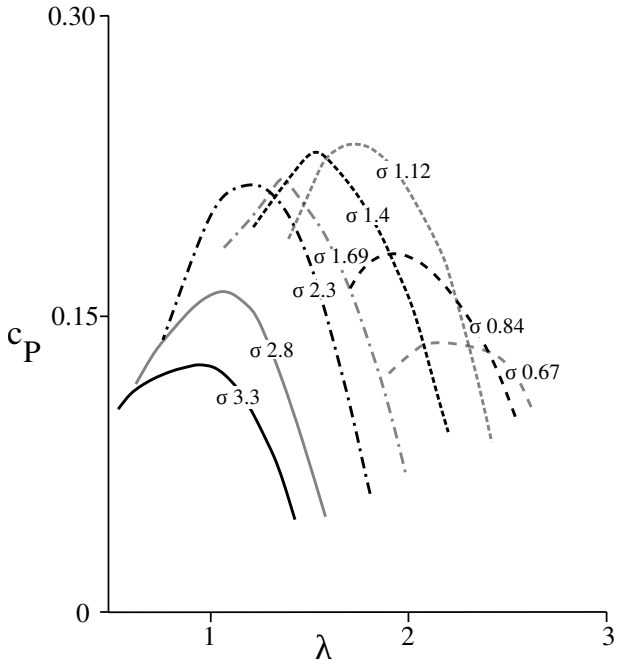

Figure 2.3: The influence of the solidity to λ_{BEP} and c_P: Experimental results from Shiono et al. (116) (labels and curves rewritten for better visibility, σ recalculated to fit to the definition in eq. (2.8)).

The solidity σ governs λ_{BEP}, the tip-speed ratio in the best-efficiency point (see fig. 2.3). λ_{BEP} decreases with increasing σ (Paraschivoiu 2002 (104)). On a three-bladed VAWT, $1.75 < \lambda_{\mathrm{BEP}} < 2.5$ for water and $3 < \lambda_{\mathrm{BEP}} < 6$ for wind turbines, since the high density ρ of the water requires compact turbines which lead to higher solidity σ. A low- λ turbine will operate with high α (see fig. 2.2). The consequence - in particular for water turbines - is a flow mainly characterized by dynamic stall. Then, as mentioned above, the reduced frequency and α_{max} are dominant for the flow characteristics.

On VAWT, thrust is generated as the lift-induced tangential force on the blade. Unfortunately the smaller sinusoidal share of the lift provides to the thrust, while the order-of-magnitude higher normal force, the cosine share, only generates structural loads on the blade (see fig. 2.1). Differences in between deep and light dynamic stall are explained by McCroskey 1986 (93). The first is characterized by an abrupt increase in drag along with an abrupt loss of lift and hysteresis effects; the phases of positive thrust will be reduced while the flow stays detached. Light dynamic stall generates vibrations and flutter caused by negative damping effects. The occurrence of light or deep dynamic stall depends on $\alpha_{\max}$ and k.

Analytical models to describe the rotor dynamics would be of strong interest in order to provide tools for performance prediction of such turbines. Paraschivoiu 2002 (104) provides a detailed description of the development of analytical and improved semi-empirical models of VAWT: as he states, first attempts to understand the flow regime in VAWT were started in the 1970s with a single streamtube model. This model is based on an actuator disc theory. It was refined and further developed with a multiple streamtubes model to take into account the relative flow speed at the blades. Later followed vortex models to capture the unsteady effects in the turbine. Loth et al. 1983 (85), Paraschivoiu 2002 (104) and following studies extended the model by two actuator discs (upstream and downstream) to capture the wakefield of the upstream part of the turbine.

On the other hand for high-λ turbines the flow convection is low compared to the tangential velocity. Secondary effects like strut or tip losses and blade-blade interaction (each blade operating in the wake of its predecessor) become more important, as pointed out by Daróczy et al. 2015 (33). The BEP is the optimum in between both extrema. The coupled parameters σ and λ and the resulting reduced frequencies k_D

for several turbine design points is shown in fig. 2.4.

These models compute with relatively low computational effort the qualitative characteristics of a design and are still under development, like the Qblade tool for HAWT and VAWT, introduced by Marten et al. 2013 (88). Their drawback is the need of experimentally-acquired airfoil data which must include high angles of incidence: it is difficult to include the dynamic characteristics of the blades in those models. However, in more recent studies, the complex flows of VAWT are mostly computed by computational fluid mechanics (CFD) with use of numerical solvers for simplified Navier-Stokes equations with fully- or partly-modeled turbulence (see sec. 3 & fig. 2.5)[1].

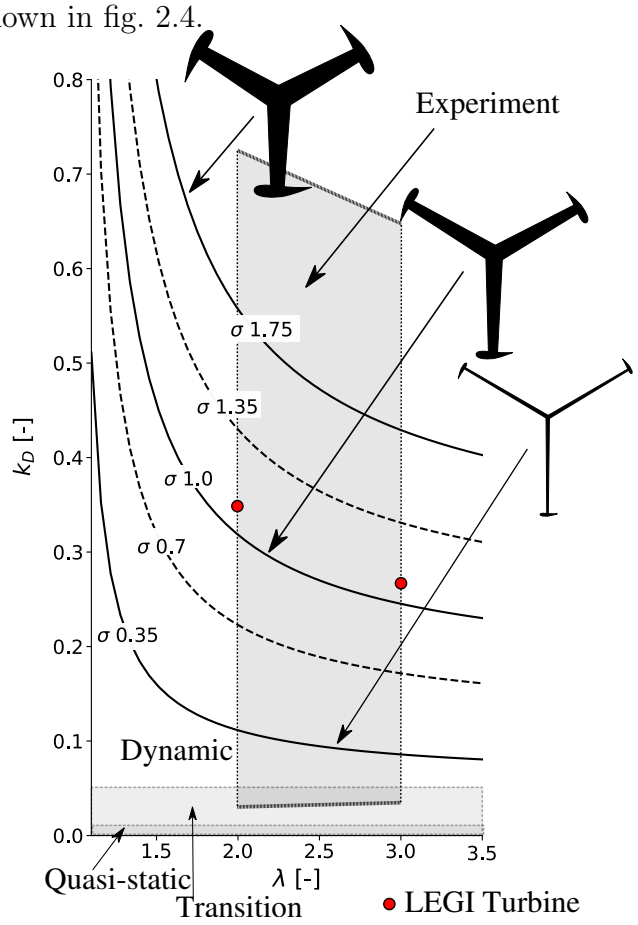

Figure 2.4: "The influence of λ and k on the turbine design, overlaid by the scope of experiments carried out in this study. Thin structures with high λ are characterized by low values of k, while massive structures with low λ have high values of k. k decreases with increasing λ as the maximum angle reduces. k increases with rising solidity, since the ratio of the cord length C to the turbine radius R increases." Reprinted from (65)

On real turbines, pulsating lift and drag from the periodical variations of α and w, as well as dynamic stall in the low-λ regimes, result in efforts on the structure. All these effects generate cyclic structural load variations which are known to provoke fatigue failure. This is a general challenge regarding the lifetime of VAWT (Paraschivoiu 2002 (104)). In consequence, an optimization of VAWT should combine two objectives:

1. To maximize the turbine efficiency in order to improve the productivity;

2. To minimize the cyclic structural load variations for lifetime considerations.

To achieve this goal, the dynamic flow characteristics at the blade have to be controlled.

[1]A video corresponding to fig. 2.5 can be accessed on the author's website:
`https://www.ovgu.de/hoerner/thesis/videos/darrieus_2d.mp4`

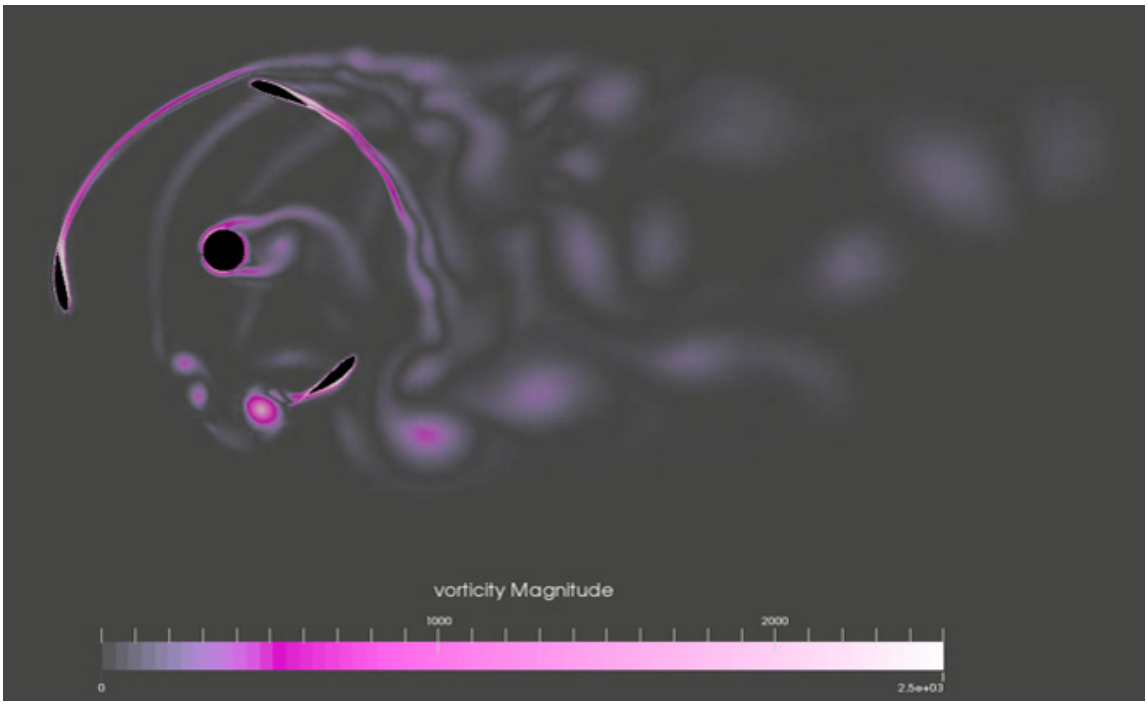

Figure 2.5: Two-dimensional Reynolds-Averaged Navier-Stokes (RANS) Simulation of a three-bladed VAWT (similar to fig. 2.1(right)) at λ=2 with the software package foam-extend. The flow field is colored according to vorticity. In this image, the upper blade is interacting with the wake of the predecessor (blade-blade interaction), the lower blade has just passed the shift-of-direction point and shed a major vortex resulting from dynamic stall. A video of the simulation can be found on the author's website. Reprint from (64)

2.2 Turbine optimization methods

2.2.1 Shape optimization

Most optimization approaches with focus on the turbine geometry investigate the optimal blade geometry. In such cases, an experimental optimization is extremely costly, as a new hardware geometry is needed for each optimization step. In consequence, numerical simulation were the chosen method for these studies.
In the following, a small selection of scientific contributions with the scope of shape optimization in VAWT is presented.

Ivanov 2017 et al. (119) presented a method with an optimizer, based on genetic algorithm to generate the blade shape through class-shape transforma-

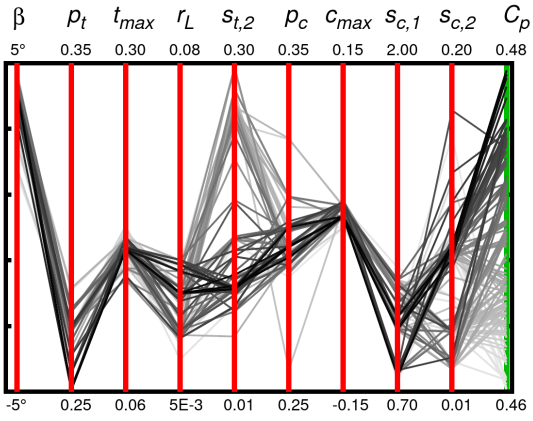

Figure 2.6: Shape optimization with genetic algorithms: Development of the population and c_P reached for a specific combination of the optimization parameters. Reprint from (32).

tion, coupled with a double-actuator multiple streamtube model introduced by Paraschivoiu 2002 (104). They used Drela's XFOIL tool (2013) (42) to calculate lift and drag for the profiles. Another, comparable study presented by Bedon et al. 2013 (17) reported a performance improvement of 10%.

Daróczy et al. 2018 (36) presented a method based on genetic algorithm coupled with fully-automatized 2D unsteady RANS simulations. The optimization in-house code OPAL++ was coupled with the commercial software package Star-CCM+. A significant improvement of 23% is reported after 14 generations and 888 evaluated individuals. Figure 2.6 shows the development of the optimization process for each parameter (red lines) and the power coefficient (objective, green) for each configuration (ordinate). Darker lines symbol higher c_P.

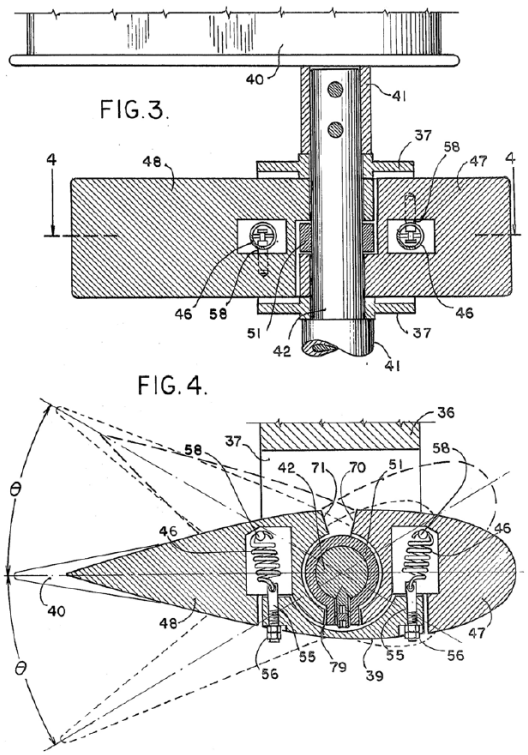

Figure 2.7: "Sketch of Liljegren's inertial and spring design (Liljegren, 1984)". Reprint from (107), as an example of the complexity of a purely mechanical, passive pitch mechanism

In 2016, Bedon et al. (16) reported an improvement of 8% for a two-bladed VAWT with an optimization based on 2D unsteady RANS simulations, using the k-ω-SST turbulence model in the software package *Ansys Fluent*.

A different approach was presented by Bianchini et al. 2014 (19). They proposed not to optimize the efficiency in the BEP, but to optimize the annual energy yield, taking into account the variations in the annual wind speed with a Rayleigh distribution.

The optimization of losses based on secondary effects like strut and tip losses require 3D simulations, which are extremely costly. Also, the performance of RANS methods must be carefully investigated, as turbulence and boundary layer models are crucial to evaluate these improvements. No lifetime considerations were performed in the above studies.

2.2.2 Blade pitch methods

Pitch methods tend to improve the turbine efficiency and raise the lifetime of a turbine by balancing the angle of incidence of foils along with the azimuth angle of the rotor, in order to increase thrust force and avoid or minimize stall.

Blade pitch can be obtained with passive or active methods. Most passive methods are based on mechanical systems containing springs and hinges (see fig. (2.7)). They

focus on a single operating point with adapted spring stiffness. An overview of these methods is given by Pawsey 2002 (107). Most active methods use a mechatronical design with actuators and transmission systems such as swash plates and tappets. According to Ferreira et al. 2014, the complexity of these designs makes them prone to failure (49), but can significantly raise the efficiency of VAWT as shown by Lazauskas & Kirke 2012 (78), Khalid et al. 2013 (114) or Delafin et al. 2014 (39). A less-explored approach is the use of decentralized actors as proposed by Zhang 2014 (135), Liang et al. 2016 (83) or Abbaszadeh et al. 2019 (1).

Numerical, semi-empirical and experimental studies were performed to find the optimal motion law for the pitch trajectory, which has to be estimated for each operating point such as done by Lazauskas & Kirke 2012 (78), Khalid et al. 2013 (114), Mauri et al. 2014 (90) or Thoennißen et al. 2016 (120). A custom experimental approach introduced by Abbaszadeh et al. 2019 (1), using a hardware-loop method and developed in collaboration with the author is presented later in sec. 5.1.

2.2.3 Bioinspired methods

A well known bioinspired method to control and improve the stall characteristics of a hydrofoil makes use of an optimized morphology, e.g. protuberances or tubercles on the leading edge as they are found on sea-mammals. Hansen et al. 2016 researched experimentally with PIV techniques and numerically the effects of leading edge tubercles (58). Pérez-Torro & Kim 2017 investigated a wavy leading edge with LES computations (109). Both reported improvements in lift along with reduced drag. However, the improvements or flow characteristics for pitching hydrofoils were not studied.

Improving performance with adaptive characteristics through structure flexibility is a less investigated approach. Significant improvements are reported by McPhee & Beyene (87) (see fig. 2.8). A flexible blade adapts its shape to the instantaneous flow field; this adaptation may avoid high angles of incidence, reducing the occurrence of both deep and light dynamic stall. Hydrodynamic forces on a VAWT blade tend to deform a flexible, symmetrical profile into a cambered profile, lowering its angle of incidence (see fig. 2.9). Flexible blades can make use of this effect: the higher the hydrodynamic forces, the stronger the deflection.

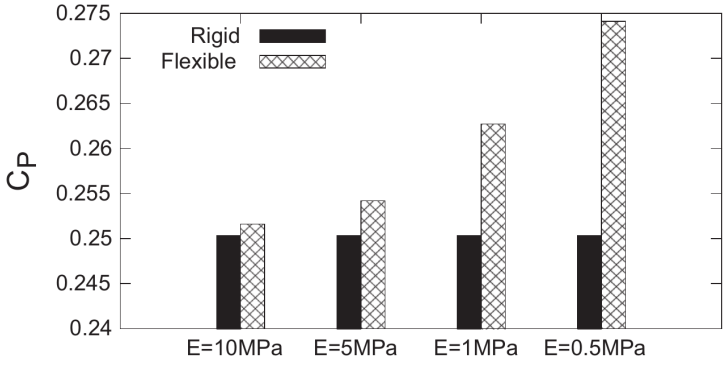

Figure 2.8: The influence of flexibility to c_P. Numerical investigation on a three-bladed VAWT. Reprinted from (87).

As a consequence, the characteristics of a rotor with deformable blades could be

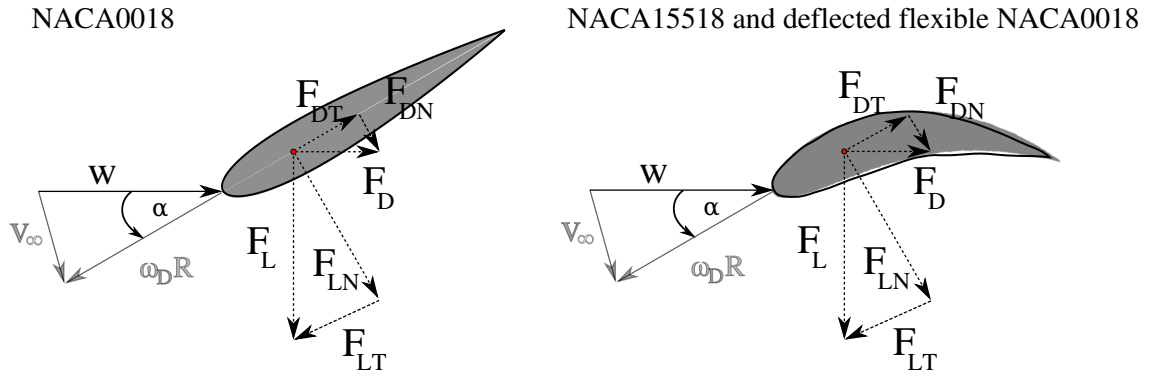

Figure 2.9: The influence of flexibility to the shape of a blade at high angles of incidence. Left: Rigid NACA0018 hydrofoil at α=-30°; right: Deformed blade at similar conditions (shape taken from experiment (black outline), see later in sec. 4) which corresponds to a NACA15518 (grey surface).

comparable to that of a rotor equipped with a passive pitch mechanism (see fig. 2.7). A full understanding of the effect of flexibility requires capturing the fluid-structure interaction (FSI) occurring on the blade: the flow field results in high deformations, which themselves feedback the flow. A realistic numerical study requires a simulation with strongly coupled (two-way) FSI to capture these effects. (see sec 3 for details). The commercial software packages *Ansys* and *Star-CCM+* provide FSI functionality, the latter through an interface to the *Abaqus* structural mechanics solver. The open-source toolbox *foam-extend* features FSI with the fluid-solid interaction library presented by Tukovic et al. 2014 (123). As of 2015, this library could not be used with sliding mesh and with rotor/stator methods. In this state, it was only usable with strong limitations for turbomachinery. An effort was made in this work to extend its functionalities (see sec. 3).

The existing work in this field is quite limited. Three key studies known to the author investigate the characteristics of flexible blades in VAWT, such as Liu & Xiao 2015 (84), Zeiner-Gundersen 2015 (133) and McPhee & Beyene 2016 (87). All studies show the potentials of flexible structures and the need for further investigations. Indeed the most important benefit of this strategy, compared to other competing approaches, is the simplicity of the solution. It promises to be less prone to failure and to reduce the maintenance effort, which is of particular interest for marine applications. The characteristics and the potentials of the usage of flexible blades is the scope of the present research.

2.3 Research methodology for VAWT with focus on FSI

VAWT were extensively researched starting from the oil crisis in the 1970s but then successively supplanted by horizontal-axis systems. A new focus on VAWT occurred with the beginning of the millennium.

However, the complex characteristics of these systems are not fully understood and are subject of ongoing research. The influence of flexible blades and the characteristics of their use in VAWT is even less investigated. This may result from the challenges for both numerical and experimental methods, brought by the FSI combined with already existing dynamics. The present work is mainly based on an experimental approach, but includes numerical methods and their development as well.

2.3.1 VAWT in experiments

Experimental studies on VAWT mostly used Particle Image Velocimetry (PIV). Fujisawa & Shibuya 2001 (53) studied a small-scale VAWT (80 mm diameter) at low Reynolds numbers (Re=3000) in a water channel. They found both the angle of incidence for onsetting stall and the growth rate of the vortices to be dependent on λ. The vortex structure growth is increasing when λ is reduced. Also, two pairs of counter-rotating vortices, stemming from leading edge and trailing edge, were observed: a first pair at θ=135° (for λ=2), and a second pair at high values α (see fig. 2.1 as reference for θ and α). Ferreira et al. 2009 (48) studied a single-blade VAWT in a wind tunnel at Re=$5 - 7 \cdot 10^5$.

Gorle et al. 2014 (55) investigated a four-bladed turbine in a towing tank at Re=$0.9{\cdot}10^5$ and $2.7{\cdot}10^5$ (see fig. 2.10). They showed that for a very common tip speed ratio of 2, the flow remained attached for an azimuth angle θ of 50-100°, while dynamic stall occurred from 120-220°. The flow progressively reattached from 240° onwards, and a second vortex appeared between 0 and 40°. Consequently, the flow was attached only 14% of the time in these operating conditions.

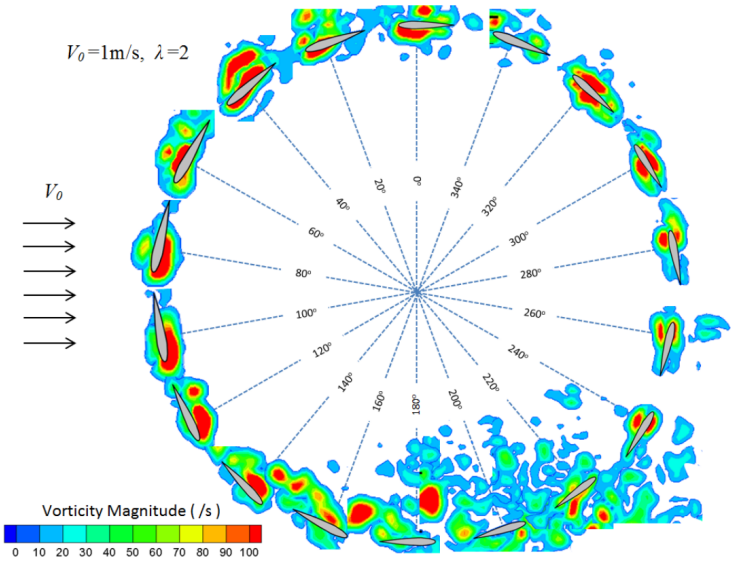

Figure 2.10: Vorticity distribution of the turbine blade at λ=2 from phase-locked PIV measurements. Reprinted from Gorle et al. 2014(55)

Buchner et al. 2018

(23) performed stereoscopic PIV measurements on a two bladed H-rotor and reported a strong influence on the flow kinematics not only from λ but also from unsteadiness and solidity. This is one scope of the work presented here.

Most other experimental work on water turbines focus on the turbine performance without measurement of the flow field, like Maître et al. 2013 (91) or Shiono et al. 2000 (116).

An experimental study dealing with flexible turbine blades in VAWT is provided by Zeiner-Gundersen 2015 for a five-bladed, low-λ VAWT (133). There, a hybrid approach with flexible blades combined with springs for passive pitch was implemented. Due to the lack of a reference point, a lifetime analysis was performed but not related to rigid turbines. A c_P of 0.37 was reported for λ=2.2. The authors stated that the flexibility improves the efficiency at low-λ and the self-start capabilities.

Using highly-flexible structures increases the complexity of such experimental setups even further. The considerable unsteadiness of the flow in VAWT and its impact on the structural deformations – which themselves influence the flow again – require knowledge not only of the flow field but also of the structure movement. Only the coupling of the instantaneous flow field (given e.g. by PIV) with the structural displacement (e.g. from surface tracking methods) would allow the full characterization of the mechanisms of this fluid-structure interaction. The turbine blade is the region of interest when evaluating the benefit of flexible structures in VAWT. In this case, the so-called secondary effects (as mentioned in sec 2.1) are of lesser interest.

The flow for a single-bladed VAWT can be seen as equal to an oscillating airfoil following the motion law from eq. (2.3) with an alternating flow speed conformal to the relative velocity w. As a consequence, the chosen experimental setup is based on an oscillating hydrofoil, a turbine surrogate model that allows to focus on the FSI and its underlying processes on the blade itself. A detailed description of the experimental work in this thesis is given in chapter 4.

2.3.2 VAWT in numerics

The numerical modeling of VAWT started with momentum-based, semi-empirical or fully analytical solutions and later extended to double-actuator-disc, multiple streamtube models with a decent number of correction approaches; a detailed description can be found in Paraschivoiu 2002 (104). They are still in use for turbine design methods or in turbine optimization, since they provide relatively fast results with sufficient accuracy for the design process, e.g. Roy et al. 2017 (113), Bedon et al. 2013 (17), Asher et al. 2010 (6) or Deglaire et al. 2009 (37).

A large number of numerical studies for vertical-axis wind turbines can be found in the literature, e.g like Hashem & Mohamed 2018 (59), Patil et al. 2018 (106), Mohamed 2012 (97) or Ferreira et al. 2007 (47). However, vertical-axis water turbines are less investigated and operate under different flow conditions due to their high solidity. Antheaume et al. 2007 studied VAWT in farm arrangements (4). Amet et al. 2009 studied the blade vortex interaction in a two-bladed VAWT (3). Maître et al. 2013 investigated experimentally and numerically a three-bladed VAWT in a confined flow (91); the turbine model in that study is used as a reference for the geometry of

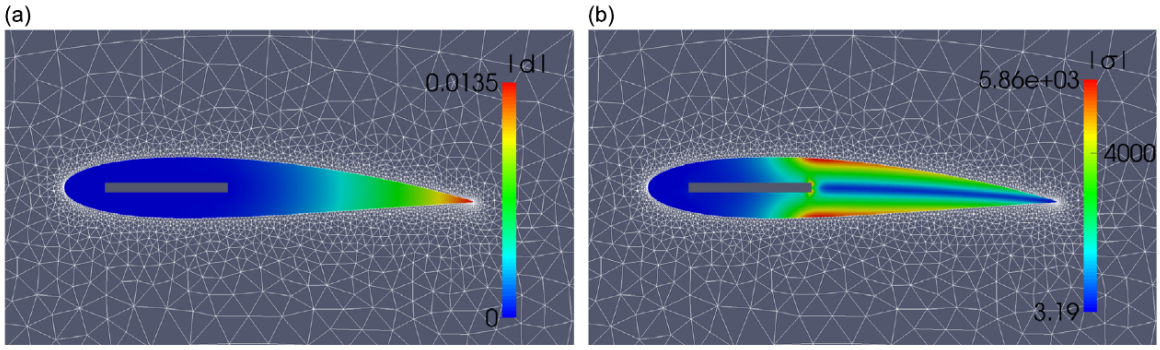

Displacement magnitude (in meters) Cauchy stress magnitude (in Pa)

Figure 2.11: Stress distribution and deformation in a flexible blade of a VAWT. Reprinted from McPhee 2016 (87)

the turbine in this thesis and will subsequently be called LEGI turbine.

In spite of the capabilities of contemporary CFD technology, modeling FSI with large deformations remains a challenging task. Most FSI simulations on present studies are based on static structures, with relatively small deformations. Shin & Kim 2008 investigated the FSI on a hydrofoil in free rotation in a water channel with a immersed boundary method (115). Krawczyk et al. 2013 studied the FSI on a wind turbine blade (73). Bazilevs et al. 2011 simulated a three-dimensional model of a 5 MW horizontal-axis wind turbine rotor (15). The existing research concerning VAWT and FSI rarely features strongly-coupled two-way FSI with large deformations combined with a rotor/stator setup.

Two contributions are known to the author which feature FSI on VAWT with flexible blades numerically; they are described below. Both approaches use a setup that avoids sliding mesh methodology: a "frozen rotor", namely, a static cylindrical mesh topology in which the effects of the rotational motion are implemented with additional source terms for the forces in a rotating inflow (or respectively a far-field) as boundary conditions. This setup cannot evaluate a setup with static and rotating parts. Because of this limitation, it is only useful for very particular cases (HAWT or a single VAWT) far from any borders or static structures like guiding vanes or multiple rotors placed

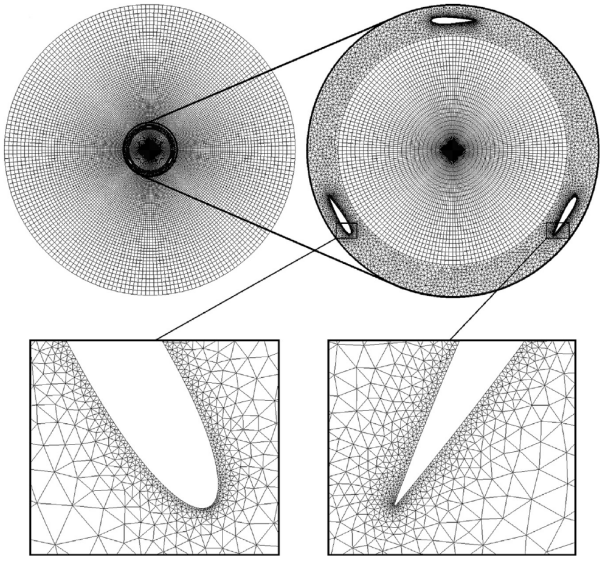

Figure 2.12: Frozen rotor setup for FSI on vertical-axis wind turbines. Reprinted from McPhee 2016 (87). This method allows to simulate single turbines in "frozen rotation". The rotational effects are implemented by additional source terms

in an array.

Liu and Xiao 2015 (84) studied a vertical-axis wind turbine numerically with a FSI in-house code. The setup was simplified to a single-bladed turbine. The flexible blades showed a significant improvement of up to 9% in c_P, in low-λ cases. There, centrifugal forces were small compared to fluid forces. For $\lambda > 6$, no positive effects could be observed, since the foil is no longer adapted to the flow field. They calculated higher stresses in the flexible blades as in the rigid blades.

McPhee & Beyene 2016 (87) studied a three-bladed vertical-axis wind turbine numerically with the *foam-extend* software package and reported a significant improvement of 9.6% in the rotor efficiency (see fig. 2.8, 2.11 & 2.12). Four different Young's moduli (and so stiffnesses) were investigated. The maximum deformation was about 3.45% of the chord length. The most flexible blade in the study provided the highest efficiency and improvement in self-start capabilities. The turbulence was modeled with a k-ω-SST model in a 2D unsteady RANS simulation.

A detailed description of the numerical part of the present study, as well as the code development carried out as part of this work, are given in the next chapter.

Chapter 3

Numerical Investigations

The main focus of this thesis is on experimental work; therefore, only a short overview of the numerical methods and the underlying Computational Fluid Dynamics (CFD) and Fluid-Structure Interaction (FSI) concepts is given. A focus will be set on the authors' own code development and its validation. Parts of this chapter were published as part of a conference talk at the *12th OpenFOAM Workshop 2017* (68).

3.1 Computational fluid dynamics

The particular challenges for numerical experiments regarding VAWT were already discussed in sec. 2. Due the high costs for LES and DES simulations, it was decided to perform unsteady RANS calculations as a starting point.

Two- and three-dimensional simulations of VAWT were performed to validate the code capabilities. The LEGI turbine, a three-bladed H-Darrieus VAWT with NACA0018 blades (see Maître et al. 2013 (91) and tab. 4.1 for details of the setup), was the focus of the investigation. The software packages used in this study were different branches and versions of *OpenFOAM*, such as *OpenFOAM*-2.4, *foam-extend*-3.1 and *foam-extend*-4.1.

Table 3.1: 3D simulation

Type	U-RANS
Cells	9,171,521
Y+(blades)	<12
Turb. model	k-ω-SST

Table 3.2: 2D simulation

Type	U-RANS
Cells	116,228
Rotor cells	88,728
Y+ (blades)	<10
Turb. model	realizable-k-ϵ

A sliding mesh approach was chosen. In the validation case, the flow shows characteristics of a confined flow. In consequence, the influence of the test section walls had to be implemented in the simulations. For the three-dimensional setup (see tab. 3.1) the meshing tool *snappyHexMesh* was used. The geometry of the turbine is given as an `.STL` file. The tool removes the turbine geometry from a background mesh built with *blockMesh*, which is then successively

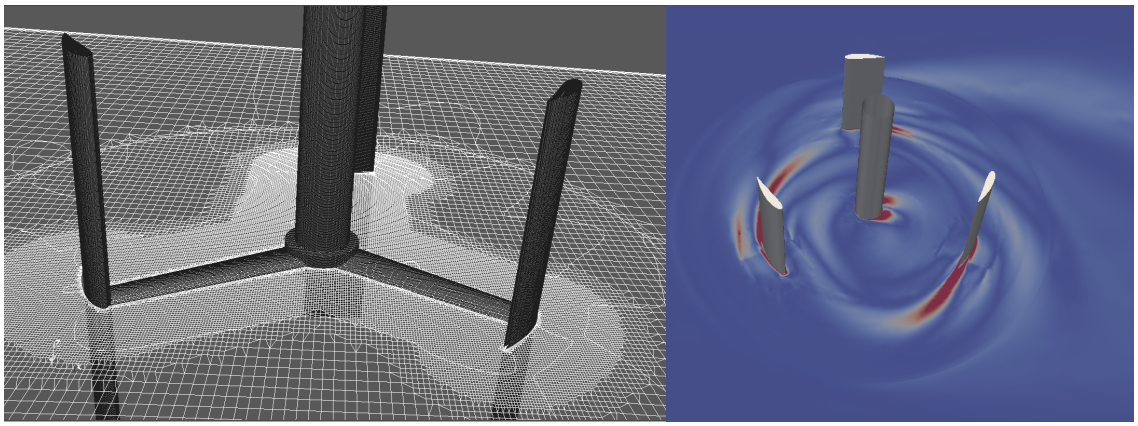

Figure 3.1: Left: Three dimensional mesh for a VAWT. The mesh is successively refined in the rotor region. Right: Vorticity field in the rotor.

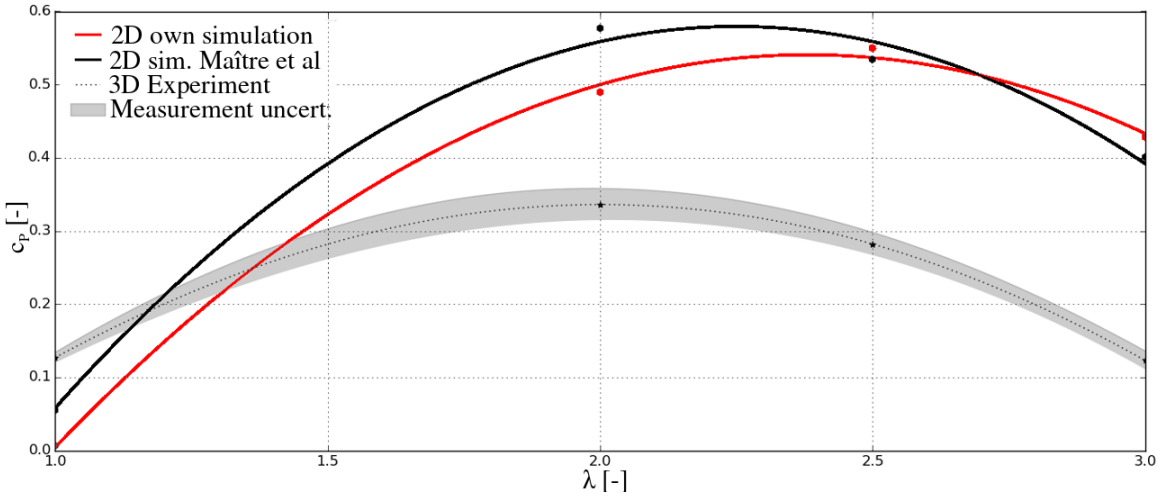

Figure 3.2: Power coefficent c_P over tip-speed ratio λ for two-dimensional numerical studies of a VAWT. Comparison between experimental and numerical results (*Ansys Fluent*) from Maître et al, 2013 (91)

refined and smoothed at the boundaries. Figure 3.1 shows a section through the spatial discretization grid (left), displaying refinement in the boundary layer of the turbine and the vorticity field in the fully developed flow (right). The generation of boundary layer cells was challenging and could not be realized directly within the tool itself. A workaround was found with the *refineWallLayer* command.
Because of the large computational effort involved, only one operating point was calculated, and the simulation was carried out on the HPC cluster SuperMUC in Munich. No mesh independence study could be performed. At the turbine's best-efficiency point, a power coefficient c_p=0.336 was calculated. This matches perfectly with experimental results from Maître et al. 2013 (91), with c_p=0.334. Subsequently, in order to reduce computational costs, two-dimensional calculations were performed to obtain the characteristic curves of the turbine (see tab. 3.2 for settings, fig. 2.5

for the velocity field and fig. 3.2 for characteristic curves). The turbulence model was changed from k-ω-SST for the three dimensional to the realizable-k-ϵ model for the two-dimensional simulations, as the results were found in better accordance to the validation case. The impact of the turbulence model for URANS simulations of H-Darrieus turbines has been studied extensively in Daróczy et al. 2015 (33; 34). The forces acting on the turbine were tracked for four operation points (λ=[1, 2, 2.5, 3]) and processed to obtain an averaged power coefficient. A good agreement was found with the results obtained with *Ansys fluent* in Maître et al. 2013 (91).

An overestimation of the experimental results can be found for $\lambda > \lambda_{\text{best}}$. This is expected, since losses depending on three-dimensional effects, like tip losses or the losses from the support structure of the rotor, are not included in this model, and depend strongly on the angular velocity λ (Daróczy et al. 2016 (35)). For the given case, the ratio of projected turbine area to cross section area (the confinement) is 0.175, and confinement of the flow has to be expected. The influence of these effects is stronger for two-dimensional simulations, since the flow gets further confined. In the given setup, the confinement ratio raised to 0.7 for two-dimensional simulations.

At very low values of λ, the numerical experiment underestimates the performance, which may be explained by an inaccurate reproduction of the stall dynamics which are dominant for this operating point.

3.2 Fluid-structure interaction

Fluids always interact with their boundaries. In single-phase flows, these boundaries consist of solid structures. Generally spoken, an interaction exists between fluid and solid structure. Hence, it is mandatory to define precisely the term *fluid-structure interaction* (FSI). Here, not only the fluid motion, but also the structural load and deformation of the solid are of interest.

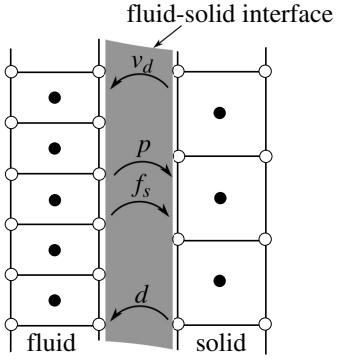

Figure 3.3: Grid coupling by patch-to-patch transfer (based on weighted interpolation) on a fluid-solid interface. The solid solver provides the displacement increment d and the displacement velocity v_d of the boundary, while the fluid solver calculates the resulting shear forces f_s and wall pressure p.

Numerically, FSI is a multi-physical problem that includes a fluid and a solid part. The physics of those two parts can be simulated with two different methodologies: 1) A single spatial discretization grid and a unified mathematical formulation solved simultaneously (monolithic). 2) A split into two regions with a common interface, one for the fluid and one for the solid, each having its own separate mathematical formulation (segregated). Monolithic approaches are known to be very stable and to provide better convergence. However, they are computationally expensive. They also require a single solver to handle both solid and fluid mediums, and are therefore less flexible compared to modular segregated approaches.

Segregated methods are used in this study. These methods require a coupling mechanism for the two grids, one grid for the fluid and one for the solid structure

(see fig. 3.3). The coupling mechanism depends on the level of interaction in between both continua. Depending on the task, FSI can be simulated with different levels of coupling, with the costs rising dramatically for each additional level:

- The most simple method is to perform a conventional CFD simulation, followed by a mapping of the pressure and the shear (forces) to a structural mechanics code which will calculate the stress and deformations. This method, called one-way or weak coupling, is suitable for rigid structures which will encounter small deformations and if only the loads on the structure are of interest. As long as the solid deformations do not significantly impact the flow, as in e.g. the vibrations of a Francis turbine runner operating away from its design point, only negligible errors will occur. However, for transient solid calculations and modal analysis, the added mass effects from the fluid body have to be taken into account, as shown by Doujak & Unterluggauer 2018 (41).

- A more complex method is to use a two-way coupling with rigid body displacement. Here, the fluid part is modeled with a classical CFD computation, while the structural deformation is implemented as a displacement of a rigid body by a spring-mass system with damping. This is suitable for example in the case of the two dimensional deformation of a cross-section of an aerodynamic profile of wind turbine blade. This can be easily implemented as an internal function of the CFD code which recalculates the body placement at each new iteration. The solver will iterate in a FSI-loop until deformations and flow field converge to a given residual.

- A more advanced method, suitable for large and complex structural deformations, is to use a two-way coupling of a solid solver with a fluid solver. In this case, a coupling interface is inserted. The deformation velocity is mapped to the fluid solver and the pressure and shear forces at the wall are mapped for the solid solver (see fig. 3.3). After a first calculation of a primary flow field and the mapping of the hydrodynamic forces, the structural code evaluates the boundary displacements and transfers them back to the fluid solver. The flow field is then recalculated with account for the displacement. This coupling loop has to iterate until the deformations or changes in flow velocity reach convergence criteria. The number of iterations depends strongly on the damping of the structure and the ratio of densities between both media. Very high and low ratios provide strong physical damping, which accelerates the convergence process.

In this study, the latter approach is taken. Subsequently, the term FSI is used to designate a strong (two-way, see fig. 3.4) coupling between fluid and structure. Calculations are carried out with a segregated approach, accounting for the hydrodynamic forces on a solid structure, the resulting stress, but also the complex structural response, whose magnitude is sufficient to influence the fluid flow.

The numerical simulation of FSI is a challenging task. Even if nowadays all commercial software vendors provide solutions for FSI simulations, a major development is still necessary for an utilization in industrial applications for cases with

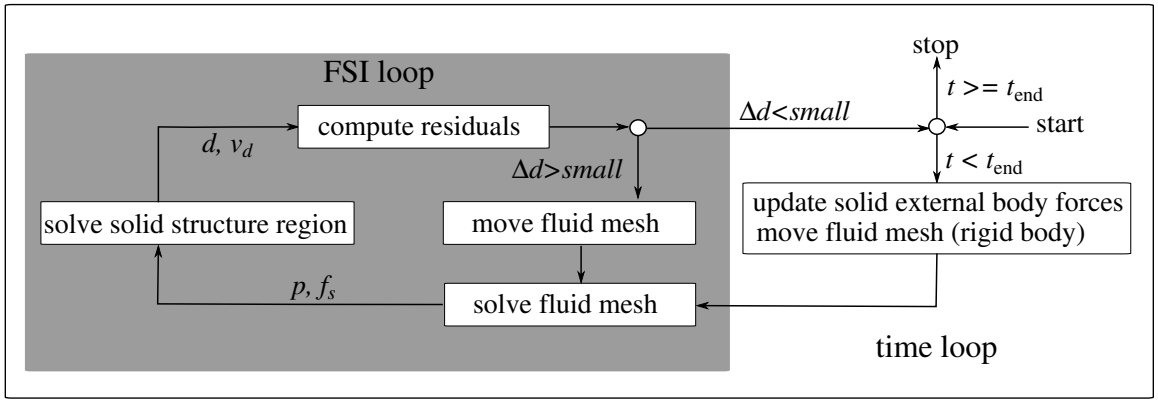

Figure 3.4: Flow diagram of a segregated FSI coupling scheme for an unsteady case with additional rigid body motion. All segregated approaches with strong coupling need a FSI loop, which iterates until the calculated deformation converges with the calculated corresponding hydrodynamic forces.

large deformations of the solid structure. It is obvious that additional FSI loops are computationally extremely expensive.
Cases with highly-flexible structures (density ratio around one) and incompressible fluid, result in significant instabilities Tuković & Jasak 2007 (124). This is the case for the present study of a composite hydrofoil with silicone embodiment (see sec. 4.2): the density ratio between silicone and water is around 1.1, while the carbon density is negligible due its the small volume share. The consequence is that instability and numerical oscillations are observed.

A way to overcome those issues is to use numerical damping, provided with extreme under-relaxation. The under-relaxation leads to an extremely slow convergence process, and the associated computational effort is compounded by the large number of time steps to guarantee only small deformations per time step. Additionally, the deformations are significant, which results in highly-deformed grids (which have to be recalculated by a mesh motion solver) and can result in low mesh quality. Further challenges of the given setup are the highly-dynamic flow conditions and the composite structure properties, which require orthotropic, multi-material solver capabilities.

Most codes available couple a mature, finite-volume (FVM) based CFD code, like *Ansys-Fluent* or *Star-CCM+*, with an external finite-element (FEM) based structural code like *Ansys structural* or *Abaqus*. Even if the integration is already quite convenient, the solving processes in these methods are segregated, and the communication between the codes is the bottleneck.

The open source toolbox *foam-extend* makes use of an approach based on the own FVM-based solid solver library, which is part of the *solid4foam* toolkit. This FSI library introduced as additional extension by Tuković et al. 2014 (123) is not directly included in the official distribution and has to be compiled from source (57). Here, the communication is performed via a so-called fluid-solid interface which is based on the General Grid Interface (GGI), a boundary condition, that is normally used for the interpolation and mapping in between two meshes on the common boundaries,

e.g. for a sliding mesh setup or for cyclic boundary conditions. A strong point of this method is that it runs code with native access to all fields. A drawback is that finite-volume-based structural solvers are less robust with respect to the mesh than finite-element-based solvers.

In the scope of this thesis, it was decided to evaluate the existing capabilities and the reliability of *foam-extend* to study fluid-structure interaction on an VAWT with flexible blades. The original intent was to carry out an adaptation of the existing software to the demands of the present case. However, due to the complexity of the setup and the computational costs, it was determined that the experimental approach developed in parallel was more efficient for the purposes of this work. Consequently, experimental work became the main focus of the thesis. In this section, a very short overview of the underlying models used will be followed by a validation of the existing code. A subsequent presentation of the code adaptation and some preliminary results of the new solver will be shown. The numerical investigations may provide an outlook for future development and research in order to improve the capabilities of the implementation at hand.

3.3 FSI modeling with *foam-extend*

The *foam-extend* FSI library is based on the solid solvers of the software toolkit. The fluid-solid interaction toolkit was first published in version 3.1. FSI cases use multiple solvers in a modular setup: the main solver e.g. *fsiFoam* governs the general solving process and performs the FSI coupling. A solid solver, e.g. *stressFoam* solves the equations in the solid region. A fluid solver, e.g. *pisoFoam* is used to solve the equation in the fluid region. Additionally a mesh motion solver is needed to provide the mesh motion in the fluid domain. A FSI case file consist of two linked subfolders `fluid` and `solid`, containing the two regions with their own configuration sub-subfolders `system`, `constant`, and `0`. These folders must be linked before the computation is launched.
The solver used was the *icoFSIElasticNonLinULSolidFoam*. A Bachelor thesis in 2015 under supervision of the author was performed by Stephanie Müller (100) in order to validate the code. This validation is carried out with the bundled tutorials based on the benchmark test introduced by Turek & Hron 2006 (125). This test case consists of a cylinder with an attached highly-flexible rubber blade. The von-Kármán vortex street interacts with the hyper flexible rubber blades of different stiffness. At that time, the code displayed strong limitations and instabilities and was considered to be in early development state. The ongoing development and the publication of a new version (4.1) in 2016 brought significant changes. Fischer et al. 2016 (50) evaluated the new code with the tutorial and two other reference cases. The FSI solver used was *fsiFoam*. They found a generally good accordance for the uncoupled solver simulations, in spite of strong deviations in particular for the lift forces. Fluid and solid region were solved separately without FSI. Errors were found to be 4.2% for drag, 20% for lift, and 6.9% for Strouhal number (Sr). The solid solver provided modal frequency error of 1%. The results for the coupled simulations achieved 16.4%

overestimation of the structure deformation and 2.4% for the vibration frequency. The bigger share of the errors was generated by the fluid solver, a variant of the *pisoFoam* solver adapted for the use in the FSI framework. The solid solver was *stressFoam*, an unsteady solver for linear-elastic material characteristics.

Most solid solvers use the finite-elements methodology. A typical finite-element formulation (see eq. (3.1)) will relate a mass matrix $\underline{\underline{M}}_{\text{solid}}$, the matrices of the material damping $\underline{\underline{D}}_{\text{solid}}$ and the solids stiffness $\underline{\underline{K}}_{\text{solid}}$, along with the displacement vector $\underline{d}$ and its temporal derivatives $\dot{\underline{d}}$ and $\ddot{\underline{d}}$. The right side of the equation shows the loads on the nodes, $\underline{F}_n$, acting on the structure.

$$\underline{\underline{M}}_{\text{solid}}\,\ddot{\underline{d}} + \underline{\underline{D}}_{\text{solid}}\,\dot{\underline{d}} + \underline{\underline{K}}_{\text{solid}}\,\underline{d} = \underline{F}_n \tag{3.1}$$

Shape and density of the matrices depends on the elements, e.g. volumes, plates, shells and their corresponding degrees of freedom.

A description of the same phenomenon in finite-volume formulation in a continuum approach is more exotic. Such a model was implemented in the *foam-extend* toolbox by Cardiff et al. 2016 (25; 24).
The formulation is obtained starting with a general formulation of the conservation of the linear momentum, using the Cauchy stress tensor $\underline{\underline{\sigma}}_{\text{solid}}$. The change of the momentum of the material is related to the sum of the surface forces (represented by the divergent of $\underline{\underline{\sigma}}_{\text{solid}}$) and the mass-specific body forces $\underline{f}_{\text{body}}$ acting on the structure:

$$\rho_{\text{solid}}\frac{\mathrm{D}\underline{v}}{\mathrm{D}t} = \nabla\underline{\underline{\sigma}}_{\text{solid}} + \underline{f}_{\text{body}} \tag{3.2}$$

The Cauchy stress tensor is expressed as a function of the strain tensor $\underline{\underline{d}}$ (in solid mechanics mostly noted ϵ) using Hooke's law for linear-elastic deformations:

$$\underline{\underline{\sigma}}_{\text{solid}} = 2\mu_{\text{solid}}\underline{\underline{d}} \;+\; \lambda_{\text{solid}}\mathrm{tr}\left(\underline{\underline{d}}\right)\underline{\underline{I}}_{id} \tag{3.3}$$

where $\underline{\underline{I}}_{id}$ is the identity matrix.

This equation 3.3, is expressed using the two non-dimensionalized Lamé coefficients μ_{solid} and λ_{solid}. In the case of plain strain, those can be expressed as a function of the Young's modulus E and the Poisson ratio ν_{solid} as follows:

$$\mu_{\text{solid}} = \frac{E}{2\left(1+\nu_{\text{solid}}\right)} \tag{3.4}$$

$$\lambda_{\text{solid}} = \frac{\nu_{\text{solid}}E}{\left(1+\nu_{\text{solid}}\right)\left(1-2\nu_{\text{solid}}\right)} \tag{3.5}$$

In the case studied here, the linear-elastic assumption embedded in Hooke's law is suitable: although silicone behaves non-linearly, it deforms without significant contribution to the hydrofoil stiffness. The carbon fiber composite (and aluminum) bears most of the load and deforms in a non-plastic manner. The deformation can be approached with linear-elastic characteristics. Problematic are the orthotropic material

characteristics, that will discussed later. The mathematical model for the solid solver is finally obtained by inserting eq. (3.3) in eq. (3.2):

$$\rho_{\text{solid}} \frac{\delta^2 \underline{\underline{d}}}{\delta t^2} = \nabla \cdot \left(\mu_{\text{solid}} \nabla \underline{\underline{d}}\right) + \nabla \cdot \left(\mu_{\text{solid}} \left(\nabla \underline{\underline{d}}\right)^T\right) + \nabla \cdot \left(\lambda_{\text{solid}} tr\left(\nabla \underline{\underline{d}}\right) \underline{\underline{I}}\right) + \rho_{\text{solid}} \underline{F_b} \quad (3.6)$$

This equation 3.6 thus relates the displacement tensor $\underline{\underline{d}}$ to the body forces $\underline{F_b}$ in the solid region.

The fluid part is described by the Navier-Stokes equations for an incompressible fluid:

$$\frac{\mathrm{D}\underline{v}}{\mathrm{D}t} = \underline{g} - \nabla \frac{1}{\rho} p + \nu \nabla^2 \underline{v} \quad (3.7)$$

As with most practical applications, this equation is not solved directly; instead the simplified unsteady Reynolds-Averaged Navier-Stokes (RANS) approach is used, calculating time-averaged flow properties, and using additional turbulence models (in this case, a k-ω-SST model). In theory the existing solvers are also capable of performing Large Eddy Simulations (LES) simulations; however this was never tested in this setup, due to the extensively high computational costs.
A detailed description of the RANS approach, as well as of the availability and suitability of various turbulence models, is out of scope of this thesis. Many numerical studies on VAWT focus on the suitability of RANS or LES simulations and the influence of the turbulence models, such as Ferreira 2007 (47), Maître et al. 2013 (91), Zanotti et al. 2014 (132), Daróczy 2015 (33; 34).
The FSI library consists of multiple solvers, for different levels of coupling. In the present study the *fsiFoam* solver was executed. This algorithm provides a scheme for a two-way coupling, with two individual solvers, one for the fluid region and one for the structure region. The coupling includes under-relaxation methods to stabilize the calculations. There are multiple approaches implemented:

- fixed relaxation: A fixed parameter is provided. This method is very stable with low under-relaxation factors, but extremely costly.
- Aitken scheme: An interpolation scheme is used for acceleration in the coupling process. The method adapts the relaxation factor for each iteration based on the previous iteration step (DeGroote et al. 2010 (38)). It speeds up the iteration loop significantly, but is not as stable as fixed relaxation.
- Interface Quasi-Newtonian/Inverse-Jacobian Least-Squares (IQN/ILS): This method introduced by DeGroote et al. 2010 (38) provides a further speed up through adaptive under-relaxation, and accelerates the convergence process in the FSI coupling loop.

The existing *foam-extend* did not provide functionality for a moving base structure to simulate a forced oscillation, so implementation of this additional functionality was begun. A sliding mesh approach is common in FSI applications in turbomachinery, due to the presence of static and moving parts, like guiding vanes and runner. The general implementation in FE of mesh motion is the *dynamicFVMesh* class which

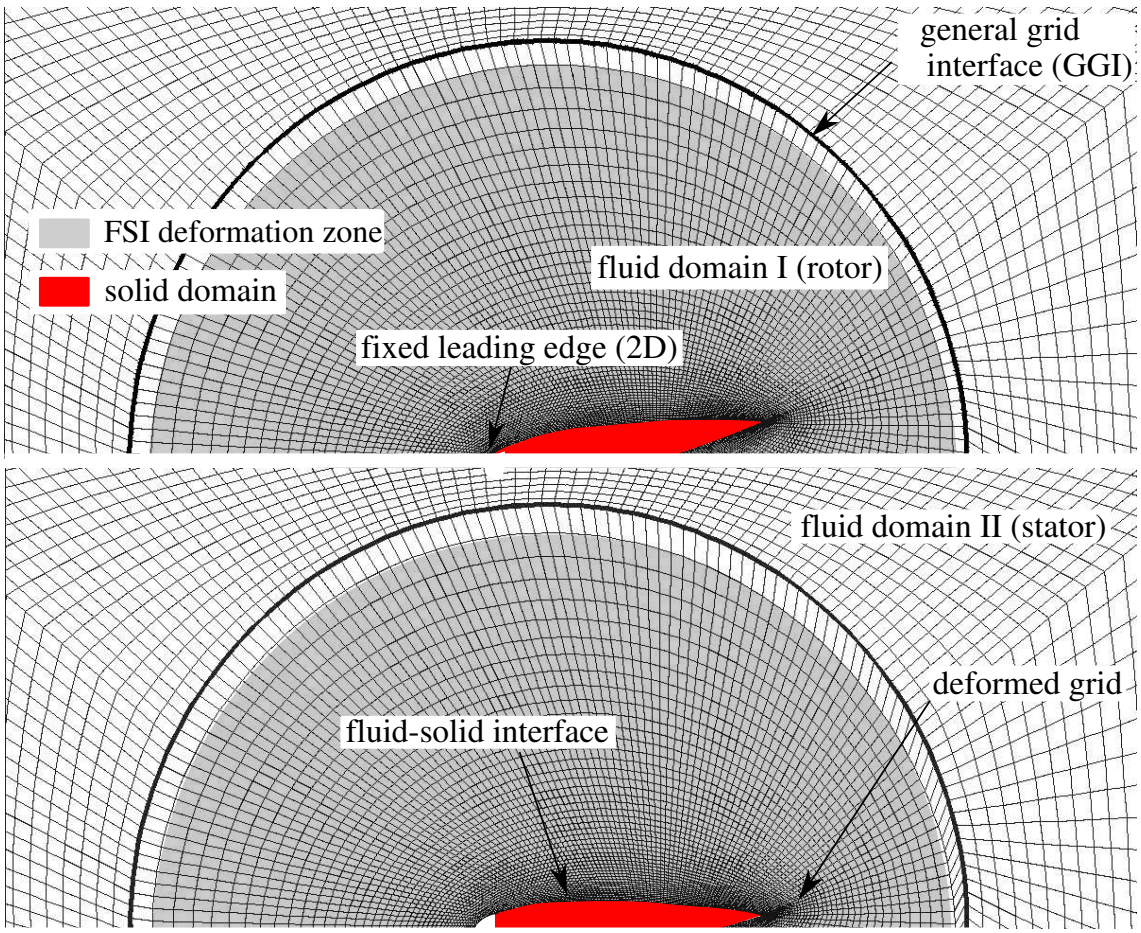

Figure 3.5: Setup of the numerical FSI case. The spatial discretization consists of three domains: a deformable and rotating fluid domain (I), a static fluid domain (II) connected with GGI, and a solid domain (red) connected with fluid-solid interface. Furthermore, there are two zones: a FSI displacement zone (light gray) and a rotating zone (represented by the entire fluid domain I). Two time steps are shown, the upper half is the non-deformed grid, the lower half is the same part for a later time step. A video of the grid deformation can be found at the author's website.

consists of a set of mesh motion solvers that calculate mesh motion or displacement and can be selected depending on the required functions. The FSI package already made use of this class for the structural displacement, therefore the additional functionality was merged into the already-present mesh displacement mechanism.

The existence of moving and static parts is already implemented by a multi-zone-based mesh where the zones are connected by an interface. In the present case, this connection is called General Grid Interface (GGI). This interface interpolates the flow parameters from one mesh to the other. A weighting function supports overlapping faces. Unfortunately, the fluid-solid interface can not be combined in one region with the GGI. This is maybe the case because the GGI interferes with its modified version that is already in use as fluid-solid-interface for FSI simulations. A workaround with a multi-zone, multi-region setup which separated the fluid-solid interface from the

general grid interface was introduced by the author in 2017 (68) (see fig. 3.5)[1]. The FSI interface interpolates the hydrodynamic forces to the solid mesh and transfers the displacement speed of the boundary points back to the fluid mesh (see fig. 3.3). The obtained cell displacement is converted into a wall velocity specification at the boundary. This translation is necessary, since the flow equations are solved in an Eulerian formulation, while the solid solver makes use of a Lagrangian approach.
The Eulerian formulation uses a static reference frame. The fluxes in the cells are computed by integration over the surfaces of the volume elements. A Lagrangian formulation is based on a dynamic grid, discretizing a structural entity that moves with time. In this case, the grid displacement at any point can be described by a motion vector for the displacement increment. Over time, one obtains a curve, analog to a pathline, for each point (updated Lagrangian). Alternatively, the motion vector of each time step can be described from the original reference point of a static, non-deformed grid. In this case, the grid point movement over time will result in a streakline (total Lagrangian).
In order to couple Eulerian and Lagrangian approach, the flow is modeled by an Arbitrary-Lagrangian-Eulerian (ALE) method. This means that the fluid grid is updated, the mesh is deformed for each iteration by a mesh motion solver, and the flow field is mapped to the new grid. The point coordinates of the fluid-solid interface are therefore shifted, according to the prescribed rigid-body motion and displacement of the solid structure. For a FSI boundary displacement, the grid point displacement is distributed over the entire mesh by a point (cell) deformation diffusion function.
In the current setup, the solid mesh itself is not deformed by a coordinate point shifting as it is the case for the fluid mesh. A displacement vector, the result of solid model equations, describes the mesh deformation for each time step with reference to the non-deformed mesh (total Lagrangian approach). However the effects of the inertia are taking into account from the deformation field of the previous time step. This method is used by the unsteady *unsTotalLagrangianSolid* solver for linear elastic solids which can be used for large deformation cases as solid solver.
The FSI package must be considered to be in an experimental state (v.4.1 in 2017). Some important capabilities are missing. In particular, there is no possibility to restart a crashed or stopped simulation. This is a serious drawback, especially considering the extreme time consuming characteristics of FSI simulations. The use of a common job queue on a high-performance computer cluster with job lengths of 24-48 hours was therefore not possible. All simulations were finally performed on a workstation (two 8-core Intel Xeon E5-2630 CPUs, 128 GB RAM) at the LEGI labs. The two dimensional test case with only 22100 cells to speed up the calculation time presented subsequently in sec.3.6, took 64 hours of calculation time to process 4 s of simulation on a single processor. Because of the number of cells in the setup, no significant speed up is to be expected when using parallel computing. Nevertheless, the code was successfully tested to be able to run in a parallel setup.
A validation of the existing code was performed. The focus was on the solid mechan-

[1] A video can be found at `https://www.ovgu.de/hoerner/thesis/videos/grid_deformation.mp4`

ics part, since the capabilities of the software for fluid mechanics were already well known and documented.

3.4 Validation of the existing code

A validation case was set up for the solid mechanic solver for linear elastic material characteristics. An analytical solution for a single, isotropic material was tested. A clamped beam of steel was set under a uniform pressure load on its upper surface. The analytical solution for this case, which is relevant for the model of the hydrofoil used in the experimental design process, is presented in the subsequent chapter (see fig. 4.11 and eq. (4.15)). The geometry and loads shown in table 3.3 lead to a maximum displacement of d_{ana}= $27.90{\cdot}10^{-3}$ m.

Table 3.3: Specifications of clamped single material beam case

parameter	symbol	unit	value
beam length	l	[m]	1.0
beam width/height	b	[m]	0.04
pressure load	p	[Pa]	250000
Young modulus	E	[N/m^2]	$210 \cdot 10^9$
Poisson ratio	ν	[-]	0.3

Table 3.4: Material properties for the multi-material case

	Young modulus	Poisson ratio	density
	[N/m^2]	[-]	[kg/m^3]
carbon/resin	$70 \cdot 10^9$	0.1	1600
PLA	$3.5 \cdot 10^9$	0.36	1250

The numerical setup consisted of an equally-distributed, hexahedra-based structured block-oriented mesh, containing 25,000 cells in one single block. Figure 3.6 shows deflection, grid and stress of the beam. The resulting maximum displacement of d_{sim}=$27.79{\cdot}10^{-3}$ m (relative error 0.14%) is in good accordance with the analytical solution.

In a later phase, the in the present code commented multimaterial support was activated. The solid test case was extended to a sandwich construction with a poly lactate acid polymer (PLA) layer surrounded by two 3 mm-thick carbon-fiber based compound layers. The materials were considered isotropic, with characteristics shown in table 3.4 and linear-elastic deformation. Due to the increased complexity, the reference result is given by a second numerical model calculated with the Ansys Structural solver. The solution produced with the *foam-extend* code is a deformation of d_{sim}=$55.84{\cdot}10^{-3}$ m. *Ansys* shows d_{sim}=$66.07{\cdot}10^{-3}$ m. The residual is found to be large, by 15% and not satisfying. It maybe due to contact modeling, or by the large deformation. However this difference was not investigated further.

Further detail regarding numerical concept and code development will be described in the subsequent sections.

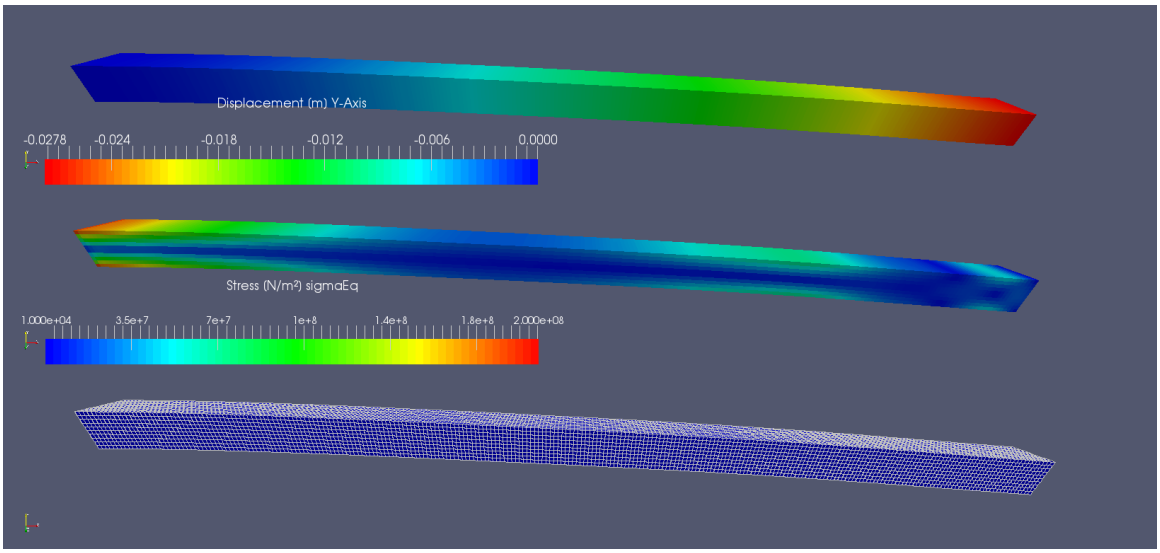

Figure 3.6: foam-extend: deflection with grid and stress distribution

3.5 Code development

After an evaluation of the research task, the following additional functionality was considered to be necessary for an adequate numerical modeling:

1. Sliding mesh methods for the fluid mesh. The FSI mesh displacement must be merged with a second, appropriate mesh motion solver for a prescribed rotating rigid-body motion. Furthermore, a non-sinusoidal rotational motion must be implemented for the current study;
2. Compatibility with the GGI interface. It should be possible to perform stable calculations with the presence of both GGI and FSI interface in one setup;
3. Multi-material support for the current setup;
4. Volume forces in the solid region;
5. Support for orthotropic material behavior for the carbon fiber compound;

The following subsections will give a short overview of the code changes carried out as part of this thesis.

3.5.1 Solver adaptations regarding mesh motion

The displacements of the solid lead to a shift of the grid nodes within the fluid mesh (see fig. 3.7)[2]. In *foam-extend*, this node displacement is managed by a mesh motion solver called within the *dynamicMesh* class. The solver used in the current setup solves the Laplacian equation for the velocity diffusion in the grid points.

[2] a video can be found at `https://www.ovgu.de/hoerner/thesis/videos/grid_deformation_detail.mp4`

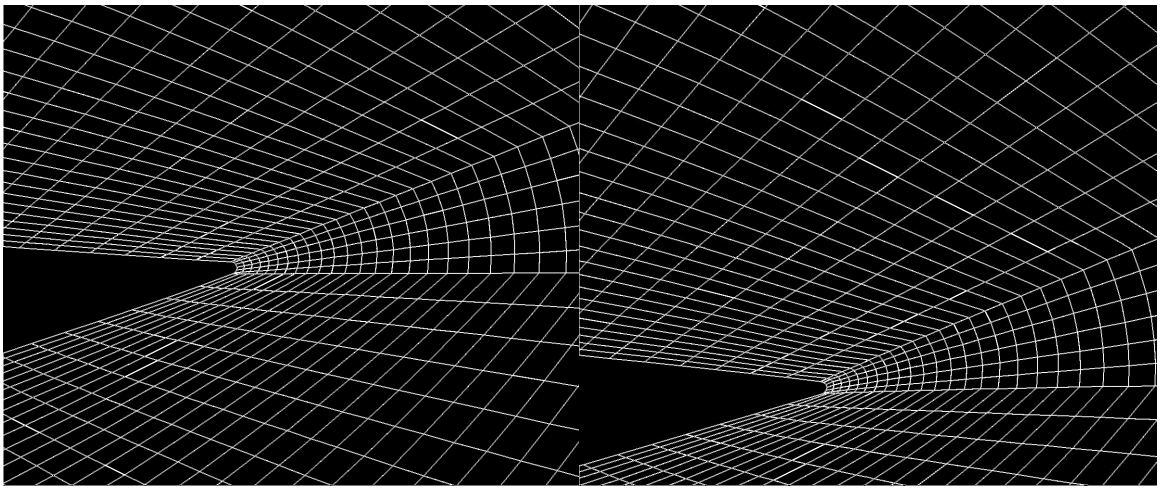

Figure 3.7: Detail of the FSI grid deformation for two time steps. The grid undergoes large displacements that are distributed in space by a diffusion of the node velocities obtained using a Laplacian-based solver. Mesh quality is an important issue, and the displacement must not lead to negative volumes or highly-skewed cells. A video of the grid deformation can be found at the authors website.

This displacement must be overlaid with the prescribed rigid-body motion (RBM), which accounts for the rotation of the rotor, or, as in the experimental investigations, the pitch motion of the hydrofoil, as described in sec.3.6.

Two attempts were made to implement the combined motion. As starting point, two so-called *motion subsets* were used:

- one subset for the displacement from FSI (FSI deformation zone in fig. 3.5). For this, the *velocityLaplacianFvMotionSolver* solver was adapted to support zones in a motion subset setup, becoming *zoneVelocityLaplacian* in order not to diffuse the mesh displacement over the entire mesh, but only for a dedicated region.

- one subset for the prescribed rigid-body motion (fluid domain I in fig. 3.5). For this, the *mixerGgiFvMesh* mesh motion solver was adapted to support zones in a motion subset setup as well as the motion law according to eq. (2.3), becoming *oscGgiSubsetFvMesh*.

This first attempt was presented at the *12th OpenFaom Workshop 2017*, but considered to be too complex; therefore, in a second attempt, both motions were implemented in a unified solver, and implemented in the *dynamicFvMesh* subclass. This new solver, *rotatingFSIFvMesh*, executes the following tasks sequentially:

1. A mask function generates a pointer to all grid points from rotating zone (fluid domain I) in order to determine the grid points displaced in the rigid-body motion (RBM)

2. The fluid mesh updates the displacement increment $\underline{d}_{\mathrm{FSI}_i}$ from the fluid-solid boundary of the FSI loop (fluid-solid interface) and subsequently diffuses the

displacements with the Laplacian motion solver *zoneVelocityLaplacian* in the FSI zone.

$$\underline{d}_i = \underline{d}_{\mathrm{FSI}_i} \tag{3.8}$$

This is applied for a pointer containing the grid points of the FSI grid zone (already implemented in the FSI solver).

3. Within each internal FSI loop (when bool(t = new) = 0), the *fvMesh* class moves the points according to the calculated displacement $\underline{d}_i$ and maps the flow field to the new mesh.
   At the start of each time step (when bool(t = new) = 1), the prescribed rotational rigid-body motion displacement increment $\underline{d}_{\mathrm{RBM}_i}$ is calculated and added to the calculated FSI displacement $\underline{d}_{\mathrm{FSI}_i}$ for each coordinate point i at the rotation fluid domain I. Then the flow field is mapped to the new grid.

$$\underline{d}_i = \underline{d}_{\mathrm{FSI}_i} + \underline{d}_{\mathrm{RBM}_i} \tag{3.9}$$

3.5.2 Integration of the body forces

In the setup previously described, no information about the rotational motion is transmitted to the solid solver. As a result, inertial effects resulting from the prescribed rotational motion are not taken into account. The solid solver has the ability to take a body force field into account and seeks for an existing field at each iteration. In the concept it was scheduled to use a function, executed for each new time step, to calculate the loads from the motion for the solid region in accordance to the instantaneous acceleration of the structure and to write them to a body force field. However, this is not yet implemented in the test case results.
The inertial body force $\underline{f}_{\mathrm{body}}$ acting on a rotating structure is expressed as

$$\underline{f}_{\mathrm{body}} = \underline{f}_{\mathrm{centrifugal}} + \underline{f}_{\mathrm{Euler}} + \underline{f}_{\mathrm{Coriolis}} \tag{3.10}$$

A body force *functionobject* is already present in the existing FSI code for initial conditions. Small adaptations would be necessary in order to calculate the instantaneous body forces for each time step. This work was not executed yet, but is mandatory to get appropriate physics in the chosen model. It is therefore mentioned here.

3.6 FSI test case with a single material

Two FSI test cases with a single, homogeneous material were set up to test the superimposed pitching motion. A static test was first carried out, followed by a case containing a rotating region. A block-oriented, hexaeder-based, structured mesh was generated using the *blockMesh* utility (see figs. 3.5 & 3.7). Large deformations can lead to highly skewed cells and negative volumes; therefore, the mesh had to be successively improved in order to obtain stable computations. Unfortunately, the software did not feature a re-meshing function of bad-quality cells at this time.

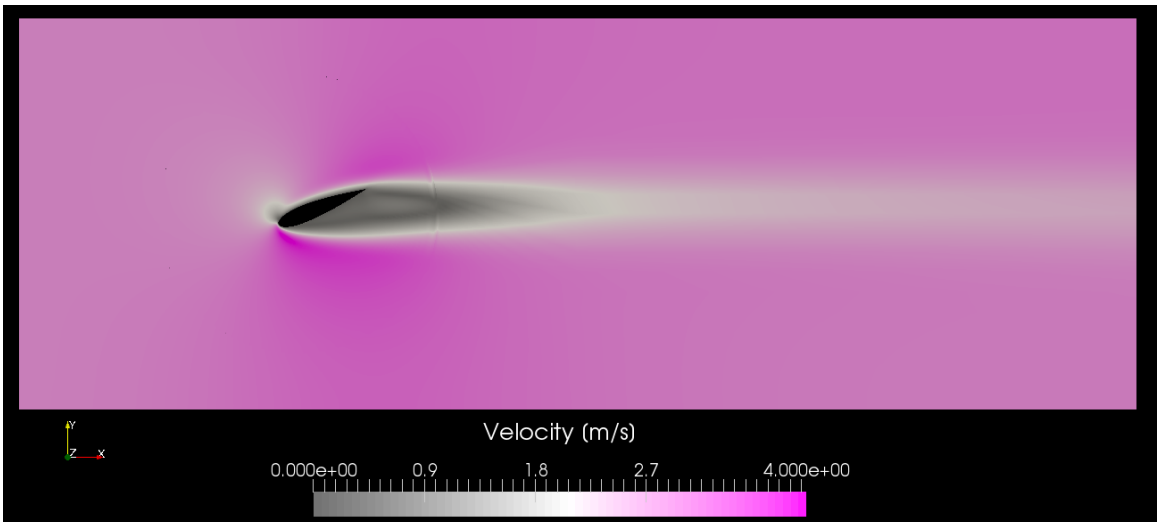

Figure 3.8: Validation of the *fsiFoam* code: velocities in a fluid-structure interaction test case. A flexible hydrofoil is oscillated in a fluid with inlet speed $v_\infty = 3$ m/s. The artificially high dynamic viscosity of the fluid, $\nu = 1 \cdot 10^{-3}$ m^{2}s, leads to high dissipation and a very smooth hydrofoil wake without shedding of vortices. A video of the test case can be found on the author's website

The FSI test case is constructed after the layout of the experimental setup described in detail in the following chapter. The case is two-dimensional (the grid possesses only one cell layer along the Z-Axis). The grid consists of a rotating cylindrical region (fluid domain I in fig. 3.5) rotating around the origin of the coordinate system surrounded by a rectangular static domain (fluid domain II in fig. 3.5). Both are coupled over a GGI as sliding meshes. The domain's bounding box is of $800 \times 280 \times 1$ mm^3.
The hydrofoil (solid domain) oscillates in a pitch motion around quarter chord, according to eq. (2.3) (with λ=2 and ω=8.31 s^{-1}) with an offset of 10°, which results in an angle of attack -10°$< \alpha <$ 30°. The profile is of a four-digit NACA 0018 hydrofoil of 66 mm chord length C built accordingly to the formula introduced by Jacobs et al. 1933 (70). The inlet velocity is v_∞=3 m/s. For the solid model, the leading edge is cut at 1% of C. As mentioned, for the numerical model of the solid region no motion is performed. The part of the hydrofoil cut out at the leading edge, can be seen as a non deformed fixation point. The cut edge is in consequence used as fixation in the two dimensional solid model. For the fluid model, the first part of the leading edge is modeled as a moving wall boundary, performing the prescribed motion. For the second part of the hydrofoil boundary (dashed red line in fig. 3.9), the fluid-solid interface maps the solid deformation and the mesh motion solver moves the boundary according to the sum of rigid-body motion and FSI deformation.

Numerical instabilities and oscillations in the inner FSI loop occurred during the FSI simulations. In order to provide higher damping and to stabilize the iterations, the relaxation was reduced up to unreasonable small magnitudes. However, no combination of time step, under-relaxation and coupling scheme could be found which would result in a stable behavior for the employed physical parameters.

In order to provide higher damping, the kinematic viscosity ν was successively increased from $\nu = 10^{-6}$ to $\nu = 10^{-3}$ m^{2}s. With this 1000 times higher dynamic viscosity, the calculations became stable with a relaxation factor of 0.1 and the use of the IQN/ILS scheme. The flow field shows the effect of the high dissipation around the hydrofoil and in its wake (see fig. 3.8)[3].

Figures 3.10 & 3.11 display the motion trajectories of the mesh for the first three oscillation periods. The trajectories are plotted as function of the rotation angle β. It is calculated as the angle in a triangle from the origin to a point in the mesh grid for two time steps, once for zero inclination (t=0), once for the current time step n:

$$\beta = \arccos\left(\frac{y(t=n)}{x(t=0)}\right) \tag{3.11}$$

Where x is the distance of the point to the origin in X-axis and y is the distance in Y of the point at the second time step n. This grid point is once situated at the sliding mesh interface and once at the trailing edge of the hydrofoil. The first grid point at the sliding mesh interface is situated outside of the FSI region, and is moved according to the RBM only. In consequence, it follows eq. (2.3). The second grid point at the trailing edge performs both RBM and deformation. The point coordinates were extracted from the case file. Each time step contains a `points` file, the coordinates for a specific point are situated in a constant line number of the file for all time steps. This allows to easily track one point with external post processing tools.
In fig. 3.10, three trajectories are plotted:

- The analytical equation for prescribed rigid-body motion of the foil (gray curve, eq. (2.3));
- The trajectory of one point at the GGI (black dotted curve). This point is situated outside of the FSI region, and is moved according to the rigid-body motion only.
- The trajectory of a point in the hydrofoil trailing edge (thick black curve).

In this figure, the RBM trajectory overlays the analytical curve with perfect accordance. Also the deformation of the flexible foil can be observed. After a first overshoot, the flexible hydrofoil follows the RBM motion with a reduced inclination angle. The deformation grows along with the angle of incidence. This is expected, as the hydrodynamic loads rise along with the inclination. The trajectories show repeatably the same characteristics for all periods.
Figure 3.11 shows the isolated hydrofoil deformations resulting from the FSI. In this figure, the trajectory of the trailing edge (thick black curve in fig. 3.10) was subtracted from the prescribed RBM (black dotted curve in fig. 3.10). Again, the periodic character of the motion is visible. The dependency of the deformation on the angle of attack can also be seen. A flapping of the hydrofoil becomes visible as well.

[3] A video of the test case can be found on `https://www.ovgu.de/hoerner/thesis/videos/FSI_test_case_1.mp4`

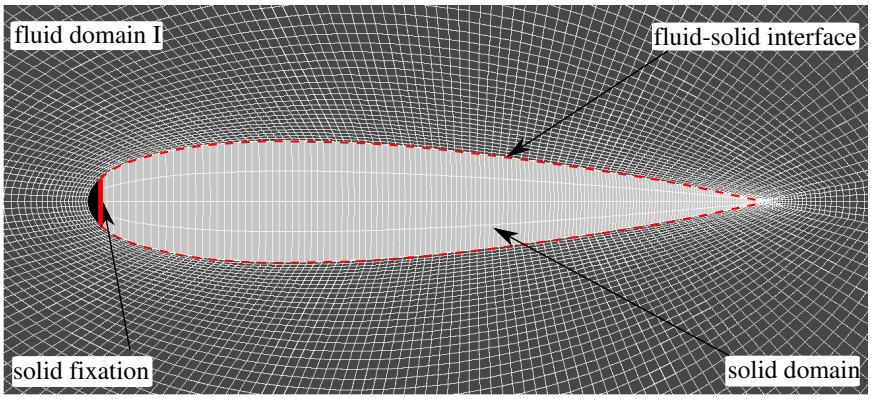

Figure 3.9: *fsiFoam* code validation: For the solid model, the leading edge is cut at 1% C. The cutting edge is used as a fixation of the hydrofoil

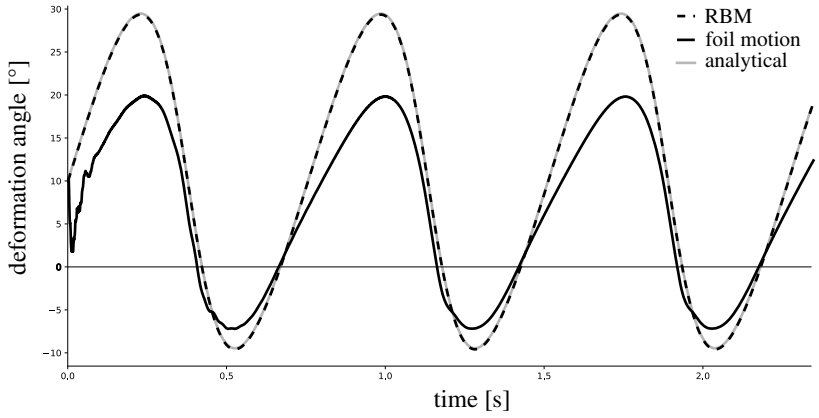

Figure 3.10: *fsiFoam* code validation: FSI deformation for a flexible pitching hydrofoil (with -10°< α <30°). The rigid-body motion (RBM) of the hydrofoil is congruent with the analytical trajectory (point tracking on the undeformed, rotating mesh, beside the sliding mesh interface GGI). The motion of the hydrofoil (deformation and RBM) is tracked at a point in the fluid mesh at the trailing edge.

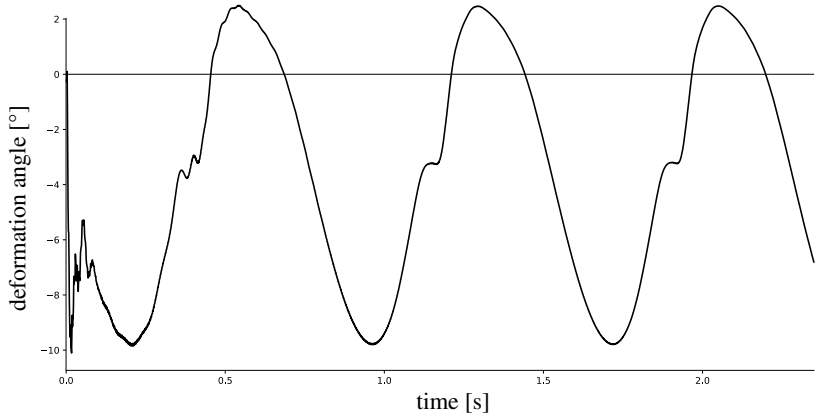

Figure 3.11: *fsiFoam* code validation: FSI deformation for a flexible pitching hydrofoil (with -10°< α <30°) for a point at the trailing edge. The angle, result of a point tracking at the trailing edge (see fig. 3.11) was subtracted from the angle of the hydrofoil at the sliding edge

3.7 FSI test case with multiple materials

The previous first test case is not appropriate to display the physics of the experiments presented in the next chapter. In those experiments, the leading quarter of the flexible hydrofoils consists of aluminum, and a carbon-fiber-based composite plate accounts for the flexibility of the rest of the hydrofoil. A silicone embodiment over the composite skeleton provides only the shape. This multi material approach provides constant stiffness over the full three quarter of the foil after the rigid first quarter of the hydrofoil. A constant stiffness promises to be less prone to strong oscillations at the trailing edge, as the stiffness for a homogeneous body would be dependent in cube to the cross section height. In consequence very low stiffness is to be expected for the very thin trailing edge. For this reason, the multi material capacities of the solver were activated.
It was not possible to obtain a multi-material grid for the hydrofoil with the *blockMesh* utility, therefore a combination of the *cfMesh* utility with the *setSet* command was used. In FE, multiple materials are defined by a properties file containing the material characteristics, such as density and Young's modulus. Furthermore, a file containing the material field must be present in the initialization folder. In this file, a material is assigned for each cell. This file can be generated with the *setFields* command.
In this setup, the calculations become more complicated, since several meshes have to be generated, after which regions, zones and materials have to be defined and initialized at startup. This process is executed in a bash script, run as follows for the subfolders `solid`, `stator` and `rotor`. The last two are later merged into a single `fluid` subfolder:

- Solid region
  - generate the mesh (*cartesian2DMesh* from *cfMesh*),
  - set up the boundaries (*createPatch*),
  - set up the material fields (*setSet, setsToZones, setFields*);
- Fluid domain II (`stator`)
  - generate the mesh (*cartesian2DMesh* from *cfMesh*),
  - set up the boundaries (*createPatch*);
- Fluid domain I (`rotor`):
  - generate the mesh (*cartesian2DMesh* from *cfMesh*),
  - set up the boundaries (*createPatch*);
- Merge the fluid domains and set the zones:
  - Merge the fluid domains (*mergeMeshes*)
  - write the two regions rotor and stator (*regionCellSets*),
  - create RBM and FSI zones (*setSet, setsToZones*);

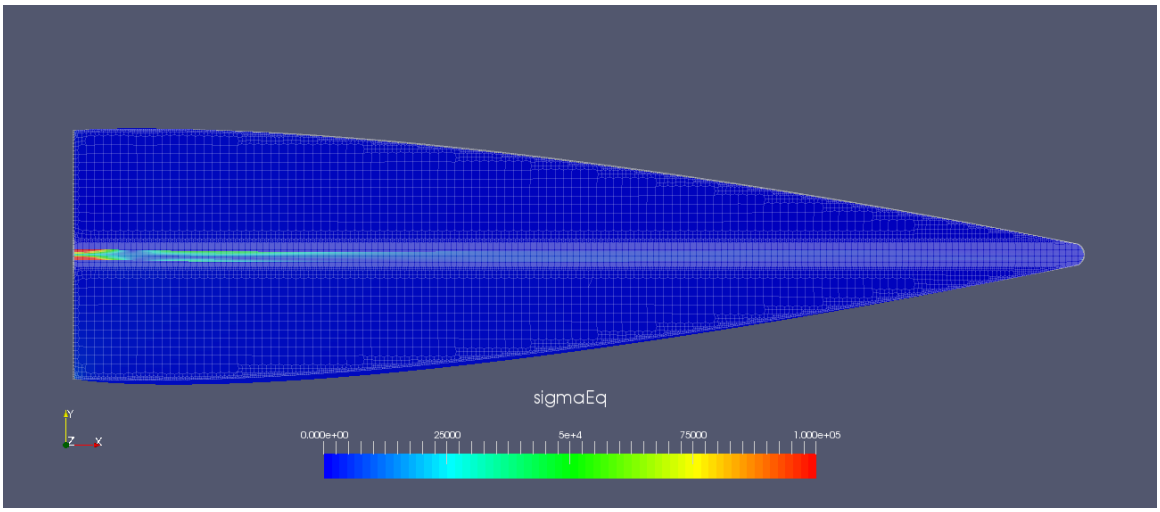

Figure 3.12: Validation of the *fsiFoam* code: stress distribution in a multi-material setup. The carbon-fiber-based composite plate displays a stress peak at the clamped fixation point (left), as expected. The silicone embodiment does not contribute to the solid stiffness. The aluminum-based first quarter of the foil was not part of the simulation.

- Link the solid domain with the fluid domains;
- Start the solver;
- Activate coupling after a stable flow field was established.

The first quarter of the hydrofoil (aluminum) was considered to be rigid. As this part is used as the fixation of the hydrofoil, it was removed in the solid model at $0.25C$ (in accordance to the experiment) and the cutting edge was used as a fixation. The underlying mechanical model for the remaining three quarters of the hydrofoil is represented as a clamped composite structure under the hydrodynamic loads. In the simulation, these loads are applied by the fluid-solid interface.
In the fluid part, the solid structure is represented by a moving `wall` boundary and moved once from the deformation at the fluid solid interface (dashed red line in fig. 3.9) or from a RBM motion which is not part of the solid model. Unfortunately, it was not possible to obtain stable computations. The calculations crashed shortly after activation of the FSI coupling. Figure 3.12 shows the stress distribution in the carbon-fiber-based blade. As expected, the stresses peak at the clamped fixation point, and low stresses are observed in the silicone embodiment as a result of the material's extremely low Young's modulus. Figure 3.13 shows the solid (top) and the fluid part (bottom) of the simulation shortly after the activation of the FSI. The solid displacement is scaled up by factor 1000 for better visualization. The stresses are once again shown, agreeing with fig. 3.12. At the bottom of the figure, the corresponding flow field is shown. No deformation is visible there since it is not magnified.

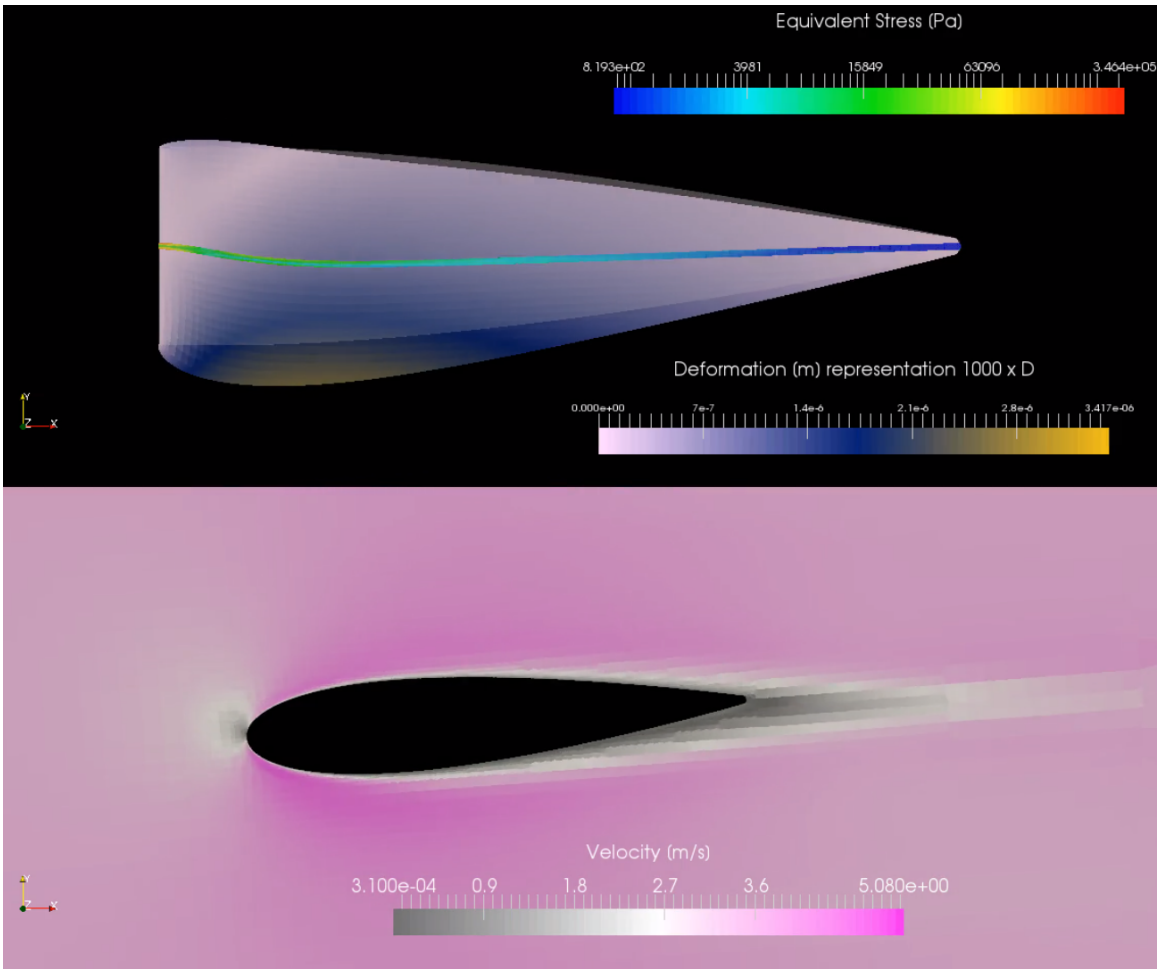

Figure 3.13: Validation of the *fsiFoam* code: deformations, stress and velocity fields in a multi-material setup. The deformations are shown scaled up by factor 1000.

3.8 Conclusions and outlook

The previous sections show the potential but also the challenges of carrying out FSI simulations with large deformations and forced additional motion with *foam-extend*. The additional RBM was successfully implemented, and the code was extended, with a new ability to carry out large time steps. The open-source code allowed to manipulate the mesh motion solvers and the FSI toolkit at low level.
Nevertheless, in spite of the impressive work of Philipp Cardiff, Zejko Tuković, Hrove Jasak and others, the existing features of the software (state *foam-extend 4.1*, 2017) were definitely not sufficient to provide a method for the given task. For this configuration, a numerical procedure is not able to compete with an experimental approach.
In particular, the lack of restart capabilities, along with the time-intensive computations, made the usage on high-performance clusters problematic. In sight of the unresolved tasks in the numerical modeling, the results from the multi-material

test case, and the remaining challenges, it was decided to exclusively focus on the experimental part; this work will be presented in the following chapters.
For future numerical studies, it should be considered carefully whether the approach presented here is suitable for the task. The density ratio close to one and the strong coupling would maybe better be tackled with a monolithic solver. The finite-volume based formulation of the solid solver used here permits a high level of integration with native access to all fields; nevertheless, a coupling with a mature structural solver like *calculix* or *code aster* with use of the *openmpi* libraries could also be considered and would perhaps be more stable. The rest of this Thesis will consider only experimental investigations and the corresponding analysis.

Chapter 4

Experimental model and setup

The experimental investigation of FSI is challenging, as it is a multiphysical problem which cannot be investigated in isolation from a fluid mechanics or a structural mechanics point of view only.

Highly-flexible structures add further complexity, because the strong deformations do not allow predictions of the structure's instantaneous shape without costly numerical simulations.

The following experimental study focuses on the characteristics of the FSI at the blade level. The experiment models the physics of a VAWT with a simplified, surrogate model. An oscillating (pitching) hydrofoil follows the motion law given by the trajectory in eq. (2.3) in order to mimic the flow conditions for a single-blade VAWT. This simplification neglects multiple secondary effects. The downstream portion of the blades' trajectory around the rotor axis is influenced by the wakes created in the upstream section, an effect that cannot be reproduced in the experiment. Also, strut and tip losses, as well as the blade-blade interaction, are not included in this approach. Despite this, the blade's behavior in the upstream part of the trajectory is considered to be appropriately modeled. As a consequence, although the performance results obtained here do not match real VAWT performance quantitatively, they allow to investigate the characteristics of flexible blades qualitatively, under consideration of the constraints of the model.

The objectives of the VAWT improvements carried out here were given in sec. 2.1: reduce structural loads and increase power (which, at a given operating point, means increasing blade thrust). The present model allows to investigate those parameters indirectly: the thrust on blades is obtained by measurement of the lift and drag on the surrogate profile model. The structural loads are obtained in the same way.

An evaluation of the benefits of flexible blades can then be obtained by comparing several hydrofoils with different stiffnesses to a fully-rigid structure serving as a reference.

The following subsections will give a description of the underlying physical model, the governing parameter of the experimental approach and their formulation. The experimental facility and the general setup will be introduced. The materials used for the flexible structures and the design will be characterized.

Parts of the section - the modeling and the experimental apparatus - were already

published as peer-reviewed journal articles in *IET Renewable Power Generation* (1) and in the *Journal of Fluids and Structures* (65).

4.1 Modeling

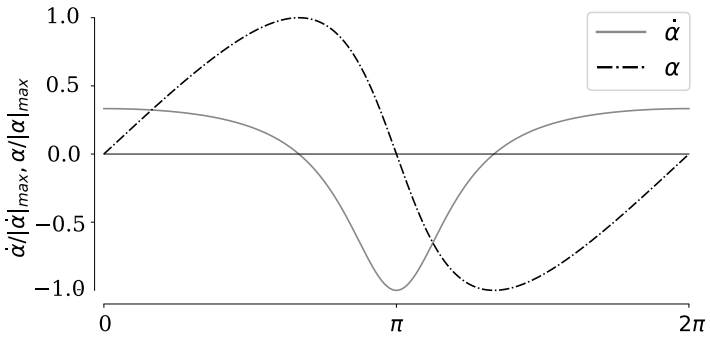

Figure 4.1: "Normalized angle of incidence α and pitch speed $\dot{\alpha}$ for λ=2. The non-harmonic trajectory leads to a maximum absolute pitch speed in the descending branch. This has to be considered in the definition of k_D and k_o."(65)

The oscillating hydrofoil is a known surrogate model for VAWT, which was already introduced in former studies such as Ly et al. 1981 (86) but also in recent studies, such as Arab et al. 2019 (5). It models a single-bladed turbine of infinite blade length observed in the rotating reference frame of the turbine. For regular VAWT the tip-speed ratio λ is the crucial factor which determines the flow characteristics. It controls the shape of the trajectory of the angle of incidence α, and in particular the maximum angle of incidence $\alpha_{\max}$. The pitch velocity of the foil, $\dot{\alpha}$, is also mainly governed by λ.

The second parameter with a strong influence to the flow field is the reduced frequency k. The existing formulations from McCroskey 1981(92) (eq. (2.5) left), Laneville & Vittecoq 1986 (77) (eq. (2.5) right), as well as Laneville & Vittecoq's formulation for VAWT (eq. (2.7)) are not sufficient in the given setup. Indeed, the rotating reference frame used in Laneville's formulations (where v_∞ is replaced by the average blade tangential velocity given by ωR) is not entirely valid. Also, McCroskey's equation from helicopter aerodynamics does not represent the sawtooth-like trajectory of a VAWT.

In order to develop a valid representation of k in the model, $\alpha_{\max}$ from (eq. (2.3)) and $\dot{\alpha}_{\max}$ from eq. (2.6) are inserted into eq. (2.5) left. The result is the reduced frequency k_o for an oscillating hydrofoil in a water tunnel with average inlet speed v_{ch}, oscillating with frequency f_o and following the trajectory from eq. (2.3):

$$k_o = \frac{\pi \cdot f_o \cdot C}{v_{\mathrm{ch}} \cdot (\lambda - 1) \cdot \arctan\left[(\lambda^2 - 1)^{-\frac{1}{2}}\right]} \tag{4.1}$$

It should be noted that the maximum of $\dot{\alpha}_{\max}$ is an absolute value. $|\dot{\alpha}_{\max}|$ occurs on the descending branch of the motion with negative pitch speed. The term $(\lambda - 1)$ leads to a singularity for λ =1 (if α jumps from 90° to -90° at $\theta = \pi$), which is illustrated in fig. 2.4 for k_D (see eq.(2.7)) over λ.

The parameter k_D features the ratio of the chord length C to the turbine radius R (for k_o, R is included in f_o) and links it to the operating point of the turbine λ.

The model allows the coverage of an entire field of turbine designs with the variation of only two parameters: the reduced frequency k_o and the tip speed ratio λ. Such a coverage is mapped in fig. 2.4. This feature is used in the experiments to cover the range relevant for most common VAWT designs without variations in the hardware.

The effects of blade flexibility are evaluated through the non-dimensionalized coefficient of thrust c_{T} and normal force coefficient c_{N}. These can be calculated from the drag and lift coefficients, which are themselves calculated from drag and lift measurements on the profile:

$$c_{\mathrm{D}} = \frac{F_D}{0.5 \cdot \rho \cdot s \cdot v_{\mathrm{ch}}^2} \tag{4.2}$$

$$c_{\mathrm{L}} = \frac{F_L}{0.5 \cdot \rho \cdot s \cdot v_{\mathrm{ch}}^2} \tag{4.3}$$

$$c_{\mathrm{T}} = c_{\mathrm{L}} \cdot \sin\alpha - c_{\mathrm{D}} \cdot \cos\alpha \tag{4.4}$$

$$c_{\mathrm{N}} = c_{\mathrm{L}} \cdot \cos\alpha + c_{\mathrm{D}} \cdot \sin\alpha \tag{4.5}$$

The thrust coefficient c_{T} allows for the comparison of the power performance of different hydrofoils. Their performance in reducing structural loads is obtained with the ratio η of the average thrust and the maximum normal forces.

This coefficient, which may be compared to the lift-to-drag ratio used in aerodynamics to evaluate the efficiency of airfoils, will be subsequently named thrust efficiency η:

$$\eta = \frac{c_{\mathrm{T}}}{c_{\mathrm{N}_{\mathrm{max}}}} \tag{4.6}$$

One important parameter for lifetime considerations with cyclic loads is the peak stress variation. High-cycle fatigue analysis is often performed using semi-empirical data provided in so-called S-N diagrams. Those display the number N of cycles required to obtain failure when loading a material with peak stress S. It is known that the number of cycles increases exponentially when the peak stress decreases (Castillo & Fernandez-Canteli 2009 (27)). In this study, the cyclic amplitude of the loads in a VAWT are measured with the non-dimensionalized average amplitude of the normal force $\hat{c}_{\mathrm{N}}$.

$$\hat{c}_{\mathrm{N}} = \frac{c_{\mathrm{N}_{\mathrm{max}}} - c_{\mathrm{N}_{\mathrm{min}}}}{2} \tag{4.7}$$

The variations of $\hat{c}_{\mathrm{N}}$ for different rigidities will allow to compare qualitatively the influence of the flexibility of the blades on the lifetime of a VAWT.

4.2 Experimental design

An experimental study of the fluid-structure interaction in turbomachinery should include both a measurement of the structural deformation (e.g with a Laser Interferometer) and a measurement of corresponding flow field (e.g. with PIV). Either the acquisition of both phenomena is simultaneous, or an adequate coupling mechanism has to be found to create a link in between two different readings.

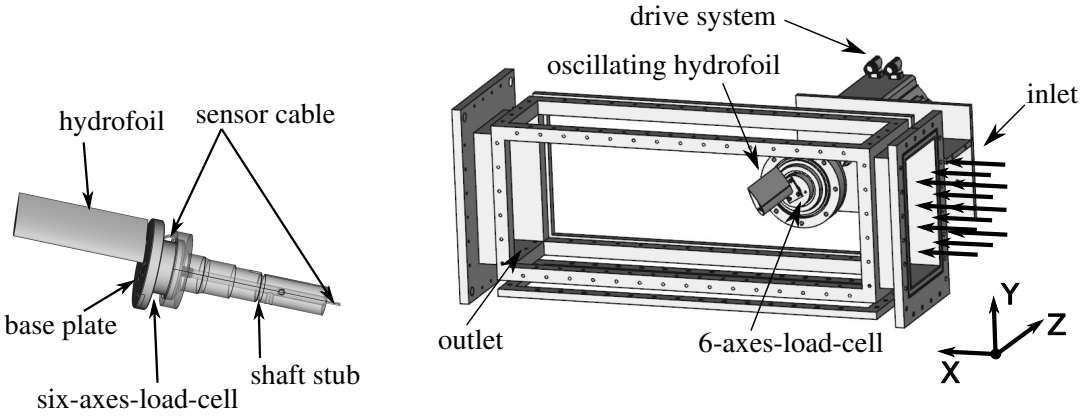

Figure 4.2: The test section at LEGI Grenoble with a streamwise length (X-axis) of 1000 mm, a width (Z-axis) of 175 mm and a height (Y-axis) of 280 mm. The origin is situated in the pivot axis of the drive shaft in between the sensor and the hydrofoil mounting plate.

In the present study, this link is created with acquisition of the position feedback, the inlet flow speed and the temperature synchronized with the hydrofoil deformation or flow field measurement, respectively. It allows to compare the measurements from different campaigns with use of normalized or non-dimensionalized parameters, like the velocity, relative to the mean flow speed, $v_\infty/\bar{v}_\infty$ or the reduced frequency k_o.

The LEGI laboratories have been researching VAWT experimentally and numerically for more than a decade. In order to be able to compare results to existing research, the experimental setup was designed to match the data in existing LEGI studies. Most experimental data had been acquired with a milled aluminum model of a three-bladed VAWT with 175 mm diameter and 175 mm height, subsequently called "LEGI turbine". The key parameters in those studies can be found in Maître et al. 2013 (91) and are listed in tab 4.1.

Table 4.1: "LEGI turbine" specifications

Type: 3-bladed H-Darrieus (91)			
Radius	R	[m]	0.0875
Height	H	[m]	0.175
Cord length	C	[m]	0.032
Inlet velocity	v_{ch}	$[\frac{\mathrm{m}}{\mathrm{s}}]$	2.8
Av. ang. velocity	ω	$[\mathrm{s}^{-1}]$	64
Opt.tip-speed ratio	λ_{opt}	[-]	2
Av. Reynolds number	Re	[-]	200 000
Red. frequency ($\lambda = 2$)	k_D	[-]	0.35
Solidity	σ	[-]	1.1

4.2.1 Experimental facilities

The oscillating hydrofoil experiment was carried out in the closed water channel at the LEGI labs in Grenoble (see figs 4.2 & 4.3 plus table 4.2 for specifications); minor

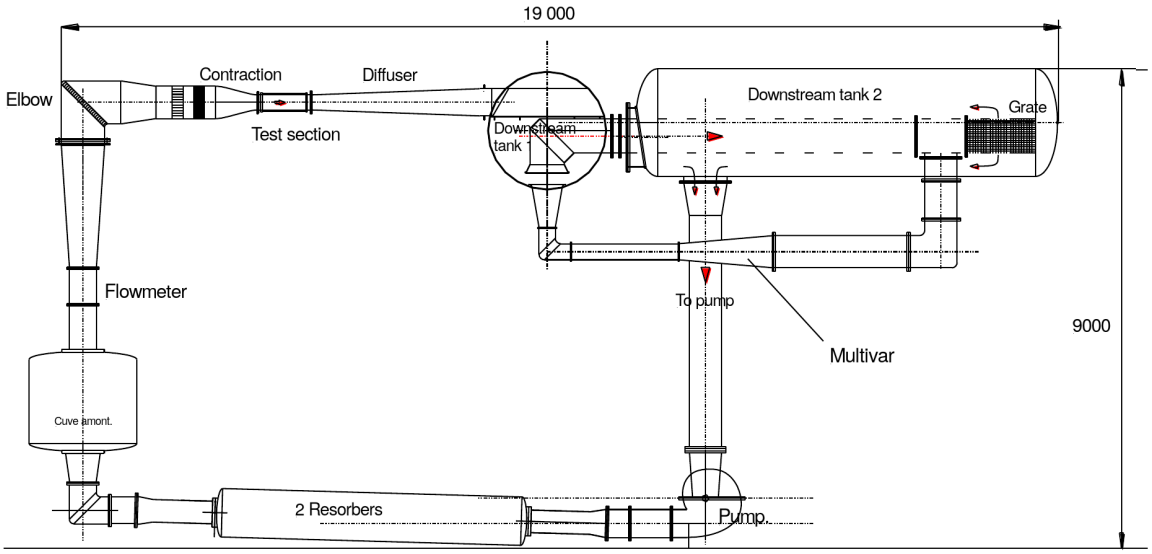

Figure 4.3: The LEGI hydrodynamic (or cavitation) tunnel was built in 1968. Its height extends over 9 m (two floors).The channel has two inbuilt tanks and a double reabsorber downstream of the test section. The channel can operate at up to 0.65 m^3/s at 20 m head.(12)

changes were made to an existing setup investigating the cavitation on a inclined hydrofoil (Carrat 2018 (26)). This setup was a given constraint for the author; the experimental setup had to be adapted to the existing hardware. A detailed description of the facility is given in Aumelas 2011 (11) and Aumelas et al. 2016 (12).

Unfortunately, it was not possible to implement an alternating flow speed with the given hardware without carrying major changes to the existing configuration. Additionally, a minimum channel inlet velocity of v_{ch}=3 m/s had to be kept to avoid the pump drive overheating due to the inefficient operating point (because of weak self-cooling and low runner rotation speed). It follows that the chord length of the oscillating hydrofoil was set to c=0.066 m in order to maintain a chord-based Reynolds number of Re=200 000. The turbulence intensity in the channel was measured with two-component Laser-Doppler Velocimetry at the inlet cross section of the test section and found to be less than 0.5% in the core flow, rising to 3.5% close to the wall and in the corners of the test section.

Table 4.2: LEGI water tunnel

Type: Closed loop			
Capacity		[m^3]	36
Pumping power	P	[kW]	165
Volume rate	Q	[$\frac{m^3}{s}$]	0.65
Turbulence int.		[%]	<0.5*

*In the core flow from LDV measurement

The volume flow rate is measured with a propeller-based sensor in the main pipe of 500 mm diameter. The uncertainty of the sensor is <0.5% (Aumelas 2011 (11)).

The chosen chord length leads to a confinement in the tunnel cross-section which reaches a maximum value of 12% (for a rigid foil at an angle of incidence α=30°), which is not negligible. West &

Apelt 1982 considered that confinement effects were negligible below 6% (129). These observations are based on measurements using a static circular cylinder. In this case drag is the dominant force since the average lift is approximately zero. According to West & Apelt 1982, the drag is not influenced by the blockage. However, significant changes of the Strouhal number Sr=$\frac{f \cdot l}{v_\infty}$ are observed, which occur because already small modifications of the pressure distribution have strong effects on the vortex shedding frequency.

In the present study, the frequency is not free, but imposed by the forced oscillation of the profile. Confinement effects are expected to result in higher lift coefficients but to have little effect on drag, and so to result in overly positive measurement results. The flexible foils tested in the experiment are the least affected by confinement. This is because their deformation results in lower blockage ratios (see fig 2.9). In the forthcoming comparison of the performance of rigid and flexible foils, confinement effects are therefore expected to favor rigid foils, artificially decreasing the observation of benefits brought by foil flexibility.

The water channel governing system is disconnected from the measurement environment. Its control parameter is the frequency of the runner of the pump drive. The resulting volume flow rate changes slightly with time, since water temperature evolves during the experiment. The channel is started manually and runs autonomously. The flow rate and temperature are recorded with a branch cable of the sensor to the data acquisition card (DAC). The flow speed is periodically readjusted. This effect has no impact on single measurement takes, where velocity variations with time remain below 1 %.

4.2.2 Drive system

The tunnel test section is equipped with a Kollmorgen servo drive system with power inverter to rotate the foil (see table 4.3 for specifications). The system is not designed to perform arbitrary oscillatory motions. The manufacturer suggested the purchase of an extension card for the inverter with associated software. Kollmorgen provides custom software for *Windows* OS and drivers for the *LabVIEW* software package, but those do not provide the required functionality, and no code libraries are available to customize the existing capabilities. Additionally, the reaction time in the communication in between the governing software *LabVIEW* and the drive system was found to be excessive.

Table 4.3: LEGI drive system specifications

Servo drive		AKM-74L	
Power	P	[W]	6080
Peak torque	T	[Nm]	143
Inertia	J	[kg m^2]	$120 \cdot 10^{-4}$
Power Inverter		AKD-P02407	
Cont. power		[W]	5000
Cont. current		[A]	48
Switch. frequency	f	[kHz]	8

It was decided to develop custom software based on *Python* with the aim to build a uniform environment for data acquisition, drive communication, and control. *Python*

was chosen because of the authors' existing knowledge in this programming language, and the expectation that the lower abstraction level compared to *LabVIEW* would provide for more responsive characteristics. The development subsequently described was carried out in close collaboration with Shokoofeh Abbaszadeh, from the Chair of Electrical Drive Systems at the University Otto-von-Guericke of Magdeburg.

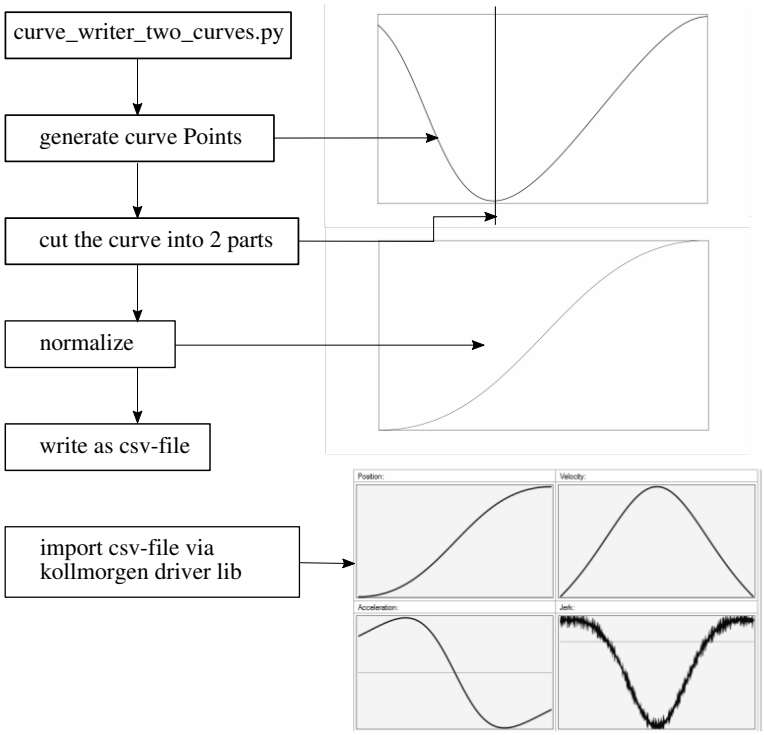

Figure 4.4: Workflow of the curve shape generation for the drive system from a given trajectory.

The inverter communicates via Telnet over a LAN connection. The *Wireshark* software package (29) was used to sniff the communication between the computer and the drive at the Ethernet interface and to reverse-engineer an appropriate *Python* driver. This allowed the implementation of all the necessary functionality for the drive communication. In foresight of a second project to investigate the optimal trajectory for an active pitch system (see sec. 5.1), the software features the creation of an arbitrary rotational motion in a fully automatized process. The software driver was implemented with object-oriented approach to allow the communication with multiple drives in a client/server setup in which every drive system acts as a self-standing server and is implemented as an instance.

The description of a motion task is given by an ID number, the endpoint of the motion, the velocity of the motion, the maximum acceleration, the maximum deceleration, the dwell time (if a following task is defined), the ID number of the following task, the shape of the motion law, and a control number. Unfortunately, it is not possible to define the time that a task could take to directly determine a motion frequency, such as angular distance/velocity. Consequently, the acceleration and the speed have to be adapted iteratively until the desired frequency is reached with the desired accuracy. In this study, the obtained accuracy is <1 ms for the surface-tracking and force measurements. The PIV measurements were realized with an older version of the governing script which showed slightly higher deviations.
The start value is the present position. The drive has to be driven to an initial position before the oscillation starts (to check the offset of the sensor at zero angle).

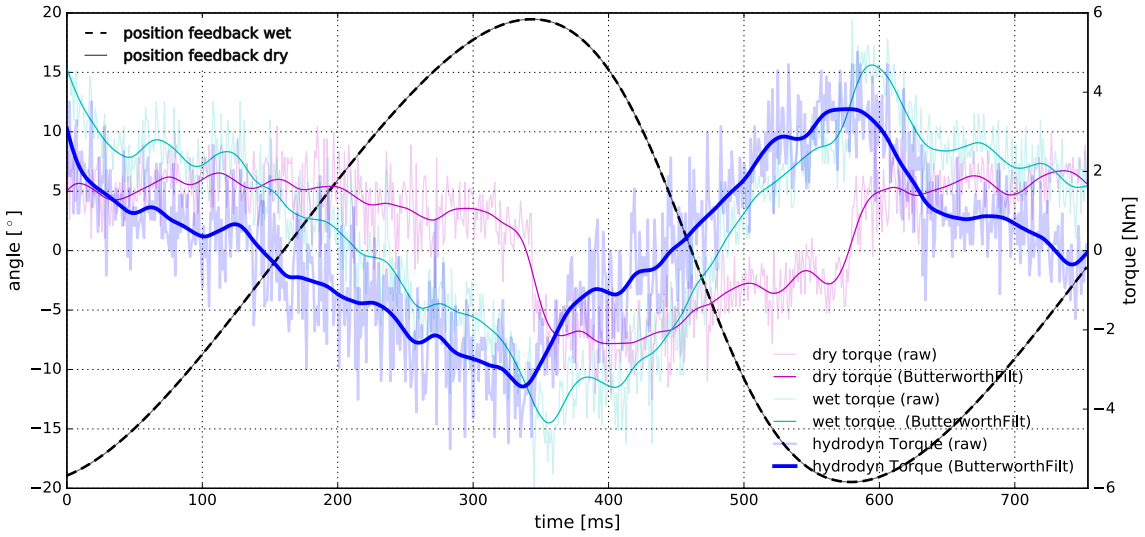

Figure 4.5: Measured deflection angle and torque during a single oscillation period. Angle is displayed on the left axis, while torque is displayed on the right vertical axis. Torque measurement is carried out over motor torque constant and motor current.

The shape of the trajectory can be trapezoidal, one-to-one, or defined with a profile table (custom shape). Acceleration discontinuities (jerks) between curves has to be avoided. In the present case a custom shape (trajectory of angle of incidence for a VAWT) was used. The drive system accepts `csv` data as input. To fulfill the requirements, the trajectory has to be preprocessed (see fig. 4.4) All motion tasks had to be verified for their shape as consequence of the indirect declaration.

The software also allows to retrieve the motor current in order to measure the torque via the motor torque constant, as $M_Z = I_e \cdot c_M$[1] (see fig. 4.5). A measurement was performed, once with water under operating conditions (cyan curve, 3.5 m/s) and once in air with an empty tunnel (magenta curve) in order to estimate the friction and inertia effects in the transmission system. The position feedback for both takes (black and grey curve) shows perfect accordance, which proves the drive system and the custom control software to be well-suited for the task. It is observed, for example, that as expected, the value of the friction changes sign with the rotational direction. Also, the friction decreases once the motion has started, because of the difference between the static and sliding friction. The friction force was found to be significant compared to the hydrodynamic torque. Consequently, it was decided to position a force sensor (described in the next section) in a fully-submerged position between the hydrofoil and the shaft stub (instead of in a dry position outside the test section in between the drive and the shaft). This position avoids the unwanted effects to be captured in the measurement and allows to measure lift and drag forces.

[1]The motor torque constant c_M was provided by the manufacturer

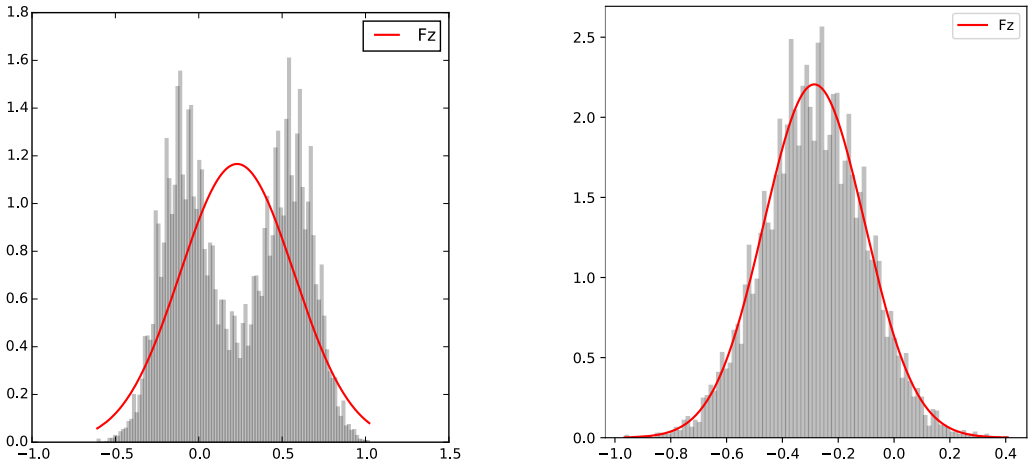

Figure 4.6: (left) Two-peak distribution of the sample values in the Z-axis. (right) Distribution of the sample values in the Z-axis after installation of a low-pass filter

4.2.3 Measurement instrumentation and software

The existing installation in the water tunnel at the LEGI lab did not include force and torque measurements. A fully-submerged, six-axis load cell (see table 4.4 for specifications) was added to provide knowledge of the hydrodynamic loads. An amplification was implemented with a custom amplifier built by the cooperation partners of the Lab of Electrical Drive Systems at the University Otto von Guericke of Magdeburg.

The sample distribution of the first measurement tests showed a two-peak distribution for the Z-axis. Figure 4.6 (left) shows the effect for a 1 kg mass load on the X-axis only. In this case, measurements on the Z-axis provide a measure of inaccuracy and noise. The data is plotted as a histogram of the distribution (grey) alongside with the expected probability density function (red line) for a normal distribution. It is supposed that the distribution is based on noise with f_N=1 kHz, while the shift of 0.6 N results from inaccuracy of the coordinate system (the Z-axis is slightly rotated and captures part of the X-axis load).

Other axes did not display this effect. This could be explained by the higher signal-to-noise ratios on those axes. A spectral analyze, performed by Roberto Leidhold, Head of the Lab of Electrical Drive Systems showed a perturbation frequency f=432 Hz. He considered the perturbation to be generated from aliasing effects of the power electronics in the LEGI lab. The switching frequency of these devices is normally >10 kHz. In this case, aliasing effects for the chosen sample rate of 1 kHz, could be filtered with a filter of half of the sample rate, following the Nyquist–Shannon sampling theorem. This is because the real perturbation frequency is $f = 432 + n \cdot f_c$, in words, the sum of the observed perturbation frequency plus n-times the capturing frequency. After a first order low-

Table 4.4: Six-axis load cell specifications

SRI sensors		M3714BP
Strain gauges	[Ω]	350
Net load F X,Y,Z	[N]	800,800,1600
Net load T X,Y,Z	[Nm]	44,44,44

pass R-C filter with f=480 Hz was built before the data acquisition card (DAC), the bimodal distribution disappeared and the expected normal distribution of the samples could be observed (see fig. 4.6 (right)).

A LabJack T7 DAC was used to capture the signals and to discretize the analog inputs. The position feedback was captured from the drive system digitally as a quadrature signal. The card features up to 100 kHz sample rate for all channels together. In the given setup, 11 channels were in use (three forces, three moments, temperature, flow speed, a trigger channel and two channels for the quadrature signal of the drive). A stable stream rate of 1 kHz could be reached. Higher streaming rates provoked arbitrary package loss during the stream, which corrupted the data.

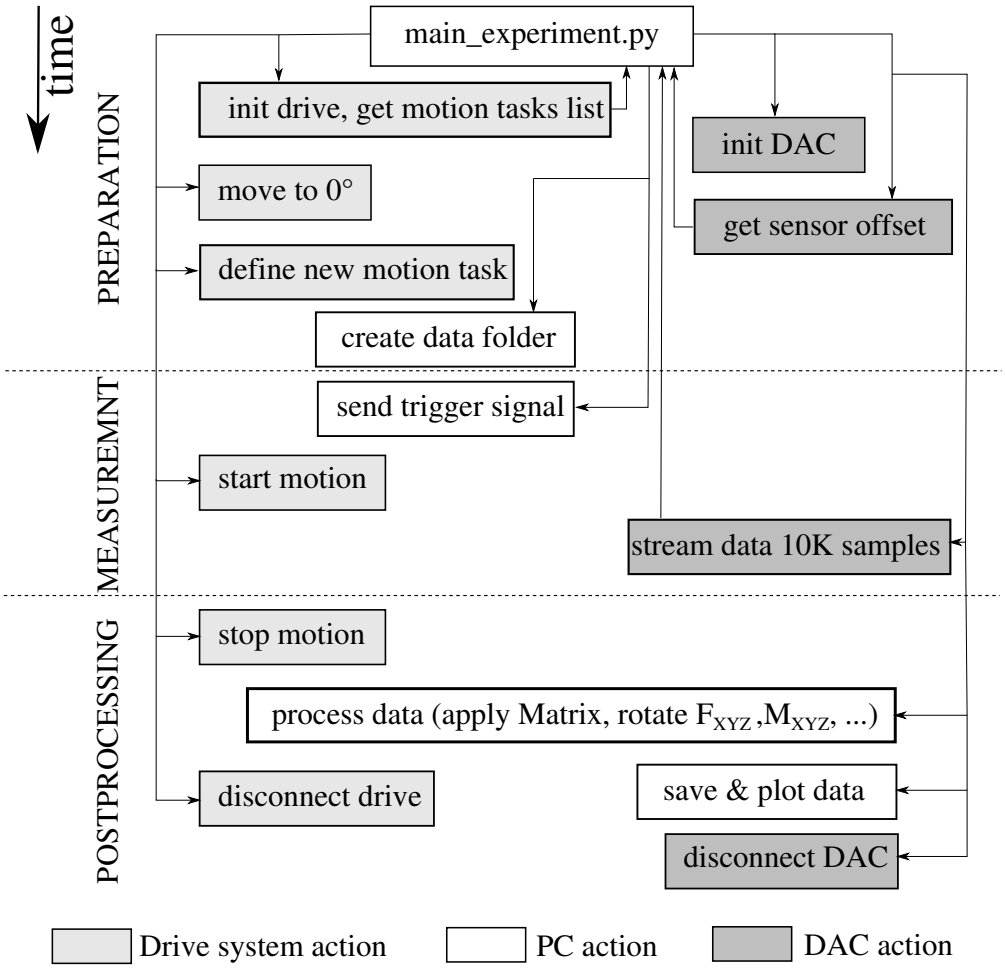

Figure 4.7: Flow chart of the main experiment script which governs the measurements.

The signals were discretized with 16 bit accuracy and streamed over Ethernet to a computer. The communication software for the DAC is based on the manufacturer's convenient *Python* libraries. The custom code implementation for the experiment features multiple acquisition cards due to the object-orientation. In this case multiple DAC could be stacked and higher acquisition rates would become feasible by the use of an asynchronous topology and server/client setup.

The experiments are governed over a main script; the flow chart in figure 4.7 shows the topology of the code. The measurement software starts by reading the parameters for the motion law provided by the script. Then the drive gets initialized with the Kollmorgen *Python* library. With established connection the drive moves to 0° while the new motion task is created and sent to the drive. The DAC is initialized and the sensor offset is read from an average of 100 samples. The motion is started with a delay of 1 s and the data stream starts.

After 10k samples are acquired for each channel, the data is processed. The offset is subtracted, the manufacturer's calibration matrix is applied to separate the different channels from each other. The forces are transformed from the rotating reference frame of the sensor to the static reference frame (laboratory) by application of a rotation matrix $\underline{\underline{R}}_Z(\alpha)$:

$$(\underline{\mathrm{F}}, \underline{\mathrm{T}})_{xyz} = \underline{\underline{R}}_Z(\alpha) \times (\underline{\mathrm{F'}}, \underline{\mathrm{T'}})_{xyz} \tag{4.8}$$

with

$$\underline{\underline{R}}_Z(\alpha) = \begin{bmatrix} \cos\alpha & \sin\alpha & 0 \\ -\sin\alpha & \cos\alpha & 0 \\ 0 & 0 & 1 \end{bmatrix} \tag{4.9}$$

The results are plotted in a diagram and as averaged value for each channel to the screen. The data, including time, position feedback from the drive, forces, moments, flow speed, temperature, trigger signal, sensor type, offset, average forces, and moments, is stored in a `JSON` format file. An `SVG` plot of the forces and position feedback is also created.

4.2.4 Measurement uncertainty

No sensor data sheet is available to evaluate the uncertainty for the temperature and flow meter sensors installed in the water channel. Aumelas (11) stated the flow meter accuracy as >0.5%; it is not known if this value corresponds to full scale (FS) or reading (R) measurements.

The set point precision of the drive system is given as 0.058° (by 0.0439° resolver resolution. The zero angle was calibrated with 0.014° accuracy (0.25 mm per meter) with a precision level. It has to be noted that the direction of rotation is counted in the view of the drive system. The measurements data was flipped horizontally to be adapted to the view point of the hydrofoil.

Single axis accuracy on the load cell depends on the amplification device, which was custom-built. Standard weights were used to determine the static accuracy of the load-cell-based force measurement system. The maximum error was found to be less than 0.009% at full scale (800 N load). It was about 0.05% reading (relative error) when calibrating with a load of a 2 kg standard weight. The uncertainty rose significantly for a load below 0.1 kg (<1N, >4.8% to reading).

Significant crosstalk is specified by the manufacturer. Furthermore, the dynamic characteristics and the sensor hysteresis raise the uncertainty. The calibration sheet of the six-axis load cell provides sensor crosstalk in % full scale (FS). The sensor was dimensioned with respect to the cyclic loads with a high security factor:

The expected range for the lift force was $F_L < 180$ N with a corresponding moment $M_X < 18$ Nm (assuming the load application point in the middle of the length of the profile). The manufacturer recommended a security factor sf=2. The best fitting sensor class (M3714B) rates moments up to 44 Nm and forces up to 800 N for X,Y axis and 1600 N for Z-axis. The uncertainty to full scale coming alongside with this capacity would be comparable to the magnitude of the interest in our study. On request the manufacturer stated that "the industrial standard to specify the performance of a multi-axis load cell is rated to full scale. therefore ... the crosstalk error could be a constant value for all load range, based on the performance specification. However, the actual performance of the SRI sensor is better than the assumption. As ... example, FZ crosstalk is 1.82% of 1600N or 29.12N for full scale loading. When the loads for all six axis are reduced by 50% , Fz crosstalk will be close to 1.82% of 800N or about 15N."[2]

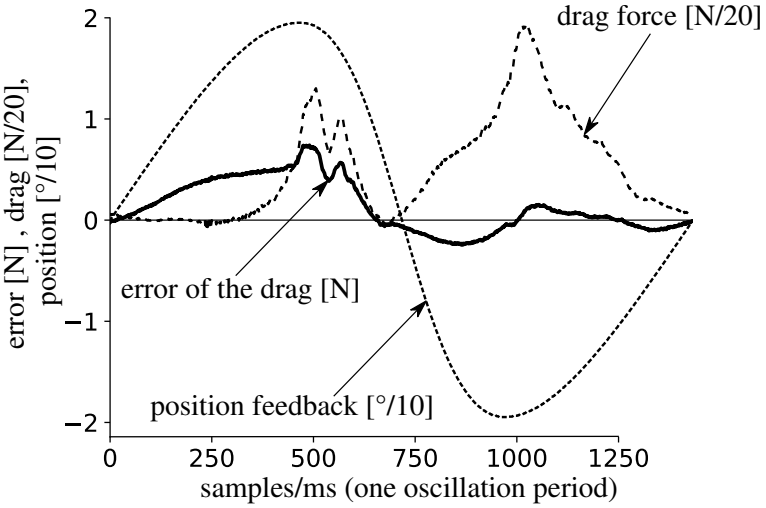

Figure 4.8: Error of the drag during an oscillation period. The drag force and the position feedback are divided by factor 10 and factor 20 for better visibility.

In this case, the estimation of the uncertainty r for each axis of the sensor has to include the uncertainty of the channel itself, and the crosstalk of the other channels. It is given as a crosstalk coefficient c_C for each channel, which leads to a 6×6 matrix. The hysteresis effects and the non-linearity of the sensor is neglected.

Eq. (4.10) shows the formulation for the instantaneous uncertainty r_{F_X} of the drag force (X-axis):

$$r_{F_X} = r_X \cdot F_X + c_{C_{F_Y}} \cdot F_Y + c_{C_{F_Z}} \cdot F_Z + c_{C_{M_X}} \cdot M_X + c_{C_{M_Y}} \cdot M_Y + c_{C_{M_Z}} \cdot M_Z \quad (4.10)$$

$$r_{F_X} = 0.009F_X + 0.0029F_Y + 0.0182F_Z + 0.0076M_X + 0.0028M_Y + 0.0M_Z \quad (4.11)$$

Figure 4.8 shows the error estimation in the X-axis (flow-wise direction). The drag is key in this study, and more prone to inaccuracy than the lift, which has order of magnitude higher values when the foils are not stalled. It has to be noted, that the error is shown in its full magnitude [N], while the drag is downscaled by a factor 20 [N/20] in this figure. The error is calculated for the rigid hydrofoil for one oscillation period at a reduced frequency k=0.039 and λ=3 using eq. (4.10 & 4.11). The RMS of the absolute error is 0.29 N, corresponding to 0.036% FS, and 2% R. The error is mainly due to the crosstalk; this is especially important when the drag force is low but the lift force is high, which corresponds to non-stall flow conditions. In this case,

[2]York Huang, Sunrise Instruments, per mail 6/12/2018

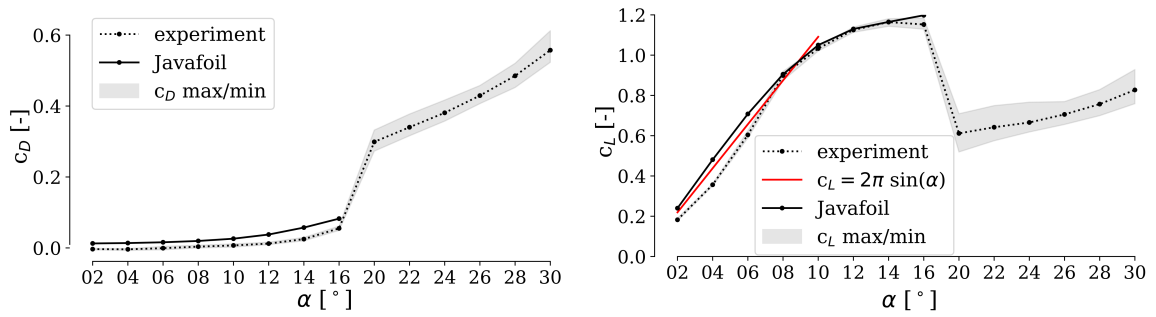

Figure 4.9: "Comparison of the experimental measured drag (left) and lift (right) coefficients with calculated values. The grey fields are the min/max variations from mean value. The results show satisfactory agreement with Javafoil and with the theoretical slope ($c_L = 2\pi \sin(\alpha)$) below the static stall angle of ≈15°." Reprinted from (65)

the error can be larger than the drag itself (see samples for 0-350 ms). In summary, the signal for the dynamic drag measurements in non-stalled flow conditions is in the range of the measurement uncertainty. This technical limitation of the sensor has to be considered in the results. However, the (negative) contribution to the thrust of the drag forces for a non-stalled profile were considered negligible in relation to the lift.

In a second step, as already published in Hoerner et al. 2019 (65), the static lift and drag coefficients for the system were captured with and without water; the results of the difference between them –the hydrodynamic forces– for the rigid hydrofoil were compared to computed results produced with the JavaFoil utility (62); the results are displayed in fig 4.9. Measurements and calculations are consistent below the static stall angle.

However, the slope of the experimental lift curve is less steep and the drag curve is shifted to lower magnitudes. The differences remain <1% of the sensor full scale and the effect on the drag can be explained by the sensor crosstalk as mentioned above. JavaFoil is not able to provide results beyond stall, and no lift and drag coefficients were computed there.

4.3 Flexible blades

An understanding of the structural characteristics of the hydrofoils deployed in the experiment is required for an experimental validation of the characteristics of flexible structures in VAWT. The geometry of the hydrofoil was chosen to match that of the LEGI turbine; the turbine is equipped with modified NACA0018 hydrofoils, which were adapted to the curvature of the flow (which is a result of the rotational motion). The chord line of those foils is bent along the shape of turbine circumference, which is a function of the radius R, according to Zanette et al. 2010 (131); this bending results in a NACA4518-alike geometry.
In the water channel, the flow can be considered to be straight. In consequence, a NACA0018 geometry was selected as an equivalent to the LEGI turbine foils. Fur-

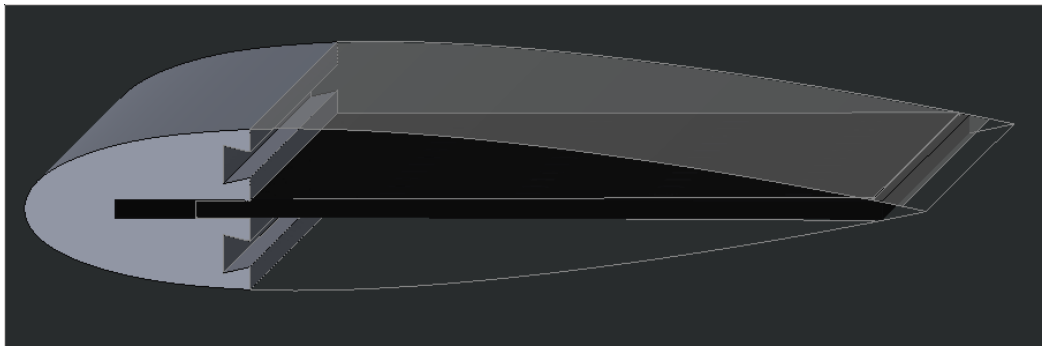

Figure 4.10: The design of the flexible hydrofoils consists of a rigid leading edge, with a bendable carbon composite plate for the stiffness of the trailing edge and a silicon embodiment for the shape.

thermore, it was decided to position the pivot point of the foil at quarter-chord, which minimizes the torque efforts. Future experiments may study the influence of the pivot point; multiple fixation points are available along the hydrofoil mounting plate.

4.3.1 Design

The design is based on a rigid milled aluminum leading edge; this results in a high span-wise rigidity for all foils. The rigidity in the flow-wise direction is given by a composite blade of variable thickness τ (see fig. 4.10). A variation of this thickness allows for the adjustment of the hydrofoil rigidity. Additionally, a major advantage of this material is the possibility to create anisotropic material characteristics: the Young's modulus E in one direction can be made an order of magnitude higher than in another direction. In this case, fiber is laid in a uniform direction in a composite material. Very high flexibility is obtained in one direction, with E_{0° of the magnitude of the resin matrix, and high rigidity is obtained in the other, with E_{90° of the magnitude of a carbon fiber. The uniform thickness of the composite blade makes for uniform bending stiffness. Its deformation can then be described with the clamped beam theory, which simplifies the design process. The shape of the structure is provided by a hyper-flexible filling material which also distributes the pressure loads to the composite plate. A two-component silicon was selected as a filling material, because of its environmentally inert characteristics and good processability.

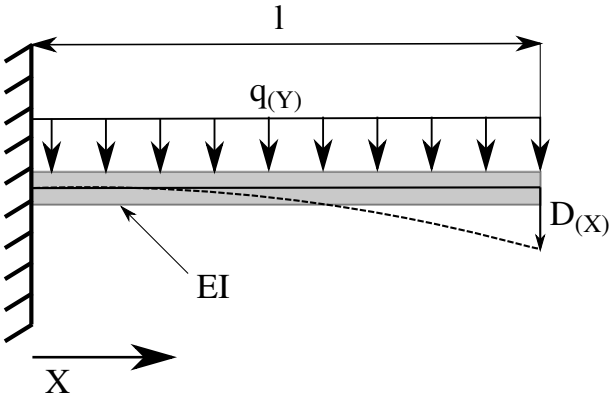

Figure 4.11: The mechanical model of a clamped beam was used for the design of the flexible hydrofoils.

The mechanical model of a clamped beam (see fig. 4.11) was

applied to roughly estimate the necessary thickness of the composite blade. This mechanical model includes important assumptions:

- a purely axial bending;
- the cross sections remain straight during the deformation (Bernoulli hypothesis);
- linear elastic material characteristics, Hooke's law is applicable:

$$S = E \cdot \epsilon \tag{4.12}$$

- constant bending stiffness.

The experimental setup in the test section of the water channel allows the assumption of a two-dimensional flow case from geometrical considerations, and so the Z-component of the flow field is neglected for the design process. The forces acting on the hydrofoil are mainly the lift force (Y) and with small contribution the drag force (X). Both generate axial bending. The contribution of the silicon was neglected, since its Young's modulus is 80,000 times smaller than that of the carbon fiber composite (see sec. 4.3.2 for detailed mechanical properties). The two-dimensional bending line (the displacement d) of a beam with length l and geometrical moment of inertia I, as caused by a line load q_Y, is obtained with the integration of a differential equation of the fourth order:

$$E \cdot I \cdot d''''_{(X)} = q_Y \tag{4.13}$$

Which becomes, after fourth integration and application of the boundary conditions:

$$d_{(X)} = \frac{q_Y \cdot l^4}{24EI} \cdot \left(6\frac{X^2}{l^2} - 4\frac{X^3}{l^3} + \frac{X^4}{l^4} \right) \tag{4.14}$$

The maximum displacement $d_{(X)\max}$ is obtained as:

$$d_{(X)\max} = \frac{q_{(Y)} l^4}{8EI} \tag{4.15}$$

The inertia I of a beam with rectangular cross-section area and width b is:

$$I = \frac{b \cdot \tau^3}{12} \tag{4.16}$$

From geometrical considerations, the deflection angle ζ is obtained as:

$$\zeta = \arctan\left(\frac{d_{(X)\max}}{l} \right) \tag{4.17}$$

After insertion of eqs. (4.15 & 4.16) in eq. (4.17), the thickness τ required to obtain a deflection angle ζ is calculated as:

$$\tau = \sqrt[3]{\frac{3 q_{(Y)}\ l^3}{3E\ b \cdot \tan(\zeta)}} \tag{4.18}$$

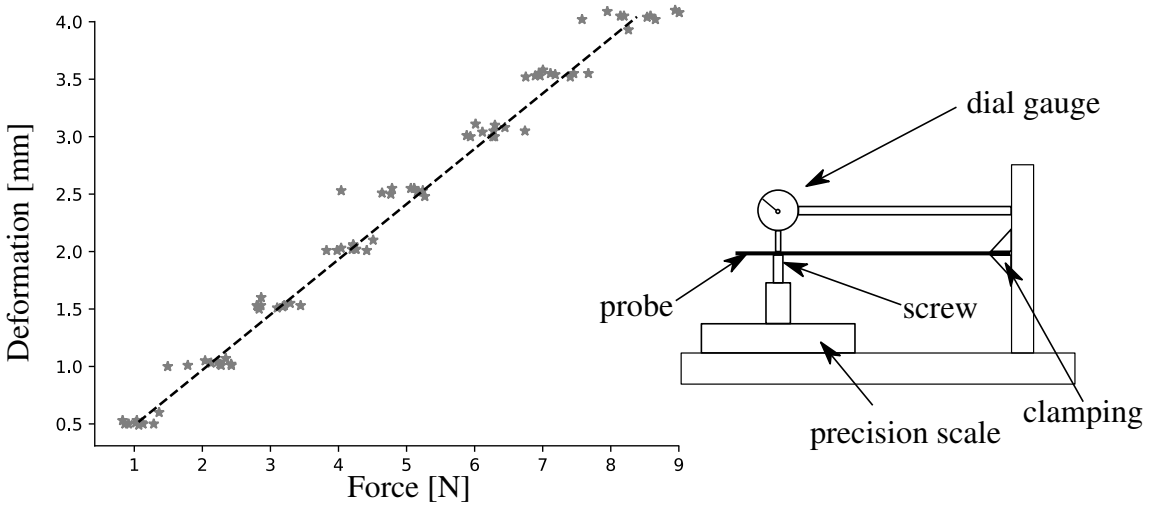

Figure 4.12: Experimental determination of the Young modulus of the carbon composite: Left: Deformation as a function of the applied load; right: Experimental setup.

4.3.2 Determination of the material properties

The mechanical characteristics of the hydrofoils were investigated next. The aluminum specifications were taken from the vendor's data sheet (conformal to European norm, EN AW-7075). The characteristics for polymers and composites depend on the specific manufacturing process. Because no usable data was available for the carbon fiber composite and silicone, an experimental investigation of the mechanical properties was carried out. The experiments provided the Young's modulus of the materials, enabling a later comparison with numerical studies.

Table 4.5: Material specifications

Aluminum alloy		EN	AW-7075
Young's Modulus	E	[Pa]	$72 \cdot 10^9$
Density	ρ	[kg/m^3]	2800
Tensile strength	$R_{p0.2}$	[Pa]	$450 \cdot 10^6$
Carbon Fibre			cg-tec.de
Young's Modulus	E	[Pa]	$52.7 \cdot 10^9$
Density	ρ	[kg/m^3]	1600
Fibre Orientation		[°]	0/90
Silicone			Wacker
Elastosil M4600			
Young's Modulus	E	[Pa]	$6.4 \cdot 10^5$
Density	ρ	[kg/m^3]	1100
Tensile strength		[Pa]	$7 \cdot 10^6$

Aluminum: The aluminum parts were milled from alloy EN AW-7075 (AlZnMgCu1,5), which was chosen for its good machinability and high tensile strength. The material characteristics are shown in table 4.5. Unfortunately this alloy is prone to corrosion and has to be treated for the use in a water channel. The fully rigid hydrofoil and the base plate were anodized black; other parts were painted.

Carbon fiber composite: Reliable data was not available, and so a bending test on a custom bending test rig was per-

formed to measure the Young's modulus (see fig 4.12). The setup consisted of a precision scale to measure the bending force and a dial gauge for the deflection. A probe was clamped in the apparatus and the deflection was adjusted by a machine screw placed on the scale. The measurement was repeated 10 times for 10 points on the plate with thickness τ=0.7 mm. The Young's modulus was calculated with eq. (4.15), resulting in an average of E=52.7 GPa. This low value for a carbon fiber composite can result from a high share of resin (matrix) compared to the carbon fibers (reinforcement). The mean deviation from the determined Young's modulus was 6%, with the maximum outlier at 26%. The tensile strength was not tested, since it does not play a role in the mechanical model of the foil deformation.

Silicone: The chosen material is a two-component system from Wacker chemistry called Elastosil M4600. This material is designed to create molds for reproduction of existing structures. It features hyper flexibility with 800% elongation at break. The mechanical properties of the silicone depend strongly on the mixing and molding process and can vary in a wide range, depending on the polymerization temperature and the ratio of the two components of the system. Experiments with aim to determine the silicone characteristics were carried out at the laboratory of steel and lightweight construction, of C.-T. Weber, at University of Applied Sciences Magdeburg. They were performed by Carsten Laddey, student assistant, under direction of the author (75). All results are extracted from his report of the experiments.

A nondestructive tensile test was carried out on three probes of different fabrication days (see fig 4.13). The polymer displayed a non-linear characteristic, hysteresis effects, and its Young's modulus varied by about 55% for different probes (from 0.28 to 0.43 MPa at a relative elongation ϵ=0.85). The non-linear characteristics do not allow to use Hooke's law (eq. 4.12) for this material. In this case, the curve slope can be approximated with negligible error with section-wise linearization. In the present case the averaged, section-wise linearized Young's modulus (red curve in fig. 4.13) is $E \approx 0.64$ MPa for a relative elongation ϵ <0.15. A finite-element simulation (FEM) with the software *Ansys Workbench* was carried out to estimate the probable deformation rate of the silicone embodiment (75). The structure was successively loaded until a tip deformation of 30° was reached. The peak elongation is 0.32, but occurs only near the sharp edge of the aluminum structure, and so may be safely neglected (see fig. 4.14). The expected elongation is thus $\epsilon < 0.2$. Table 4.5 shows the material properties of the silicone embodiment.

The following points have to be considered for the evaluation of the results:

- The number of probes (n=3) was too low for reliable results (a minimum of five probes is required according to the norm);
- The variations of the Young's modulus of the probes was approximately 55%;
- The probes were not built in a shape according to the norms;
- Air inclusions in the silicone varied significantly.

However, the Young modulus of the silicone is 80,000 times smaller than that of carbon-fiber based composite materials, which will consequently carry most of the

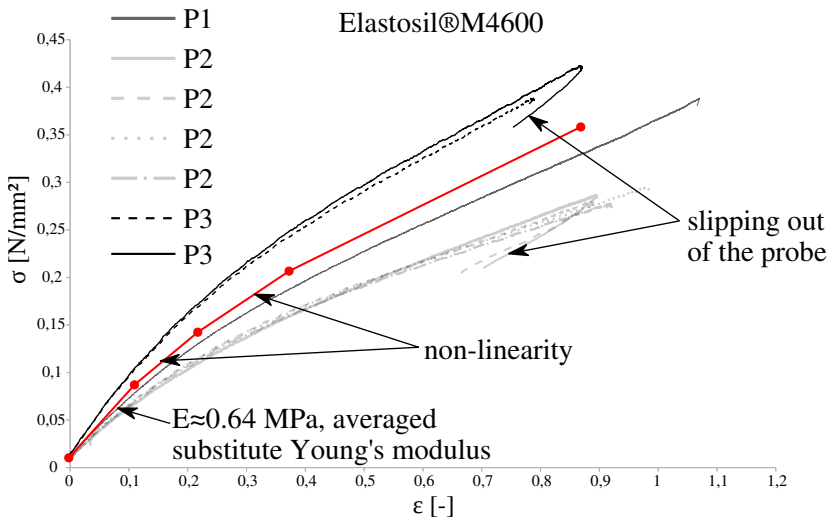

Figure 4.13: Nondestructive tensile tests of three silicone probes show non-linear characteristics and hysteresis effects. The Young's modulus can be approximated with $E \approx$ 0.64 MPa

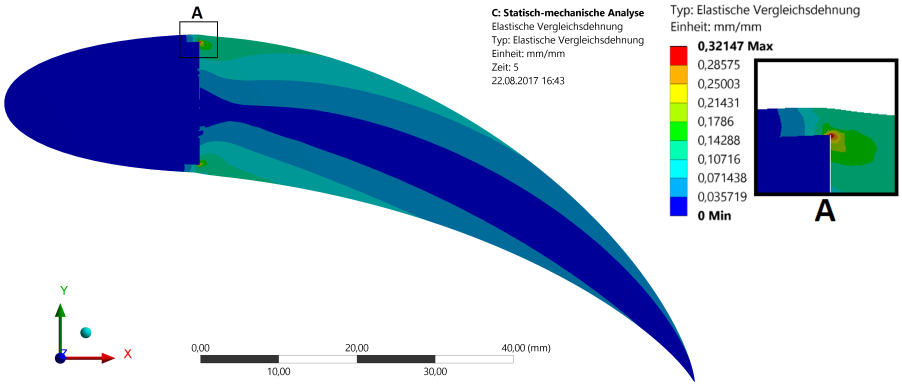

Figure 4.14: Maximal elongation of the silicone: FEM Analysis (*Ansys Workbench* software package) of the elongation at 30 °deformation of the hydrofoil (75)

hydrodynamic loads. The contribution of the silicone to the stiffness is negligible in the present case. Nevertheless, the silicone body not only provides the shape of the hydrofoil tail, but also smoothes out the pressure load distribution on the fiber composite plate.

4.3.3 Manufacturing

A maximum deflection angle ζ=15° was selected for the design. This value was chosen since $\alpha_{\max,\lambda=2}$=30° and the static stall angle of the foil is close to α_{stall}=15°. With a Young modulus for carbon-fiber composite materials of E=90 GPa the thickness resulting from eq.(4.18) is τ=4.98·10^{-4} m. It was decided to produce three flexible hydrofoils with varying blade thicknesses of τ=[0.3, 0.5, 0.7] mm. Unfortunately, the vendor for the carbon fiber composite sheets could not immediately deliver τ=0.5 mm,

and so the PIV measurements were performed for flexible foils with τ=0.7 and 0.3 mm only. Subsequently, the flexible hydrofoils will be named following the convention: flex[0.3] for τ=0.3 mm and so on.

A professional model maker external to the lab (CATLAB Berlin) milled all the

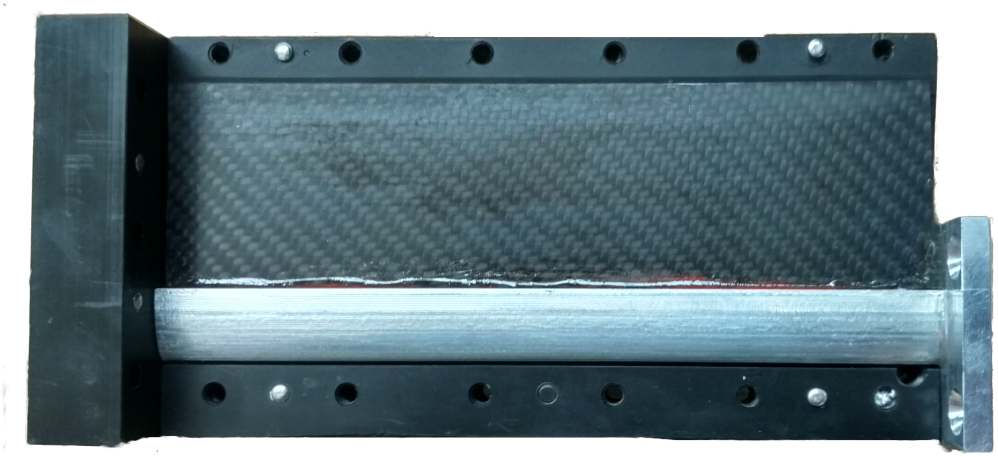

Figure 4.15: The aluminum milled head flexible hydrofoil with bonded carbon composite plate in the opened casting mold

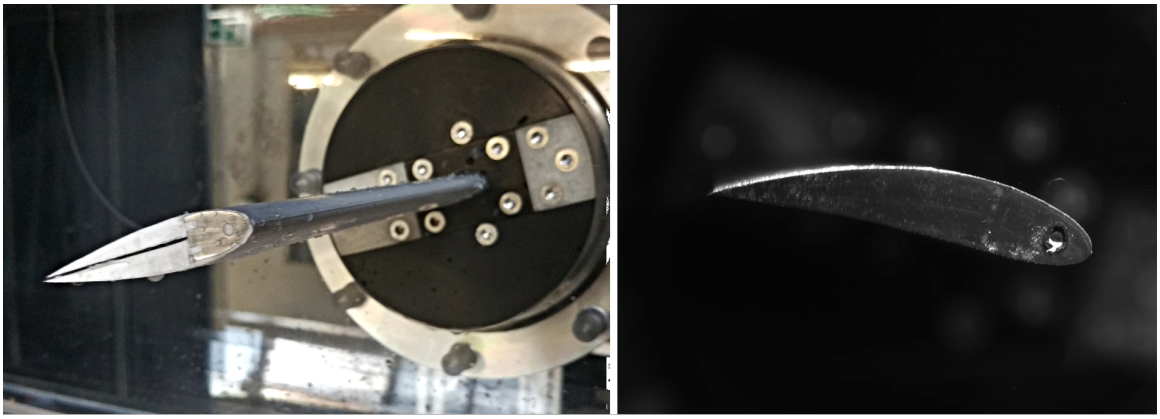

Figure 4.16: "Left: The composite hydrofoil consists of a leading edge milled from aluminum, a skeleton of carbon and a body of silicone. The rigidity of the foil is adjustable through the thickness of the carbon core. It is mounted on a six-axes load cell via an aluminum base plate. Right: The most flexible design (carbon blade thickness 0.3 mm) performs large deformations during one period. The picture shows the deflection for the λ=3 case at α = 20 °". Reprinted from (65)

necessary parts for the hydrofoil installation, a fully-rigid NACA0018 hydrofoil for reference, as well as the aluminum parts for the flexible hydrofoils. A milled casting mold for the silicon embodiment was also delivered (see fig.4.15). The carbon fiber composite plates were bought as sheets in A4 size from an external supplier. They were cut, roughened and bonded in the aluminum part with two-component epoxy-based adhesive.

The molding process was challenging. In order to obtain homogeneous material characteristics, the silicone embodiment must be molded with the least possible air

inclusion. A self-designed mixer for the two components, used in combination with an evacuation pump to achieve pressure below atmospheric level, was used. The empty mold was first filled up with the silicone, before the aluminum head glued together with the carbon composite blade were inserted. 37 tests were necessary to optimize the process and to achieve satisfying results. A black color is required for Particle-Image Velocimetry measurements (see sec. 5.4), while a white color is required for the Surface-Tracking measurements (SFT, see sec. 5.3); this coloring was achieved by adding pigment paste in the material during the mixing process. A video (in French) of the molding process was created by Nicole Lambert, CNRS, LEGI (76)[3].

The resulting hydrofoils, deployed in the subsequent measurements, are shown in fig. 4.16: The (left) picture shows a white pigmented, flexible hydrofoil with a 0.7 mm thick carbon blade (flex[07]) for SFT measurements mounted in the channel test section. Figure 4.16 (right) shows a black pigmented, deflected hydrofoil with a 0.3 mm thick carbon blade (flex[03]) for PIV measurements during an oscillating pitch motion. With this in place, the measurements can be started as described in the next chapter.

[3]see: `https://www.ovgu.de/hoerner/thesis/videos/fabrication_profil_souple.mp4`

Chapter 5

Water tunnel measurements

In the following sections, water tunnel measurements with oscillating hydrofoils will be presented. The experimental investigations are divided into five parts. The chapter begins with a collaborative project: the experimental optimization of an active pitch function for VAWT with rigid blades (sec. 5.1). Subsequently, the benefit of flexible blades in VAWT is evaluated and a characterization of the underlying FSI is given. Four different methods are used, constituting the remaining four sections of the chapter:

- Force and torque measurements, conducted with a six-axis load cell (sec. 5.2);
- Structural deformation measurements, carried out using two methods:
  - Surface tracking (SFT, sec. 5.3));
  - Cross-section tracking (CST, sec. 5.5);
- Instantaneous flow field measurements, conducted with Particle Image Velocimetry (PIV, sec. 5.4).

The experiments reported in this chapter were performed in two measurement campaigns at the LEGI labs. The first period was scheduled during a 15-month research stay which was part of the thesis in joint supervision of the University Otto von Guericke of Magdeburg and the University Grenoble-Alpes in 2017.
In parallel to the developments made in the numerics (see sec. 3.5), the experimental setup was defined, the methods and software required was developed (see sec .4.2.2, 4.2.3, 5.3.4). The experiment was set up, and force measurements were conducted once with synchronous, high-speed Particle Image Velocimetry and once with Surface-Tracking measurements. The six-axis load cell deployed in this first campaign, broke down due to material fatigue after operating in resonance mode in frequencies above 3.5 Hz and being overloaded in off-limit operating conditions with cavitating flow during a demonstration. After this event, the force measurement data was no longer reliable, because it was not clear at what point the deformations in the sensor had become plastic.

Therefore, a second campaign was conducted after purchase and delivery of a new sensor with higher stiffness (and capacity) in April 2018. However, this second campaign was limited in time. The setup of the PIV measurements could not be rebuilt.

5.1 Optimal active pitch trajectory

As mentioned in sec. 2.2.2, a promising approach for improving the characteristics of VAWT is to adapt the angle of incidence α with a blade pitch motion. The pitch trajectory (trajectory of $\gamma = \alpha - \alpha\prime$, see fig. 5.1) is the crucial point for this method. In this section, an experimental approach to estimate this trajectory is presented. It was developed in collaboration with the Chair of Electrical Drive Systems at the University Otto von Guericke of Magdeburg. A publication describing the experimental setup and the results of the work in this section was published by Abbaszadeh et al. (including the author) in 2019 in the journal *IET Renewable Power Generation* (1).

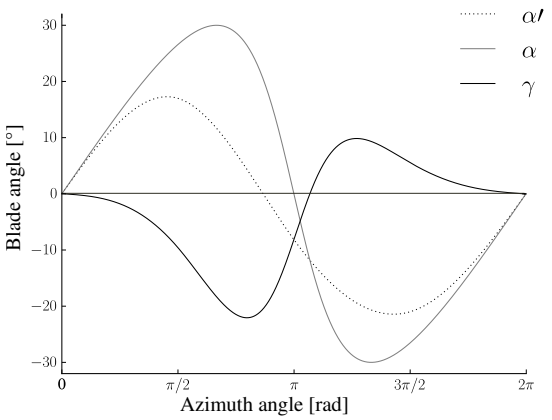

Figure 5.1: "Presumptive diagram of the probable relation between angle of incidence α, additional angle of incidence $\alpha\prime$ and pitch angle γ"(1) .

5.1.1 Optimization method and experimental design

Most of the studies aiming to estimate the optimal pitch trajectory for VAWT blades are based on numerical simulations, e.g. Khalid et al. 2013 (114). While they may reach high levels of accuracy, they also infer high costs, since one simulation is required for each operating point. Furthermore, significant uncertainty is embedded in results when two-dimensional RANS-based simulations are used (Ferreira et al. 2014 (49)). Other studies are based on analytical considerations, e.g. Thönnißen et al. 2016 (120). As mentioned in sec. 2.1, momentum-based models are known to reproduce phenomena like dynamic stall only insufficiently. In contrast to the above, the present method makes use of a hardware loop-based experimental approach. The experimental approach allows to overcome the drawbacks of both methods mentioned above. Its limitations are expected to be mainly the suitability of the underlying experimental model, and the sensor accuracy. A Design-Of-Experiment (DOE) was first carried out. With the variation of λ (trajectory shape) and k_o (oscillation frequency), a full set of turbine designs can be covered (see fig. 2.4) in a short time: indeed, each variation can be investigated in only 35 s. Unfortunately, the variation in the relative hydrofoil speed cannot be implemented in this model (see sec. 4.1). The existing setup described in sec. 4.2 was slightly modified for the optimization (see fig. 5.2). The objective of the optimization process was to maximize the objective function OF

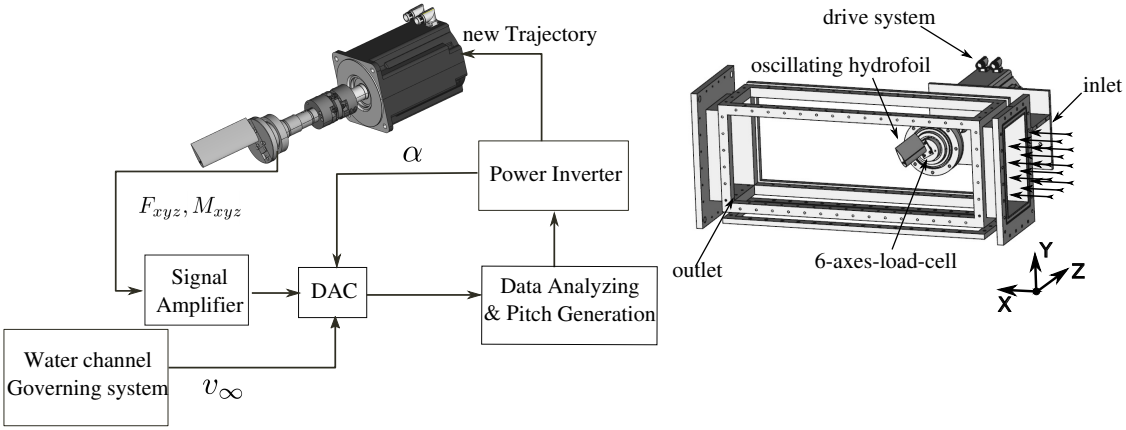

Figure 5.2: "Experimental setup at the LEGI closed-loop water tunnel. The hydrofoil performs non-harmonic forced oscillations induced from the drive systems with parallel force and torque measurements from the fully-submerged load cell." Reprinted from (1)

given in eq. (5.1) as the integral of c_T over one oscillation period. To this purpose the lift and drag forces were captured and processed following eqs. (4.2-4.4) with the instantaneous values for the flow speed.

$$\mathrm{OF} = \int_0^{2\pi} (c_L \cdot \sin\alpha - c_D \cdot \cos\alpha)\mathrm{d}\theta \tag{5.1}$$

The motion law of the drive oscillation is given by the maximum oscillation angle and the non-dimensionalized motion trajectory shape. A higher-level control script was introduced to govern the multi-scale, full-factorial parameter study. The motion law begins with eq. (2.3) and modifies the trajectory shape by adding a virtual pitch angle γ which results in a new motion law (see fig. 5.1):

$$\alpha' = \alpha + \gamma \tag{5.2}$$

In the present study, for each so-called outer step, m=3 parameters (x_1, x_2, x_3) were varied from the base spline with n=4 steps altogether (see fig. 5.3). One outer step results in a m, n-sized matrix with 4^3=64 variations. For each variant, a spline was generated and sent to the drive system, which performed the oscillation according to the spline. After 1 s of idle time to establish stable flow conditions, the forces and moments acting on the blade were captured, synchronous with flow speed, position feedback and temperature.

After completing the set of 64 motion laws, the governing script evaluated all splines of the given outer step, and selected the best spline as the base for the subsequent outer step. In the present case, the initial variation step size was 4°; this increment was then successively reduced in case of convergence. Once no improvement could be reached, the result was considered to be converged (see fig. 5.4). The study was performed for one operation point, determined by λ=2 and k_o=0.45, which

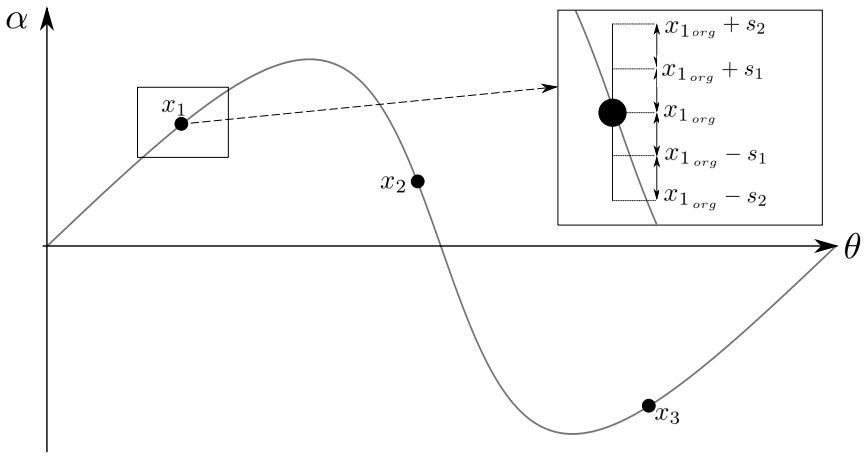

Figure 5.3: "Generation of the knots for the base spline. The start and endpoint of the spline is always fixed to zero, while the 3 parameters x_1, x_2, x_3 are varried in the inner steps S_i in positive and negative direction."(1)

.

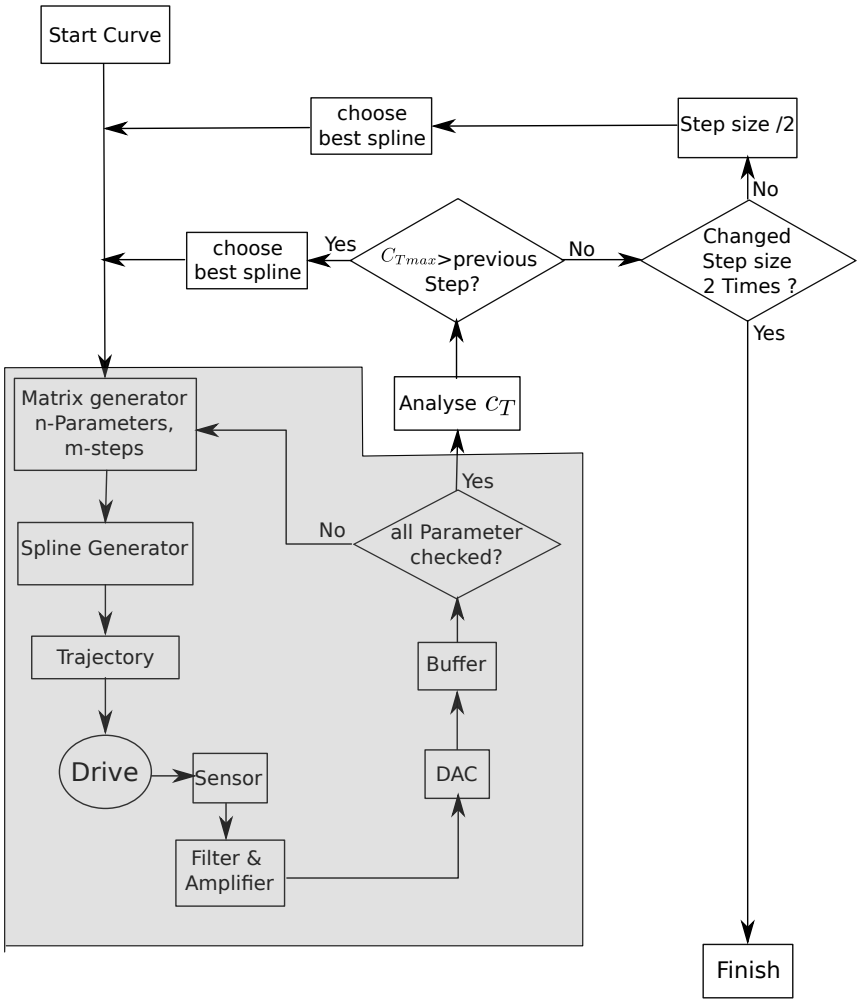

Figure 5.4: "Flowchart of the hardware in the loop-based optimization with inner (dark grey) and outer step (light grey). The step size is changed if the objective function did not improve in the last step, after two successive steps without improvement the optimization is stopped."(1)

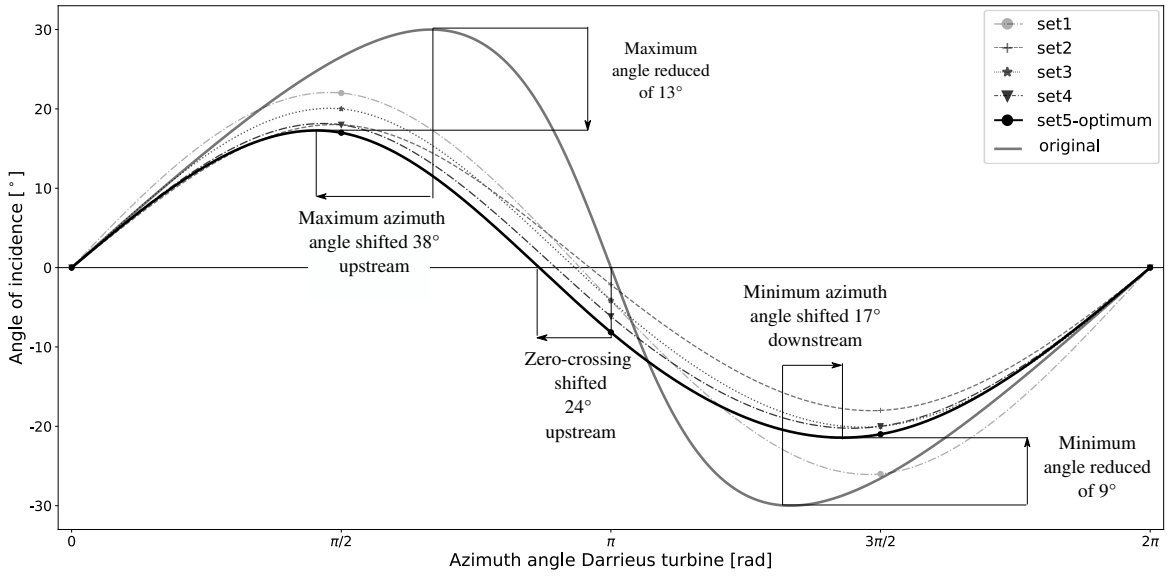

Figure 5.5: "Original trajectory and the evolution of the motion law until the optimum is reached. The motion law becomes smoother with smaller angle change rates $\dot{\alpha}$. Also, the point where α changes sign is shifted." Reprint from (1)

models a high-solidity VAWT with σ=1.4. The resulting frequency was f_o=3.5 Hz, the maximum angles of incidence varied in the range -38° < $\alpha_{\max}$ < 38°. The whole process took 5 h with 3.5 h of experimental runtime.

The setup required a fully-automated governing system, which was implemented in the custom libraries described in sec. 4.2.3. In the future, it is planned to investigate the whole field of operating points from 1.5< λ <3 and for 0.5< σ <1.5. The process will be governed by an external module, e.g. OPAL++, an LSS in-house optimizer based on a genetic algorithm, in order to speed up the process.

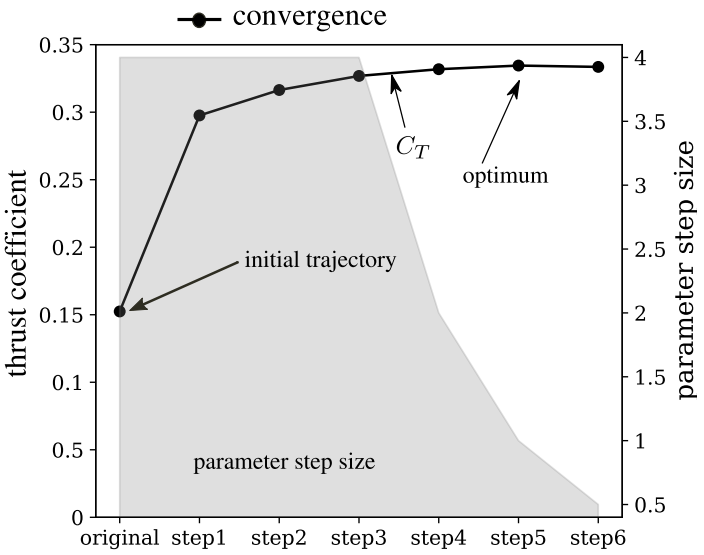

Figure 5.6: "Measured thrust coefficient evolution (dark curve with dots) as a function of time during the complete optimization process. In the background as a light gray area, and with a scale on the right vertical axis, is the size of the steps taken to change the parameters." Reprint from (1)

5.1.2 Results

The optimization converged towards a smoothed angle of incidence curve (see fig. 5.5) with a maximum c_T=0.333 after 5

steps, starting from c_T=0.15 for the initial trajectory without active pitching. The step size was reduced from 4° in the first three outer steps, to 2° in the fourth 1° in the fifth, and 0.5° in the sixth outer steps (see fig. 5.6).

The optimal spline results in a reduced slope in the accelerating part of the trajectory (for $\pi/2 < \theta < 3\pi/2$), and in a reduced maximum angle of incidence α'. The zero-crossing occurs earlier, which seems to compensate partly for the hysteresis effects in the thrust force.

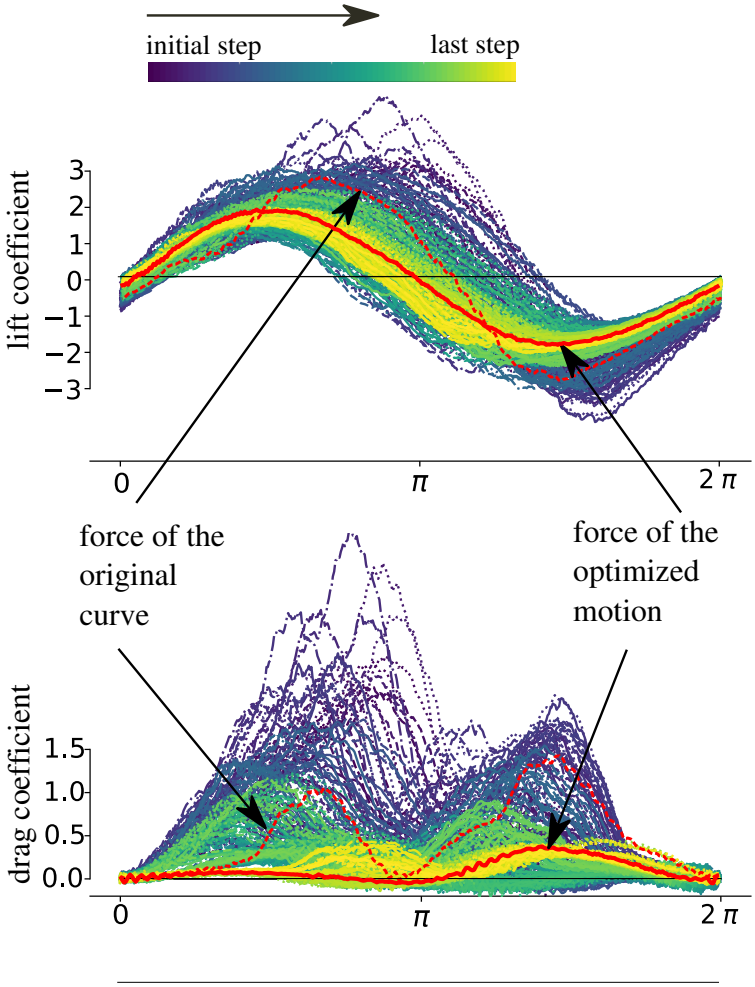

Figure 5.7: "Lift and drag force coefficients displayed as a function of phase angle, during the whole parameter variation." Reprint from (1)

When considering the fluid forces, displayed in fig. 5.7, it can be seen that the lift is less affected by the new pitch trajectory than the drag. As stated in (1), "The original curve is highly unsteady with overshooting drag. The parameter variation is mapped starting from violet curves and is shifted to brighter colors for each outer step. The variations are successively smoothed out until the optimum is reached, which shows very low drag and an almost symmetric lift trajectory." The reduced maximum angles result in significantly lower values of lift, but avoids the sharp increases in drag

associated with deep dynamic stall. The increase in performance can be explained by the fact that the drag contributes to thrust with its cosine share, while the lift contributes to the thrust by its sine share; this effect becomes important when α >30°. Both the motion law for α' and the corresponding lift forces approximate to a sine-shaped trajectory. The zero-crossing occurs earlier in both cases, the first almost at θ=0, the second zero crossing is shifted to θ=π. An investigation of the similarities in the flow characteristics between the optimally-pitched hydrofoil and the optimal flexible hydrofoil would be of high interest for future work.

5.2 Force and torque measurements

The results presented in the following section were partly published in 2019 in the *Journal of Fluids and Structures* (65).

The experiments were performed with the hardware and software setup described in sec. 4.2. For each hydrofoil, two parameters were varied:

- the tip-speed ratio: λ=[2, 3] in form of the shape of the pitch trajectory from eq. (2.3) with corresponding $\alpha_{\max}$=[30°, 20°]
- the reduced frequency k_o, represented by the variation of the oscillation frequency f_o, with:
  - $k_o(\lambda = 2)$=[0.03, 0.06, 0.16, 0.28, 0.33, 0.46, 0.71]
  - $k_o(\lambda = 3)$=[0.03, 0.07, 0.13, 0.24, 0.34, 0.49, 0.62, 0.65]

The rigid hydrofoil was measured as a reference for a VAWT without flexible blades. At Re=200 000, the static stall angle for this hydrofoil was found experimentally at α_{stall}=16°(see fig. 4.9). Since the first investigated reduced frequency represents a quasi-static state, static characteristics were expected. The reduced frequency was then raised up to f_o=5.71 Hz for λ=2 (k_o=0.71) and f_o=6.45 Hz for λ=3 (k_o=0.65). Beyond these frequencies, the system encountered strong vibrations and the frequency was not further raised to prevent sensor damage. After a full variation of the parameter set, the hydrofoils were changed for a testing of the influence of the rigidity under similar conditions. All measurements shown were similarly repeated at least once and generated comparable results.

Evaluating performance lifetime improvements on the turbine requires knowledge of the lift and the drag forces, as well as their position. The force in the Z-axis and the corresponding moments, while they are out of the scope of this study, could be used to calculate the position of the load application point: the moment is divided by the corresponding force, so that the resulting lever arm is the distance of the load application point to the sensor moment measurement axis. This additional data was acquired but not evaluated and could be subject of further studies.

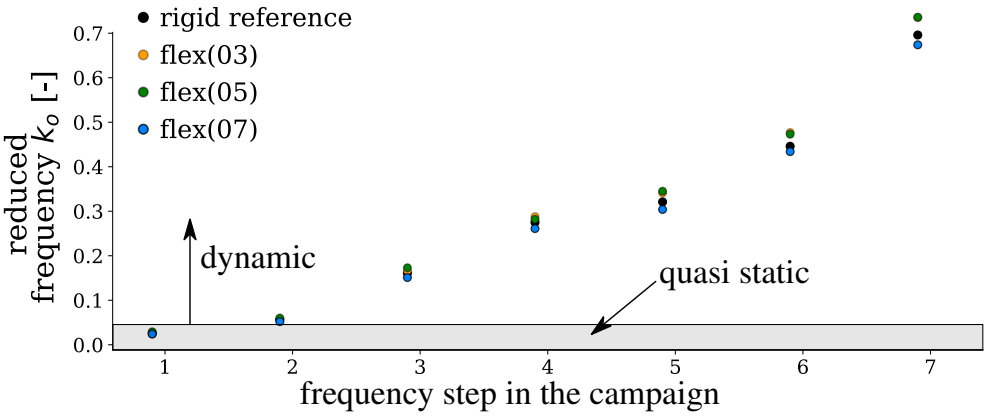

Figure 5.8: Reduced frequency for each of the seven tested values, for each of the four hydrofoils, in the case where λ=2 (non-visible markers are covered by matching k_o from other hydrofoils).

5.2.1 Setup and preliminary considerations

As mentioned in sec. 4.2.1, the governing system of the water channel provides no interface for an external set point transmission. The mass flow rate of the pump is also known to shift over time. The variation of the inlet speed v_{ch} was <1% for each data acquisition (each single k_o and λ on a single foil) and was consequently considered to be negligible.

The variations of v_{ch} were observed to be higher across separate hydrofoil testings. This led to changes in the reduced frequency as shown in fig. 5.8 for λ=2. The absolute deviation Δk_o was calculated from eq. (5.3) with the rigid hydrofoil as reference.

$$\Delta k_o(i) = |k_{o_{\text{foil(i)}}} - k_{o_{\text{reference}}}| \tag{5.3}$$

At small values of k_o (0.026), the maximum absolute deviation is 0.004. These deviations have minor influence and do not translate into changes in the flow characteristics, since quasi-static flow characteristics are found for k <0.05 (McCroskey 1981 (92)). This was confirmed in the present study. For high values of k_o (0.46), the deviation in between the hydrofoil testings is 0.04. Nevertheless, no significant changes in the dynamic flow characteristics which could be related to the v_{ch}-related frequency shift were observed. In consequence, the results for the four hydrofoils are considered to be comparable for the corresponding reduced frequencies.

Lift and drag forces acquired from the experiment were non-dimensionalized with the corresponding instantaneous value of v_{ch} (see eqs. (4.2 & 4.3)), which suppresses the influence of flow speed variation. v_{ch} was captured together with forces, moments, temperature, trigger channel and position with 1 kHz acquisition rate (see sec. 4.2.3). In the post-processing, individual periods in the output were identified when a sign change in the position feedback was observed (evaluation of $\text{sgn}(\alpha_n)/\text{sgn}(\alpha_{n-1} + \epsilon_{\text{small}}) < 0$, with $\epsilon_{\text{small}} = 10^{-15}$). One representative period was constructed for each take. For this, values for c_D, c_L and α at any time point within a period were averaged across periods. For example, in a representative pe-

riod constructed with n periods for each sample j of the position feedback α, the period-averaged lift coefficient $\overline{c_L}(\alpha_j)$ is obtained as:

$$\overline{c_L}(\alpha_j) = \frac{1}{n}\sum_{i=1}^{n} c_{L_i}(\alpha_j) \tag{5.4}$$

The coefficients of tangential and normal force, c_T and c_N were calculated from the time-averaged values of $\overline{c_D}$, $\overline{c_L}$ and $\overline{\alpha}$ with eqs. (4.4 & 4.5). The force signal was already filtered with a hardware-based low-pass filter to prevent aliasing (see sec. 4.2.3). No additional, software-based filtering was applied to the signal shown in the subsequent sections.

The installation of the load cell in between the shaft stub and the hydrofoil led to vibrations of the structure, and in particular strong vibrations for the force measurements, since the hydrofoil and the sensor constitute a common mass spring system of low rigidity-to-mass ratio. The strain gauges of the load cell require (small) deformations in order to measure the applied loads. The consequence is a low natural frequency of the complete system caused by the combination of the added mass of the hydrofoil and the force lever from the load application point of the hydrodynamic forces. These vibrations appear in particular for high oscillation frequencies and are investigated in chapter 6.

5.2.2 Results of static force measurements

The static polar curves for the four hydrofoils were acquired with similar methodology as described in sec. 4.2.4 for the lift and drag curves of the rigid foil (see fig. 4.9). The hydrofoils were inclined from 2 to 30°. Figure 5.9 displays the results for the four hydrofoils. The maximum lift force increases together with the stiffness. The rigid hydrofoil performs best (highest lift along with low drag) for low angles of incidence, before the static stall angle of α=16° is reached. At this point, the flex[03] foil provides a c_L of 0.9 and the rigid foil reaches a c_L of 1.1. However, in a stalled state, the data suggests that the flexible hydrofoils perform better (higher lift-to-drag ratio). With rising angles of incidence, the optimal rigidity diminishes. The hyperflexible flex[03] provides the lowest drag for all hydrofoils at very high angles of incidence.

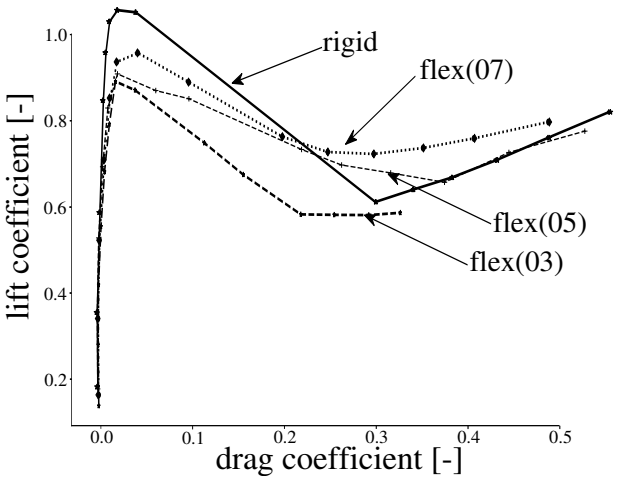

Figure 5.9: Static lift plotted as a function of drag (polars) for four NACA0018 hydrofoils: one rigid and three flexible foils with different blade thicknesses: [0.3, 0.5, 0.7] mm.

Subsection 5.2.3 will present the results of the dynamic force measurements exactly following (65).

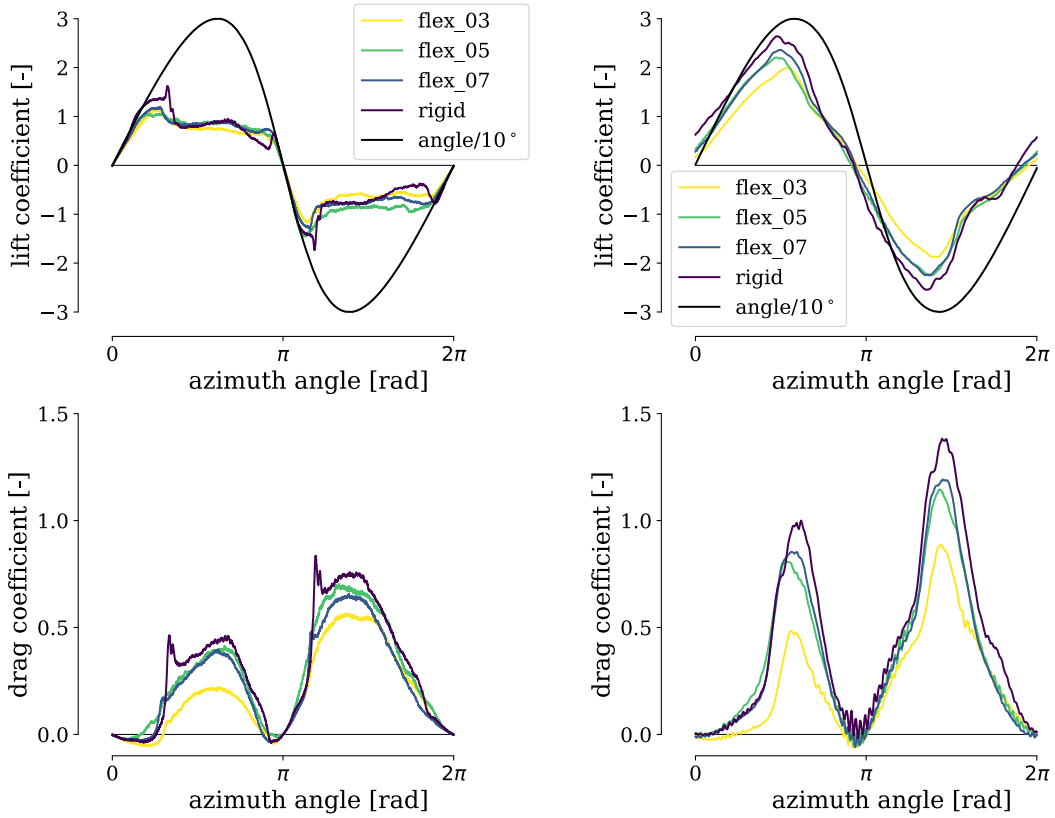

Figure 5.10: "Results at λ=2 for four NACA0018 hydrofoils: one rigid and three flexible foils with different blade thicknesses: [0.3, 0.5, 0.7] mm. The black sinusoidal curve in the upper plots displays the angle of attack α [°/10°], with α_{max}=30°. Left: Transitional state at k_o=0.026; Right: Full dynamic state with deep dynamic stall at k_o=0.277;". Reprinted from (65)

5.2.3 Results of the dynamic force measurements

Figures 5.10-5.11 & 5.15-5.17 show the phase-angle averaged lift (top) and drag (bottom) coefficients for the four hydrofoils (three flexible, flex[03]-flex[07] and the rigid) for one normalized period (azimuth angle) along with the pitch angle divided by 10° to fit in the plot (α/10°, black curve).

5.2.3.1 The λ=2 case

Only a selection of the results is shown. They are plotted in the subsequent figs. 5.10 & 5.11 with rising reduced frequency.

Transitional state at k_o=0.026 (fig. 5.10 (left)): Rigid hydrofoil: From starting point $\theta = 0$ the lift increases with the angle of incidence until the static stall angle of α=16° (c_L=1.4) is reached. The lift remains constant until it suddenly decreases to c_L=0.8 at α=19°after a short peak to c_L=1.7. It then remains almost constant with

further losses after $\alpha_{\max}$ is reached; a small positive peak is visible when the flow reattaches at α=7.5°. At the zero-crossing (when the profile becomes horizontal), c_{L} is zero. The drag coefficient c_{D} is very low for $\alpha < \alpha_{\mathrm{stall}}$ and remains in the range of the measurement uncertainty. When the stall point is reached, c_{D} displays a large peak and then remains at a high value, increasing until $\alpha_{\max}$ is reached. The drag then steeply decreases until the flow reattaches: There again c_{D} becomes lower than the measurement uncertainty.

Flexible hydrofoils: The flexible foils provide a smoother trend than the rigid foil. None of the three foils feature a pointed peak, on either the lift or the drag curves. Apart from the area close to the stall point, all flexible foils display values of c_{L} similar in magnitude to those of the rigid foil, while their values for c_{D} are significantly reduced in the stalled regime.

Similar trends are observed for both rigid and flexible foils in the second half of the period T. Compared to the first half of the motion, the magnitude of both c_{L} and c_{D} is increased, as is the stall angle. This is due to the different motion $\dot{\alpha}$ (quantified by eq. (2.6) and visible in fig. 4.1 and as the slope of the black curve in figs. 5.10-5.11).

Dynamic stall at k_o=0.277 (fig. 5.10 (right)):

Rigid hydrofoil: With this increase in k_o, the stall angle is raised very significantly (α_{stall}= 27°, $c_{\mathrm{L}_{\max}}$ 2.7). Beyond this angle, the loss of lift is less pronounced than for lower k_o; however, a hysteresis loop becomes visible and the flow does not seem to reattach before the shift in direction. At the zero-crossing point, c_{L} already takes the value -1.5. The point of zero lift α_{zl} is reached at α_{zl}=12° in the descending and α_{zl}=-10° in the ascending motion. Thus, the lift trajectory is shifted leftwards with respect to α. In the meantime, the integral of the lift for one period increases.
The drag curve also changes significantly: the characteristic spike with onset of stall disappears, while the two maxima are increased and display a slender shape. The hysteresis concerning lift does not appear for drag. The drag coefficient peaks at 1.0 in the descending branch (at α= 27°) and at 1.5 in the ascending branch (at α= -28.5°).

Flexible hydrofoils: All flexible foils display less lift than the rigid foil. The integral of the lift over the trajectory is lower and it decreases together with the stiffness. The stall angle is increased, with the most flexible foil (τ=0.3) achieving $c_{\mathrm{L}_{\mathrm{max.}}}$=2 at α_{stall}=29°.
The drag curves display similar behavior to those of the rigid foil. Nevertheless, the drag is everywhere lower, and the maxima are reduced by 25 to 50% compared to those of the rigid foil.

Dynamic stall at k_o=0.45 (fig. 5.11 (left)): For all foils, for both lift and drag, some weak oscillations begin to appear.

Rigid hydrofoil: As the reduced frequency is increased, the stall angle increases to reach α_{stall}=29°. However, the lift coefficient never exceeds $c_{\mathrm{L}_{\max}}$=2.7. Peaks in the drag coefficients which were observed at lower frequencies diminish.

Flexible hydrofoils: All three foils follow the trend described above. The two

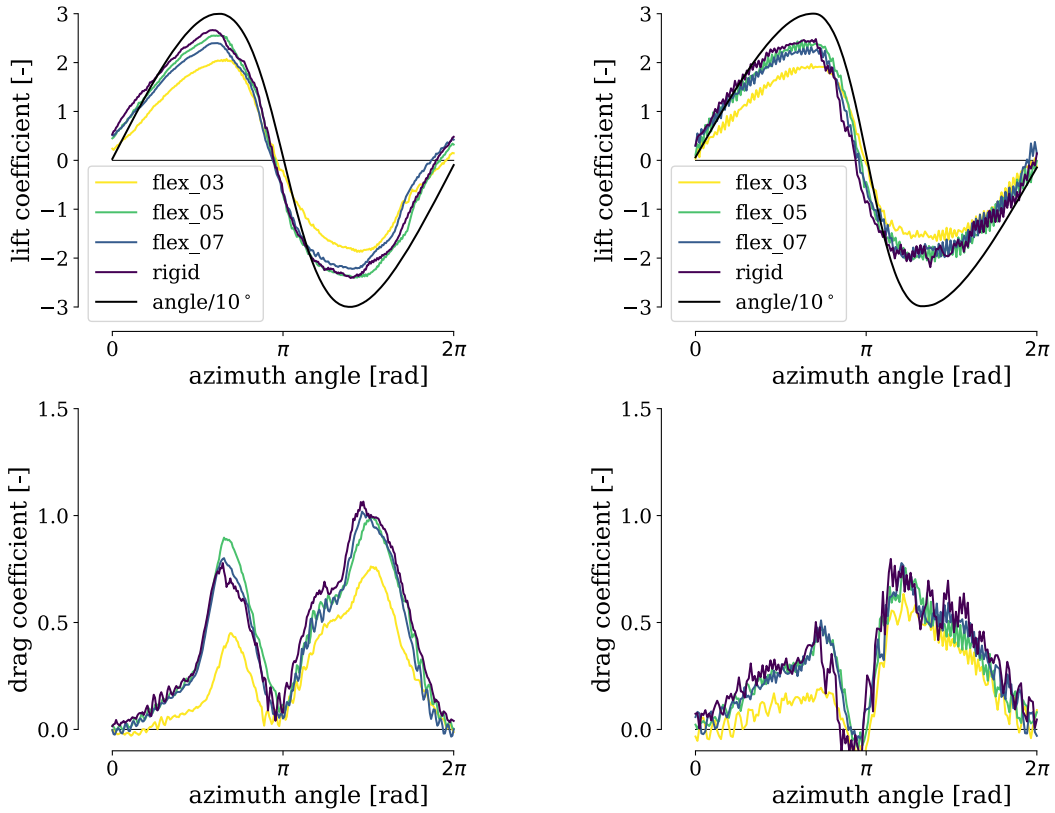

Figure 5.11: "Results at λ=2 for four NACA0018 hydrofoils: one rigid and three flexible foils with different blade thicknesses: [0.3, 0.5, 0.7] mm. The black sinusoidal curve in the upper plots displays the angle of attack α [°/10°], with α_{max}=30°. Left: Fully-dynamic state at k_o=0.45; Right: Fully-dynamic state at k_o=0.71." Reprinted from (65)

most rigid foils (τ=0.5 and 0.7 mm) have lift and drag curves almost identical to those of the rigid foil. For the most flexible foil, maximum lift occurs past the maximum angle of attack, and the curve is close to zero at both zero-crossings, suggesting that hysteresis, one indicator for dynamic stall, vanishes with higher k_o.

Dynamic state at k_o=0.71 (fig. 5.11 (right)): Larger high-frequency oscillations are now observed for all curves and all foils. It is possible that the natural frequency of the multi-mass system containing the sensor, the base plate and the hydrofoil (fig. 4.2), is approached. A light dynamic stall with negative damping (McCroskey 1986 (93)) may also play a role. Those effects are under further investigation, requiring deeper knowledge of the structural properties and especially of the flow field.

Rigid hydrofoil: There are only light indications of stall, in the descending branch, with $c_{L_{max}}$=2.3 at α_{stall}= 30°. Compared to the previous (lower) frequency, the maximum drag is significantly reduced.

Flexible hydrofoils: As for the rigid foil, stall indicators become less dominant. The loss of lift and the overshoot of drag are shifted to higher azimuth angle, while

the hysteresis loop becomes narrower.

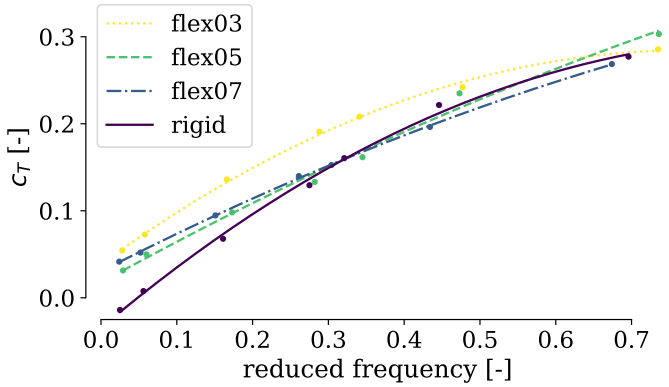

Figure 5.12: "Thrust coefficient c_T, a measure for the qualitative performance, as a function of reduced frequency. A second-order polynomial curve fit of the data was added. These results correspond to λ=2 for four NACA0018 hydrofoils: one rigid and three flexible foils with different blade thicknesses: [0.3, 0.5, 0.7] mm." Reprint from (65).

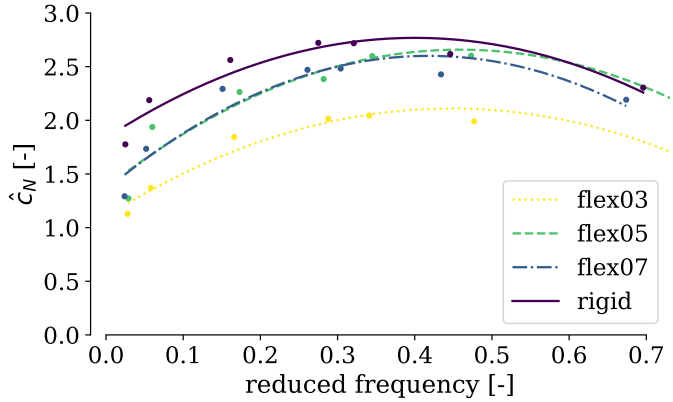

Figure 5.13: Amplitude of the normal coefficient ($\hat{c}_N$), an indicator for the turbine lifetime, as a function of the reduced frequency k_o. Lower values are favorable, since lifetime rises exponentially with diminishing stress; A second-order polynomial curve fit of the data was added. These results correspond to λ=2 for four NACA0018 hydrofoils: one rigid and three flexible foils with different blade thicknesses: [0.3, 0.5, 0.7] mm." Reprint from (65).

Performance and lifetime improvements: The relationship between reduced frequency and thrust coefficient is shown in fig. 5.12. It displays the thrust coefficient averaged over one rotor revolution as a function of reduced frequency. It can be seen that the most flexible hydrofoil performs best, with significant improvement compared to the rigid reference especially in low-k_o region. The effect becomes less important with higher k_o.

A maximum could not be obtained for these curves, likely due to the experimental

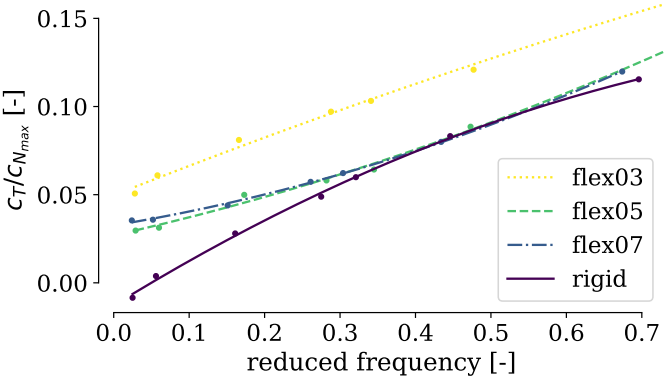

Figure 5.14: "Thrust-to-normal-force ratio η, a measure for the benefit-to-cost ratio, as a function of reduced frequency. λ=2 for four NACA0018 hydrofoils: one rigid and three flexible foils with different blade thicknesses: [0.3, 0.5, 0.7] mm." Reprint from (65) .

limitations on the oscillation frequency. The model allows to examine the effect of flexibility in specific design points, one for each k_o. It has to be considered that a comparison between two k_o or design points is not possible in this model.

In this case, the power output c_P would have to include the turbine radius (which grows as k_o increases, since the chord length is constant) and further parameters like secondary effects as tip losses or blade-blade interaction, which is not possible with the current measurements. For k_o=0.71, the intermediate flexible foil (τ=0.5 mm) overperforms the most flexible one (τ=0.3 mm). This suggests that the optimal stiffness is related to k_o, but demands further investigations. The LEGI turbine model features its BEP at λ=2 and has a σ=1.1 and so k_D=0.35 (91). At this operating point (k_o=0.35), the most flexible hydrofoil (τ=0.3 mm) provides best performance with 20% improvement of thrust compared to the rigid reference.

The influence of foil stiffness on the turbine lifetime is displayed in fig. 5.13, which displays the mean amplitude of the normal force coefficient, $\hat{c}_N$ (see eq. (4.7)), as a function of the reduced frequency. The trend is parabolic for all foils. It becomes obvious from this figure that flexibility can contribute to lower structural loads compared to the rigid reference, decreasing the cyclic stress, which translates into exponential increase in structural lifetime. The thrust efficiency η is also displayed as a function of the reduced frequency in fig. 5.14. All curves show improved characteristics with increasing k_o. For the same reasons as above, no maxima can be obtained. Nevertheless, the most flexible foil is clearly advantageous over the whole examined range, delivering an improvement ranging from 35% (high k_o) to 75% (low k_o). Force trajectories along with corresponding deformation for the flex[03] and the rigid foil for further reduced frequencies are shown in sec. 5.3.7.

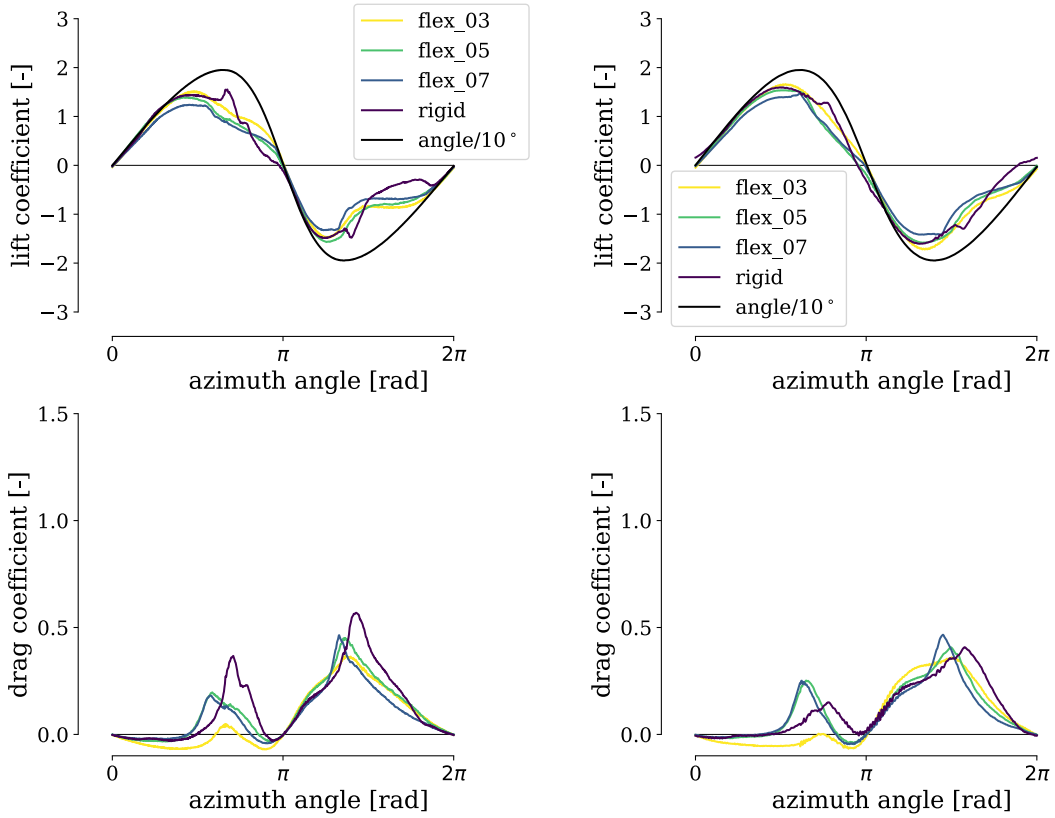

Figure 5.15: "Results at λ=3 for four NACA0018 hydrofoils: one rigid and three flexible foils with different blade thicknesses: [0.3, 0.5, 0.7] mm. The black sinusoidal curve in the upper plots displays the angle of attack α [°/10°], with α_{max}=20°. Left: Transitional state at k_o=0.069; Right: Dynamic state at k_o=0.130." Reprint from (65).

5.2.3.2 The λ=3 case

The motion law for λ=3 (eq. (2.3)) results in a maximum angle α_{max}=20°. The setup for λ=3 begins at k_o=0.033; the reduced frequency is then increased step-wise until it reaches k_o=0.653.
For all measurements carried out at λ=3, the measured drag for the first half of the period is partially negative. This unphysical behavior is a consequence of the sensor's cross-talk and hysteresis, combined with the low magnitude of the forces (see section 4.2.4 for details).

Transitional/dynamic state with dynamic stall at ko=0.069 (fig. 5.15 (left)): Rigid hydrofoil: Lift increases together with angle of attack up to the static stall angle α_{stall} = 16°, reaching a wide and smooth maximum. An abrupt peak is visible at α_{max} on both the ascending and descending branches. From this point on, the lift reduces until the flow reattaches at the zero-crossing, where the lift is zero. Differences with the λ=2 case displayed in fig. 5.10, where the stall occurred far before α_{max}, are a consequence of the different maximum angle, but may also be

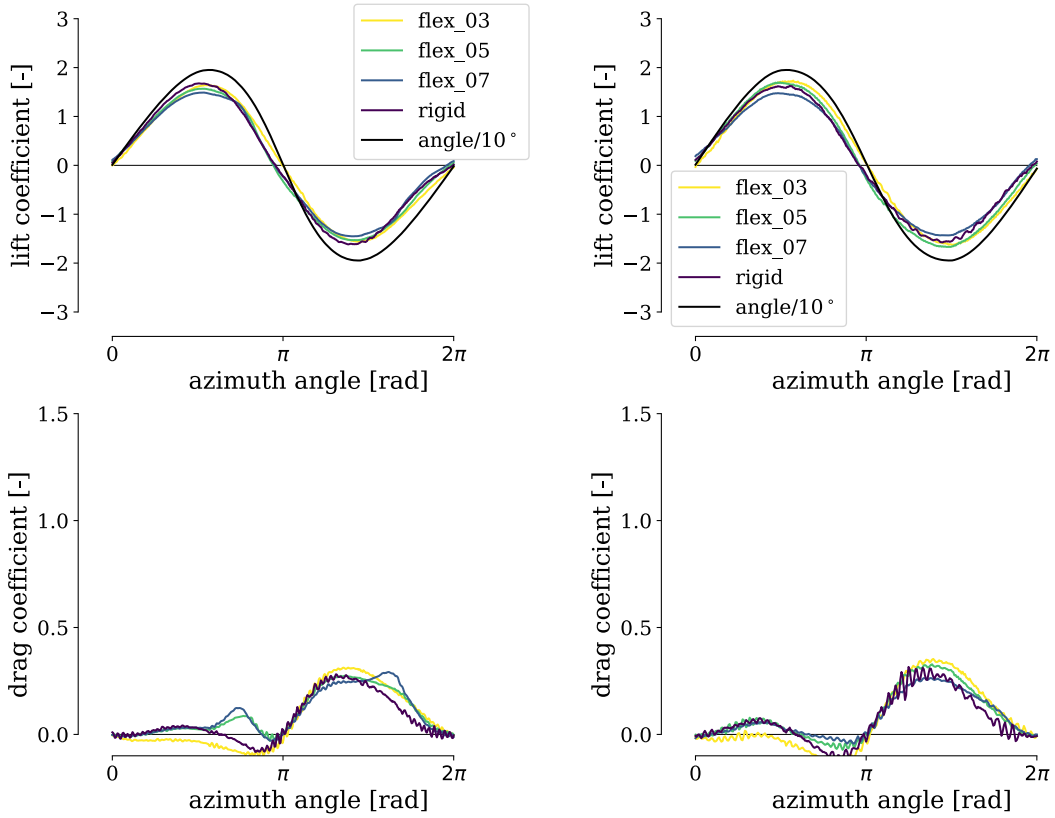

Figure 5.16: " Results at λ=3 for four NACA0018 hydrofoils: one rigid and three flexible foils with different blade thicknesses: [0.3, 0.5, 0.7] mm. The black sinusoidal curve in the upper plots displays the angle of attack α [°/10°], with α_{max}=20°. Left: Fully-dynamic state at k_o=0.241; Right: Fully-dynamic state at k_o=0.344." Reprint from (65).

affected by the higher value of k_o.
The drag features a peak at the stall point, whose magnitude in the ascending branch is 55% larger than in the descending branch.

Flexible hydrofoils: The lift curves are smoothed out compared to those of the rigid foil. The lift developed by the most flexible foil slightly overtakes that of the rigid foil. All foils develop zero lift at the zero crossing.

Dynamic state at k_o=0.130 (fig. 5.15 (right)): Rigid hydrofoil: The lift reaches a larger maximum ($c_{L\max}$=1.6) at a higher angle (α=19°) than at the lower-frequency case. The dynamic stall characteristics are less significant; however, hysteresis with negative lift at zero-crossing, and smoother characteristic lift and drag peaks at the stall point can be reported, particularly in the ascending branch.

Flexible hydrofoils: The lift curves are smoothed out for all flexible foils, except for the intermediate foil flex[0.5] which features a stall peak shortly before $\alpha_{\max}$. The most flexible foil flex[0.3] provides slightly higher lift than the rigid foil, although the increase remains below the measurement uncertainty.

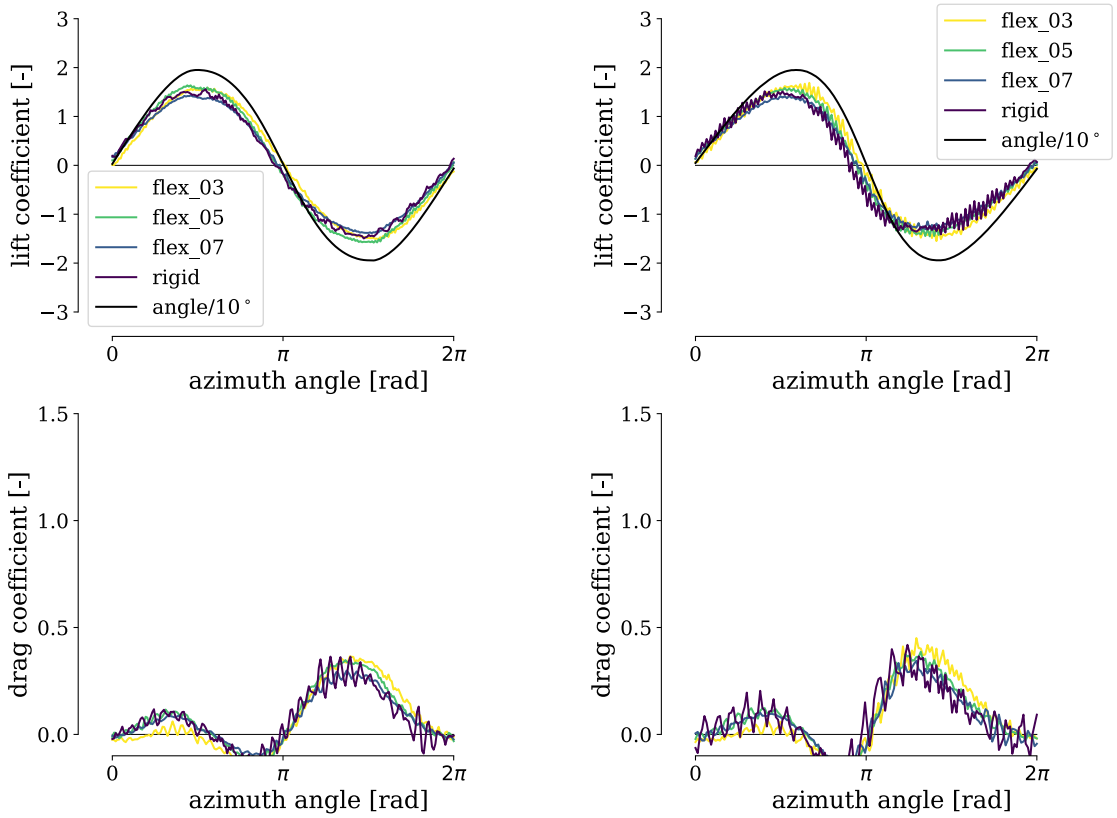

Figure 5.17: " Results at λ=3 for four NACA0018 hydrofoils: one rigid and three flexible foils with different blade thicknesses: [0.3, 0.5, 0.7] mm. The black sinusoidal curve in the upper plots displays the angle of attack α [°/10°], with α_{max}=20°. Left: Fully-dynamic state at k_o=0.486; Right: Fully-dynamic state at k_o=0.653." Reprint from (65).

The drag peak for the two most rigid flexible foils is higher and occurs earlier than for the rigid foil, especially in the ascending branch. The highest drag peak is provided by the intermediary foil in the ascending branch.

Fully-dynamic state at k_o=0.241-0.653 (figs. 5.16-5.17): Starting from k_o=0.13, the fully-dynamic state is reached, and the maximum angle of attack α_{max}=20° is no longer sufficient to cause the hydrofoil to stall. The dominant factors are the resonant high-frequency oscillations, which require further investigations. Neglecting those oscillations, the differences in lift and drag coefficient trajectories for k_o=0.344 to 0.653 remain in the range of the measurement uncertainty.

Perfomance and lifetime improvements Figure 5.18 again displays the average torque coefficient for one rotation as a function of the reduced frequency. Results are similar to the case for λ=2 displayed earlier in fig. 5.12: the most flexible hydrofoil performs best. The maximum thrust coefficient at k_o=0.35 is obtained with the most

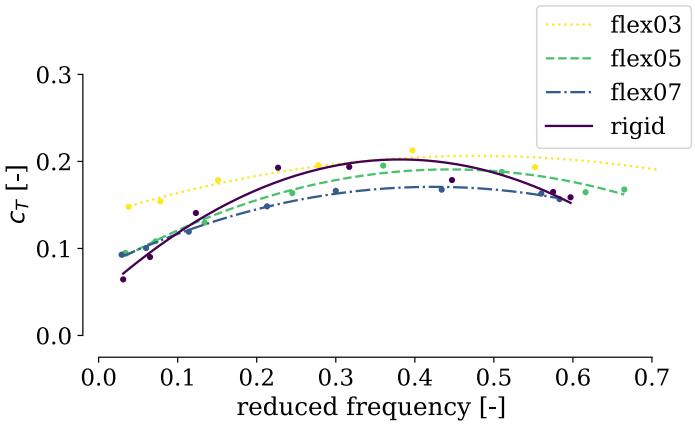

Figure 5.18: "Thrust coefficient, a measure for the qualitative performance, as a function of reduced frequency." Reprint from (65)

.

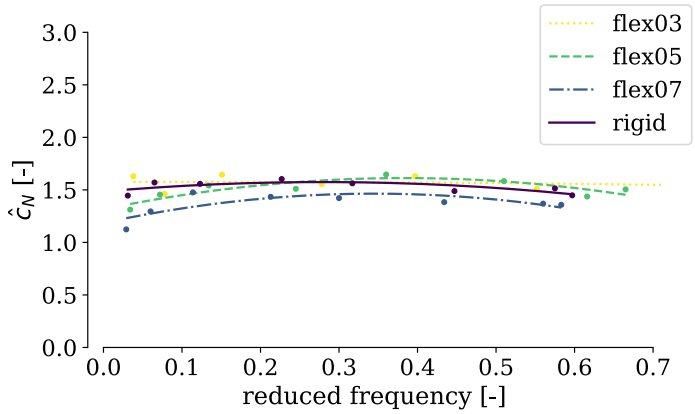

Figure 5.19: "Amplitude of the normal coefficient ($\hat{c}_N$), an indicator for the turbine lifetime, as a function of the reduced frequency k_o. Lower values are favorable, since lifetime rises exponentially with diminishing stress; A second-order polynomial curve fit of the data was added. Results at λ=3 for four NACA0018 hydrofoils: one rigid and three flexible foils with different blade thicknesses: [0.3, 0.5, 0.7] mm." Reprint from (65) .

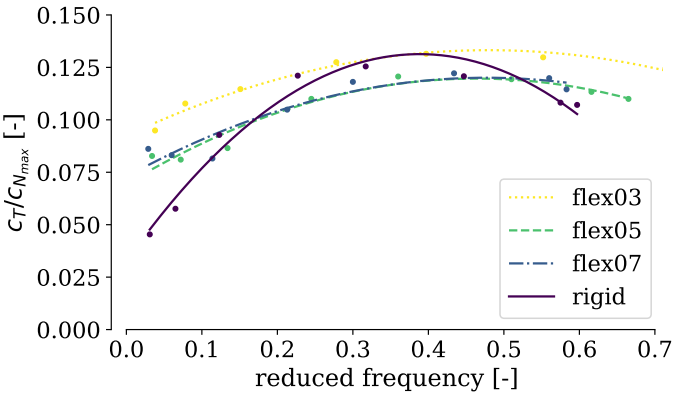

Figure 5.20: "Thrust-to-normal-force ratio η, a measure for the benefit-to-cost ratio, as a function of reduced frequency. Results at λ=3 for four NACA0018 hydrofoils: one rigid and three flexible foils with different blade thicknesses: [0.3, 0.5, 0.7] mm. "(65)

flexible foil, with c_T=0.2. Nevertheless, the differences between all foils in fig. 5.18 are small: the results may not be significant and have to be taken with caution. Figure 5.19 displays the value of $\hat{c}_N$ for all four foils: no influence of flexibility on the lifetime is evidenced in the case λ=3.

5.2.4 Conclusions of the force and torque measurements

Force and torque measurements combined with the surrogate model of an oscillating hydrofoil provide a well-suited tool for the evaluation of the benefit of flexible blades in a VAWT. The results of the force measurement are not uniform regarding the benefit of the flexibility. A significant dependency to the tip-speed ratio λ is observed:

- In the λ=2 case, the hyper flexible structure provides significant improvements over the rigid reference. Even if the strong simplifications of the model do not allow quantitative predictions of the turbine performance or lifetime, the rise of the thrust coefficient c_T for flex[03] of 20% at k=0.35 compared to the rigid hydrofoil, in particular for k <0.5, indicates a benefit for the use of flexible blades in VAWT. This is in accordance to the results reported by McPhee & Beyene 2016 (87). Regarding lifetime considerations, the flex[03] reduced the normal force amplitudes of 30-40% in dependence of k. The logarithmic dependency of the stress - and so of the load - to the number of cycles before material fatigue failure, allows to expect a non-negligible extension of the lifetime of a VAWT equipped with flexible blades.

- The λ=3 case does not allow such clear statements. The results do not differ significantly for the four hydrofoils. The small improvements observed should be considered carefully, since the uncertainty of the measurement may exceed the different results for the investigated parameters. Overall, the smaller variations in the forces may result from the lower angle of incidence, and lower forces cause less deformation.

- The benefits of flexibility decrease when the reduced frequency is increased. This indicates either that turbines of lower solidity are better application candidates than those of higher solidity (see fig. 2.4) or that the performance for low-λ operation points improves with flexible blades. The latter hypothesis is of particular interest for fish-compatible devices, since the angular velocity is crucial for fish injury risk models (see sec. 1 for details). In addition, the blades of high-λ turbines feature centrifugal loads orders of magnitude higher than their low-λ counterpart, because the angular velocity ω increases for a given flow speed and centrifugal loads increase with ω^2. In those cases, flexible blades may deform more due to the centrifugal loads than due to the hydrodynamic loads.

In summary, the force measurements provide answers to the main questions of the thesis, regarding lifetime and performance. However, they cannot provide knowledge about the underlying mechanisms. The characterization of the FSI on highly-flexible structures ought to include an investigation of the deformations generated by the hydrodynamic forces. In the following sections, two approaches will be presented:

- A surface tracking (SFT): A method based on structured light pattern analysis first presented by Takeda et al. 1982 (118) and adapted to the requirements of the setup at hand will be presented.
- A cross-section tracking (CST), based on the PIV imaging: This is a practical application of the masking algorithm presented later in sec. 5.4.3. The segmentation of the PIV images allows for the tracking of the cross-section of the structure.

5.3 Structural deformation measurements - Surface Tracking

The following considerations (5.3 - 6.2) were partly published in the *Journal of Experiments in Fluids* (66). However, the paragraphs 5.3.1, 5.3.2, 5.3.4 and 5.3.5 differ from (66) in order to provide more detailed information of the method and the validation process.
A second publication with particular focus on the results of the deformation measurements was recently submitted to the journal *Experiments in Fluids* (67). Its findings are discussed in section 5.3.7 - 5.3.9.

In order to measure structural deformations, a common technology is a Laser Interferometer or a Laser-Doppler Vibrometer. This type of sensor is used in many studies investigating FSI, e.g. Astolfi et al. 2015 (7), Ducoin et al. 2012 (43), Pärsinnen et al. 2007 (105) or Naik et al. 2003 (102). They can track the distance to a surface with high precision and temporal resolution, are non-intrusive, and easy to handle because they do not require any post-processing steps. The results are

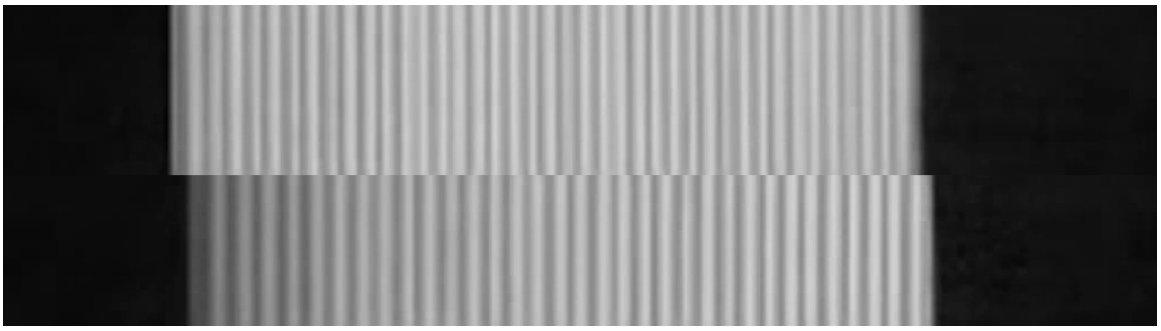

Figure 5.21: "SFT fringe pattern detail of two arbitrary frames of a recording of the rigid hydrofoil. The fringe deformation of the pattern is visible as well as the changes in the apparent surface length, the latter is a result of the two dimensional camera view and the three dimensional oscillation and deformation. The black areas are regions without a surface and so without projection, which irritate the processing algorithm." Reprinted from (66). A video of the fringe pattern and of the fringe pattern detail can be found on the author's website.

comparable to those from LDV measurements for fluid flows which only measure at one single point.

Rojratsirikul et al. 2009 measured a cut section of a membrane wing using a Laser sheet for illumination, and a video camera to capture it. They were able to perform spectral analysis and to find spatial modes in the longitudinal but not in the transversal direction of the membrane (111).

A time-resolved measurement of a whole surface provides a wealth of information about the characteristics of the structural response, much like PIV measurements do about the flow in fluid dynamics. A study with acquisition of the instantaneous deformation field was presented by Tregidgo et al. 2013 (122). Their investigations of the FSI on a pitching membrane wing included digital image correlation measurements based on two cameras to achieve stereographic view of the wing. The time-resolved acquisition of the instantaneous deformations of the surface allowed to characterize the transient effects on the membrane after the pitch motion stopped.

Structured-light based surface measurements also allow such instantaneous measurement of the entire surface. These methods are very common, well documented and also widely used in particular for medical applications, industrial surface quality control or face recognition tasks. A detailed overview of the state of the technology with focus on shape recognition is given by Zhang 2010 (136). In this method, a pattern is projected on a surface and subsequently recorded by a single high-speed camera[1]. When the light is projected on a non-uniform shape, the pattern is deformed in the image, and information about the surface height can be obtained.

Van der Jeught et al. 2016 (127) distinguish different methods of structured-light based profilometry, according to the color mode, the pattern, the analysis and the acquisition method. A variety of methods have been developed and adapted to

[1] A video of the pattern (`https://www.ovgu.de/hoerner/thesis/videos/fringe_pattern.mp4`) and a detail (`https://www.ovgu.de/hoerner/thesis/videos/fringe_pattern_detail.mp4`) can be found on the author's website.

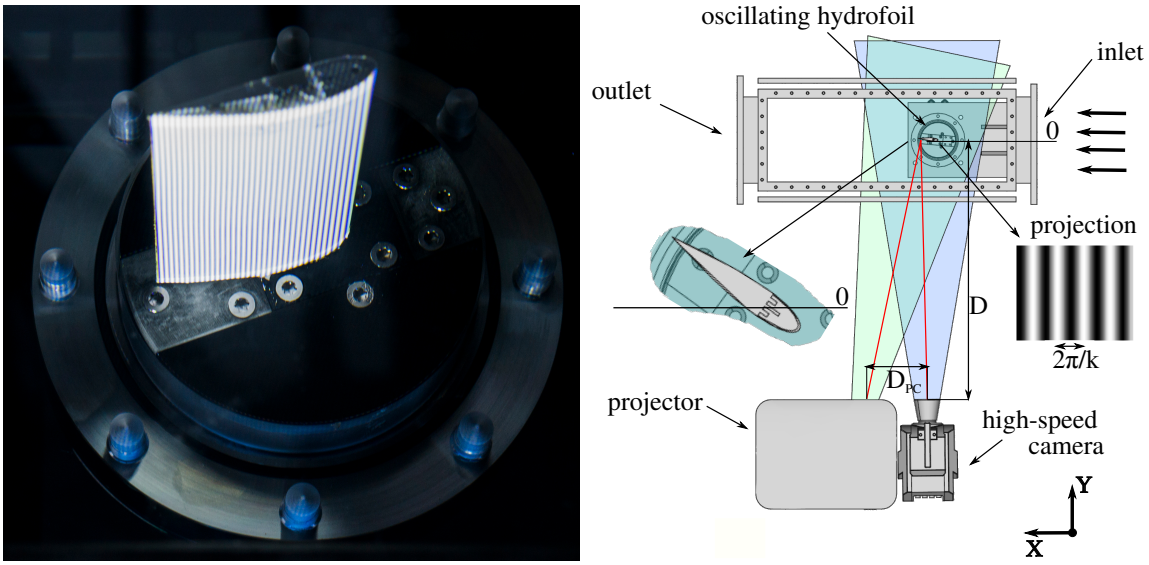

Figure 5.22: Left: Flexible hydrofoil with fringe pattern projection. Re printed from (67). Right: Setup of the surface tracking experiment. Reprinted from (66). The camera and projector are placed underneath the test section of the water channel. The sinusoidal fringe patterns are projected on the hydrofoil surface.

specific application fields. Common applications of these methods in fluid dynamics are the classification of fluid films or the acquisition of droplet shapes. Li et al. 2017 studied the dynamics of water droplet impacts using structured-light based profilometry (82). Hassaini et al. 2018 studied wave turbulence with profilometry techniques, with tracking of the air-water interface of a free-surface flow (60).

In this study, the distance from a surface to the camera-projector couple (see fig. 5.22) is determined by measuring the shift of the phase angle of the projected fringes (see fig. 5.21). The comparison with the undistorted pattern obtained from a flat reference surface provides knowledge of the reference phase angle and allows to retrieve the deformation. An advantage over stereoscopic methods is that a three-dimensional surface can be tracked with a two-dimensional video recording.

5.3.1 Object distance and refraction

The experimental setup (fig. 5.22) leads the projector beam through the different materials (fig. 5.23). According to the Snell–Descartes law, eq. (5.5), the beam will be refracted while it passes each of the material boundaries.

$$\frac{n_1}{n_2} = \frac{\sin \Phi_2}{\sin \Phi_1} \tag{5.5}$$

Starting from air (D_1), an acrylic wall with D_2 =0.04 m thickness has to be crossed, which is followed by D_3=0.14 m of water. In consequence the object distance between the zero reference D=1.07 m appears magnified to the camera. From geometrical consideration the beam angle Φ_1 is given by the arctangent of half of the distance of the projector to the camera D_{PC}=0.36 m divided by D:

$$\Phi_1 = \arctan\left[\frac{D_{PC}}{2D}\right] \tag{5.6}$$

From the intercept theorem we get the shifted projector to camera distance $D_{PC\,1}$ and by analog calculation $D_{PC\,2}$:

$$D_{PC\,1} = \frac{D_{PC}}{D \cdot (D - D_1)} \tag{5.7}$$

The Snell–Descartes law provides the angle Φ_2 and by analog calculation Φ_3:

$$\Phi_2 = \arcsin\left[\frac{n_1}{n_2} \sin \Phi_1\right] \tag{5.8}$$

The magnified distance in the water D_3 as result of the refracted beam angle is found as:

$$D_3 = \frac{D_{PC\,2}}{2 \tan \Phi_3} \tag{5.9}$$

The magnified object distance D' is the sum of the distance to the water channel wall D_1, the wall thickness D_2 and the magnified distance in the water D_3:

$$D' = D_1 + D_2 + D_3 \tag{5.10}$$

The apparent object distance is about D'=1.15 m due to the refraction indexes of the materials (air = 1.00029, polyacrylic = 1.4899 and water = 1.3333). Also, the distance in between projector and camera appears to be smaller because the refracted angle Φ_3 appears to be steeper (red dashed line in fig. 5.23). From the intercept theorem, the apparent distance between projector and camera is obtained as D'_{PC}=0.28.

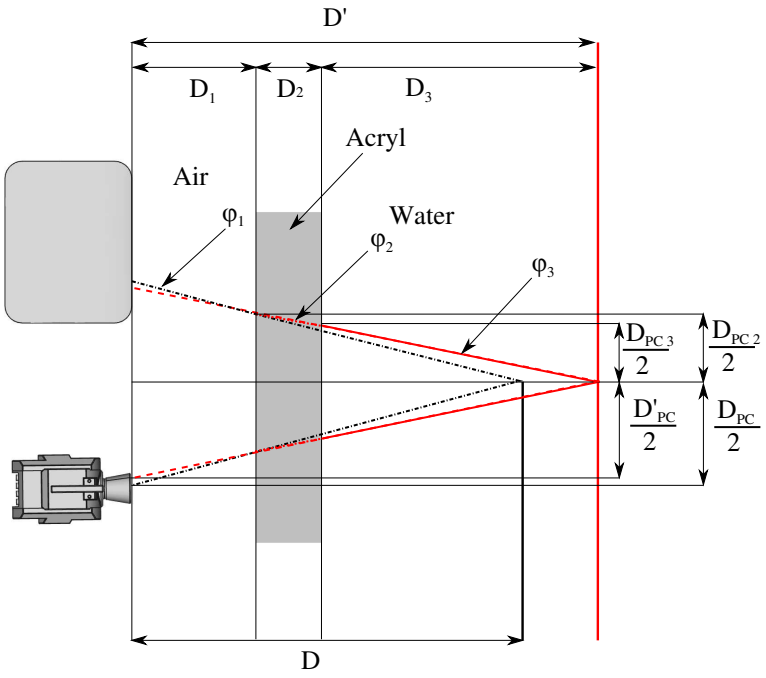

Figure 5.23: Surface tracking refraction magnification: The differences in the refraction index of the materials lead to a magnificated distance from the object to the camera and has to be taken into account for the surface tracking measurement.

5.3.2 Setup

The required hardware implementation consists

of a highly-luminescent projector and a high-speed camera, placed parallel one to each other and perpendicular to the surface of interest. In this case an Epson-H715B projector and Phantom-V2511 camera (see later tab. 5.6 for camera specifications) were used. The projector-camera couple was placed underneath the water channel test section (see fig. 5.22). The projection on the hydrofoil was captured with an objective lens of 105 mm and an exposure time of 60μs for a recording time of 4.125 s for each set.

For the purpose of the SFT measurements, the hydrofoils were produced with a white embodiment, by addition of a pigment paste to the two-component polymers during the mixing process. The rigid foil was painted mat white. The algorithm was tested on an orange cube, in order to perform simultaneous measurements for flow field (with PIV) and structural deformation (SFT). In this case, camera filters could be used as a band pass for the wavelength of the light source of the corresponding method, e.g. 532 nm for the PIV Laser. Unfortunately the contrast of the fringes was not strong enough to provide accurate data. Future work may include the use of more elaborated pre-processing steps like an adapted gain function. In the present case it was decided to separate the measurement campaigns for fluid and structure.

Apart from the mentioned specific setup, all parameters concerning the experimental setup were consistent to those for the force measurements and described in detail in sec. 4.1.

5.3.3 SFT: Methodology

As mentioned in the previous section, the underlying methodology is based on a fringe pattern analysis of structured light, projected on a surface. A structured greyscale light pattern of a sine function with wave length $\lambda_{\sim\mathrm{pro}} = 2\pi/k_{\sim\mathrm{pro}}$, with $k_{\sim\mathrm{pro}}$ the wave vector, is projected on the surface to be tracked. The wave length is chosen with respect to the resolution of the projector and the projection plane.
The recording will result in a different wave length than the one projected, because of projector/camera resolution and projection magnification. The wave length of the recording $\lambda_{\sim\mathrm{rec}}$ has to be determined during initialization before the processing of the videos starts.

For optical reasons, any deformation of the structure results in a change of the distance from the structure to the projector and will lead to a change of the projected pattern caused by a local defocussing of the projection. This will result in a new phase angle ϕ'. The phase angle shift $\Delta\phi_{i,j,t}$ is calculated for each pixel with coordinates (i, j) at each time step t/f_c with:

$$\Delta\phi_{i,j,t} = \phi'_{i,j,t} - \phi_{i,j,t_0} \tag{5.11}$$

where ϕ_{i,j,t_0} is the original phase recorded by the camera. After unwrapping the phase angle and calculating the phase shift, the surface height can be extracted with

$$h_{i,j,t} = \frac{D' \cdot \Delta\phi_{i,j,t}}{\Delta\phi_{i,j,t} - \frac{2\pi}{\lambda_{\sim\mathrm{rec}}} \cdot D'_{\mathrm{PC}}} \tag{5.12}$$

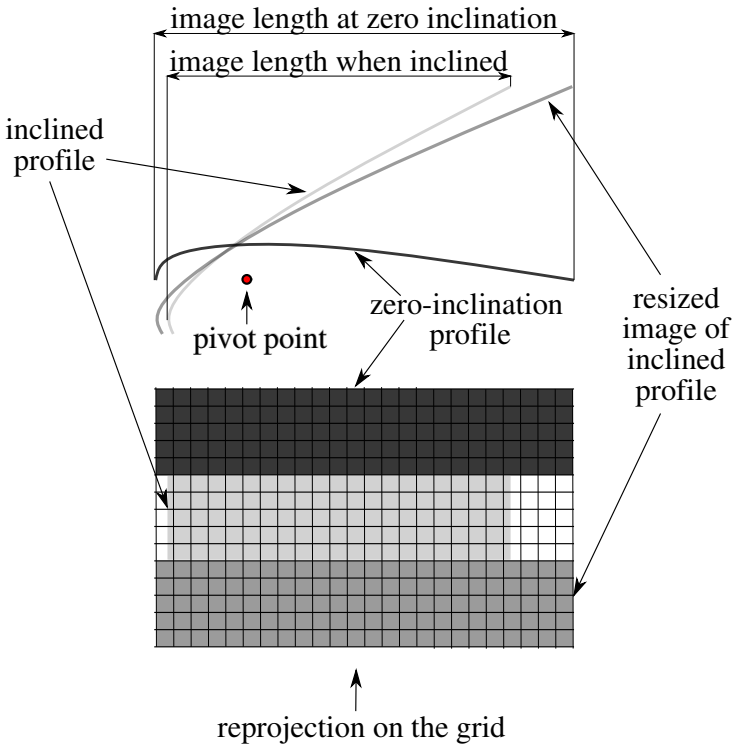

Figure 5.24: "The two-dimensional recording leads to a change of the projected length perpendicular to the rotation axis. Resizing and reprojecting the image to a grid whose length is that of the of zero-inclination profile simplifies the processing and visualization of the data."(66)

where $\lambda_{\sim}$rec is the recorded wave length, D' is the apparent distance, and D'_{PC} is the apparent distance between projector and camera. Maurel et al. 2009 (89) determine a coordinate shift in dependence to the surface height. However the correction proposed,

$$x_{i,j,t} = \frac{x'_{i,j,t}}{1 - \frac{h_{i,j,t}}{D'}} \tag{5.13}$$

(here displayed with notation adapted to the present case; $x'_{i,j,t}$ and $x_{i,j,t}$ being respectively the apparent and real position in X-axis corresponding to the measured height $h_{i,j,t}$), is time-intensive.

At its maximum, with h_{max} =0.02475 m, D'=1.15 m, and x'_{max}=0.066 m, the shift is about $\Delta x_{i,j,tmax}$=1.3 mm which is about 2% of the total width. Given this relatively minor aberration and the fact that the matrix containing the surface height is resized at pixel level and projected on a standardized pixel grid –as described subsequently– a detailed calculation of this coordinate deviation is not considered necessary in the presented application and, as a consequence, was not performed for the given setup. However, this systematic error is found in the results presented in section 5.3.6.

Since the recording is in two dimensions, the apparent profile length changes as a function of the profile inclination ($C' = C \cdot \cos\alpha$, see fig. 5.24). This results in a shift of the apparent coordinates, since the recording remains in a fixed reference frame while the foil is moving. In the current application, this results in further challenges.

The method cannot deal with areas where the fringe is not projected. These

appear as a black band and disturb the Fast-Fourier-Transform (FFT) algorithm, performed in the later processing stage of the method (see fig.5.21 for a sample of the recording for two different inclination angles). A segmentation algorithm tracks the area containing the hydrofoil, and crops the image accordingly; as a result, the size of the matrix varies with time. To be able to process these varying image details, they are inserted in an image matrix of the reference surface with the size of the non-inclined hydrofoil. This will replace the black areas by the undistorted fringe pattern. After processing, the surface area results are cropped again and then mapped on a fixed size pixel grid of 276×600 pixel^2 for each frame, by resizing of the matrix with a spline interpolation function of first order (see fig. 5.24). The physical length l can be found by multiplication of the pixel grid with the pixel size and the cosine of the inclination angle:

$$l = l_{\mathrm{px}} \cdot px_{\mathrm{size}} \cdot \cos(\alpha) \tag{5.14}$$

The practical implementation of the method includes further steps:

- For the initialization, the wave length of the recording $\lambda_{\sim \mathrm{rec}}$ has to be determined. It is calculated using the maximum peak frequency $f_{\max}$ of a FFT over several frames, the number a_{px} of pixels in the image, and the number n_{px} of pixels in the direction of the wave propagation:

$$\lambda_{\sim \mathrm{rec}} = \frac{n_{\mathrm{px}}}{f_{\max} \cdot a_{px}} \tag{5.15}$$

- In each frame of the high-speed video, the structure is detected and the image is cropped with a segmentation function;
- The signal in each frame is normalized by subtraction of the frame's signal average to generate a value range from -1 to 1, amplifying with a gain of $e^{-\iota \cdot k_{\sim \mathrm{rec}} \cdot x}$ and subsequent filtering with a band pass close to the wave vector $k_{\sim \mathrm{rec}}$ in the Fourier space to remove noise;
- The phase angle is retrieved from the complex function and subsequently unwrapped;
- A spatial 2π discontinuity detection and correction is performed to obtain a continuous surface;
- The surface height $h_{i,j}$ is extracted by application of eq. (5.12);
- A temporal discontinuity detection and correction is conducted in order to remove 2π jumps in time (in contrast to the method of Takeda et al. 1982 (118) where this was not performed);
- The result is stored in h5 containers to allow an easy and direct access to the data.

Finally, a wrapper function transforms the surface data in VTK format so that the data may be visualized in the open-source toolkit *Paraview*, where the data can also be further post-processed. Additional *Python* utilities related to the following example case are also published under a GPLv3 license (63).

5.3.4 Software development

An earlier implementation of the method in Matlab by Aubourg 2016 (8) was used as a first template for the present code. Aubourg 2016, and later Hassaini & Mordant 2018 (60), investigated wave structures in a vibrating box filled with pigmented water.

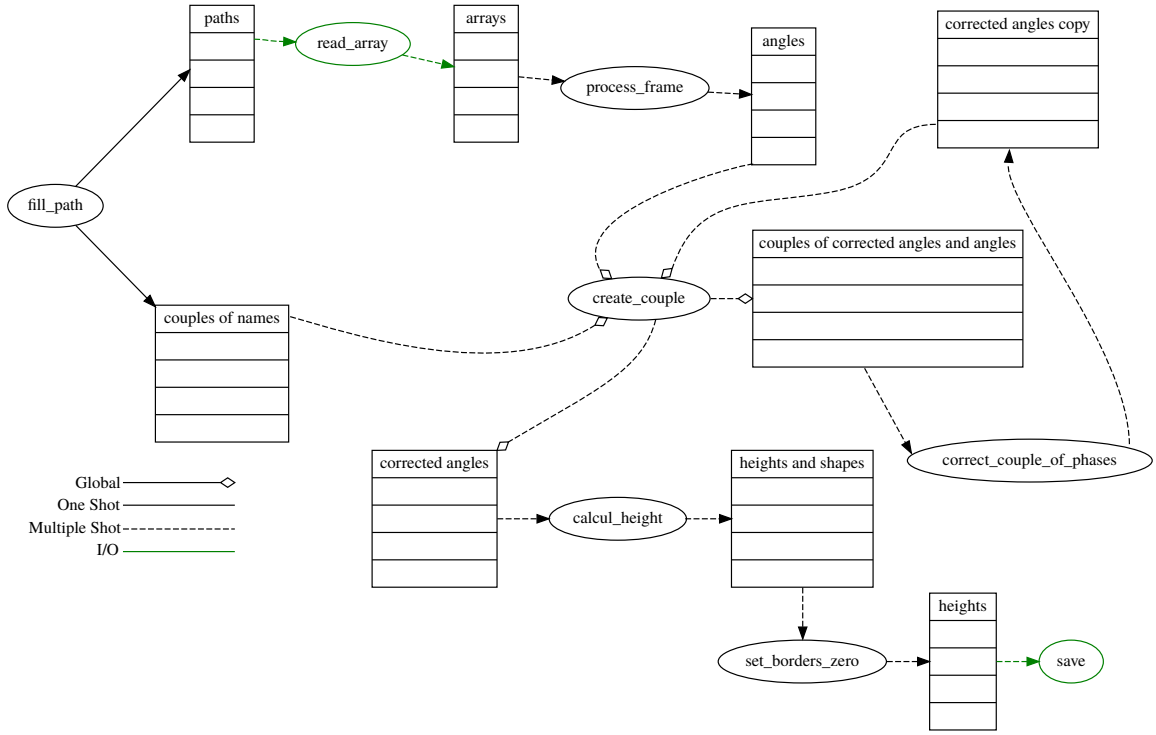

Figure 5.25: Topology of the SFT algorithm integrated in the `fluidimage` framework. The code was partly parallelized with the use of multiple queues for parallel tasks. The bottleneck of the algorithm is the temporal discontinuity correction (`correct_couple_of_phases`).

For the SFT conducted in this work, the code was rewritten in *Python* and extended due to new requirements. The development was made in collaboration with Cyrille Bonamy at the LEGI labs. The following new features were included:

- A spatial, two-dimensional 2π discontinuity correction: the template version detected only temporal jumps. The spatial detection and correction was implement according to Takeda et al. 1982 (118). The surface height gradient is considered to be small for a small change in space (continuous change of the height). The method seeks for discontinuities of 2π when the angle is shifted from one period to the next. Therefore the phase angle ϕ for a position x_i is compared to its predecessor x_{i-1}. If the height is close to 2π, the position and direction of the jump is mapped. In a second step the algorithm cuts or adds another phase shift of 2π for all following positions until the next jump occurs, where, depending on the jump direction, an additional 2π value is added or removed for the following positions. This is performed first in X then in Y-direction for the whole matrix, and results in a smooth progression of the phase

angle.

- A foil border detection (segmentation): since the method cannot deal with parts of the image where no fringe pattern is present, an adaptive border detection was implemented to crop the image.
- Projection of the cropped foil image: since the gain and filter matrices are defined for the reference size of the non inclined foil, a "stretch" of the inclined foil images was carried out, as explained above, using the `sft_mask.py` unit in the code base (63).

The code was implemented in the LEGI in-house code *Fluidimage*, a *Python* framework for PIV post-processing, presented in detail in sec. 5.4. The integration was mainly realized by Cyrille Bonamy. One aim of the integration was to use the highly-optimized Fast-Fourier-Transform (FFT) algorithm of the framework, and parallelization. Unfortunately, the temporal 2π discontinuity correction function needs information of the predecessor frame. This prevents full parallelization. Multiple queues were created, in order to process multiple jobs in parallel.

The code is published under a CeCILL-B licence, the latest development version can be found in the git repository of Cyrille Bonamy (20). Further development will focus on a fully-parallel processing with subsequent non-parallel time discontinuity correction to speed up the processing. The code's current pseudo-parallel topology is shown in fig. 5.25.

5.3.5 SFT: Surface calibration

The calibration is carried out to overcome inaccuracies related to the installation, optical aberrations related to the angle separating camera and projector from the investigated surface, as well as to the distance separating them.

The calibration and subsequent uncertainty considerations of the method are carried out using the rigid reference profile (see fig. 5.26). The surface tracking results are compared to a model surface of the hydrofoil which performs an oscillation according to the position feedback of the drive system (see sec. 4.2.2).

According to the different acquisition rates of position feedback and high speed recording each fourth frame of the high speed film was evaluated. The deformations of the rigid hydrofoil can be considered negligible.

The modeled reference hydrofoil surface is built using eq. (5.16), an expression describing a four-digit NACA hydrodynamic profile contour (70). The shape is calculated for a relative thickness τ=0.18 (the foil thickness in percent of the chord length/100) for a discrete number of points corresponding to the number of pixels in the X-axis. The resulting curve is rotated in accordance to the position feedback of the drive at quarter chord, scaled and finally extruded in Z-direction.

$$\begin{aligned} y &= \frac{\tau}{0.20} \cdot (0.2969\sqrt{x} - 0.126x \\ &\quad -0.3516x^2 + 0.2843x^3 - 0.1015x^4) \end{aligned} \tag{5.16}$$

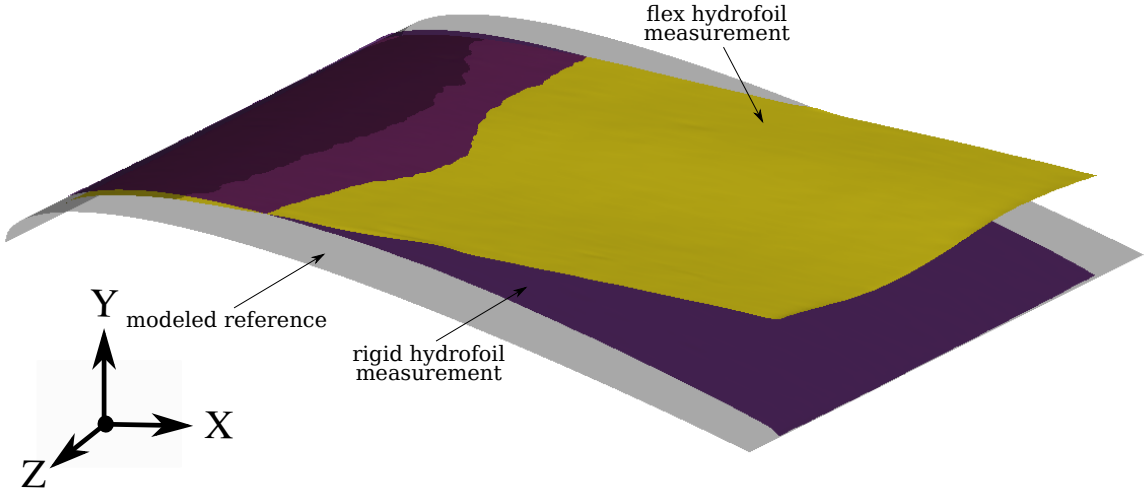

Figure 5.26: "Surface measurement of a rigid hydrofoil (dark violet), a flexible hydrofoil (orange) and the artificial reference surfaces (grey and black). For convenience, the shape is turned upside down, that the surface appears to be the upper side of the profile." Reprinted from (66). A video of the moving structure can be found at the author's website

A calibration algorithm was implemented as a utility (see `sft_cal.py` in (63)). The algorithm converts the calculated heights from the pixel-based grid to the physical profile length in X- and Z directions ($n_X \times n_Z$). 100 pixels were cropped on each side in the Z-axis of the profile to remove reflection noise from the wall of the test section of the channel (see fig. 4.2 for coordinates).

Table 5.1: SFT calibration matrix

	X	Y	Z
Translation [m]	0	0.00106	0.015
Rotation [°]	0.014	0	-0.045

The measured surface S_{mes} is centered in this axis with respect to the modeled surface S_{mod} (see fig. 5.26)[2]. As a consequence of the projection of both surfaces in a rectangular grid (see fig. 5.24), only three degrees of freedom remain unknown for a surface fit, as shown in fig. 5.27. Because it is assumed that the shape differences between the two surfaces are small, one translation vector and two rotation angles are sufficient to calculate the gap in Y direction between the two (similar) surfaces. This can be conducted with three points.

The points p_1/p'_1 ($0.25{\cdot}l_X$, $0.25{\cdot}l_Z$), p_2/p'_2 ($0.25{\cdot}l_X$, $0.75{\cdot}l_Z$) and p_3/p'_3 ($0.75{\cdot}l_X$, $0.75{\cdot}l_Z$) are the vertices of a right triangle, where l_i is the length of the edge in the direction i. Points p_{1-3} and their peers p'_{1-3} are separated by three vertical vectors $\vec{\text{dist}}_{1-3}$. rot_X and rot_Z can be calculated by geometry from $\vec{\text{dist}}_1$ and either $\vec{\text{dist}}_2$ or

[2] A video can be found on the author's website.
`https://www.ovgu.de/hoerner/thesis/videos/sft/sft_lambda2_k046.mp4`

$\vec{\text{dist}}_3$

Height differences between both surfaces were calculated for a set of 500 frames. The calibration vector is shown in tab. 5.1; the values for the rotation are negligible, and the height shift is 1.06 mm. The position in the Y-axis is affected by the luminosity of the projection, which unfortunately flickers with a 60 Hz frequency. The height has to be adjusted once for each take using a known reference point at quarter chord (where no deformation occurs) at zero inclination angle. Figure 5.28 compares the measured and predicted height of a point situated at the trailing edge in the mid-span position of the foil ($\alpha_{300,260,t}$). Generally the measurement method delivers accurate results. However, the deviations increase significantly for high inclination angles. This is due to a general drawback of the method as the measurement of a motion parallel to the zero plane is not feasible. This share of the motion increases with rising angle of inclination of the foil. The deviations are discussed and analyzed in detail in the following section.

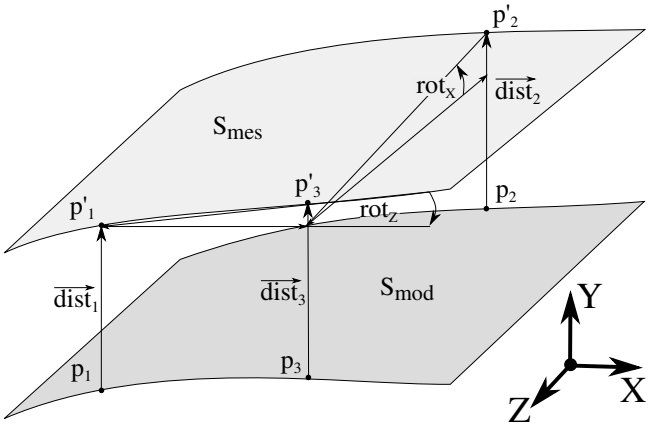

Figure 5.27: "Surface tracking calibration: The calibration of the measurements is performed with three points for each sample. The calibration vector (containing $\vec{\text{dist}}_1$, rot_X and rot_Z) is then averaged over time so that error for the whole set is minimized." Reprinted from (66).

5.3.6 Method validation

The modeled surface created from the position feedback and the measurement of the rigid hydrofoil are compared in order to validate the method. The difference between the modeled height $h_{mod_{i,j,t}}$ and the measured height $h_{mes_{i,j,t}}$ over a set of frames are evaluated using eq. (5.17).

$$\delta h_{i,j,t} = h_{\text{mes}_{i,j,t}} - h_{\text{mod}_{i,j,t}} \tag{5.17}$$

The validation is performed with the help of a postprocessing class (see `SFT_post.py` in (63)). In a first step, the temporal error δh_t at the point $h_{i,j} = h_{300,260}$ near the trailing edge (situated at $j = 276$) is estimated.

This is followed by an evaluation of the spatial error $\delta h_{i,j}$ for an arbitrary frame in the time line t. Here the calculation is evaluated for all pixels of the surface. The result is a three dimensional error matrix of size 276×600 with a depth of the evaluated set. Subsequently, the error relative to the motion is normalized with respect to the amplitudes of the surface heights:

$$\delta h_{\text{rel}_{i,j,t}} = \frac{\delta h_{i,j,t}}{\max\limits_{i,j,t}(h_{\text{mod}}) - \min\limits_{i,j,t}(h_{\text{mod}})} \tag{5.18}$$

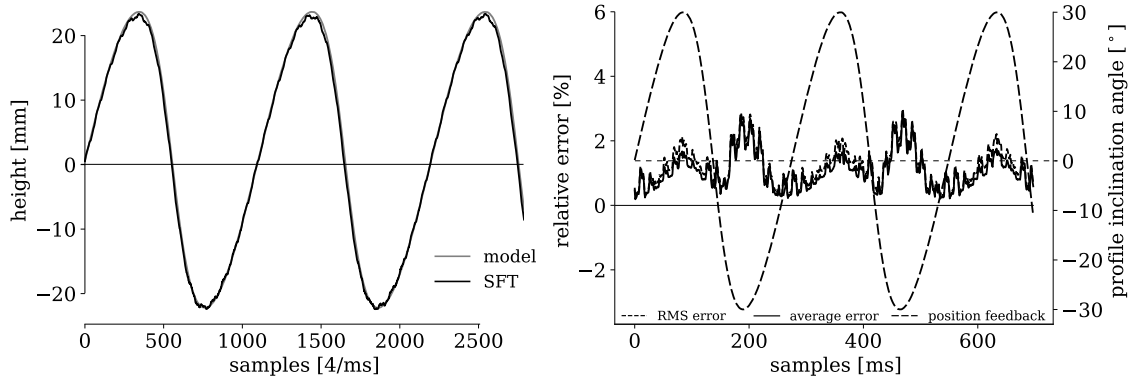

Figure 5.28: "(left)Surface height over time, measurement compared to the model surface for one point ($h_{300,260,t}$) at the trailing edge for 2700 samples after calibration. (right) Relative error over time for the surface tracking measurement, compared to the model surface for one point ($_{300,260}$) at the trailing edge for 675 samples (the difference in the number of samples is due to the different sample rates for position feedback (1 kHz) and SFT (4 kHz)). The error is set in relation to the foil motion with eq. (5.18). The corresponding inclination angle (from position feedback of the drive) is plotted in the same diagram to highlight the correlation between profile inclination and error." Reprinted from (66).

The relative error is shown in fig. 5.28. The influence of the inclination angle is significant; the flicker frequency of 60 Hz from the projector is also visible.

Applying a low-pass filter to cut off the flicker effect would have significantly attenuated the error. Nevertheless, it was decided to keep the data unfiltered, in order to preserve the entire spectra of the motion. The method provides highest accuracy for low pitch angles, with a relative error below 1%.

The mean error was evaluated for all pixels of the surface, except the first 20 pixels at each border. The maximum foil displacement (see eq. (5.18)) was used as the normalization reference to calculate the relative error. The average relative error is 1.06% over an entire oscillation period, which corresponds to an absolute value of 0.66 mm.

In figure 5.29, the measurement error is shown for a chord-wise foil section at t=223 s, in the middle of the Z-axis ($\delta h_{i,300,223}$) and subsequently for a section in the span-wise (X-axis) direction near the trailing edge ($\delta h_{265,j,223}$). The obvious aberrations on the hydrofoil borders become visible in particular for the chord-wise cut. The shape of the error profile with its maximum of about 1.4 mm in the middle of the chord is in accordance to the errors reported by Maurel et al. 2009 (89). A treatment of the position shift (see eq. (5.13)) may further reduce these deviations if necessary. In the Z-axis the error remains at an almost constant level except at the borders.

Tables 5.2 & 5.3 summarize the method accuracy for the case at hand. It must be kept in mind that the accuracy depends significantly on the constraints of the experiment. Higher accuracies may be achieved for smaller height differences and higher spatial resolution.

Figure 5.26 displays the two surfaces of the rigid and the flexible structure along

with the analytical reference from eq. (5.16) imported to *Paraview*. A good agreement with the modeled reference can be found for the rigid hydrofoil measurement, both surfaces overlay with negligible error, in particular at the rear region of the structure.

5.3.7 Results and discussion

5.3.7.1 Preliminary considerations

Figures 5.31 & 5.32 provide a visualization of the results for the validation case. The flexible three quarters of the chord at the rear of the structure are deformed as a result of the hydrodynamic forces. The maximal height difference is about 14 mm compared to the rigid hydrofoil, which means 20% of the chord length.

A "flapping" of the profile's trailing edge occurs periodically with stronger preference for the slower motion (direction of increasing α) starting at -20°. The faster pitch motion towards negative α features a less distinct flapping motion (starting at 20°), which can in consequence be assumed to be dependent on the pitch speed.

In the subsequent paragraphs, the results of the surface tracking are shown - along with the force measurements - for both rigid and flex[03] hydrofoil in a common diagram. This will allow to compare the characteristics of the deformation and their influence to the hydrodynamic forces with changing reduced frequency. The upper graph shows the position feedback of the drive system (dashed black for the flexible and dashed grey for the rigid) in order to show the repeatability of the motion trough the drive system. β, the angle of

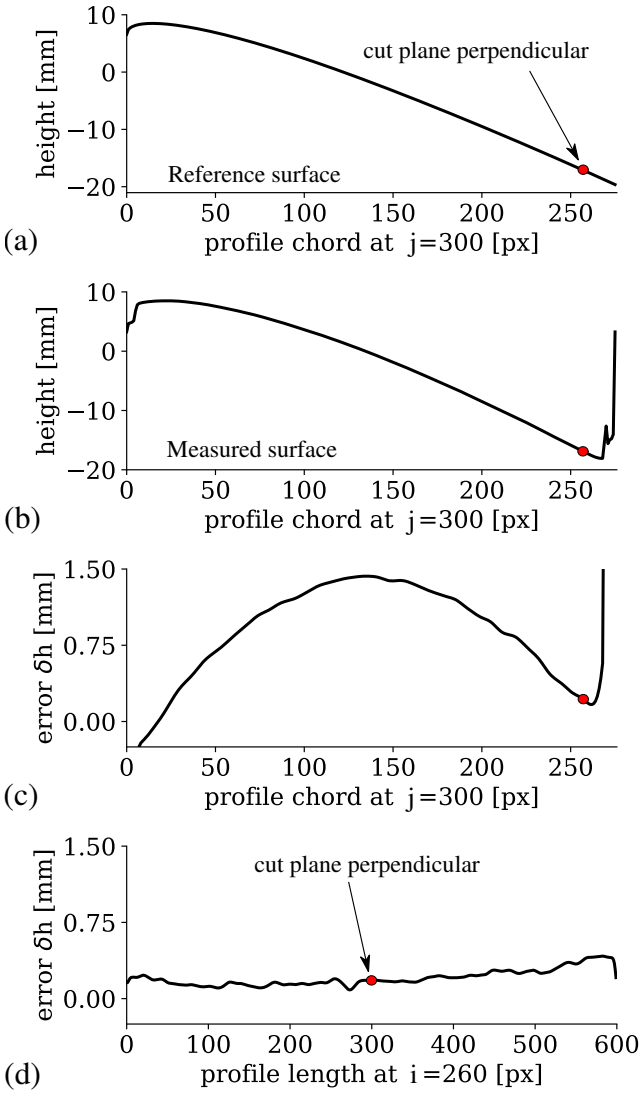

Figure 5.29: (From top to bottom) Modeled surface (a) measured surface of the inclined hydrofoil (b) and a measurement error to the reference surface for an arbitrary frame (t=223). The maximum chord wise error is found in the middle of the profile with around 1.4 mm (c) The maximum absolute error in the profile length is less the 0.4 mm (d). The inclination angle for this instant of time is α=28°

a virtual line in between the measured trailing edge height h and the pivot point at quarter chord, compared to the non-deformed profile camber line through the height at zero angle h_0 at trailing edge and the pivot point, is also shown in the upper graph (solid black for the flexible foil and solid grey for the rigid). It is calculated using eq. (5.19), explained in fig. 5.30:

$$\beta = \arctan\left(\frac{\Delta h}{\frac{3}{4}C}\right) \tag{5.19}$$

(The profile length l is constant, as the height matrix from the measurement is projected to a fixed-size lattice).

The hydrodynamic forces displayed different characteristics for the two operating points (see sec. 5.2.4), the flex[03] foil displayed the most promising potential. In consequence the two intermediate rigidities flex[05] and flex[07] were not further evaluated as they do not provide significant improvements. In the case of λ=2, the maximum inclination angles α are approximately 50% higher compared to the λ=3 case. This is also true for the lift force, which peaks at up to 150 N (cases with k_o >0.16) for λ=2. They are found to be clearly below this magnitudes for λ=3 with approximately 100 N. However, the stiffness of the hydrofoil is a crucial factor. The lower lift peaks for higher tip-speed ratios may demand lower foil stiffness to improve the benefit from this approach.

Table 5.2: Error determination I

absolute error		
average error	[m]	0.00066
RMS error	[m]	0.00077

Table 5.3: Error determination II

error relative to the motion		
relative average error	[%]	1.06
relative RMS error	[%]	1.23

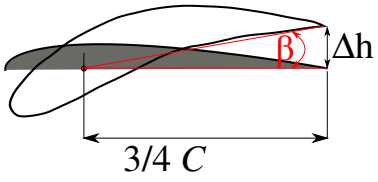

Figure 5.30: Deformation angle β: The hydrofoil is projected on a fixed pixel grid. (The projected length remains constant)

However, the centrifugal forces rise with rising tip-speed ratio. The approach presented may fail if centrifugal forces become dominant over the fluid forces; this is in particular the case for wind turbines. As a consequence, the focus is set on the λ=2 operating point for the rest of the section.
The data subsequently presented in fig. 5.33-5.41 is filtered after the SFT processing and force measurement using a zero-phase, low-pass Butterworth filter of second order at 35 Hz, in order to fully eliminate the effects of a 60 Hz flicker from the projector and vibrations from load-cell measurements.

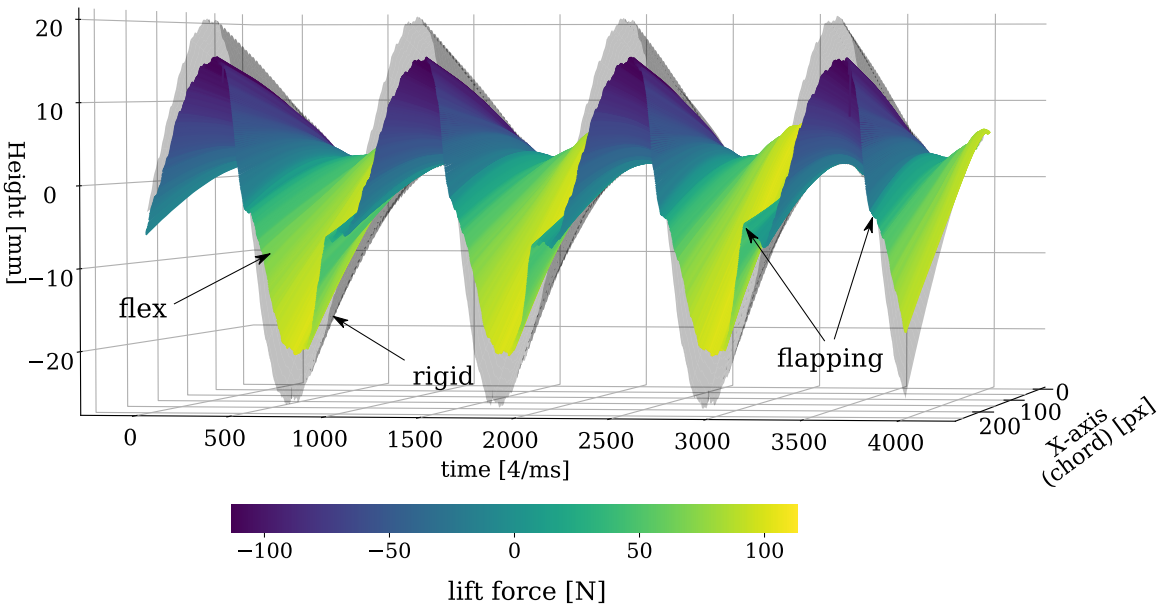

Figure 5.31: SFT measurements of the position of the rigid and the flex[03] foils. Three-dimensional representation of the trajectory of a mid-span section of the rigid (grey) and the flexible hydrofoil, colored according to the magnitude of the instantaneous lift force. The data is plotted over time with 4 samples/ms. Reprinted from (66).

5.3.7.2 The λ=2 case

The surface tracking measurements were performed for seven oscillation frequencies, corresponding to seven reduced frequencies:

- f = [0.21, 0.45, 1.30, 2.25, 2.63, 3.64, 5.68] Hz
- k_o = [0.03, 0.06, 0.16, 0.28, 0.33, 0.46, 0.71]

Transitional state at k_o=0.06: The campaign starts with a transitional case (fig. 5.33). The flow dynamics for a reduced frequency k <0.05 can be considered to be quasi-static (McCroskey 1981 (92)): here, flow convection dominates over the pitch motion. The rigid profile static stall angle was found experimentally to be at 16°. The insetting dynamics of the pitch motion shift the stall point of the rigid foil to 22°. The lift force peak is about 120 N on the rigid hydrofoil. The deformation peaks of the flexible hydrofoil and the lift peaks of the rigid foil coincide. The lift curves for the flexible hydrofoil show none of the "classical" characteristics of static foil stall (abrupt drop in lift with increase in drag). Local maxima in rigid lift force and flexible deformation coincide repeatedly, e.g. at 1800, 2000, 5400, 5600 samples. The lift force drops occur simultaneously with the drag peaks.

Stall at k_o=0.016 - k_o=0.33 At k_o=0.016, a fully dynamic state is reached. The pitch motion leads to a further phase shift of the stall point towards higher angles

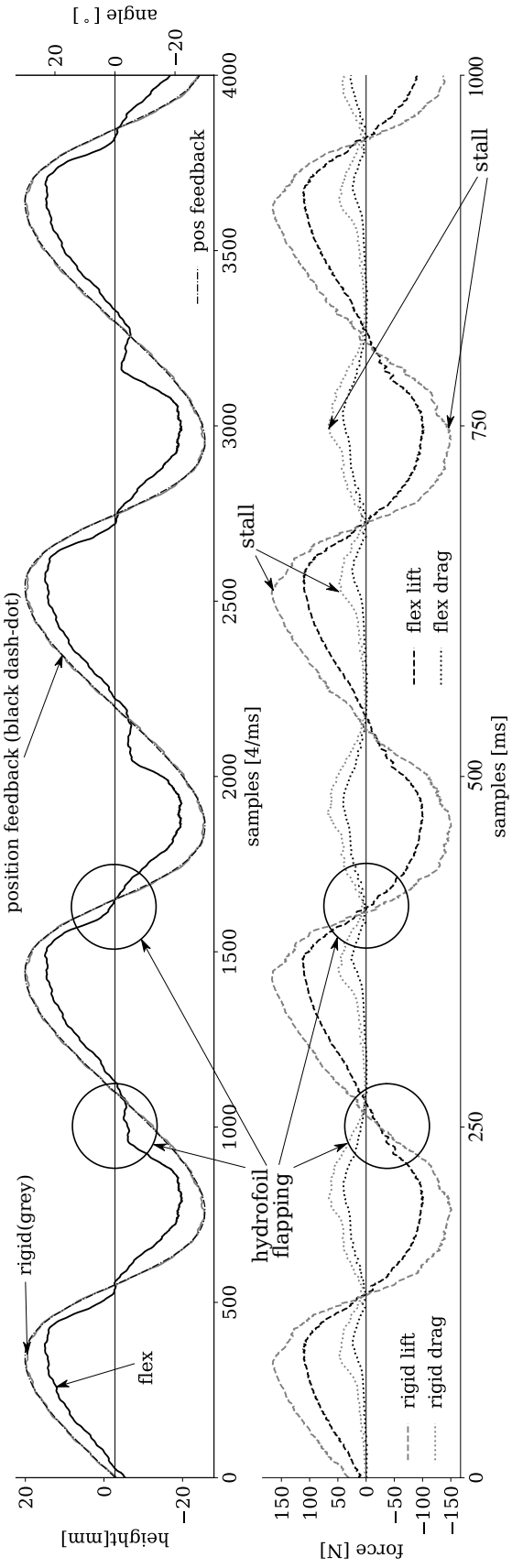

Figure 5.32: Measurements of height and force for a flexible and a rigid foil, over a 0.5 s measurement sample.
Top: height of a single point at 97% chord on the rigid and flex[03] foils (left axis), and angle read from the position feedback (right axis). Those curves were acquired with a 4 kHz sample rate.
Bottom: Lift (dashed) and drag (dotted) forces on both foils over the same time period. Those curves were acquired with a 1 kHz sample rate. Reprinted from (66)

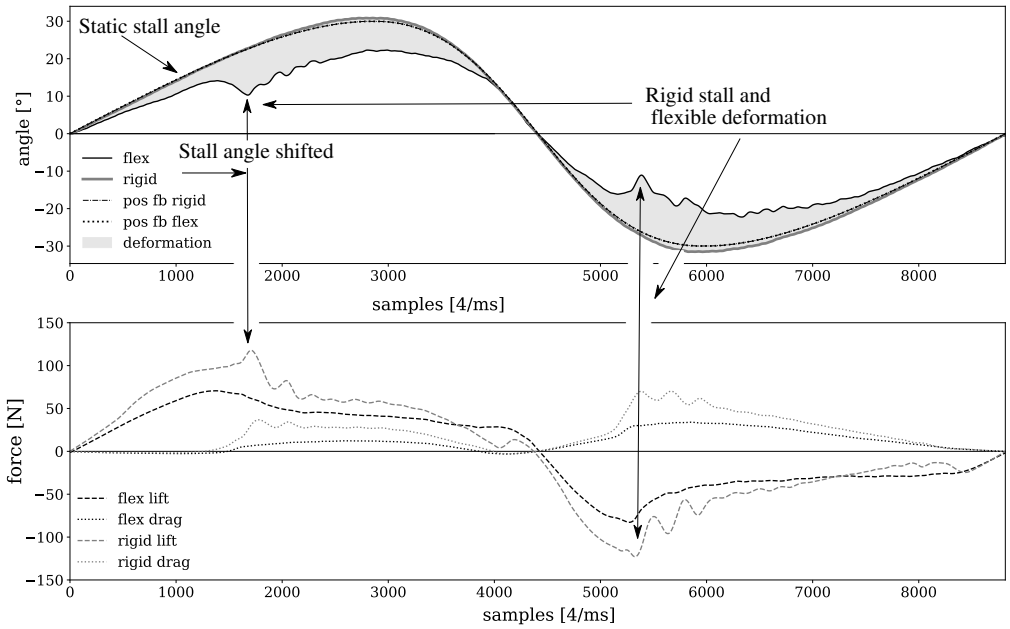

Figure 5.33: Deformation (top) and hydrodynamic forces (bottom) for λ=2 and k_o=0.06 (transition between quasi-static (k_o <0.05) and dynamic state). The stall point is shifted to higher angles of incidence. The force peaks on the rigid hydrofoil (bottom: grey dashed line) occur at the same pitch angle as the deformation peaks on the flexible structure (top: solid black line). One oscillation period is shown.

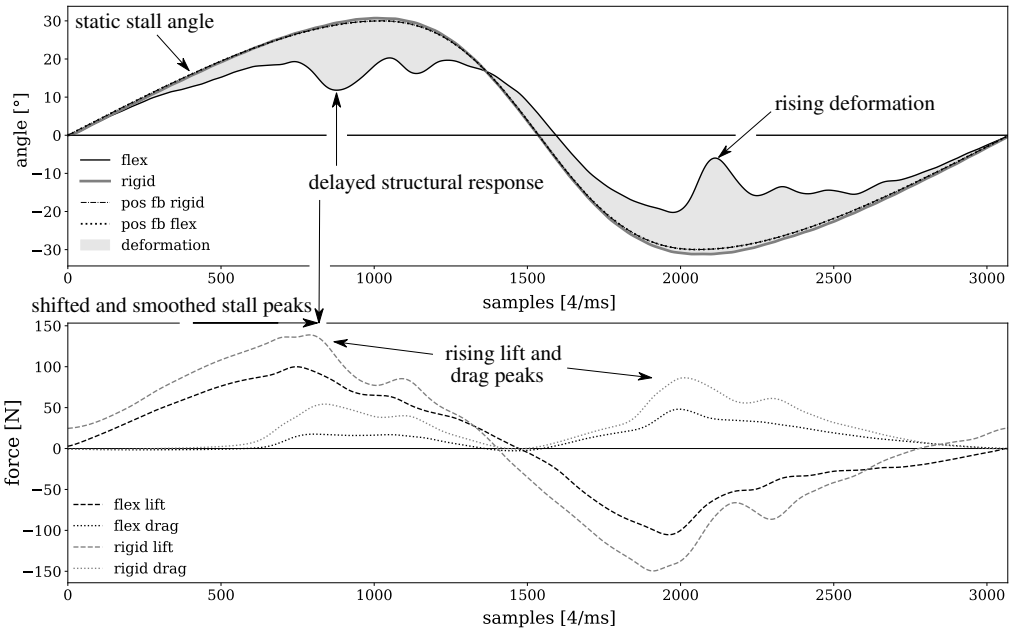

Figure 5.34: Deformation (top) and hydrodynamic forces (bottom) for λ=2 and k_o=0.16 (fully dynamic state is reached). The stall point is further shifted. The force peaks on the rigid hydrofoil (bottom: grey dashed line) occur earlier than the deformation peaks on the flexible structure (top: solid black line). Lift loss and drag peak occur at the same moment.

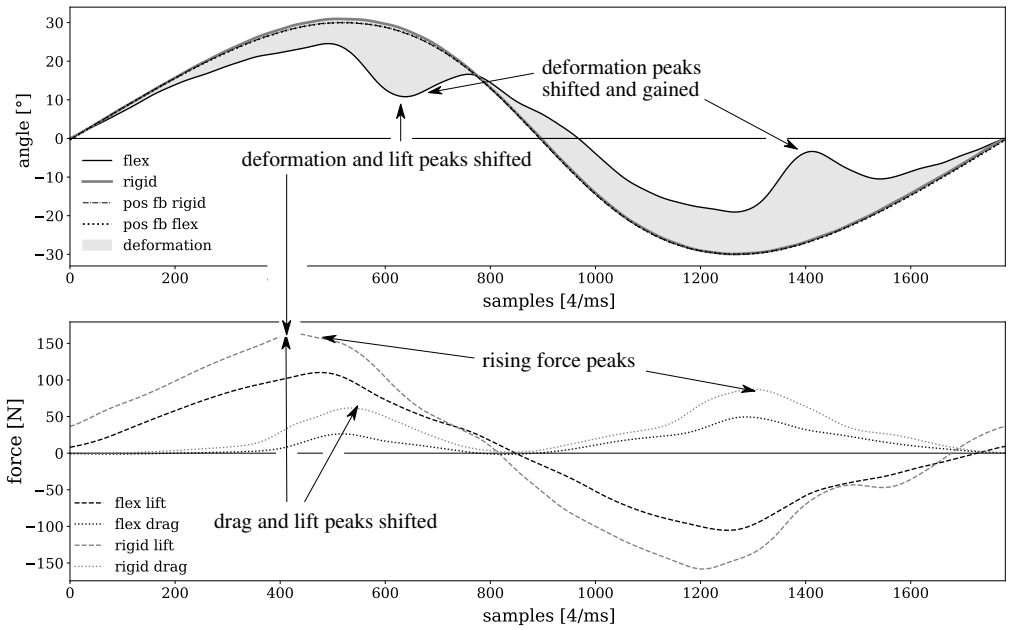

Figure 5.35: Deformation (top) and hydrodynamic forces (bottom) for λ=2 and k_o=0.28. The trend of figure 5.34 continues. Lift loss and drag peak do not occur at the same moment anymore. Force and deformation peaks are gained.

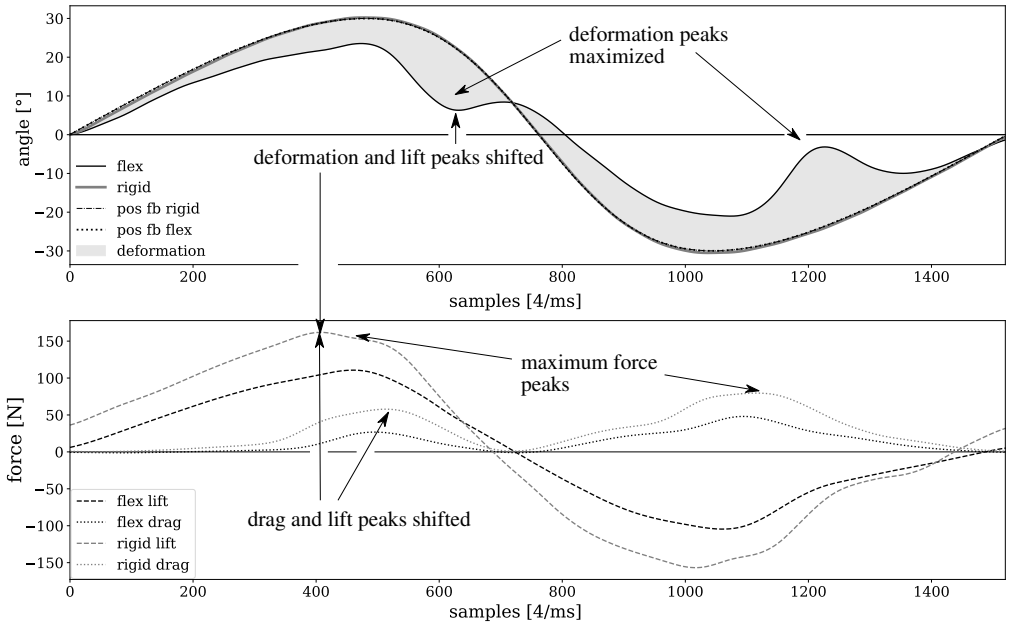

Figure 5.36: Deformation (top) and hydrodynamic forces (bottom) for λ=2 and k_o=0.33. The trends shown in figure 5.34 & 5.35 further continue. Deformation and force peaks reach their maximum.

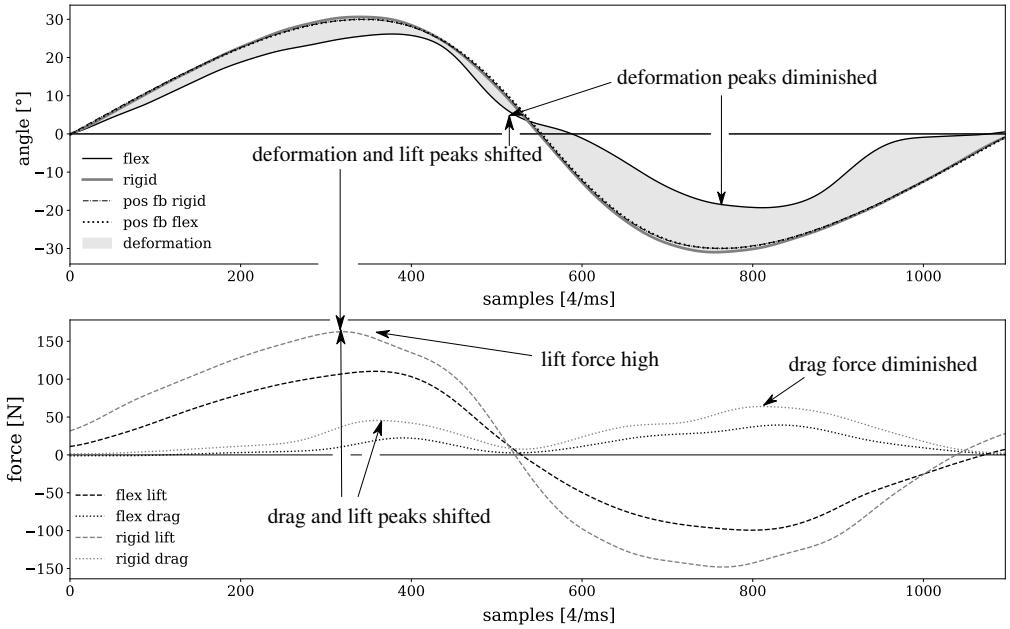

Figure 5.37: Deformation (top) and hydrodynamic forces (bottom) for λ=2 and k_o=0.45. The force and deformation peaks diminish after a maximum at k_o=0.33 in figure 5.36. The highest peak is shifted to the descending branch of the trajectory of α for the flexible hydrofoil.

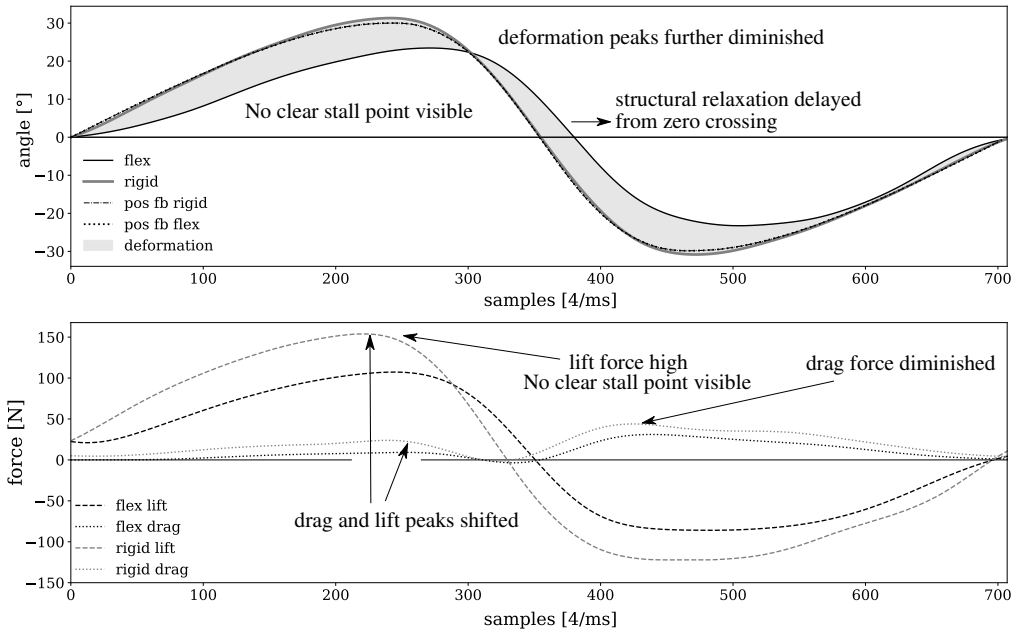

Figure 5.38: Deformation (top) and hydrodynamic forces (bottom) for λ=2 and k_o=0.71. No stall insetting is visible from the hydrodynamic forces. The structure relaxation is delayed (zero angle crossing of β at -12° pitch angle α).

of incidence and to further rising lift force peaks (F_L >150 N for k_o=0.33). However these peaks are smoothed out compared to the previous case. The structure deflects more than before, due to the increased lift forces.

The rigid force peaks still coincide with the flexible deformation peaks. However a short delay time becomes visible (see figure 5.34). This trend continues with rising k_o. At k_o=0.28 and k_o=0.33 the deflections increase and further shift to later occurrences in the phase angle, while the lift and drag peaks further increase. The deflection of the flexible structure and the lift peaks still coincide, but the coincidence is less evident than for the transitional state, since the delay time becomes more important relative to shorter oscillation periods (see figs. 5.35 & 5.36). The lift and drag peaks do not coincide anymore, with the drag peaks occurring later than the drops in the lift forces. For the case of k_o=0.33 ($\sigma \approx 1$ with n=3), the deformation peaks of the flexible structure remain for a quarter of the period.
The analysis of the results from the force measurements showed an improvement of 20% on the blade thrust coefficient compared to the rigid hydrofoil. This improvement is explained by the significant reduction observed in the drag (of around 50%) along with relatively smaller reductions in the lift forces (30%).

Fully dynamic state at k_o=0.45 - k_o=0.71 In fully dynamic state, the pitch motion dominates over the flow convection. For k_o=0.45 the stall point of the flow is phase-shifted from the ascending branch at 16° to the descending branch at 5°. The peaks in the lift and drag usually associated with stall become invisible. The deflection peaks of the flexible structure remain only for a shorter part of the period of about 15%. However the drag remains at a high level of up to 60 N for the rigid hydrofoil (see fig. 5.37). For the highest reduced frequency investigated, k_o=0.71 (see fig. 5.38), the dynamics were characterized by strong vibrations in the forces (low-pass filtered), which had no visible impact on the structure. The trend from the previous case continued. The deformation leads to a delay in the height trajectory compared to the inclination angle. The zero-crossing of the flexible hydrofoil occurs later in the period than for the rigid structure (zero angle crossing of β at -12° pitch angle α). This is not the case for lower reduced frequencies.

5.3.7.3 The λ=3 case:

Once again, the surface tracking measurements were performed for seven oscillation frequencies, corresponding to seven reduced frequencies:

- f = [0.70, 1.33, 2.46, 3.42, 4.84, 6.20, 6.45] Hz
- k_o = [0.07, 0.13, 0.24, 0.34, 0.49, 0.62, 0.65]

Generally the results show comparable characteristics to the λ = 2 case and will not be discussed in detail for each k_o. However, the main difference is the decreased maximum pitch angle for the hydrofoil of α=20°. The curve shape of the pitch trajectory is smoother than the sawtooth-like shape of the λ=2 case. In consequence, the maximum deformation of the hydrofoils is smaller as well. This is due to the

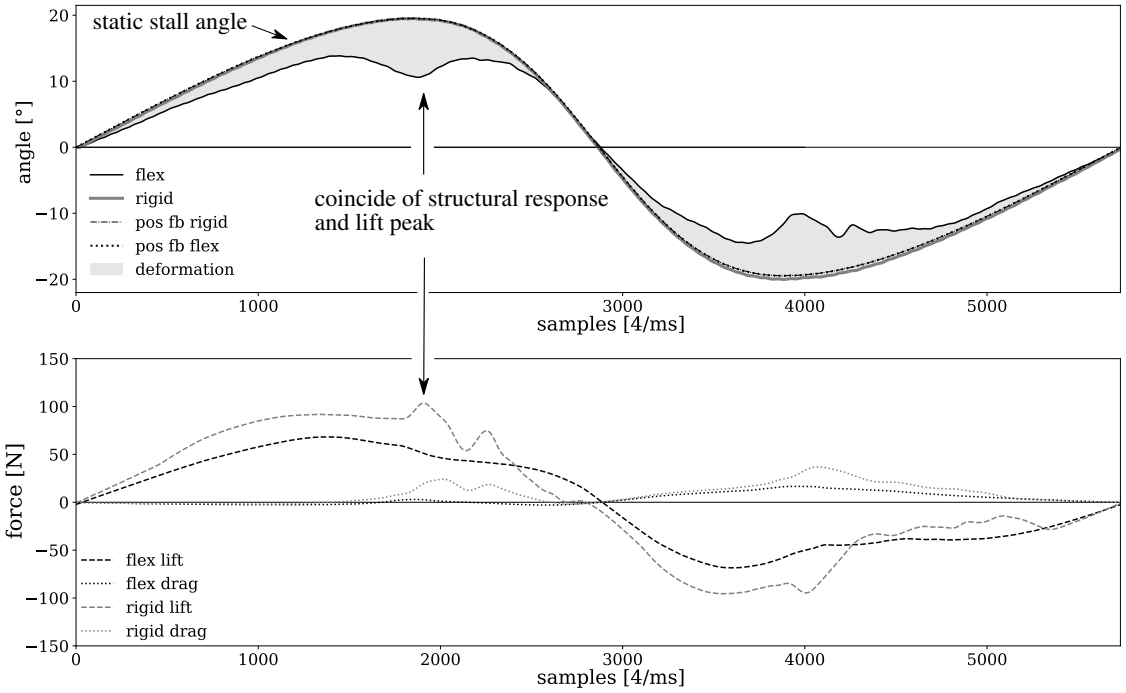

Figure 5.39: Deformation (top) and hydrodynamic forces (bottom) for λ=3 and k_o=0.07

smaller lift forces of F_L=100 N (see figure 5.39 - 5.41). This is, compared to the $\lambda = 2$ case, a reduction of 33% and comes along with the reduction of the angle of incidence of 33%.

The characteristics reported in the previous operating point occur already for lower k_o in the λ=3 case. The rigid hydrofoils stalls only in the quasi-static/transitional cases at k_o <0.24. The shape characteristics of k_o=0.07 are comparable to those from k_o=0.16 at $\lambda = 2$. Even there, the drag peaks remain very moderate compared to the previous case. For higher k_o values, no drag peak at all can be observed. The characteristics of deformations at k_o=0.71 for λ=2, are already found at k_o=0.24 for λ=3: This in particular the case for the phase shift of the deformation to higher phase angles. The curve shape is once more reminiscent of a sine function, the structural relaxation from the deformation is delayed compared to the hydrodynamic forces. For λ=3, a typical VAWT (with $\sigma \approx$1) operates at k_o=0.26. This operation point is shown in figure 5.40 with k_o=0.24. In general no significant influence of k_o on the deformation is observed. This is maybe due to the low angles of incidence and the hydrofoil stiffness.

5.3.8 The influence of k_o and λ

The deformation characteristics of the flexible structure at λ=2 are strongly influenced by the reduced frequency. Figure 5.42 displays this dependency. A regression based on radial-basis functions has been applied to display trend curves on the data. The uncertainty bandwidth is based on the accumulated measurement error of δ=0.8 mm

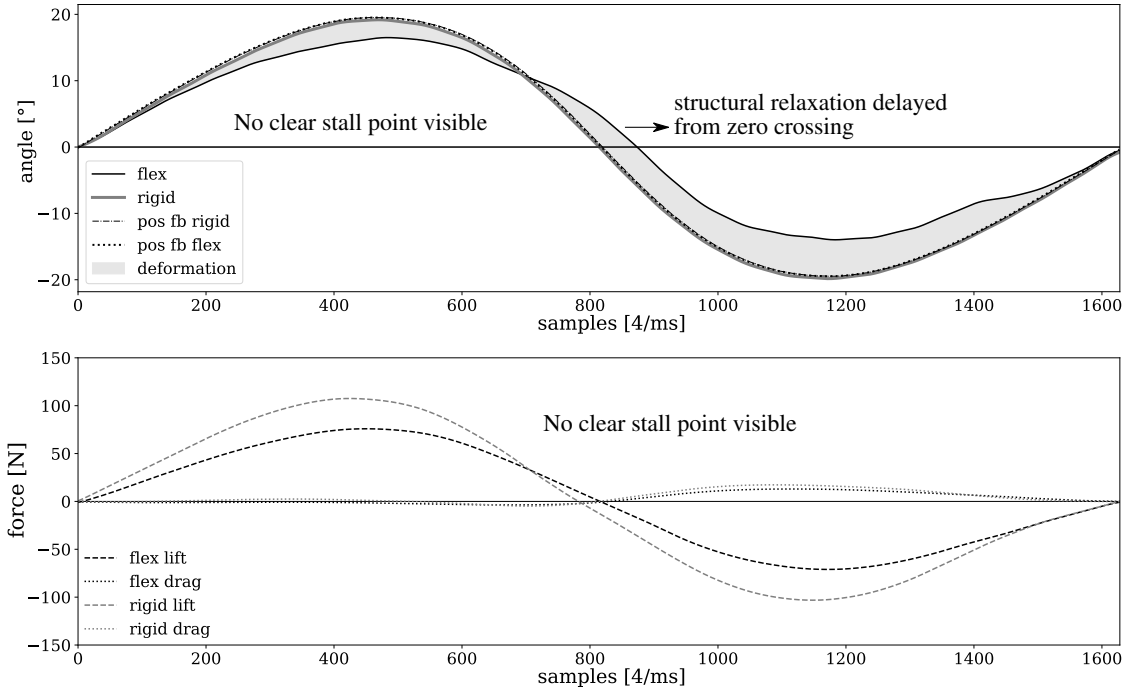

Figure 5.40: Deformation (top) and hydrodynamic forces (bottom) for λ=3 and k_o=0.24

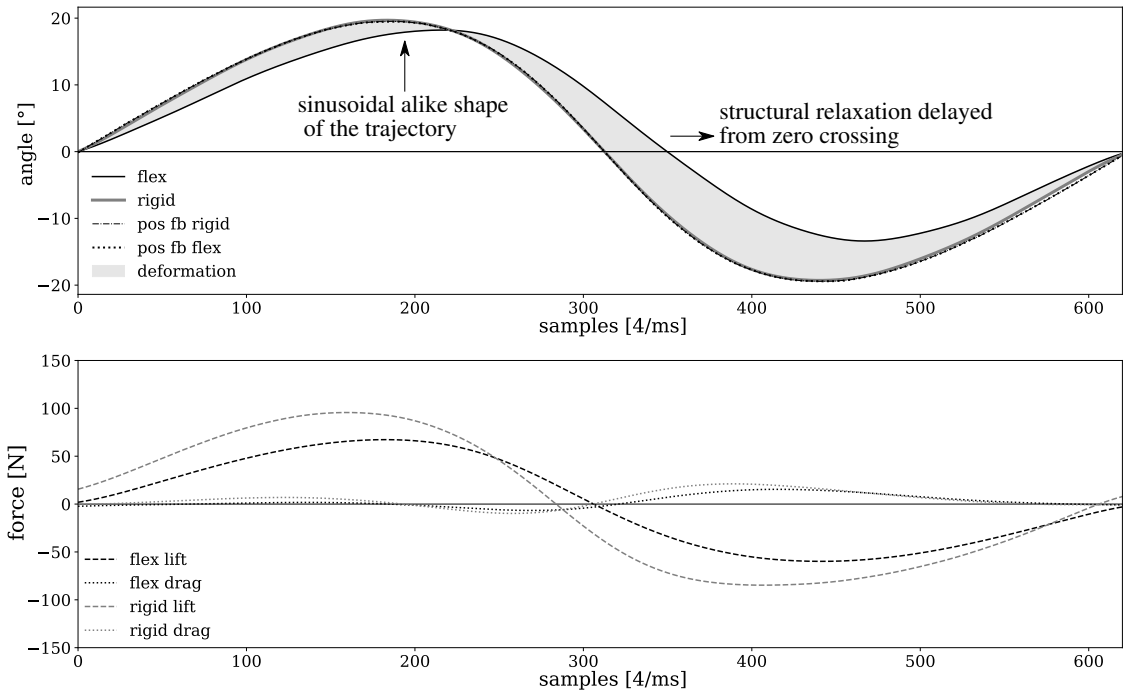

Figure 5.41: Deformation (top) and hydrodynamic forces (bottom) for λ=3 and k_o=0.65

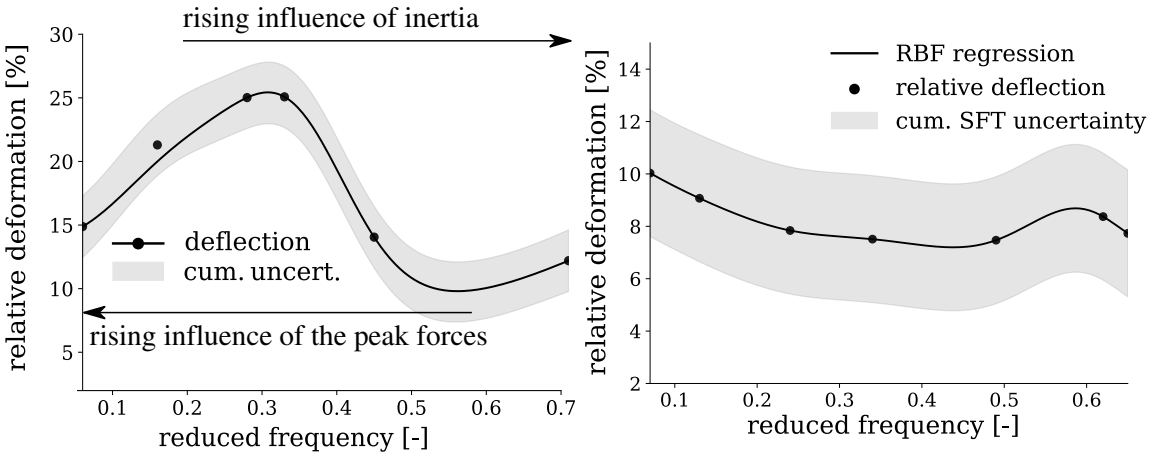

Figure 5.42: Maximum relative deformation plotted as a function of reduced frequency, for λ=2 (left) and λ=3 (right). The deformation is quantified relative to the chord length. Radial-basis functions were used to perform curve regression.

for all hydrofoils. The deformation d is calculated as the maximum height difference between the rigid and the flexible surface at the trailing edge over a period. It is shown as a percentage of the chord length:

$$d = \frac{\max|h_{\text{rigid}} - h_{\text{flexible}}|}{C} \cdot 100\% \tag{5.20}$$

The last 10 pixels (2.4 mm) on the borders were removed in the calculation because of the inaccuracy of the measurement method in these regions.
For λ=2, the deformation has a maximum at k_o=0.31, which also coincides with the BEP of common VAWT. Lower values of k_o result in smaller lift force peaks, which cause smaller deformations. For higher k_o, the structural inertia damps the deformations. Differences between values obtained above $k_o > 0.4$ are in the range of the measurement uncertainty; further measurement data would be necessary to define a reliable trend in this region. For λ=3, the deformation is not significantly influenced by the reduced frequency. The range of measurement values (2.5% deformation) is within the range of the accumulated uncertainty in the SFT measurement itself.

5.3.9 Conclusions of the SFT measurements

The structured-light-based SFT method developed by Takeda et al. 1982 (118) was successfully adapted to the FSI case and implemented in the Python framework *Fluidimage* (66).
An instantaneous surface height with high temporal (4 kHz) and spatial (around 0.25 mm) resolution was acquired. The average uncertainty within the method is 0.66 mm. The method requires only standard equipment in a fluid mechanics laboratory, and provides a credible low-cost alternative to commonly-used Laser interferometer or stereoscopic digital image correlation techniques.
In the present setup, the hydrodynamic forces were captured together with the syn-

chronized SFT measurements. This allows to link hydrodynamic forces with structural deformations. The investigations led to the following conclusions:

1. The structural deformation of the flex[03] profile coincides with the hydrodynamic forces acting on the rigid hydrofoil. This effects are clearly visible at λ=2 and low k_o. They become less significant with rising k_o and λ.

2. The maximum deformation of the flexible hydrofoils depends on the character of the forces acting on the surface, which is dominated by the reduced frequency k_o and tip-speed ratio λ:

   – for low k_o and low λ, the magnitude of the lift and drag forces governs the behavior; the magnitude of the deformation is proportional to those forces;

   – the magnitude of the deformation decreases with increasing k_o once the peak deformation has been reached. There, the inertial forces become dominant over the hydrodynamic forces;

3. The temporal occurrence of the deformation peak within an oscillation period depends on the reduced frequency k_o as well:

   – when k_o is increased, the deformation peak occurrence is phase-shifted to a later point in the period;

   – inertial effects in both structure and flow lead to delay in the relaxation of the structure. They keep the structure bent for a significant part of the period after the zero-crossing of the profile inclination. This happens for high k_o values for $\lambda = 2$ (figs. 5.38) and also for fully-dynamic cases (k_o>0.07) at $\lambda = 3$ (figs. 5.40-5.41).

4. The maximum peaks were found in a range of k_o=0.28 to 0.45. In a three-bladed turbine design, this range corresponds to a solidity of about σ=1 (retrieved from equation 4.1). Such a turbine's best efficiency point is found at λ=2, as shown by Shiono et al. 2000 (116) (see fig. 2.3). It is a common design point for three-bladed H-rotors studied in the literature: e.g., the VAWT investigated by Maître et al. 2013 (91) performs best at λ=2 with k_o=0.35.

The SFT methods presented in this section allow to further characterize the fluid-structure interaction in VAWT. However, a study of the mechanisms governing FSI in VAWT also requires understanding the fluid flow structure. In consequence, the two remaining sections of this chapter will present results obtained from Particle Image Velocimetry (PIV) measurements.

5.4 Particle Image Velocimetry

The instantaneous flow field around the hydrofoil is of high interest in order to understand the influence of the highly flexible structures on the performance of a VAWT. The focus of this study was set on describing large vortex structures and the general flow dynamics. The camera resolution and the seeding density do not allow for an investigation of the boundary layer. This is also a restriction of the applied processing algorithm, which does not feature a specific wall treatment (this aspect is discussed further in sec. 5.4.7). Finally, the wake of the hydrofoil is only captured up to 30 mm downstream of the trailing edge.

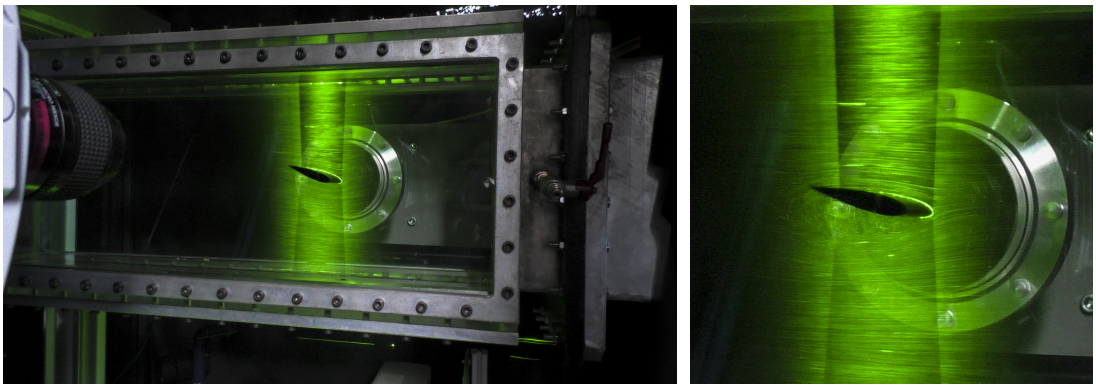

Photos: Nicole Lambert, CNRS/LEGI 2017

Figure 5.43: Laser sheet of the 2D2C PIV measurement with two synchronized Lasers. (Left) The high-speed camera appears in the left of the image. The pathlines of the particles become visible. (right) Detail of the inclined rigid hydrofoil, with flow separation.

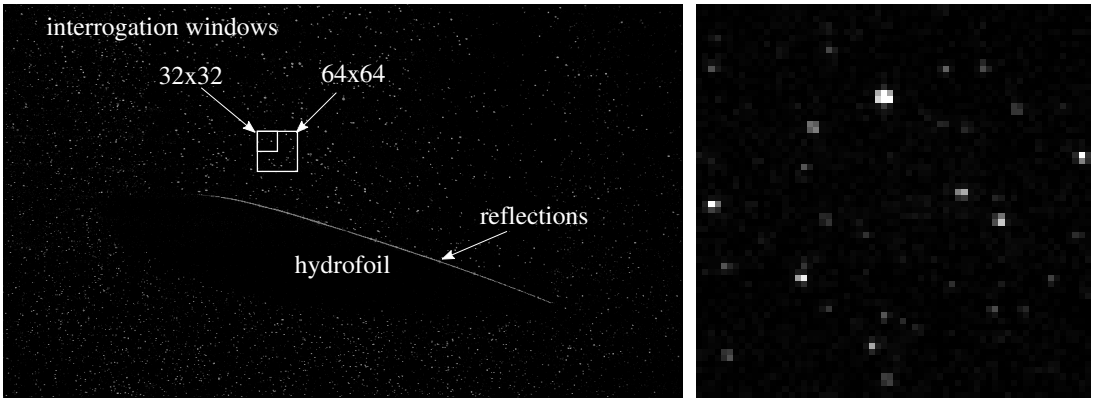

Figure 5.44: (left) Raw image of the PIV recordings (preprocessed). The reflections on the hydrofoil perturb the PIV algorithm and must be eliminated by an adaptive mask. Interrogation windows of size 128x128 (first step) and 32x32 (last step) of the multi-step processing are shown. (right) Arbitrary chosen interrogation window of size 64x64 pixel, with particle pattern for the cross-correlation.

5.4.1 Methodology

Particle Image Velocimetry is a non-intrusive, optical measurement technique. It delivers two- or three-dimensional instantaneous velocity fields of the fluid flow. One (for two dimensions) or several (for stereoscopic or tomographic view) high-speed cameras are used to record the flow in a strongly-illuminated volume or plane. The plane is focused on by the cameras positioned perpendicular (2D) or with defined angles (3D or 3C) to it (see fig. 5.43). The flow is seeded with particles that reflect the light and appear as small illuminated points in the non-reflecting fluid. The result is a grayscale image of the particles (see fig. 5.44).

The measurement method is based on the determination of the displacement of groups of particles from a set of two images acquired in a known (short) time delay, named interval time. Then the particle velocity vectors are recovered using the displacements and the interval time. It is assumed that the particle speed is equal to the local flow speed, which is true with negligible error if both density differences and particle sizes are small enough. An instantaneous vector field of the flow with local velocities can be obtained from the particle speed with negligible error.

No single particle is tracked in PIV. In fact, a cross-correlation of two interrogation windows (one for each image, see fig. 5.44) is performed. This allows to find a matching pattern and to determine the window displacement according to the particles' motion. A single displacement vector is obtained for the group of particles in the window. Both the size of the interrogation window and the overlap between the windows, determine the resolution of the vector field.

Several methods can be used in order to calibrate the measurements and convert lengths in pixels to physical distances. The simplest way, as it was performed in this study, is to compare the pixel distance in one or more images to a known physical distance. In the present case, the length of the rigid hydrofoil was used for calibration. More sophisticated methods use calibration plates which compensate for aberrations from the camera lenses and provide higher accuracy.

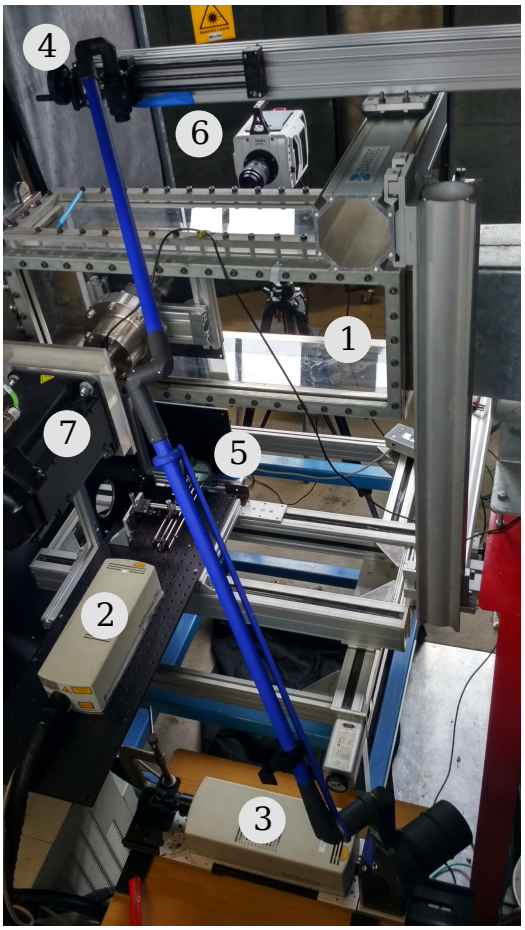

Figure 5.45: PIV setup: Test section (1) of water channel equipped with NACA0018 hydrofoil driven by the servo drive (7) and measurement devices (situated behind the drive system). The 2D2C PIV system consists of two continuous lasers (2 & 3), laser optics and sheet generators (4), (5) and a high-speed camera (6)

A common way to perform PIV measurements is to acquire a set of pairs of two images (double shot) at chosen intervals. In case of turbomachinery, pairs may be acquired for a certain rotor phase angle, and the resulting vector fields can be later phase-averaged over multiple periods. In the present study, the images were acquired with a high-speed camera in a continuous recording, which lead to time-resolved PIV having the temporal resolution of the acquisition rate of the camera. Then, the raw images are evaluated in pairs, pairing images 1-2, then 2-3, 3-4, and so on.

5.4.2 Setup

This subsection contains the PIV setup details. The general experimental setup, including water channel, drive system and data acquisition, has been used for the force measurements and described in sec. 4.2.

The instantaneous flow field was captured with a time-resolved, two dimensional, two-components (2D2C) PIV setup with 4 kHz temporal resolution (see fig. 5.45). The light sheet of 2 mm thickness was built with two continuous lasers placed in parallel and pointing towards each other, in order to remove shadow effects from the hydrofoil. The plane was situated along the X-axis with a negative shift of 0.145 m in the Z-direction (see fig. 4.2 for axes).

Table 5.4: Laser I specifications

Spectra Physics	Millenia	pro 2 SJ
Wave length	[nm]	532
Type		NdYV04
Power	[W]	2

Table 5.5: Laser II specifications

Spectra Physics	Millenia	pro 5 SJ
Wave length	[nm]	532
Type		NdYV04
Power	[W]	5

Table 5.6: Phantom V2511 High speed camera specifications

Resolution	[px^2]	1280×800
Pixel size	[μm]	28
CMOS area	[mm^2]	35.8×22.4
color depth	[bit]	12
focus	[mm]	105
Acquisition rate	[fps]	25,000

Both lasers were placed behind the test section: Laser I was equipped with an optical arm and a sheet generator which enlightened the measurement plane from the top, while Laser II generated the plane with a set of lenses from the bottom. The specifications of the lasers are given in tab 5.4 & 5.5; both were set to 500 mW power. The high-speed camera, a Phantom V2511 (see tab 5.6 for specs) covers a area of 120×74 mm^2 with 1280×800 pixel at 12 bit gray-scale depth. The data was acquired with lens aperture of focus/4 and an exposure time of 50μs. Each recording consists of 16,500 frames, amounting to 4.125 s. The flow was seeded with silver-coated hollow glass spheres of 10μm diameter. The time synchronization of the force measurements and video recording is given by an external trigger signal from a pulse generator.

The PIV measurements were performed with the variation of three parameters:

- the rigidity of the hydrofoil: [flex03, rigid]
- the tip-speed ratio: λ=[2, 3] in form of the shape of the pitch trajectory from eq. (2.3) with corresponding $\alpha_{\max}$=[30°, 20°]
- the reduced frequency k_o, represented by variations of the oscillation frequency f_o, with:
  - $k_o(\lambda = 2)$ = [0.06, 0.14, 0.24, 0.28, 0.38]
  - corresponding to $f_o(\lambda = 2)$ = [0.45, 1.30, 2.25, 2.63, 3.65] Hz
  - $k_o(\lambda = 3)$ = [0.06, 0.12, 0.21, 0.25, 0.32, 0.39]
  - corresponding to $f_o(\lambda = 3)$ = [0.69, 1.32, 2.32, 2.8, 3.64, 4.39] Hz

The variations lead to 22 permutations for flex[03] and for the rigid hydrofoil. Regarding the results of the force measurements only the results of λ=2 and a selection of k_o are presented in the following sections.

5.4.3 Preprocessing and masking

A particular challenge for the present study was the sticking of particles to the silicone body, resulting in agglomerations on the surface. Reflections at the boundaries perturb the cross-correlation algorithm. In the present case, the mask generation becomes a challenging task. The structure is in motion and synchronously deforms, because the rigid body displacement is overlaid by a structural deformation. While the first can easily be predicted by the trajectory of the drive control or the position feedback, no reliable information is available for the deformation of the flexible body. To overcome this issue, a segmentation algorithm was developed to provide an adaptive mask for the PIV raw data. It was realized by Mr. Iring Kösters as part of his work as a student assistant of the author. His work is submitted as a conference contribution to the *20th International Symposium on Applications of Laser and Imaging Techniques to Fluid Mechanics 2020* in Lisbon (72) and is currently under review. The algorithm allowed to recover the shape of the deformed hydrofoil with good accuracy. In consequence, it was decided to use the information of the structural deformation for a cross-section tracking method. The method is shown in detail in a dedicated section and provides details of the generation of the mask and the subsequent use (sec. 5.5). As mentioned, the segmentation algorithm allowed to recover the shape of the deformed NACA0018 hydrofoil with good accuracy (see sec. 5.5 for details). Nevertheless, in raw images, three-dimensional effects artificially "thicken"

Figure 5.46: Mask with thickened tail (grey) to cover three dimensional deformation effects and recognized NACA0018 structure (black).

the area corresponding to the structure, because the hydrofoil deformation is not uniform across its span (in the Z-axis, see the later fig. 6.3 for details). In the view of the camera, which is perpendicular to the cross-section, this results in a thicker dark (particle-less) area, especially near the trailing edge. In consequence, a corrected mask (fig. 5.46), thicker than the NACA0018 geometry, was used as a mask in the PIV processing.

5.4.4 Processing

Fluidimage, a PIV processing framework introduced by Augier et al. 2019 (10) was utilized to perform the PIV processing of the raw data.
A flow chart of the processing, identifying the contributions of the author and of Iring Kösters, is given in fig. 5.47. The process starts with image preprocessing and mask generation, described in sec. 5.4.3. The main processing (the cross-correlation) is performed in a multi-step setup. Starting with 128×128 px^2 and a final window size of 32×32 px^2. In the current state only quadratic interrogation windows are supported. The windows overlap of 50% leads to one vector for each 16×16 px^2 or 1.5×1.5 mm^2 respectively.

5.4.5 Post-processing

In the present recordings, the particle density is relatively low for PIV measurements (see fig. 5.44). This issue could not be resolved even with continuously seeding of the flow. The particles may have sedimented in the two tanks and the reabsorbers of the water channel (see fig. 4.3 for water channel details). The low particle density, in combination with three-dimensional vortex structures in the detached flow result in voids in the images, which themselves result in low correlation values during post-processing. This reduces the accuracy of the result in those areas.

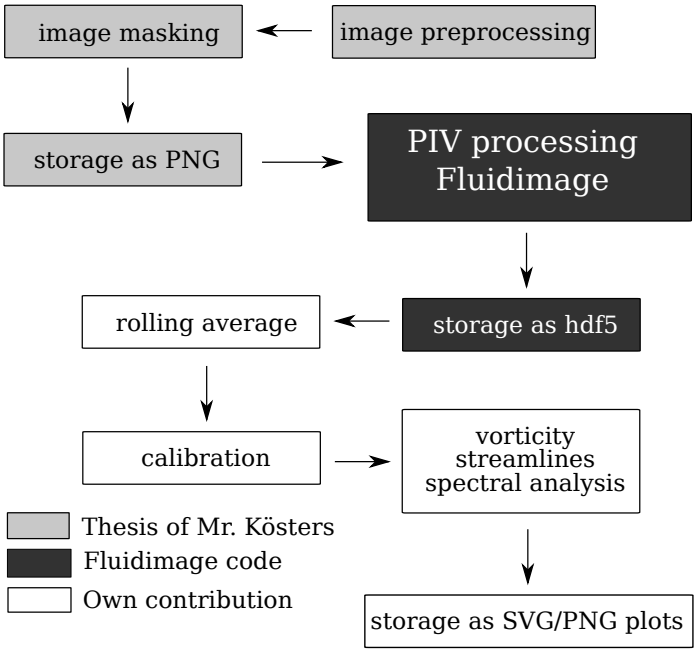

Figure 5.47: The data flow of the PIV data processing, and the contributions of different authors to the work presented here

A correlation peak value of 0.3 was chosen as a threshold during the multi-step process to ensure reliable results. All vectors obtained with lower correlation values were discarded and replaced by the output of a thin-plate-spline (TPS) interpolation algorithm.

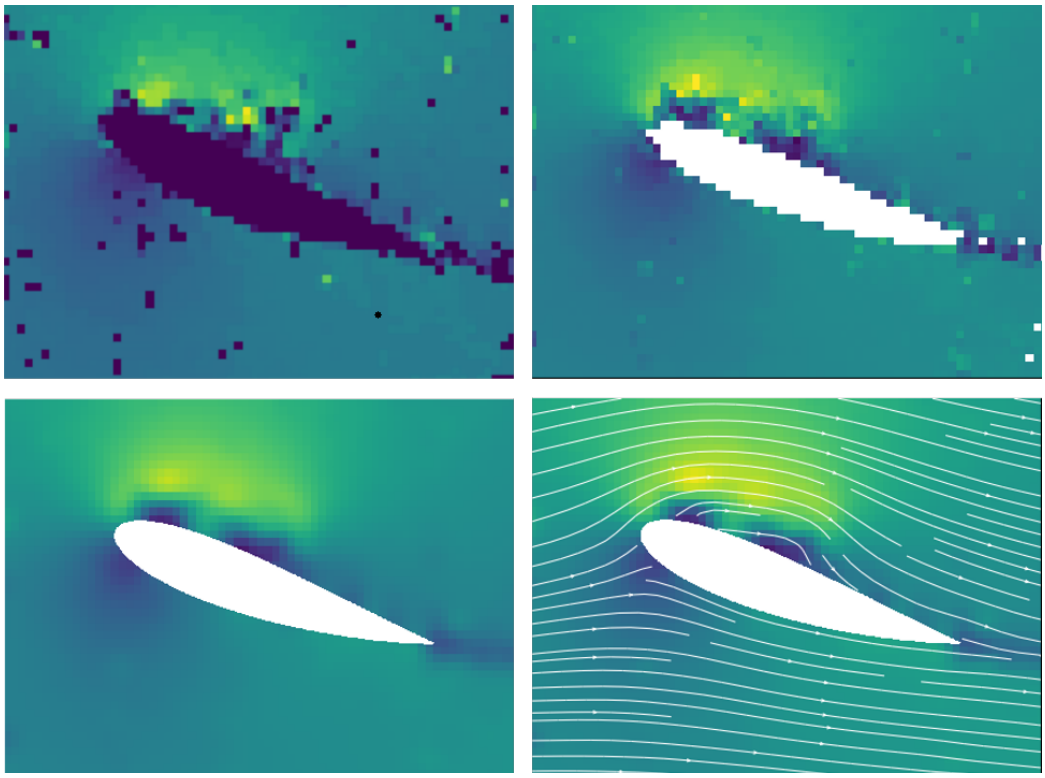

Figure 5.48: (upper left) Raw vector field with magnitude of the pixel shift and empty spaces from low correlation (< 0.3). (upper right) Resulting field after application of the temporal rolling average with window size 4 (lower left) final velocity field, after application of a Gaussian filter and calibration. (lower right) Filtered vectorfield with streamlines: The velocity is displayed as non-dimensional velocity relative to the average flow speed $v/\bar{v}$.

The threshold of 0.3 was also used in the later post-processing of the data (see fig. 5.49). In a first step, the interpolated vectors for each time step were discarded and replaced by *NaN* (see fig. 5.48 (upper left)). The measurement data was oversampled by a factor 4 compared to the force and position measurement with 1 kHz. A time-based rolling average with a window of four frames replaced most of the removed vectors with reliable values from the neighboring time steps (see fig. 5.48 (upper right)). To this effect, the average value of all available velocities in a given coordinate was calculated. *NaN* were sorted out before averaging over the remaining data points. The effects of the rolling average are similar to those of a low-pass filter. This allows to relate the flow field to the force measurements.

In the next step, a Gaussian filter was applied to the field. In order to work around the *NaN* in the velocity field, the filter was applied once for a field containing the *NaN* values, and once for a field with *NaN* replaced by zeros. The division of the second field by the first removes the influence from the zero velocities (a process proposed in an online Q&A article[3](see fig. 5.48 (right)).

[3]For details see https://stackoverflow.com/questions/18697532/gaussian-filtering-a-image-with-nan-in-python

The resulting field does not contain the masked region. A second, NACA0018 foil-shaped mask, generated in parallel to the processing mask during the preprocessing, is applied on the velocity fields.

5.4.6 Software

Fluidimage is a *Python*-based framework for image processing related to fluid mechanics. The code provides tools for PIV and SFT methods (a contribution by the author) and is mainly developed and maintained by Pierre Augier and Cyrille Bonamy from the LEGI lab. The topology of the code allows a massively parallelized computation of the data on high-performance computing (HPC) clusters. Highly optimized and accelerated methods are provided in particular for two-dimensional DFT computations. The code is published under CeCILL-B licence (9). The software does not have a graphical user interface (GUI) and is governed by a *Python* script.

An effort was made by the author to write the output of *Fluidimage* into a VTK structured file. This allows to visualize all results from experiments as well as from the numerical simulations in Paraview, an open source visualization toolkit with special filters for OpenFOAM. The code can be found at the authors code repository (63).

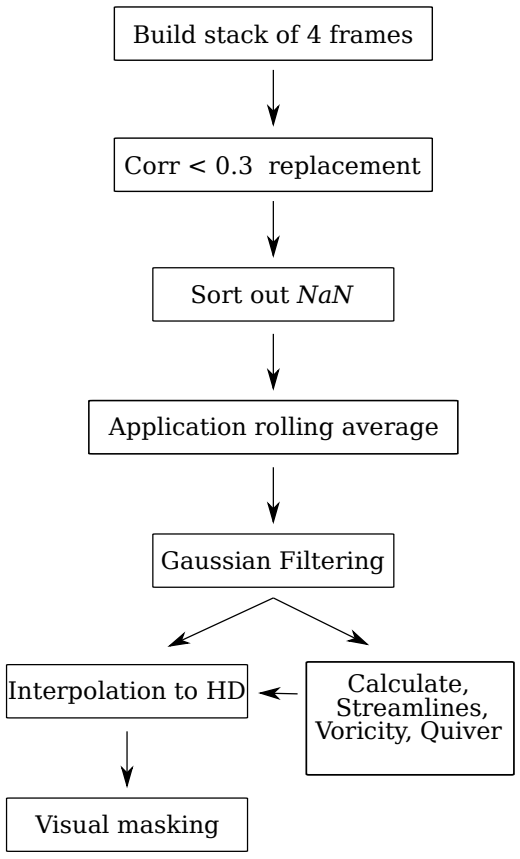

Figure 5.49: The data flow of the PIV data post-processing

5.4.7 Uncertainty estimation

The uncertainty estimation for PIV measurements is challenging. In order to evaluate the reliability of the results, the author decided to compare the results with those obtained with the commercial software solution *DaVis*. The data was processed by Fabio Martins, post-doctoral researcher at OvGU. The adaptive masks described in sec. 5.4.3 were stored as binary PNG files and used in the process. Table 5.7 shows the settings for the *DaVis* and *Fluidimage* software.

The results of the comparison are visualized in fig. 5.50 based on the velocity magnitudes in m/s. The upper part shows the velocity fields retrieved from the two software solutions. The lower parts shows the uncertainty of the PIV measurement obtained from *DaVis*, which is mainly based on the correlation peaks of the cross-correlation. The lower right displays the difference between the two velocity fields.

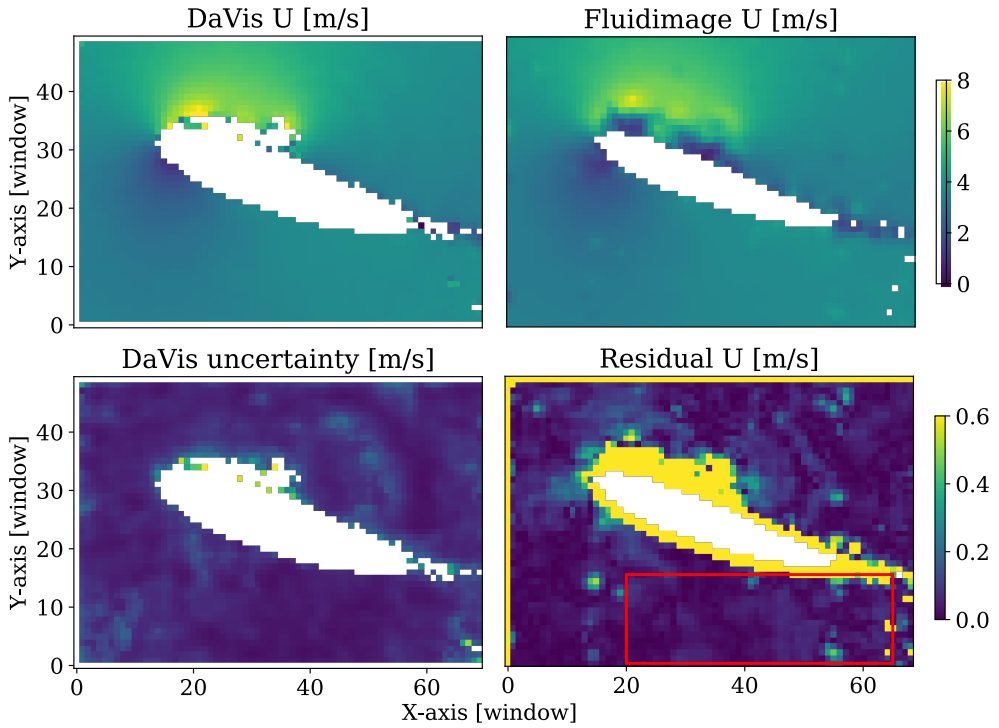

Figure 5.50: (Upper left) Velocity field in m/s obtained by *DaVis*; (upper right) Resulting field from *Fluidimage* with temporal rolling average with window size 4 and a Gaussian smoothing; (lower left) Uncertainty of the PIV measurement in m/s from *DaVis*; (lower right) difference between the magnitudes of the velocities from *DaVis* and *Fluidimage*, in m/s.

Table 5.7: *DaVis* and *Fluidimage* software settings

	Davis		*Fluidimage*	
Denoise	counts substraction	1000	threshold	counts>85%
Vector calculation	time-series	multi-pass	time-series	multi-step
Window size/Steps	64×64	2	128×128	1
Overlap		0		50%
Smoothing	Gaussian weight	1:1	TPS*	
Correction	standard		correl<0.3	
Window size/Steps			64×64	1
Overlap				50%
Smoothing			TPS*	
Correction			correl<0.3	
Window size/Steps	32×32	2	32×32	1
Overlap		50%		50%
Smoothing	Gaussian weight	1:1	TPS*	
Correction	standard		correl<0.3	

*TPS thin-plate-spline interpolation

In fig. 5.50 , it becomes visible that the two software packages have a different treatment of masks. *Fluidimage* sets the masked area to zero velocity. This results in a smearing of the boundaries and produces artificially low velocities at the boundaries of the hydrofoil. This effect is not visible for *DaVis* where the mask seems to be treated explicitly. This increases the reliability of the velocity fields close to the mask boundaries. This specific boundary treatment is not implemented in *Fluidimage* at this stage. The velocity differences were evaluated for a detail (interrogation window) of the vector fields to avoid unrepresentative results resulting from the different mask treatment (red box in fig. 5.50). The maximum was found with 0.16 m/s, the minimum was an outlier with -4.04 m/s. The average difference is about -0.02 m/s, which is less than 1% of the average flow speed.

5.4.8 Results and discussion

The flow described with the PIV is highly dynamic. Videos of the main results can be found at the author's website according to tab. 5.8.

Table 5.8: High speed videos, base address: `https://www.ovgu.de/hoerner/thesis/videos/piv/`

k_o	rigid video	flex[03] video
0.38	rigid_k038.mp4	flex_k038.mp4
0.28	rigid_k028.mp4	flex_k028.mp4
0.14	rigid_k014.mp4	flex_k014.mp4
0.06	rigid_k005.mp4	flex_k006.mp4

The reduced frequency was identified as the crucial non-dimensional number to be kept constant for flow similarity. McCroskey et al. 1976 identified the influence of changes of the Reynolds number in a turbulent flow ($1 \cdot 10^6 < \mathrm{Re} < 3 \cdot 10^6$) to the dynamic stall characteristics to be weak (94). However it has to be considered, that in between the PIV and the SFT setup, the Reynolds number changed from 250,000 to 200,000. The hydrodynamic loads are around 40% higher in the PIV results. A direct comparison of deformation and forces to the flow field is therefore to be considered carefully.
The reduced frequencies for SFT and PIV for each corresponding set are shown in tab. 5.9.

Table 5.9: SFT/PIV couples

k_{SFT} [-]	k_{PIV} [-]
0.33	0.38
0.28	0.28
0.16	0.14

In the subsequent figures, the velocity v is non-dimensionalized with the average incoming flow speed $v/\bar{v}$, the color scale is constant for all subsequent velocity plots and videos from $0 < v/\bar{v} < 2$. Strong variations of velocity are observed near the fully inclined rigid hydrofoil (see fig.5.51 as an example). This effect may result partly from the flow confinement in the test section and is not found for the flexible hydrofoil. The influence of the confinement was discussed in sec. 4.2.1.

The separated flow field appearing above stalled hydrofoils feature complex three-dimensional structures with multiple interacting, sometimes counter-rotating vortices, e.g. for the rigid foil at α=30° for k_o=0.05 (fig. 5.51)

or the flex[03] at α=30° for k_o=0.14 (fig. 5.52). The term wake region is subsequently used for these chaotic structures in the flow field with a fully detached boundary layer, that feature multiple rotating structures. In the two-dimensional recordings, three-dimensional vortex propagation perpendicular to the PIV plane will appear as a spot with high velocities and fast changes of the flow direction over time, e.g. in flex_k006.mp4 at t=2:14 min.

The general mechanisms of foil stall are not in the focus of the present work. The high measurement uncertainty in the boundary layer (see sec. 5.4.7) does not allow for investigations of the propagation of the boundary layer separation in detail. However, observation of the high-speed videos allows to observe that the separation begins from the leading edge, with the appearance of a Laminar Separation Bubble (LSB) and subsequent detachment of the flow.

On the flexible structure, the stall process starts also with a LSB. Then, the flow separation point moves upstream from the trailing edge to the leading edge until it reaches the LSB. At this point, the entire suction surface of the foil features separated flow. A leading-edge vortex is formed, convected over the surface, and then shed. This process is in accordance to the investigations presented by Benton & Visbal 2019 (18) (a video is available as supplementary material).
On the rigid hydrofoil, stall sometimes occurs near the trailing edge without initial separation at the leading edge (such as in k_o = 0.05 or k_o = 0.14). Nevertheless, no reliable data is available that would allow for a definitive characterization of the stall phenomena.

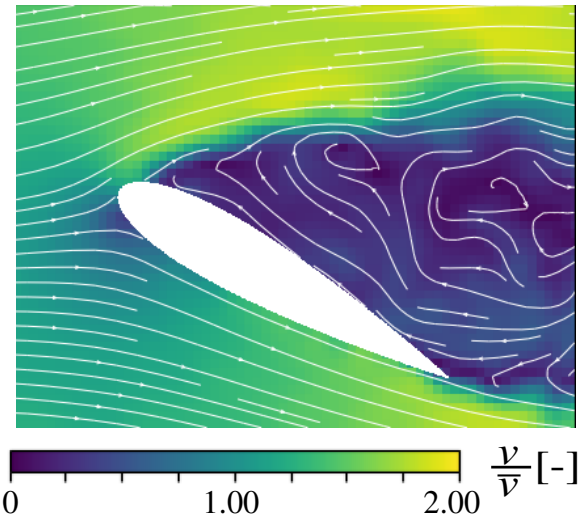

Figure 5.51: PIV: Confinement for rigid hydrofoils at full inclination and low k_o (k_o=0.05, α=30°)

The focus of those investigations is set on the influence of the flexibility and reduced frequency on the flow field. As a starting point, selected phase angles of a period are shown, providing an overview of the bandwidth of the study, once for the flex[03], once for the rigid hydrofoil respectively (see fig. 5.52). From top to bottom, the reduced frequency is increased, starting from a quasi-static state at k_o=0.06, ending up with a fully dynamic state at k_o=0.38.

The influence of the reduced frequency is clearly observed. With rising k_o, the stall inset is shifted to higher phase angles, while the period length decreases. The rigid hydrofoil is fully stalled for 30° at k_o=0.05 (see fig. 5.51). Keeping this inclination angle constant, the amount of the surface covered by the separated region decreases with rising k_o. At k_o=0.38, the flow remains (at least partly) attached, a LSB is found (see fig. 5.53).

At high values of k_o on the rigid hydrofoil, in addition to the phase lag, a

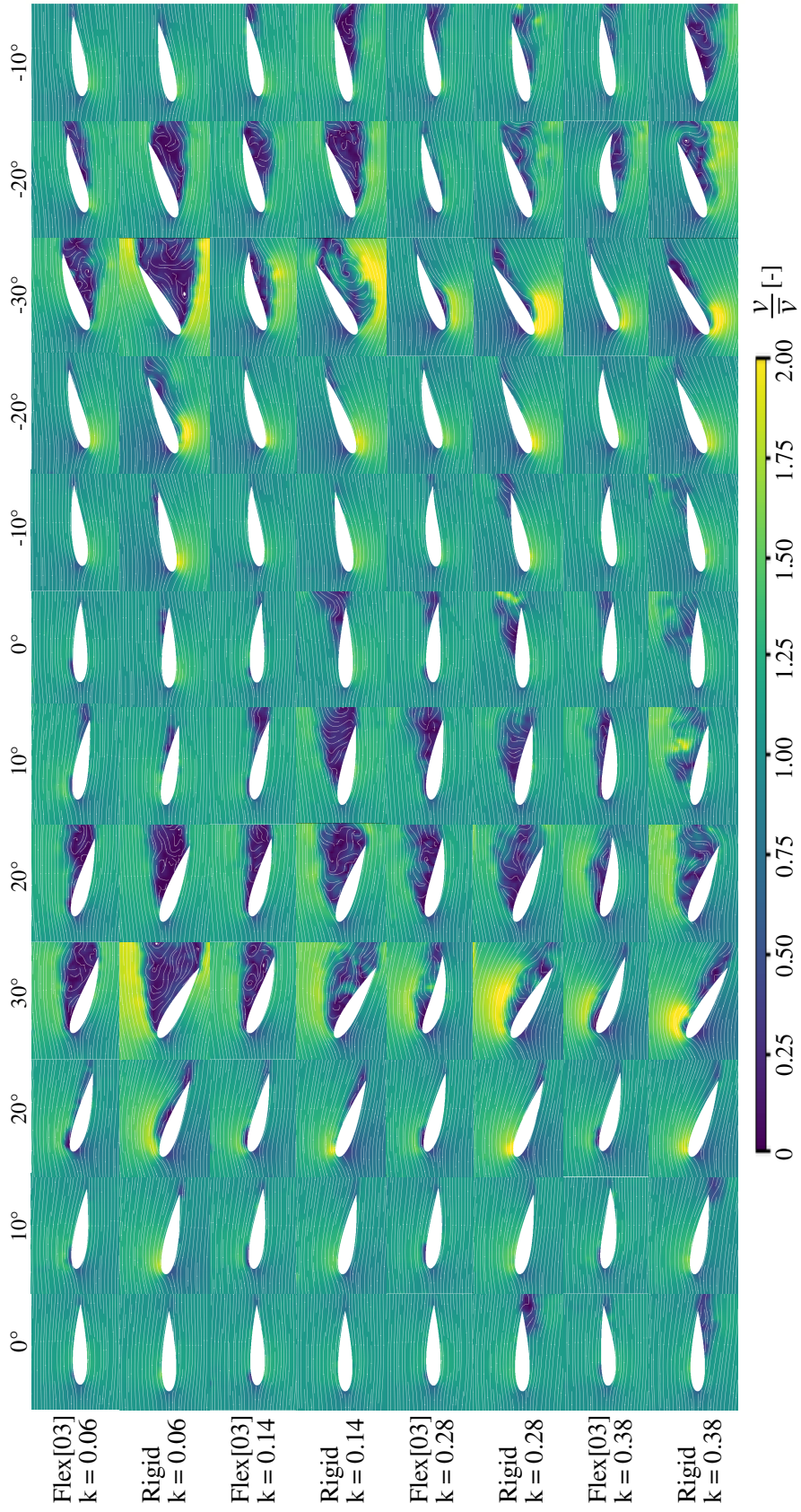

Figure 5.52: PIV influence of k_o: Flow field for selected phase angles for various k_o for rigid and flexible hydrofoils

second effect is that the flow only reattaches for very short parts of the period (see fig. 5.53). This is in accordance to Gorle et al. 2014 and their findings from PIV on a four-bladed VAWT at λ=2 and k_D=0.255 (55).

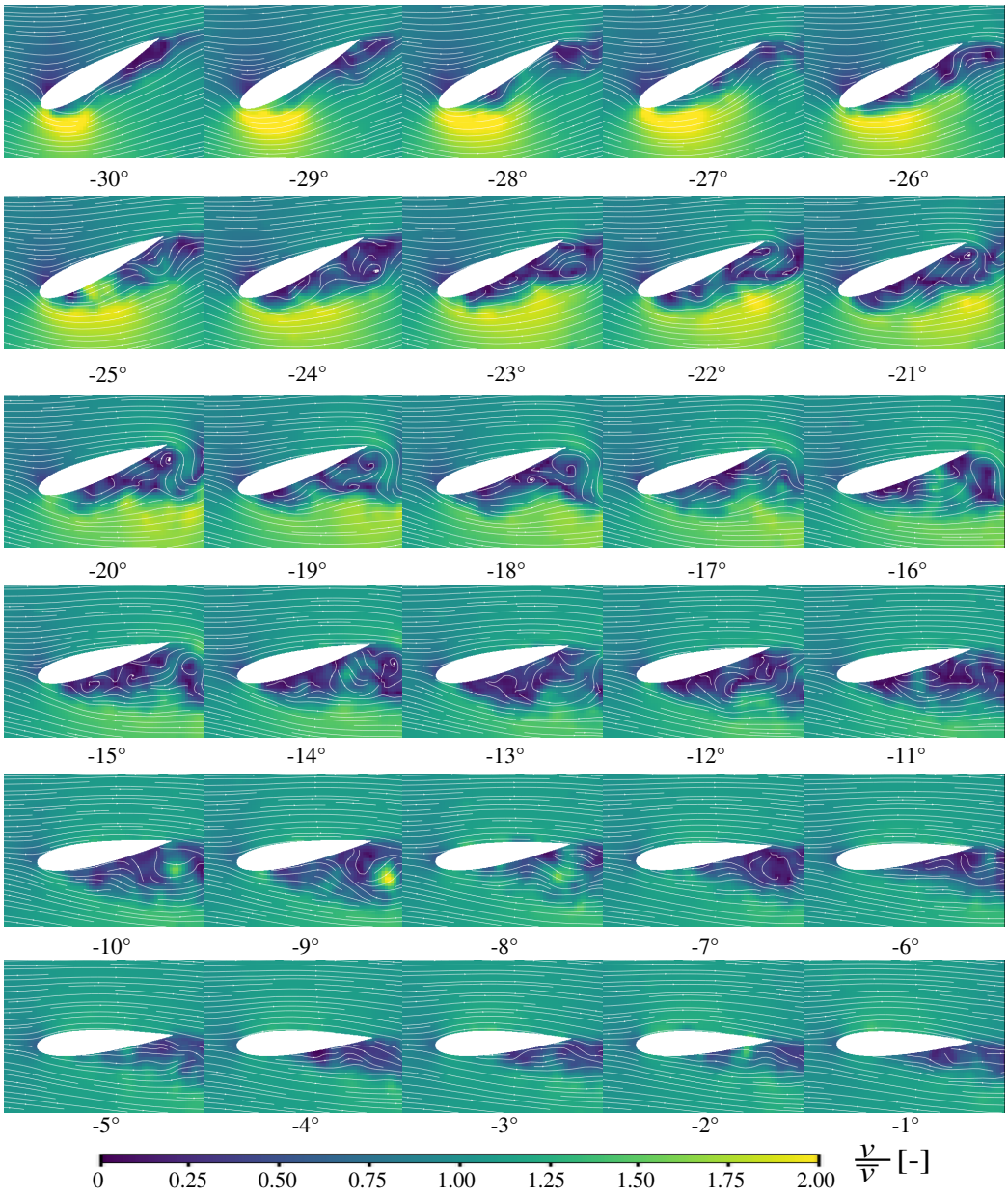

Figure 5.53: Stall on the rigid hydrofoil at $k_o = 0.38$. Three-dimensional, chaotic structures with multiple, partly counter-rotating vortices are found in the separated zone.

The flow reattaches when a specific angle of incidence α_{reatt} is reached. The magnitude of α_{reatt} also depends on k_o. For the quasi-static state this reattachment is found close to the static stall angle. A rising delay is visible along with rising k_o (see fig. 5.53). This effect is stronger for the rigid hydrofoil.

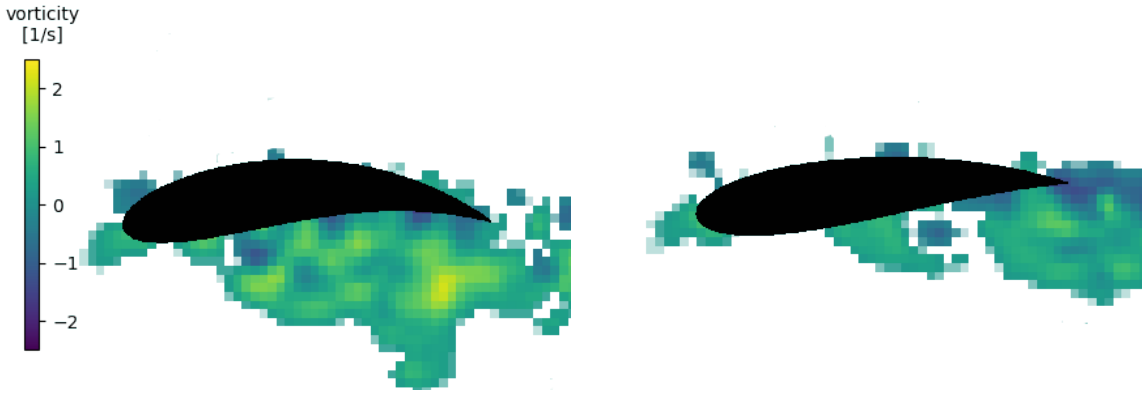

Figure 5.54: Tail flapping: Vorticity field for the flex[03] hydrofoil at $k_o = 0.38$. The flapping of the tail can be related to a vortex shedding. (Left) Vorticity for flex[03], α=-22°; (right) Vorticity for flex[03], α=-14°. The time difference in between the two fields is Δt=18.75 ms

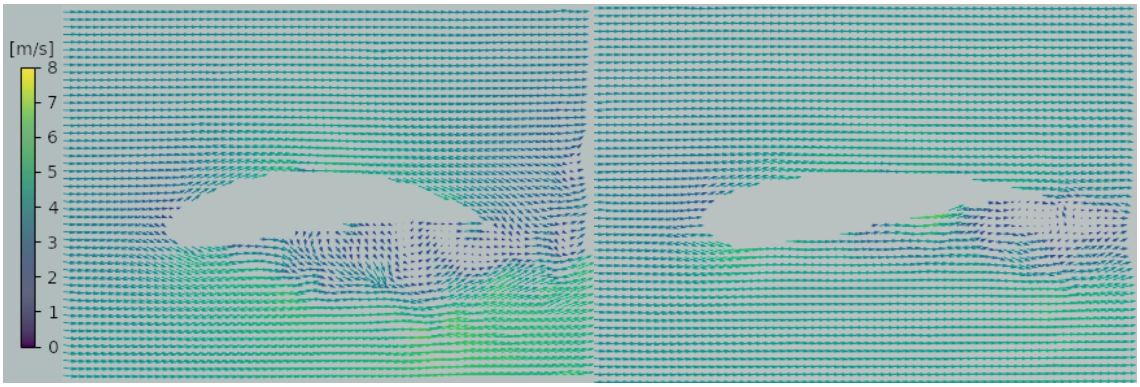

Figure 5.55: Tail flapping: Velocity field for the flex[03] hydrofoil at $k_o = 0.38$. The flapping of the tail can be related to a vortex shedding. (Left) Quiver field for flex[03], α=-22°; (Right) Quiver field for flex[03], α=-14°.

The strongest reduction of the stalled area from effects of the flexible structure and k_o is found for the flexible hydrofoil at k=0.38 in the flow field measurements.

The flapping of the flex[03] hydrofoil is from interest as it shows the dynamics of a strong FSI with large deformations on the flexible blade. The corresponding flow field for a flapping occurrence was investigated with help of a vorticity and the quiver field (see fig. 5.54 & 5.55). A coincidence of the vortex shedding and the flapping can be observed. The pressure differences on the surface deform the stalled hydrofoil. The maximum deformation is reached when the vortex is convected to the tail. The tail deforms stronger with rising distance to the fixation (in cube of the distance of the load application point, for $F = q \cdot l$, see eq. (4.15)). This is the case even if a constant stiffness can be assumed, due to the constant thickness of the carbon structure. When the vortex sheds, the loads disappears instantaneously. The flapping is the structural response.

The strongest flapping effects were found for $0.28 < k_o < 0.46$ (see fig. 5.35-5.37 & 5.42). This is also the design and operation point where foil flexibility is likely to

deliver the highest improvements for the thrust coefficients (see fig. 5.12-5.14).

5.4.9 Conclusions

An instantaneous flow field provides a wealth of information which helps with understanding the hydrodynamic loads and the balance mechanisms of the adaptive structure.
& The setup with two continuous light sources allowed to visualize both sides of the hydrofoil during the period. In consequence, the non-symmetric motion could be measured for the upward and the downward motion simultaneously.
The general dynamic stall process could be visualized in the high-speed videos. The flexible and the rigid hydrofoils display different characteristics, even if the unresolved boundary layer and the high measurement uncertainty at the trailing edge do not allow for detailed investigations. The findings have to be considered carefully.
Geometrical considerations may have suggested that the flow would be mainly two-dimensional; however, the real flow field shows a highly chaotic, three-dimensional flow for the stalled hydrofoils, featuring counter-rotating, small-scaled structures in the separated region and their propagation perpendicular to the main flow.
The flexible blade's ability to adapt to the hydrodynamic loads through deformation leads to smaller wake structures during stall, an earlier reattachment of the flow and shorter phases of detachment during a period. Also a relation between the foil flapping and the vortex shedding could be found.
The influence of k_o could also be shown. The stall inset is shifted to higher phase angles, as is the reattachment of the flow. This leads to long phases with separated flow for periods with high k_o.
Further investigations will be based on spectral analysis (see sec. 6). Subsequently, the flow field will be related to deformation and hydrodynamic loads (see sec. 6.6).
The next section will introduce an alternative method for the deformation measurements, based on the raw PIV data and using the segmentation algorithm of the PIV mask generation.

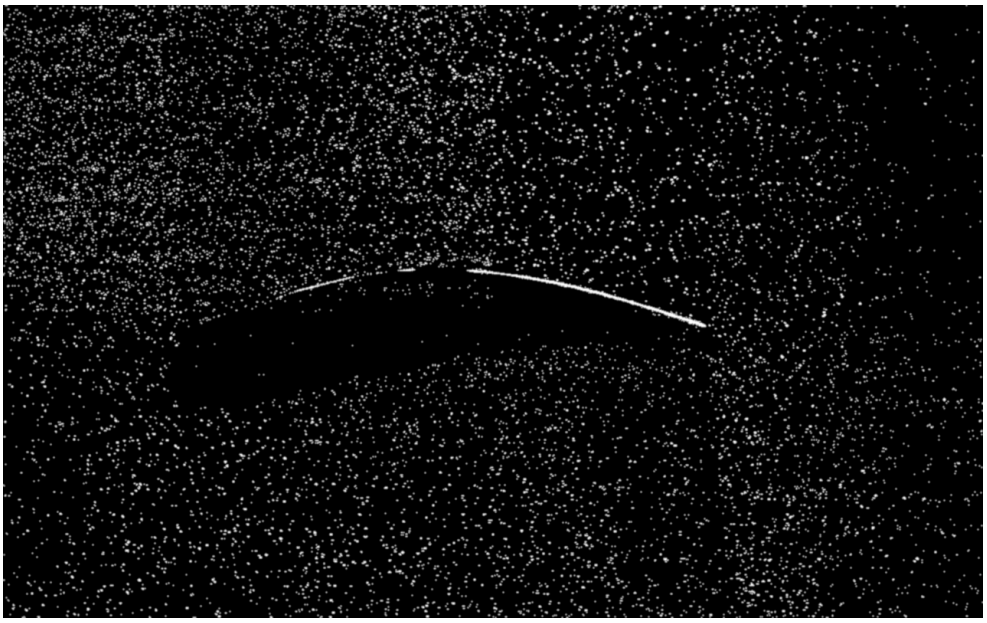

Figure 5.56: A raw image acquired from PIV measurements in the water channel. Particles are visible in white against the black background, with a flexible hydrofoil displayed in the center. The particle density is low due to the particularities of the experimental setup (see sec. 5.4) (particles highlighted for better visibility).

5.5 Structural deformation measurements - Cross section tracking

As mentioned in the previous section, the PIV raw data had to be preprocessed in order to remove the reflections on the hydrofoil surface (see fig. 5.56). The unknown deformation of the structure required an adaptive masking, which was realized with a conventional segmentation algorithm. Due to the good accuracy in capturing of the cross section, the mask was later also used to track the cross section deformation of the flexible hydrofoil.

This tracking method was developed during the bachelor thesis of Mr. Iring Koesters under supervision of the author.

5.5.1 Method

The base data on which the CST is conducted are the raw images from PIV, acquired in a two-dimensional, two-component (2D2C) setup with 4 kHz sample rate. The experimental setup for the PIV has been described in detail in sec. 5.4.
The raw data (see fig. 5.56) features low particle density. The edge of the hydrofoil surface becomes visible as the particles stick on the silicone embodiment; however, these reflecting edges cannot be simply used for identifying the structure position, since they appear only at specific angles, either for the upper or the lower surface. Instead, it was decided to make use of a neighbor-search algorithm that detects regions

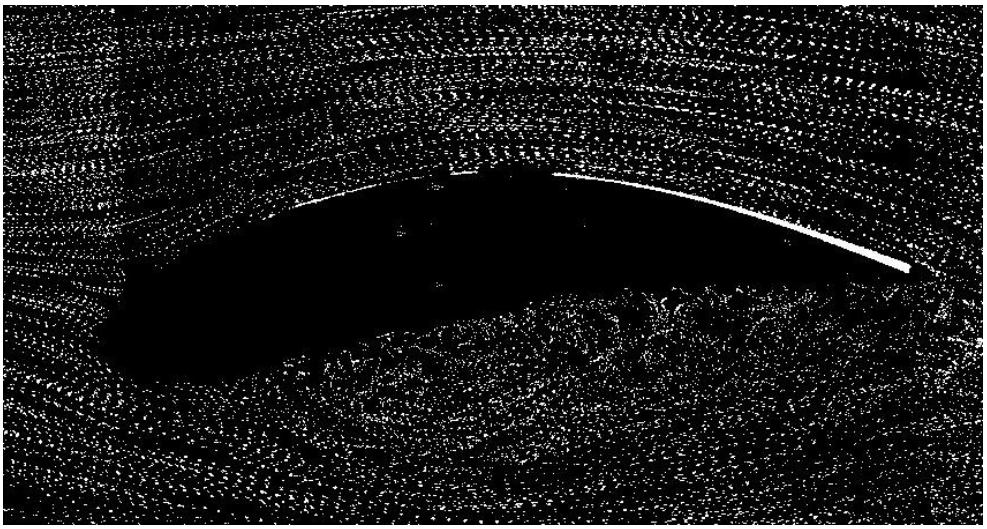

Figure 5.57: Groups of eight raw images from the PIV are summed up in order to achieve higher particle density, before the segmentation algorithm is run.

with sparse and dense particles.

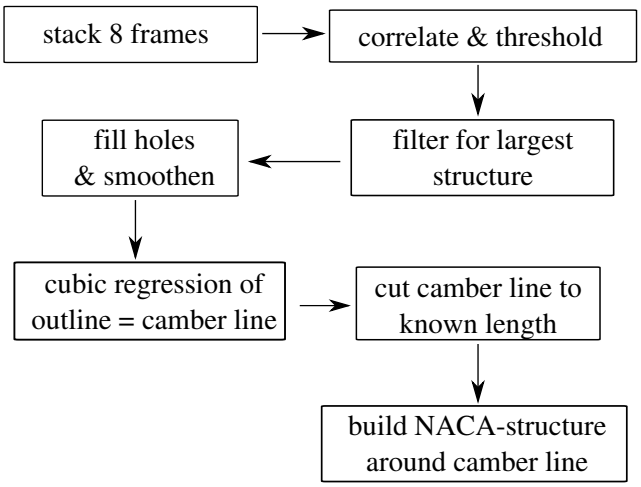

Figure 5.58: Flow diagram of the CST method

In a first step, eight frames are summed up in order to increase the particle density (see fig. 5.57). Given the acquisition rate of 4 kHz, this summation leads to data according to an effective sample rate of 500 Hz. In the next step, after binarizing the image, a neighboring algorithm estimates whether a region (defined by its kernel size) contains particles with use of a correlation kernel. The resulting image (see fig. 5.59 left) allows to identify the structure already, but it does not provide clean edges around it. The correlation kernel size and shape can be found as well. In order to remove artifacts from regions with sparse particles, a filter is applied which seeks for the largest area. Existing holes in the structure are filled, and the outline is smoothed by a dilution function (see fig. 5.59 right). Subsequently the camber line is recovered from the profile. To this effect, the length of the camber line is calculated under two assumptions from the Euler-Bernoulli bending beam theory: 1) that the neutral line of a bending beam does not change its length, and, 2) that the thickness remains constant for the cross sections. A cubic regression of the mid-line points produces the hydrofoil's camber ("skeleton") line. The order 3 is chosen with respect to the deformation of a clamped beam, which depends in third order of the beam length with a single force load (with $F = q \cdot l$ in eq. (4.15)).

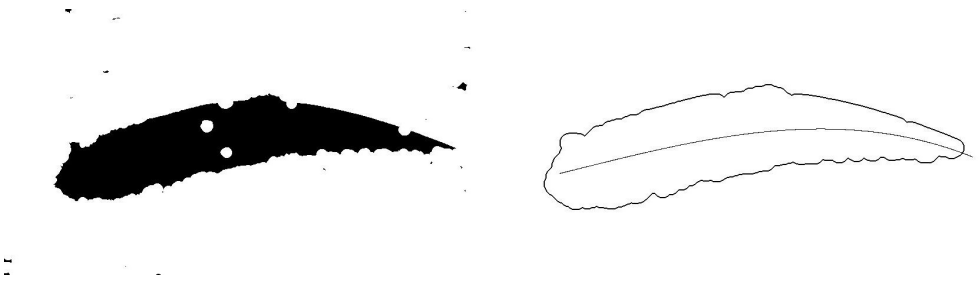

Figure 5.59: Left: A neighbor search algorithm correlates with a moving kernel whether the region contains either particles or not, after binarization with a threshold function. Right: Structure after filtering for the largest region, filling of holes, smoothing of the resulting geometry, and cubic regression of the camber line.

In the last step, the final shape is reconstructed around the camber line, with the thickness (taken as the distance normal to the camber line) distributed according to the NACA foil formulation.

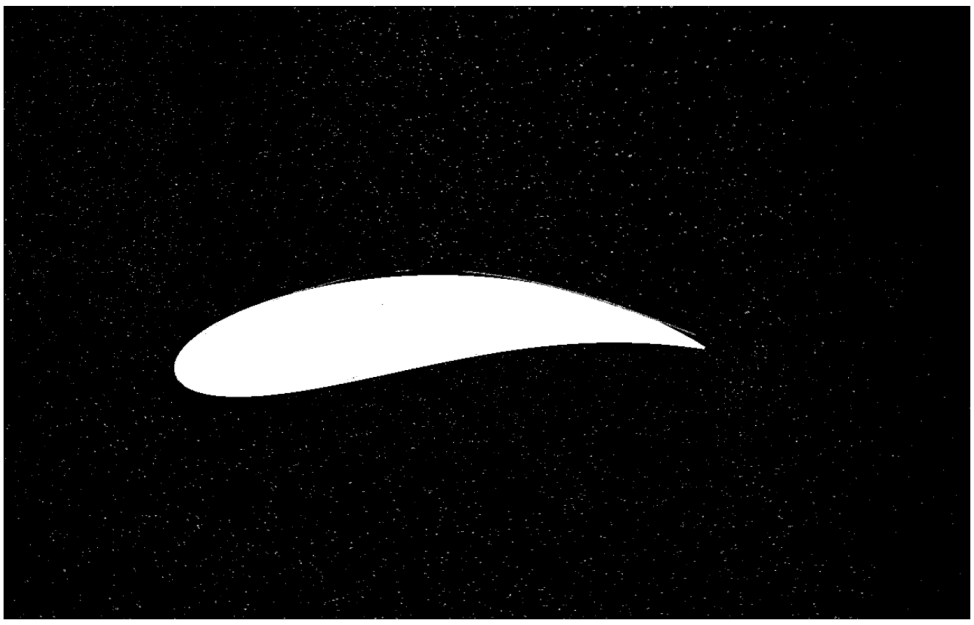

Figure 5.60: The structure retrieved from the segmentation algorithm, embedded in the raw data. The deformed hydrofoil is found with good accuracy. However, because of a phase lag, reflections at the trailing edge become visible in some samples.A video is accessible at the author's website.

Figure 5.60 displays the reconstructed hydrofoil geometry for an arbitrary frame[4]. By visual comparison, the reconstructed structure is found to be in good agreement with the raw data. However, a phase lag becomes visible at the trailing edge, so that the position is not accurately reproduced there. In spite of this weakness, the method is adopted for subsequent masking of PIV data.

[4]A video is accessible on the authors website `https://www.ovgu.de/hoerner/thesis/videos/cst_naca_raw_overlay.avi`

Finally, the camber line obtained in the reconstructed method is used to track the deflection of the hydrofoil in time. To this effect, the angle of deflection β already used in sec. 3.6 and defined as eq. (3.11) is used.

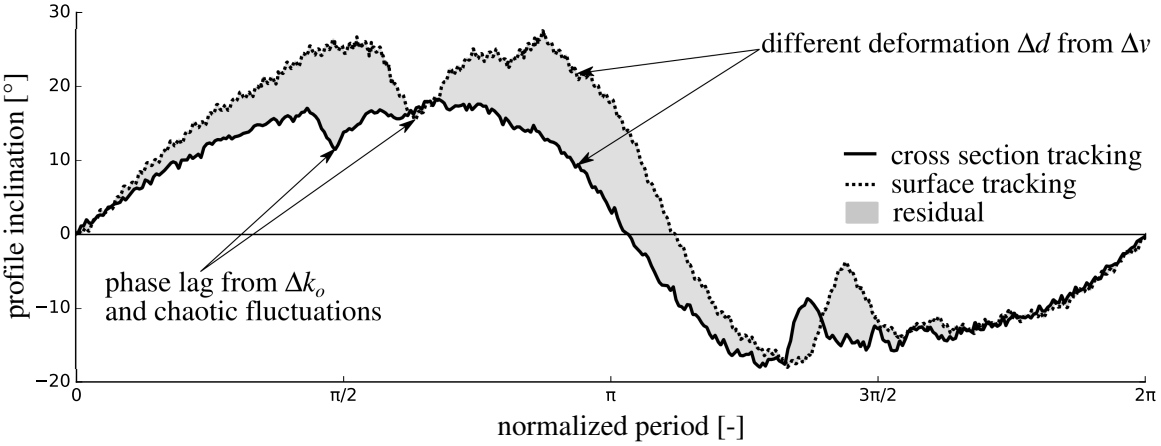

Figure 5.61: Trajectory of the deformation angle β for one normalized oscillation period retrieved with the CST method for k_o=0.14 and with the SFT method for k_o=0.16. Similar characteristics are observed on both curves. However, significant differences in the phase angle and the deformation magnitudes are found. Those can be explained by the differing flow speed and reduced frequencies, as well as by chaotic fluctuations in the flow around the stalled hydrofoil.

5.5.2 Validation

A direct, quantitative validation of the method is not possible in this setup, because no additional deformation measurements were carried out simultaneously to the PIV measurements. The reduced frequencies and flow velocities from the SFT and CST campaigns are different. A qualitative comparison is nevertheless possible based on the SFT measurements, even if they are not directly comparable. The two measurement campaigns were linked by use of the similarity theory as discribed in the PIV section. The comparison of the deformation angle trajectory over one normalized period is performed for a reduced frequency with similar characteristics. This leads to the pairs of measurement data shown in tab. 5.9 and subsequently presented in figs. 5.61-5.63.

The trajectories for β are shown for a normalized period for both methods, with the difference between the curves highlighted as a gray surface. It has to be noted that the forces for the CST measurement are ≈40% higher than for the SFT measurement, due to the increased flow velocity.

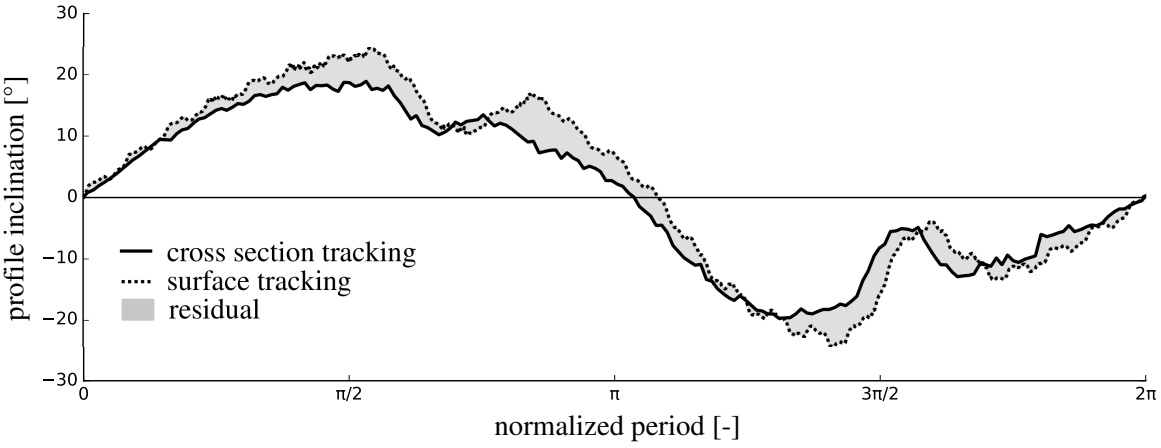

Figure 5.62: Trajectory of the deformation angle β for one normalized oscillation period retrieved with the CST method for k_o=0.28 and with the SFT method for k_o=0.28, in different measurement campaigns at two different speeds.

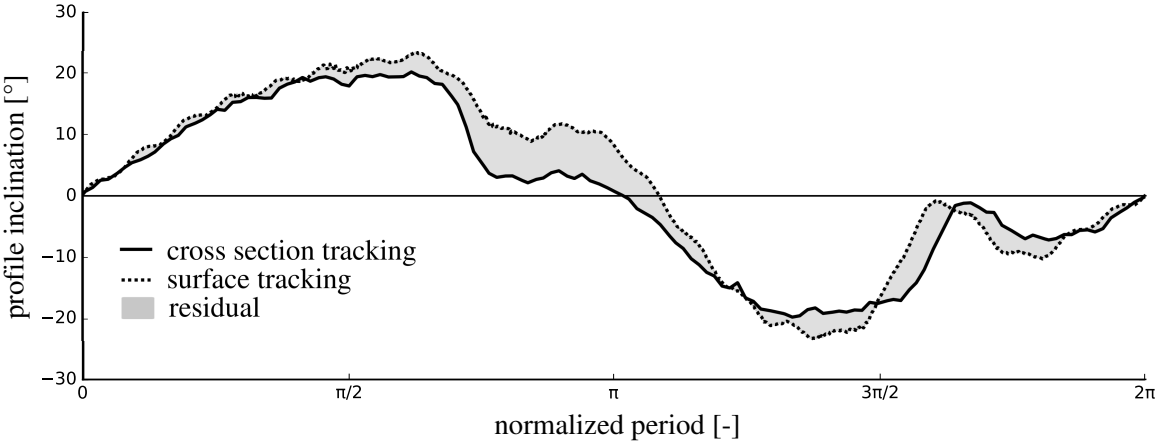

Figure 5.63: Trajectory of the deformation angle β for one normalized oscillation period retrieved with the CST method for k_o=0.38 and with the SFT method for k_o=0.33, in different measurement campaigns at two different speeds.

Furthermore, the flow is partly chaotic when the hydrofoil is stalled, which leads to phase-to-phase differences in the phase angle at which the detached flow structures are shed. Both of those effects, in addition to the different reduced frequencies, may explain differences between results obtained with each method.

In fig. 5.61, the same qualitative characteristics are found for both curves. A lower k_o will result in lower stall angles α_{stall}, as shown in the force and SFT measurements in sec. 5.2 & 5.3. This effect is stronger for lower k_o, as observed.

The couple in fig. 5.62 fits best for reduced frequency (0.28/0.28) as well as for the deformation curves. A small phase lag is visible and a deformation difference. The latter can easily be explained by the higher hydrodynamic loads.
For higher k_o in fig. 5.63 the general shape characteristics are in accordance for both methods. Phase lag and differences in the deformation angles decrease as k_o increases,

which is expected from the previous results of the SFT measurements.

5.5.3 Conclusions of the CST measurements

A method to track the cross section deformation of a flexible hydrofoil was introduced, implemented and published as a *Python* based code under GPLv3 license. It could be shown that the deformation of a flexible structure can be tracked with high temporal resolution from PIV raw images. The results show qualitative accordance to the SFT method presented in the previous section (see sec. 5.3).

The method provides a very interesting alternative to track cross-section deformations in FSI applications compared to other methods, like structured-light profilometry or laser-interferometer. One advantage is the possibility of a dual-use of the masking function for PIV measurements.
The accuracy depends strongly on the seeding of the flow. Higher particle densities are expected to provide better accuracy and would allow a better spatial but also temporal resolution. In future work, synchronous, high-accuracy Laser-Doppler measurements would allow to validate the method and measure its associated uncertainty.

Chapter 6

Post-processing

The dynamics of flexible blades in a VAWT are dominated by the turbine rotation and the FSI at blade level. In the experimental surrogate model, the rotation of the VAWT is replaced by a forced oscillation, which acts as a base excitation of the system. On top of this, a self-excitation can result from the interaction of the structure and the fluid. Self-excitation means that the structure extracts energy from the system (in this case the flow) at its natural frequency, even when the feeding energy spectra is of a different frequency. In the experiments, vibrations were observed in the force measurements for high reduced frequencies. This is an indication for self-excitation.

The subsequent postprocessing has two objectives:

- The determination of the natural frequencies and the modes of the hydrofoils, compared to the spectra of force measurements and position feedback. This should provide information to the origin of the vibrations.
- The investigation of the blade dynamics, in order to distinguish between different mechanisms, such as forced motion and the FSI. In this context, the spectra of the flow velocities and the deformations of the hydrofoil surface are investigated.

The analysis of the dynamics of such complex systems is challenging. The water environment provides damping for the structure and becomes part of the vibration system; its mass shifts the natural frequencies. In addition to the water environment, the system is influenced by the the composite structure of the foils, the forced oscillation, and features self-excitation as well as changes of modes and natural frequencies due to the strong deformations (like a pendulum whose natural frequency depends on the amplitude).

Dujak & Unterluggauer 2018 (41) studied the vibrations of a Francis runner in partial load and added the surrounding water mass in the model equations for a modal analysis of the multi mass system. Hassan et al. 2019 (61) investigated the dynamics and instabilities of flexible structures in a potential flow and linked the normal modes of the structure to the flow field. The already highly complex formulation of their model is still not appropriate to cover the dynamics in a VAWT. In the present study, the vibrations were investigated in three different manners.

The first investigation is a free vibration experiment, in which the water environment is neglected: the foils were studied isolated in air. This allows to measure the foils' natural frequencies; those are used to calibrate the material properties for a numerical modal analysis, which allows to obtain the shape of the modes.

Second, the spectra of measurements are analyzed for foils installed in the water tunnel under static conditions. The static condition allows for an observation of the natural frequencies of the sensor-hydrofoil system, according to the approach shown by Lelong et al. 2017 (81).

Finally, the spectra are analyzed for foils under dynamic conditions. The frequencies observed in the measurements can then be compared with those of the static case. However, it is expected that small deviations will be found.

Once this analysis is completed, the force, position feedback, and deformation measurements are linked to the flow field in a common diagram for four pairs of reduced frequencies.

6.1 Natural frequencies of the hydrofoils

The natural frequencies of the hydrofoils were evaluated experimentally and numerically as part of the Bachelor Thesis of Carsten Laddey (2019) under the direction of C.-T. Weber and the co-direction of the author (74). Yanneck Kiiski further post-processed the data.

In this section, the foils were studied isolated in air. They were clamped at one end to a structure, and their structural oscillations were measured using a laser interferometer (see fig. 6.1).

In a purely experimental modal analysis, displacement must be measured at multiple points, and a measurement grid must be established. This guards against measuring the vibrations at an equilibrium point where no displacement occurs. A further analysis of the frequency response to a bandwidth of excitation frequencies leads to the full spectra of the natural frequencies and allows to distinguish between noise and structural response. In the present study, the experimental data was used to calibrate a numerical model. The hydrofoils were excited with slight strikes at the leading edge, at the trailing edge, and at the tip of the foil. The excitation frequency was below 1 Hz.

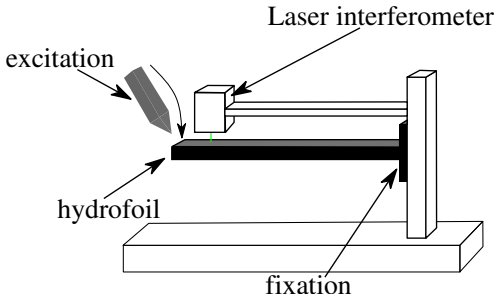

Figure 6.1: Nondestructive experimental setup for the evaluation of the natural frequencies of the hydrofoils

The vibrations of the structure were captured with a laser interferometer (Keyence LK-G5000) with 5 kHz sample rate with a DAC (vendor HBM) with 16-bit discretization (see fig. 6.1 for the setup) at one point. The laser point was placed at the corner of trailing edge and tip of the hydrofoil (with distance of 1 cm from both edges). No

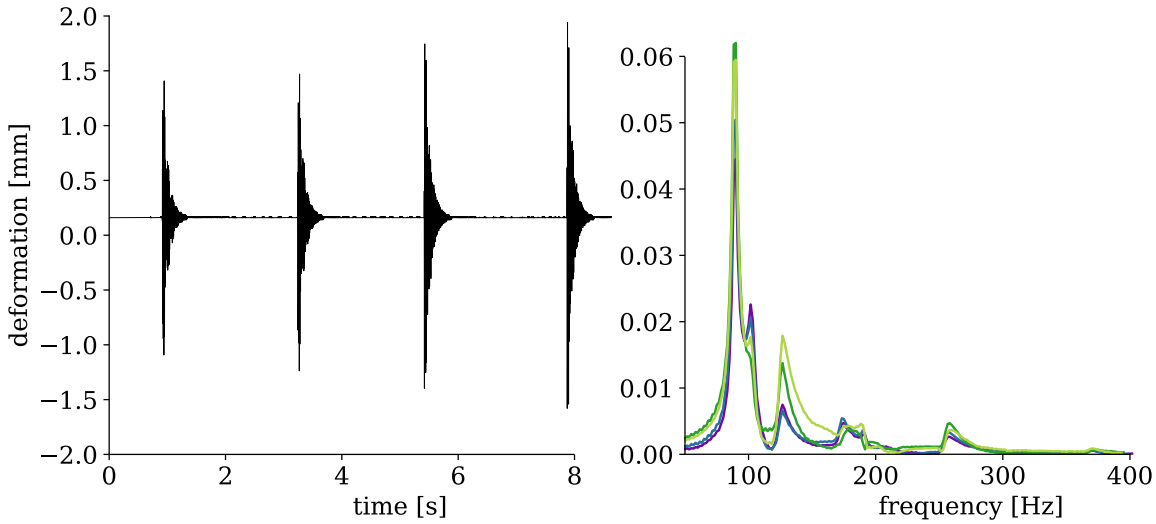

Figure 6.2: Experimental determination of natural frequency: (left) Excitation and vibration of the flex(05) hydrofoil at the trailing edge, captured with a Laser Interferometer. The structure was excited by slight strikes. (right) Spectra of the vibration. The natural frequencies appear as peaks in the spectra.

equilibrium point was expected in this region for the first 6 modes, and this assumption was verified in the numerical model. The strikes were repeated 5-10 times for all hydrofoils. Figure 6.2 (left) displays an example of the free vibrations. Here, the flex[05] was excited with strikes at the trailing edge. It can be seen that vibrations are highly damped, perhaps due to the silicone body.

A Fourier transform was performed to extract the frequencies of the vibrations (see fig. 6.2). The spectral analysis was carried out by self-developed post-processing scripts for each single vibration separately, without application of a window function. A fast Fourier transform (FFT) for the whole measurement, performed with a built-in function of the DAC vendor with use of a Hann window function, showed negligible differences. Only the first natural frequencies are of interest in order to predict the occurrence of an excitation in the water tunnel. Fortunately, the water in the hydrodynamic channel provides damping for the total system, preventing the system from failing due to resonance. Only those frequencies found for all of the excitation points were taken into account.

A modal analysis (for a setup without sensor) was performed with the structural mechanics toolbox *Ansys Workbench*. The experimental data was used in order to calibrate the numerical model. This was necessary in particular due to the remaining uncertainty regarding the foils' material properties (see sec. 4.3.2). The normal modes and the corresponding frequencies of the hydrofoils were calculated. As expected, the simulation showed significantly more modes than were observed during the experiment (see tab. 6.1).
The results for the first and third mode shapes are in accordance with those found in the measurements. It must again be noted that the numerical investigations were performed without the surrounding fluid. Figure 6.3 displays the first and third mode of the flex[03] found in the simulation and in the deformation measurements from the

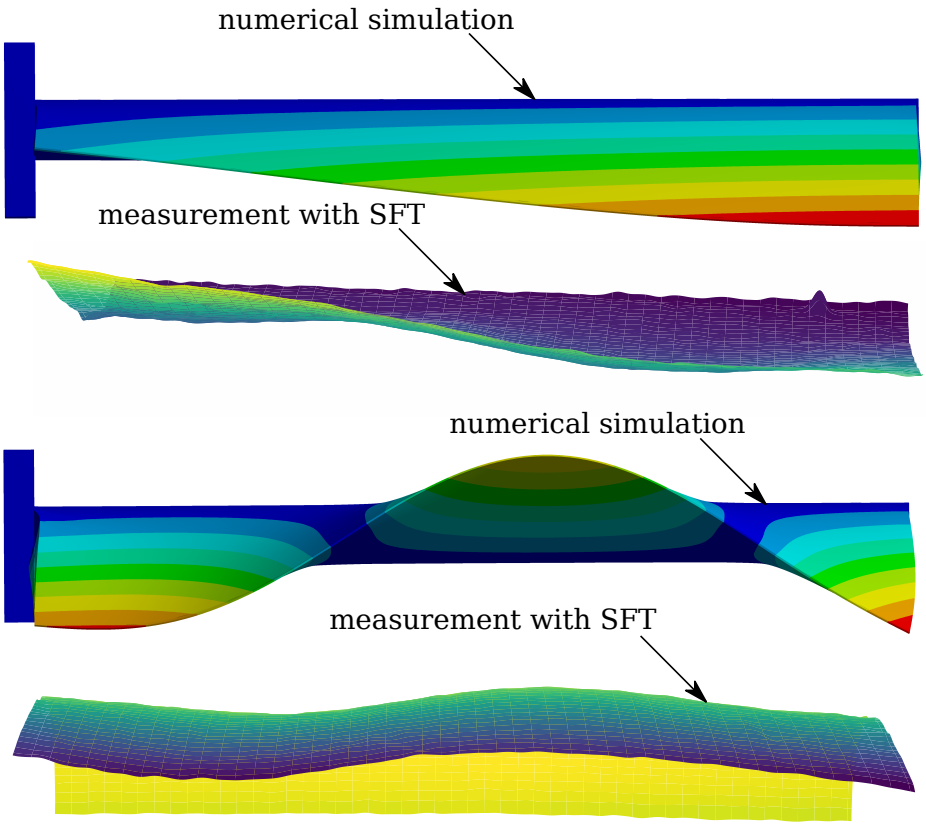

Figure 6.3: First (top) and third normal mode (bottom) of the flex[03] obtained from numerical modal analysis and extracted from the SFT measurement. The second mode was not observed in the measurement. SFT: The surface is the difference of rigid and flexible structure in order to remove the rotation from the result and mirrored horizontally for visual matching. The magnitudes of the deformation in the FEM is exaggerated.

SFT in the water tunnel measurement campaign (see sec. 5.3). The second normal mode was not clearly observed in the SFT results.
In order to extract the normal modes, the surface in fig. 6.3 displays the difference between the position of the surfaces of the flex[03] and the rigid hydrofoils. This allows to subtract the rotational motion from the experiment. The resulting plot was mirrored horizontally to achieve a better visual matching.

The determination of the natural frequencies for the total system consisting of the hydrofoil, the mounting plate and the sensor, which together act like a system of multiple springs and point masses, was performed under same conditions. The sensor was installed in between the fixation and the mounting plate. The sensor stiffness has to be low, because some amount of deformation is required in order to obtain a measurement with the strain gauges in the sensor. In consequence natural frequencies of the multi-

Table 6.1: Natural frequencies of the hydrofoils (from experiment (black) and numerical modal analysis (grey)

Hydrofoil		first	second	third	fourth	fifth	sixth
flex[03] no sensor	[Hz]	53 52	64	87	122	162 160	168
flex[03] sensor	[Hz]	57				150	
flex(05) no sensor	[Hz]	90 86.5	115	167	190 180	240	334
flex(05) sensor	[Hz]	83			160		
flex(07) no sensor	[Hz]	113 114	175	225 218	266	385	460
flex(07) sensor	[Hz]	100 108	186 177	211	271	284	391
rigid no sensor	[Hz]	255 254	895	1493	1658	4049	4892
rigid sensor	[Hz]	98	130				

mass system were significantly lower than those of the single hydrofoil (see fig. 6.4). The results for all hydrofoils with and without sensor are shown in table 6.1. The sensor was modeled as a flexible mount with the stiffness provided by the manufacturers' data sheet. The modal analysis was computationally expensive due to the large deformations from the flexible mount; for this reason, it was only calculated for one foil. The sensor is found to influence the natural frequency f_n significantly, in particular for the rigid hydrofoil, where it results in more than 60% decrease of the natural frequency. The stronger decrease of the rigid compared to the flexible hydrofoils can be explained by its higher mass m. For a single mass-spring system, the natural frequency can be found as:

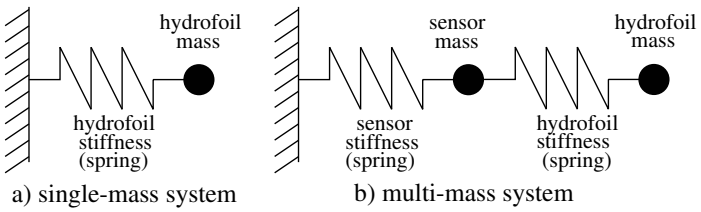

Figure 6.4: Spring mass system surrogate model: (left) the hydrofoil can be modeled as a single spring-mass system (right) the additional sensor leads to a multi-mass system

$$f_n = \frac{1}{2\pi}\sqrt{\frac{K}{m}} \tag{6.1}$$

Only half of the sensor mass is taken into account, since the other half is fixed and mounted on the shaft. This mass is low compared to the hydrofoil's mass as well; additionally, the sensor's stiffness is very low in comparison to that of the rigid hydrofoil. This low sensor stiffness thus becomes a dominating parameter. For the flexible hydrofoils, these effects are less distinct. The stiffness of the flexible foils is lower than the sensor's and also the difference between the weights is smaller. Those trends can be observed in the results presented in tab. 6.1.

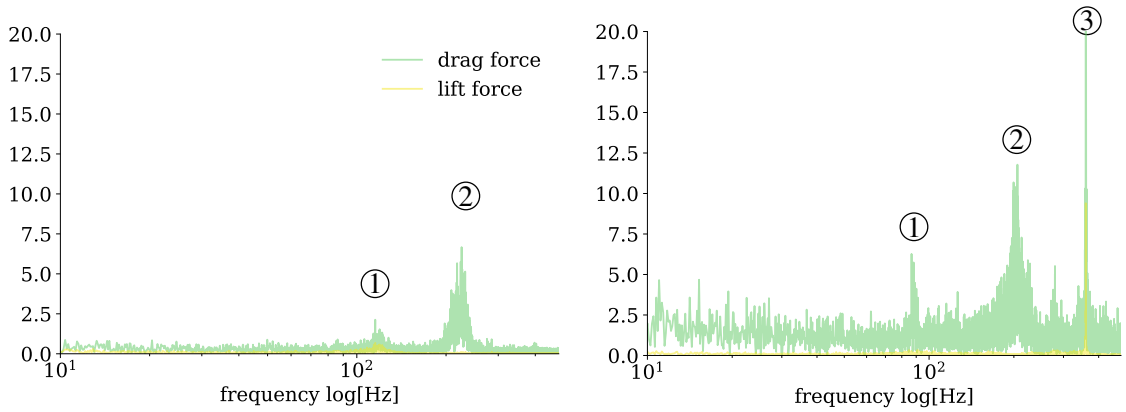

Figure 6.5: Spectra of the static measurements at α=10°: (left) rigid hydrofoil, (right) flex[03].

6.2 Forces and forced oscillations

In this section, spectra of force measurements were first analyzed for foils positioned in the water channel in static positions. The data presented in this section were partly collected by Yanneck Kiiski with use of post-processing scripts built by the author.

The measurement data of the static polar curves (see fig. 4.9) of the hydrofoils were performed for 8 seconds at 1 kHz acquisition rate, which leads to 8000 samples. An FFT of the lift and drag forces was performed for four inclination angles in pre-stall, stall and post-stall conditions for the flex[03] and the rigid hydrofoil at α=[10°, 12°, 16°, 20°]. The spectra for α=10° is shown in fig. 6.5. The natural frequencies are presented in tab. 6.2. A significant frequency shift due to the surrounding water is found for both profiles. Both spectra feature two peaks, a smaller around 100 Hz and a second higher peak at around 200 Hz. The spectra of the flex[03] show additionally a strong peak at 366 Hz.

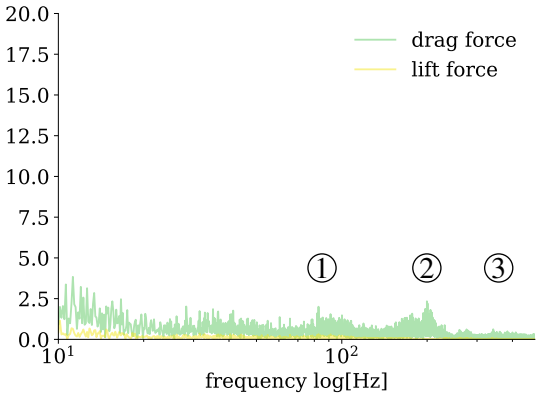

Figure 6.6: Spectra of the flex[03] hydrofoil at α=20°: a strong influence to the amplitudes of the spectra is visible for profile stall conditions. The frequency peaks are attenuated compared to the pre-stall flow spectra in fig. 6.5 (right)

The natural frequencies show only small variations when the angle of incidence is changed. This is in accordance to Lelong et al. 2017 (81). However, as presented in tab. 6.2 an attenuation of the first and third natural frequencies is observed for the flex[03] in stall and post-stall conditions (see fig.6.6). The rigid hydrofoil shows

Table 6.2: Natural frequencies of the hydrofoils from static water tunnel experiments

Hydrofoil		10°(pre-stall)	12°(pre-stall)	16°(stall)	20°(post-stall)
flex[03]	[Hz]	88	87	-	-
	[Hz]	200	201	203	200
	[Hz]	366	361	-	-
rigid	[Hz]	117	118	116	115
	[Hz]	223	223	224	220

similar characteristics for post-stall.

Finally, spectra were analyzed for experiments carried out in the dynamic state. There, they are dominated by the forced pitch motion of the hydrofoils. Vibrations were observed for f_o >3 Hz, in particular on the rigid hydrofoil. A first occurrence of the vibrations is observed for the drag force at k=0.277 and λ=2 (see fig. 5.10). This corresponds to an average oscillation frequency f_o=2.1 Hz and a maximum angle of incidence of α=30°. As foil oscillation frequency is increased, vibrations appear also in the lift force measurements. They display increasing amplitudes and frequencies (see fig. 5.11).

Probable reasons for a later onset of the vibrations for the flexible structures could be the damping exerted by the silicone body or the different mass of the flexible hydrofoils compared to the rigid one. However, the effect of the bending stiffness of the composite blade seems to be most important. As shown in eq. (6.1), the stiffness K governs, together with the mass, the natural frequency. In the results, the rigidity has a higher influence than other material properties: higher vibration amplitudes are found for the stiffer structures. As an example, at k_o=0.45 and λ=2, in fig. 5.11(left), vibrations occur for rigid, flex[07] and flex[05] but not for flex[03]. All flexible hydrofoils are built with the same materials, in consequence, material damping and mass differ only in negligible magnitudes. Only the composite blade rigidity differs.

The spectra of lift (yellow), drag (green) and position feedback of the drive (purple) were calculated with an FFT for each signal, and are presented in fig. 6.7. The different characteristics for the highly flexible structure flex[03] and the rigid hydrofoil are shown at λ=2 and k_o=0.71. For this reduced frequency, strong oscillations were observed for all hydrofoils in drag and lift force measurements.

- Figure 6.7 (left) displays the rigid hydrofoil case. The base frequency from the pitch motion and its first five harmonics in a range of (5.65-28.25 Hz) dominate the spectra. Three further peaks are found in a band of 75-450 Hz, at 112, 170 and 272 Hz. The first frequency in particular is in accordance to that observed in the static curves in fig. 6.5.

- Figure 6.7 (right) shows the spectral analysis for flex[03]. Again the base frequencies from the pitch motion are present. Further peaks in the spectra of the hydrodynamic forces are observed in bands around 80, 165 and 240 Hz. The

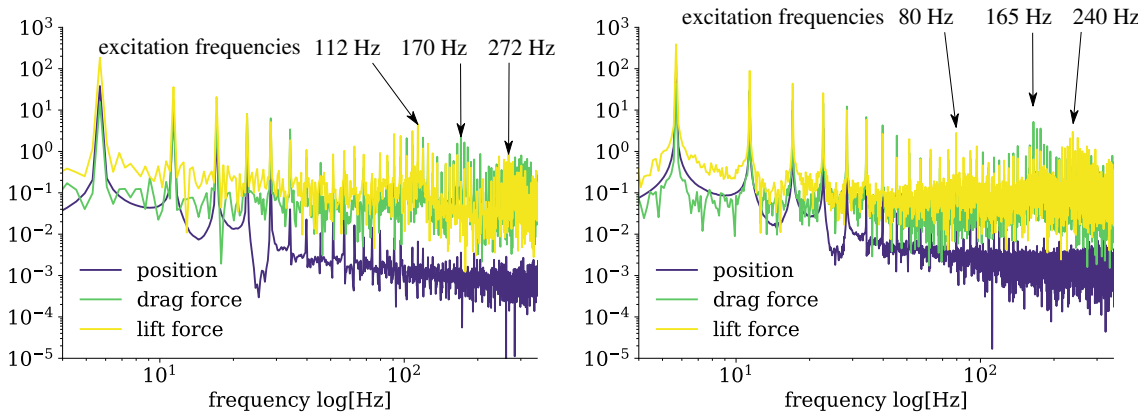

Figure 6.7: Spectral analysis of the lift, drag and position feedback at λ=2 and k_o=0.71 for the rigid hydrofoil (left) and the flex[03] (right). The scale of both axis is logarithmic. The spectra feature, beside the base frequency and its harmonics, three excitation bands for both hydrofoils.

first natural frequency also matches results from the static measurements.

6.3 Deformation measurements

The following results have been partly published in the Journal *Experiments in Fluids* (66). Important contributions to this section were made by the co-author Cyrille Bonamy.
The subsequent findings are based on data obtained at a reduced frequency of k_o=0.46 and λ=2. This corresponds to an oscillation frequency f_o=3.64 Hz for the SFT campaign. A spectral data analysis of the complete deformation field on the surfaces was performed. The spectra were calculated with the following expressions :

$$H_{i,j,m} = \frac{1}{f_c} \sum_{t=0}^{n_t-1} h_{i,j,t} \cdot e^{-2\pi\iota \frac{mt}{n_t}} \tag{6.2}$$

$$H_{i,k,m} = \frac{1}{f_c} \frac{1}{px_{size}} \sum_{j=0}^{n_x-1} \cdot \sum_{t=0}^{n_t-1} h_{i,j,t} \cdot e^{-2\pi\iota \left(\frac{mt}{n_t} + \frac{k_\lambda j}{nx}\right)} \tag{6.3}$$

where $H_{i,j,m}$ is the single-point spectrum value at point $_{i,j}$ at a frequency $\frac{mf_c}{n_t}$, n is the number of pixels $(_{x/y})$ or samples $(_t)$ in the measurement, f_c the sample rate. $H_{i,k,m}$ is the two-dimensional spectrum for a slice at transversal position j for a chord wave number equal to $\frac{k_\lambda}{n_x \cdot px_{size}}$ and the frequency equal to $\frac{mf_c}{n_t}$.
The number of temporal snapshots n_t is chosen to be exactly proportional to the period of the forced oscillation. It avoids the use of a temporal weighting window. In the two-dimensional processing (eq. (6.3)) a Hanning spatial weighting window is applied to the $h_{i,j,t}$ signal in order to limit the spectrum leakage (Prabhu 2014 (108)).

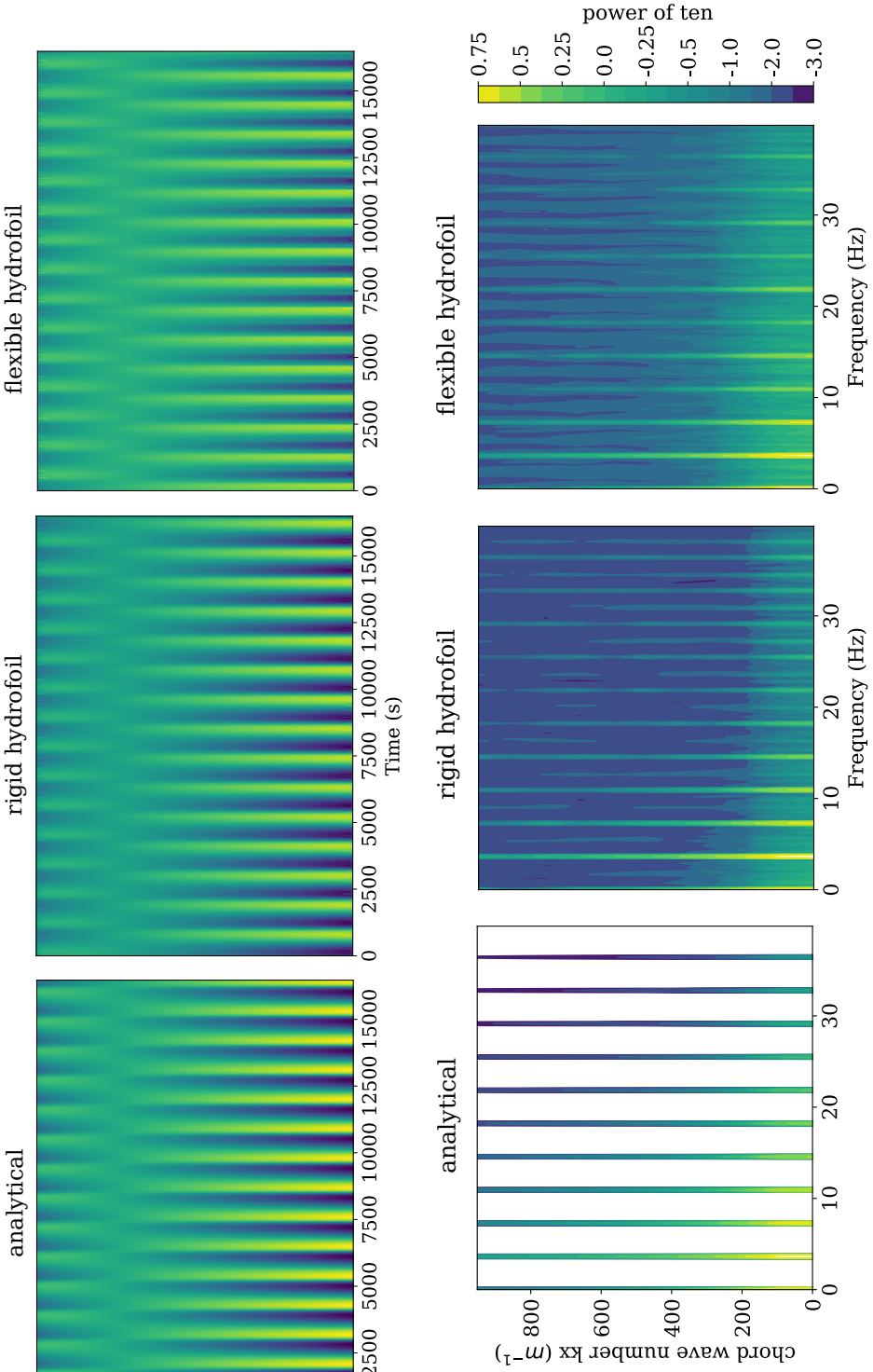

Figure 6.8: (top) Plot of the height of the top surface of the hydrofoil, measured in a mid-span section, and displayed as a function of time. (left) Heights corresponding to the analytical equation for the movement; (middle) measured heights of the rigid hydrofoil; (right) measured heights of the flexible hydrofoil;(bottom) Longitudinal two-dimensional spectra, wave-number over frequency, of the data shown above. (left) analytical; (middle) rigid hydrofoil; (right) flexible hydrofoil. The color levels are equal for all plots. Reprinted from (66)

Then, in a second step, a spectral analysis of the rigid hydrofoil surface is performed from the measured data, $h_{i,j,t}$; both steps are displayed in fig. 6.8. The measured deformations show good accordance with the analytical results in their spectra. The results of the spectral analysis of the flexible hydrofoil are shown in fig. 6.8. The two-dimensional spectra show no resonance in the spatial modes. Indeed, although the spectra of the flexible hydrofoil case are more intense, this can be explained by a response of the flexible structure, there is no specific trace for any kx. However, the two dimensional spectra of the flexible hydrofoil show an attenuation of some harmonics by comparison to the rigid case; e.g. the third and the fifth harmonic (at f=10.98 & 18.3 Hz).

6.4 Flow field

The high-speed recording of the PIV measurements allows for a spectral analysis of the data.

Due to the high acquisition rate and low particle density, low correlation peaks had been obtained in the data processing. A threshold of 0.3 had been set in order to filter out the vectors with high uncertainty. For the data shown in sec. 5.4, a sliding stack of four frames had been used to replace these missing vectors with substitutes obtained by temporal interpolation from an average of the neighboring time steps (see sec. 5.4.5).
This data can not be used for spectral analysis, since it is manipulated in time. The spectra feature complex characteristics, different from low-pass filtered data. This was shown by Viswanathan 2014 (128).

To avoid this issue, the spatially-interpolated fields from *fluidimage* were used in this case. Here, holes in the velocity vector field are automatically filled up with a thin-plate-spline interpolation by the software. In this section the spectral analysis is performed for the PIV data at k_o=0.38, which corresponds to an oscillation frequency of f_o=3.65 Hz. This means that the reduced frequency is different due to the difference in the flow velocity, but similar motion law than for the structural deformation in sec. 6.2.

In fig. 6.9, a velocity field is presented from an arbitrarily-chosen time point. Frequency spectra were calculated for three points in a vertical line 25 mm behind the hydrofoil. The base frequency of 3.65 Hz from the pitch motion is seen to dominate the plots, and its harmonics are visible as well. This is according to the expectation. However, the peaks display different intensities. A two-dimensional FFT was performed in order to investigate the difference in the spectra as a function of the vertical position.

Figure 6.10 shows these two-dimensional spectra of the flow field for the rigid and the flex hydrofoil at k_o=0.38, with frequencies up to 45 Hz. In those diagrams, a point FFT of the fluid velocity is carried out over time for each discrete point in a vertical line 25 mm behind the hydrofoil (the red line in fig. 6.9, containing 49 points). The spectra are normalized using the magnitude of the base frequency (3.65 Hz), the plots have common color levels.

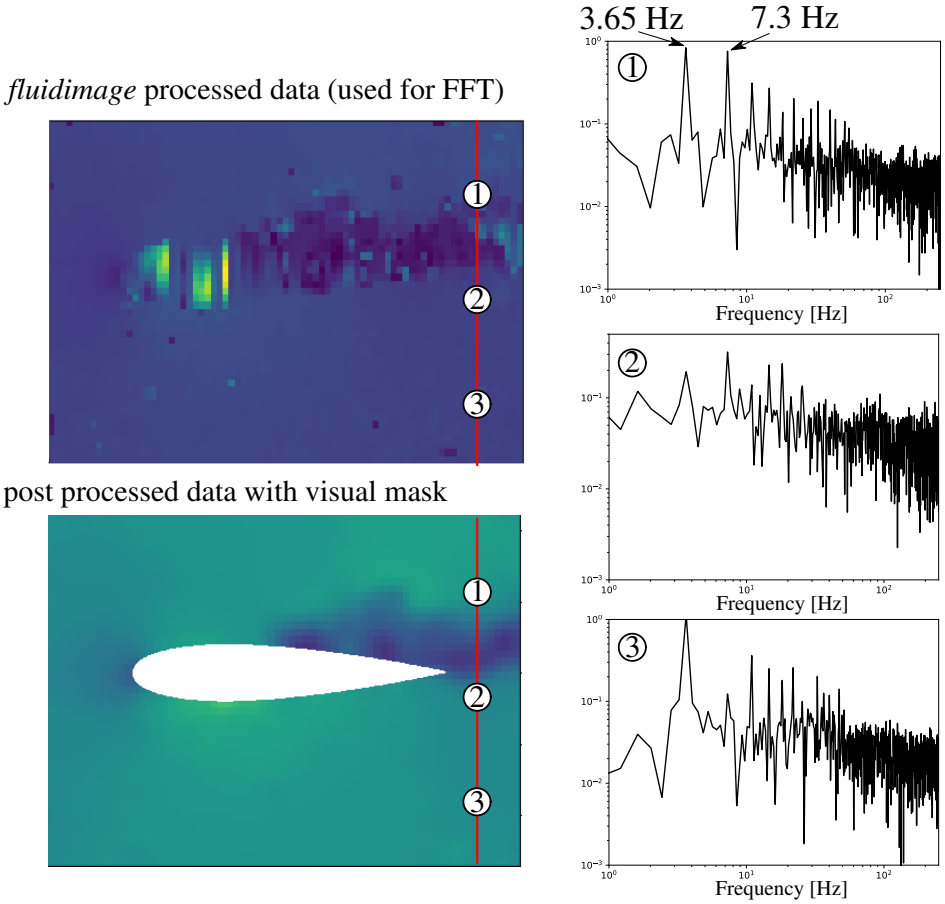

Figure 6.9: Flow field and point spectra for three positions at k_o=0.38 for the rigid hydrofoil. (left upper) Field of the pixel velocity obtained from *fluidimage* with spatial interpolation for missing vectors. (left lower) postprocessed, masked and calibrated relative velocity field; after temporal interpolation and application of a Gaussian filter. (right) Point spectra at three positions 25 mm behind the trailing edge. 1) is situated in the upper third of the flow field. 2) in the middle position and 3) in the lower part third. The point spectra show a maximum peak for the base frequency (3.65 Hz) for 1) and 3). At position 2) the base frequency has a lower amplitude than the first harmonic (7.3 Hz). The red line is the position for the two-dimensional spectra in fig. 6.10.

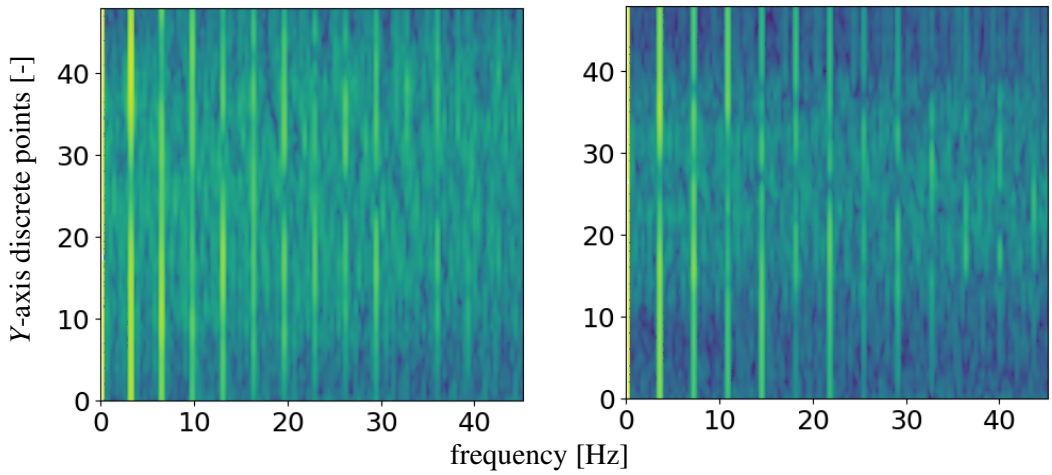

Figure 6.10: Details of the two-dimensional spectra (ordinate in space (Y-axis) abscissa in frequency spectra) of the flow field at k_o=0.38 for the rigid (left) and flexible (right) hydrofoil. On those diagrams, each horizontal line displays the frequencies observed in the flow at one vertical position in the red line shown in fig. 6.9. Frequencies are only plotted up to 45 Hz. Identical color levels in logarithmic scale are used for both plots. The color levels are normalized by the magnitude of the base frequency (3.65 Hz) of the rigid hydrofoil.(Color levels: Yellow is equal to one, dark blue to zero)

For frequencies above 45 Hz, no particular energy peak was found. The base frequency of 3.65 Hz and its harmonics from the pitch motion are dominant in both spectra, which shows the high level of periodicity of the signal.
The spectra of the flow velocities of the rigid hydrofoil show generally higher intensity (i.e., energy). This is expected due to the assumption, that the rigid hydrofoil transmits the pitch motion to the flow efficiently, and provides additional energy to the system. In contrast, on the flexible hydrofoils this effect is moderated by the structural deformation (the flexible hydrofoil shows higher intensity in the surface tracking spectra in the previous section).
Also, the base frequency and its harmonics are attenuated in the middle region of the flow field downstream of the profile. The diagrams are not symmetric around a horizontal mid-line, since the motion law is non-sinusoidal but of a saw-toothed shape.
The flex[03] displays higher intensities in the region situated in the middle of the ordinate (around $15< Y <35$). This is in accordance with the lower deformed inclination angle of the flex[03], which limits the height of the region over which the structure is sweeping. The harmonics are less attenuated in the middle position than for the rigid foil. In general, the spectra are more segmented and asymmetric than those of the rigid. This is expected, since the motion of the flexible structure is much more complex.

In a next step, the spectra of all 49 points in the vertical line (red line in fig. 6.9) were averaged to one single spectra. The results are shown in fig. 6.11 and will be used for further investigations. These spectra are individually normalized using the base frequency. This allows for a comparison of the peak height distribution within

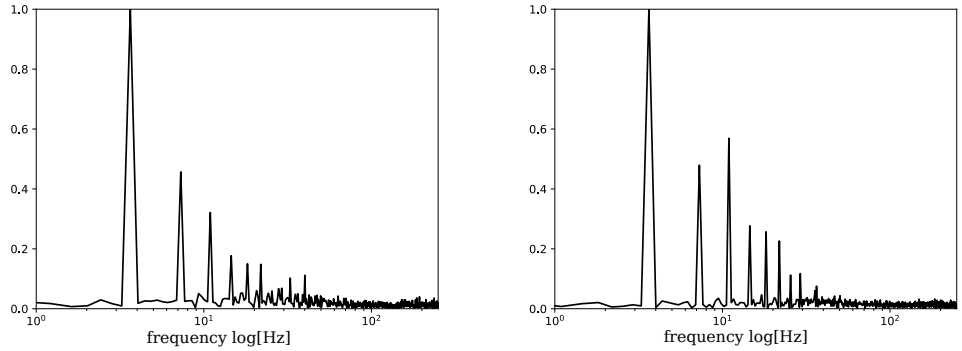

Figure 6.11: Summed point spectra of the flow field for of the 49 points on the vertical line (see red line in fig. 6.9) for the rigid (left) and the flex[03] (right) hydrofoils. The point spectra are summed and subsequently normalized to the magnitude of the base frequency (3.65 Hz).

each plot. On the left, the rigid hydrofoil spectra is shown. The peaks features a continuously decreasing magnitude from the base frequency to the subsequent harmonics. On the right, the flexible structure does not show these characteristics. The second harmonic has higher magnitude than the first.

6.5 Spectra of the fluid-structure interaction

To get further insight, a spectral analysis of all data sources is performed. In fig. 6.12 the point spectra of the FSI are shown for rigid (left) and flex[03] (right). The curves denote:

1. The position feedback angle achieved as a software signal from the drive system. This signal is the base excitation acting on the structure (red solid line);

2. The solid height from SFT for a point near the trailing edge (purple solid line). This signal represents the structural response to base excitation and FSI;

3. The fluid velocities (solid blue line) summed up over 49 points on a vertical line 25 mm behind the hydrofoils (already plotted in fig. 6.9);

4. The lift force from the load cell (dashed yellow line);

5. The drag force from the load cell (dashed green line);

The ordinate values are plotted in linear scaling with amplitudes normalized using the individual values of the base frequency. The abscissa has logarithmic scale to better reveal lower frequencies.

The spectra for the rigid foil (left) show almost perfect accordance between the position feedback and the solid height (the black curve is overlaid by the purple curve). This is expected, as there is only small deformation, and this in fact validates the SFT method. The fluid velocity curve shows multiple peaks, in particular the

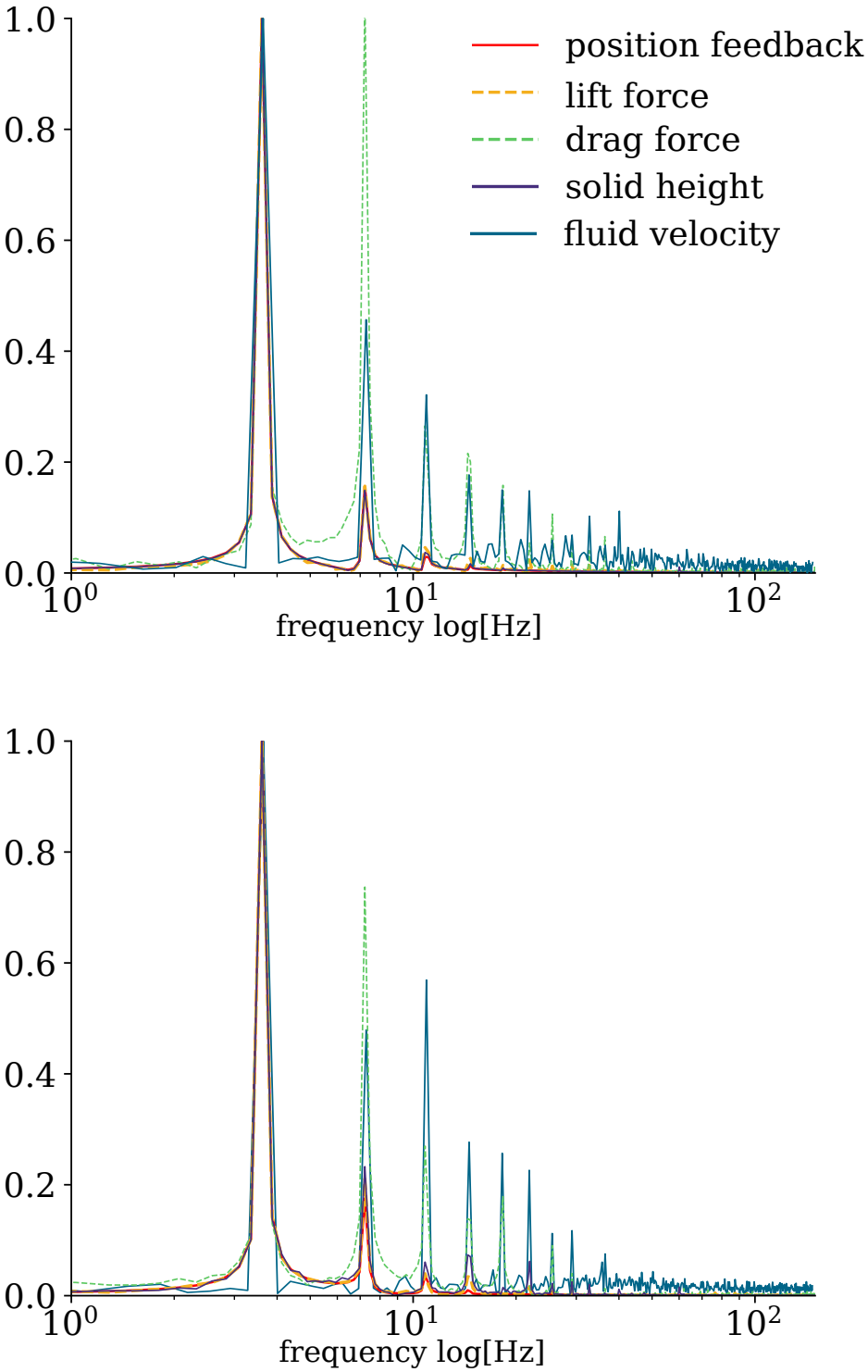

Figure 6.12: Point spectra of the hydrodynamic loads, the position feedback, the surface and the fluid velocities for the rigid (top) and the flex[03] (bottom) hydrofoils. The spectra are normalized using their individual magnitude at the base frequency (3.65 Hz). The solid height point spectra (purple) is generated from the SFT height measurements near the trailing edge (point coordinate Z=875 mm, X=63 mm). The fluid velocities spectra (blue) is summed up over 49 points over a vertical line (red line in fig.6.9).

first to fifth harmonics of the base excitation from the drive system. Similar peaks are found in the spectra of the drag. The drag force features a high peak at the first harmonic. This is a result of the positive drag for both parts of the period. The lift force spectrum is almost similar to that of the position feedback with small increase of the amplitudes in the higher harmonics.

For the flexible structure (right), the spectra of the position feedback show small differences compared to the rigid hydrofoil in the first harmonic of the base frequency. This is considered to be an effect of the different loads on flex and rigid hydrofoil, which have to be balanced by the drive controller. Generally, the flexible structure shows peaks for the same frequencies as they were found for the rigid one. This is expected, since the dominating pitch motion is identical and the harmonics show the periodicity of the oscillations. However, the spectra, in particular for the flow velocity, feature higher amplitudes relative to the base frequency, for all harmonics from the second (14.6 Hz) up to the seventh (29.9 Hz). There, the ratio between the peaks of the flex and rigid foils is around 1.8 (e.g. 0.32 for the rigid and 0.57 for the flex[03] profile at 14.6 Hz, and 0.15 for the rigid and 0.27 for the flex[03] hydrofoil at 21.9 Hz) In order to improve the visibility of the data shown, a detail of the plot is given in fig. 6.13, for a frequency band of 6 Hz $< f_o <$ 40 Hz and amplitudes up to 30% of the base frequency. The plot design is kept the same. The numbers indicate the harmonics, e.g. 1 for 7.3 Hz.

For the rigid hydrofoil (top), the first to the fourth harmonics are visible in position feedback and structural response; higher harmonics are attenuated. Curves for drag and fluid velocity agree for the first four harmonics.
The flexible hydrofoil (bottom) shows more complex spectra. First, a different peak height has to noted for the position feedback at the first harmonic in between flex[03] and rigid profile: the flex[03] profile shows an increased peak of about 15% higher magnitude than the rigid one.
A structural response to the hydrodynamic loads is observed in the first to third and fifth to eighth harmonics: the solid height amplitudes do not follow the position feedback of the drive, due to the deformation of the structure. The fourth harmonic is attenuated, although fluid velocities and drag feature a strong peak there. For the fifth harmonic, no peak can be found either in the hydrodynamic loads or in the position feedback, however, a peak of 7% of the base frequency is found in the solid height and in the fluid velocity spectra.

Analyzing the results, a self-excitation should occur in the natural frequencies of the hydrofoils. The first natural frequencies were determined to be around 117 Hz for the rigid and 88 Hz for the flex[03] hydrofoils. No peaks were found there, which is in accordance to the force measurements. At k_o=0.33 (shown here) only small vibration amplitudes were observed in the corresponding force measurements.

The structural response as well as the fluid velocities and their interplay, the hydrodynamic loads, show significant differences in between rigid and flex[03] profile in the characteristics of their spectra. These peaks for fluid, solid and loads depend on the interaction of the fluid and the flexible structure.

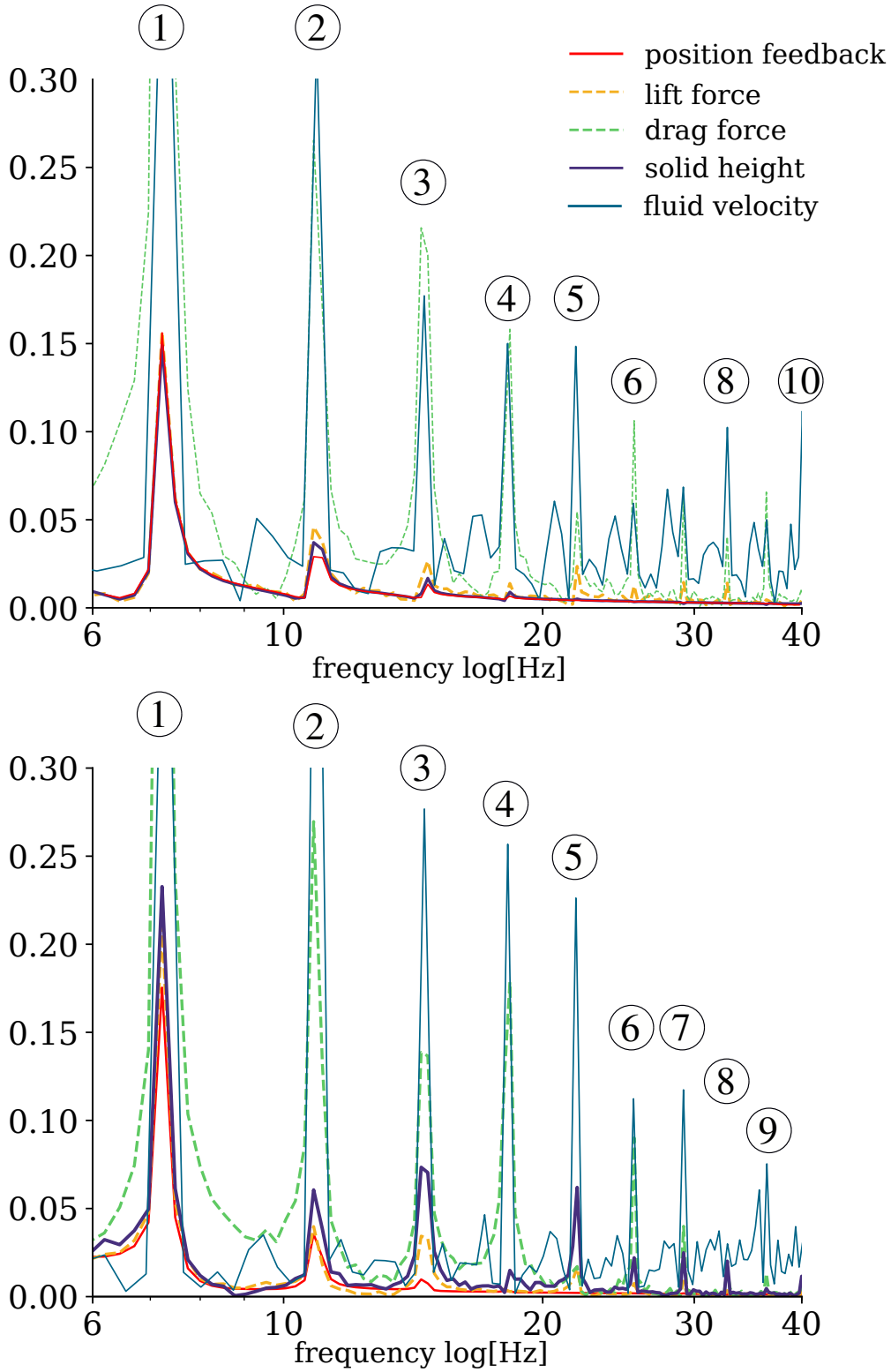

Figure 6.13: Detail of fig. 6.12, with the point spectra of the hydrodynamic loads, the position feedback, the surface and the fluid velocities for the rigid (top) and the flex[03] (bottom) hydrofoils. The spectra are normalized according to their individual magnitude at the base frequency (3.65 Hz). The detail shows a frequency band from 6-40 Hz with amplitudes from 0 to 0.3. The flexible structure shows relative magnitudes in the harmonics which do not match with the base excitation.

6.6 Synopsis of the fluid-structure interaction

The FSI of a VAWT was experimentally investigated with different methods in the previous sections. A measurement of the hydrodynamic loads synchronous with surface tracking was realized. The subsequent high-speed PIV delivered an instantaneous flow field. In figs. 6.14-6.17, the combination of these different findings are shown. The flow fields are presented for selected phase angles in a period, together with deformation and hydrodynamic loads. Images of the flow field are positioned around two diagrams, once for the flex[03] on the upper part and once for the rigid on the lower part of the plot. Their position in the period is indicated by the numbers which can be used to read the corresponding phase angle. The SFT results are shown in the top diagram, i.e. the deformation angle β (black solid line) along with the position feedback (red solid line). The hydrodynamic loads for one normalized period are presented in the bottom diagram. The lift forces (grey solid line) and drag forces (grey dashed line) for the rigid profile are shown, as well as the lift forces (black solid line) and the corresponding drag (black dashed line) for the flex[03]. This plot is similar to the SFT results in fig. 5.33-5.41. Only results for λ=2 are shown. It has to be noted again that the PIV results have been acquired for different fluid velocities but similar reduced frequencies.

As a starting point, the transitional case for k_o=**0.06** in fig. 6.14 is discussed:

(1)-(2) 0° to 16° the deformation increases continuously along with the inclination angle from 0° (0) to 16° (3).

(3) 16° A separation bubble can be found for the flex[03] profile, while on the rigid hydrofoil the boundary layer is separating from close to the trailing edge.

(4) 20° Separation is observed on the upper surface of the flex[03]. A strong acceleration of the flow can be observed above the rigid hydrofoil. The lift forces for the flex[03] reach their maximum.

(5) 23° The flex[03] profile deforms noticeably. A peak is observed in the lift force exerting on the rigid profile. The flow on the rigid foil is fully separated and chaotic structures cover the surface.

(6) 28° The deformation remains constant with vibrations of the tail for the flex[03] profile. The rigid profile is fully stalled, with lift loss and overshooting drag. The flow field shows growing wake structures and strong acceleration of the surrounding flow, a likely result of confinement in the test section.

(7)-(8) 30° to 28° The maximum inclination angle is attained, without significant changes in flow field, forces or deformation for flex[03] and rigid profile. The wake structure for flex[03] grows. It remains large for the rigid profile. Strong drag is measured on both hydrofoils, about twice as much for the rigid profile.

(9) 16° The static stall angle is reached again. The flex[03] shows a reattached boundary layer with only small parts of the trailing edge detached. The defor-

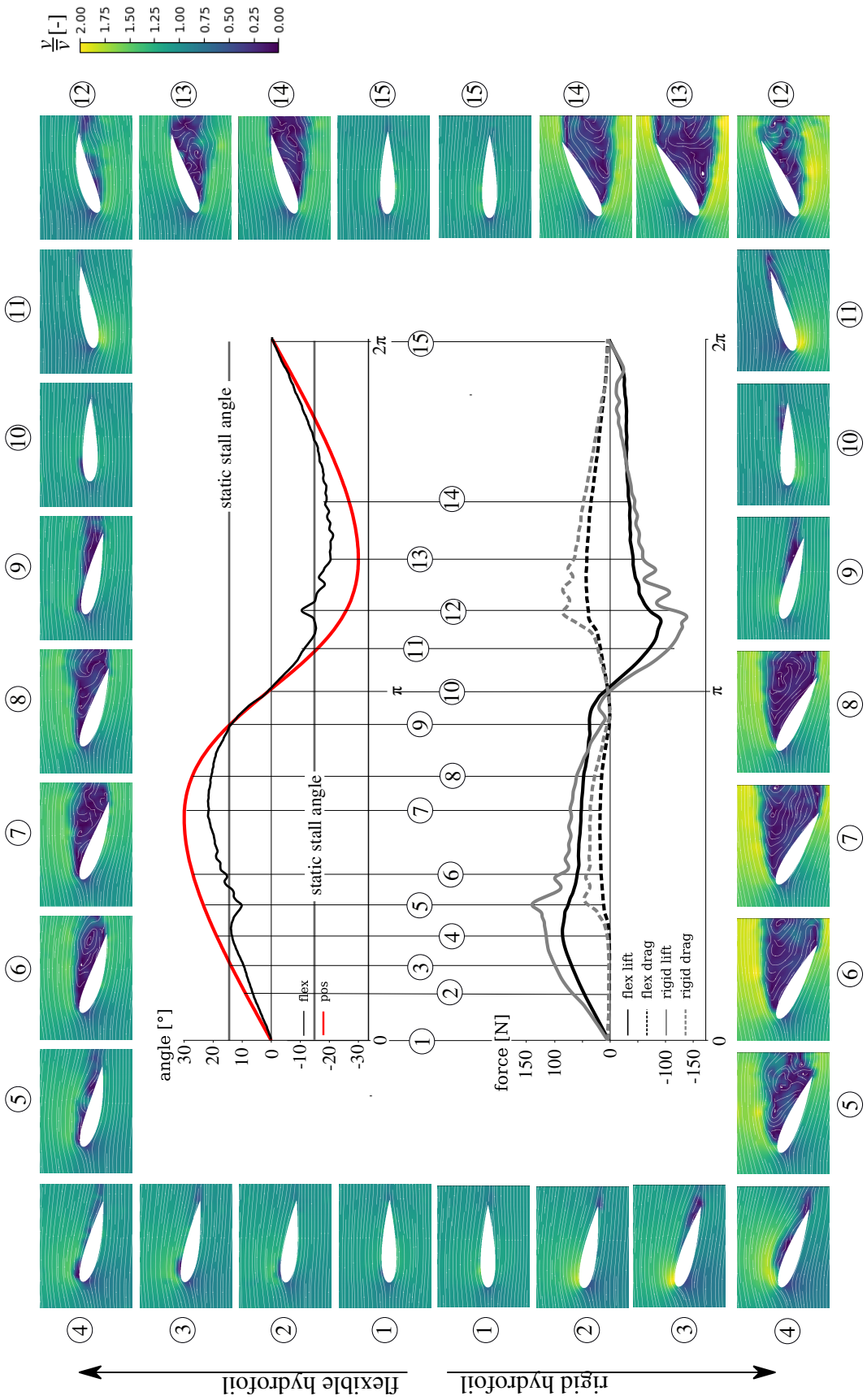

Figure 6.14: Fluid velocity fields (top half for the flex[03], bottom half for the rigid profile) for selected phase angles surrounding two diagrams, showing deformation angle and position feedback (top) and hydrodynamic forces (bottom): SFT at k_o=0.06, PIV at k_o=0.05

mation angle is zero, flex[03] generates lift with low drag. On the rigid foil, lift decreases strongly.

(10)-(11) 0° to -16° The flow is fully attached for both foils, no deformation is observed.

(12) -25° A deformation peak occurs combined with lift loss for the flex[03] profile. The rigid profile is fully stalled; large vortex structures, a loss of lift along with an overshoot of drag are observed.

(13)-(14) -30° to -25° Stall of both hydrofoils similar to (6)-(7).

(15) 0° The flow is fully attached, no lift and no significant drag.

In fig. 6.15 the results for a dynamic case at k_o=**0.14** are shown:

(0)-(4) 0° to 20° Similar observations as in k_o=0.06 (see fig. 6.14) are found.

(5) 25° The boundary layer of flex[03] is separated. The separated wake structures grow. Strong deformations of the surface are found. The lift forces still rise for both foils. Again, the stall dynamics for the flex[03] are delayed compared to the rigid foil.

(6)-(8) 25° to 28° The profiles are both fully stalled. A lift loss and drag peak are observed for the rigid profile at 30° (7). A local deformation peak is observed for the flex[03] profile at (8).

(9) 16° The flow reattaches from the leading edge for flex[03]. The rigid profile stays fully stalled with decreasing vortex size.

(10) 0° The flex[03] profile deforms against the motion and produces no lift. The rigid profile is still not fully reattached.

(11)-(12) -16° to -29° Increase of the lift force magnitude. Both flows are attached, however the rigid profile begins to stall. Overshoot of the drag at (12) for the rigid foil with lift remaining at high level.

(13)-30° Deformation peak (flapping) of the flex[03] profile, lift loss of the rigid profile.

(14) -29° Reattachment of the flow for the flex[03] profile with shedding of the vortex structure; the rigid profile is fully stalled.

(15) 0° The flow is fully attached, no lift and no significant drag for flex[03]. Positive lift force for the rigid foil.

In fig. 6.16 the results for a dynamic case at k_o=**0.28** (twice of the previous value) are shown:

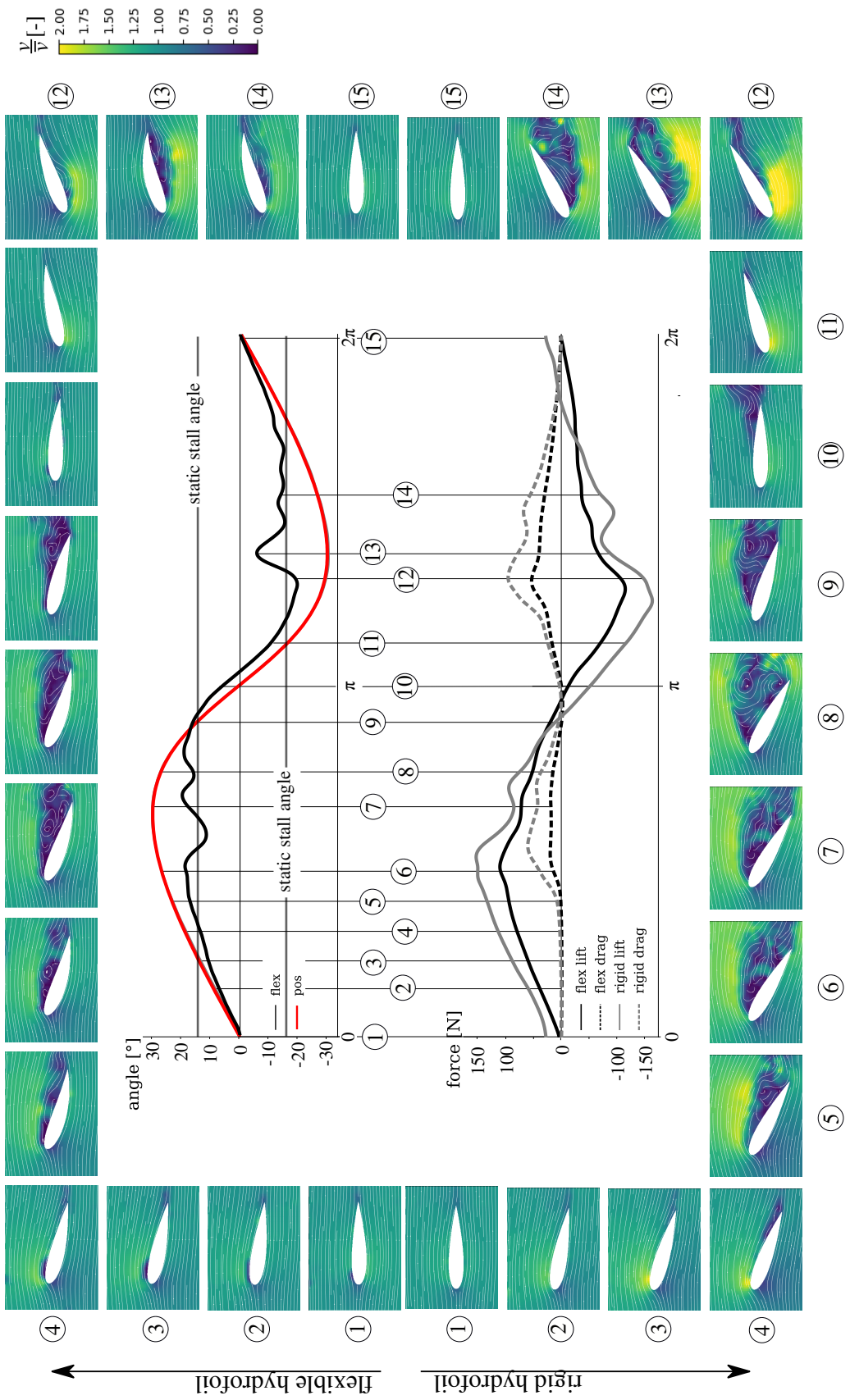

Figure 6.15: Fluid velocity fields (top half for the flex[03], bottom half for the rigid profile) for selected phase angles surrounding two diagrams, showing deformation angle and position feedback (top) and hydrodynamic forces (bottom): SFT at k_o=0.16, PIV at k_o=0.14

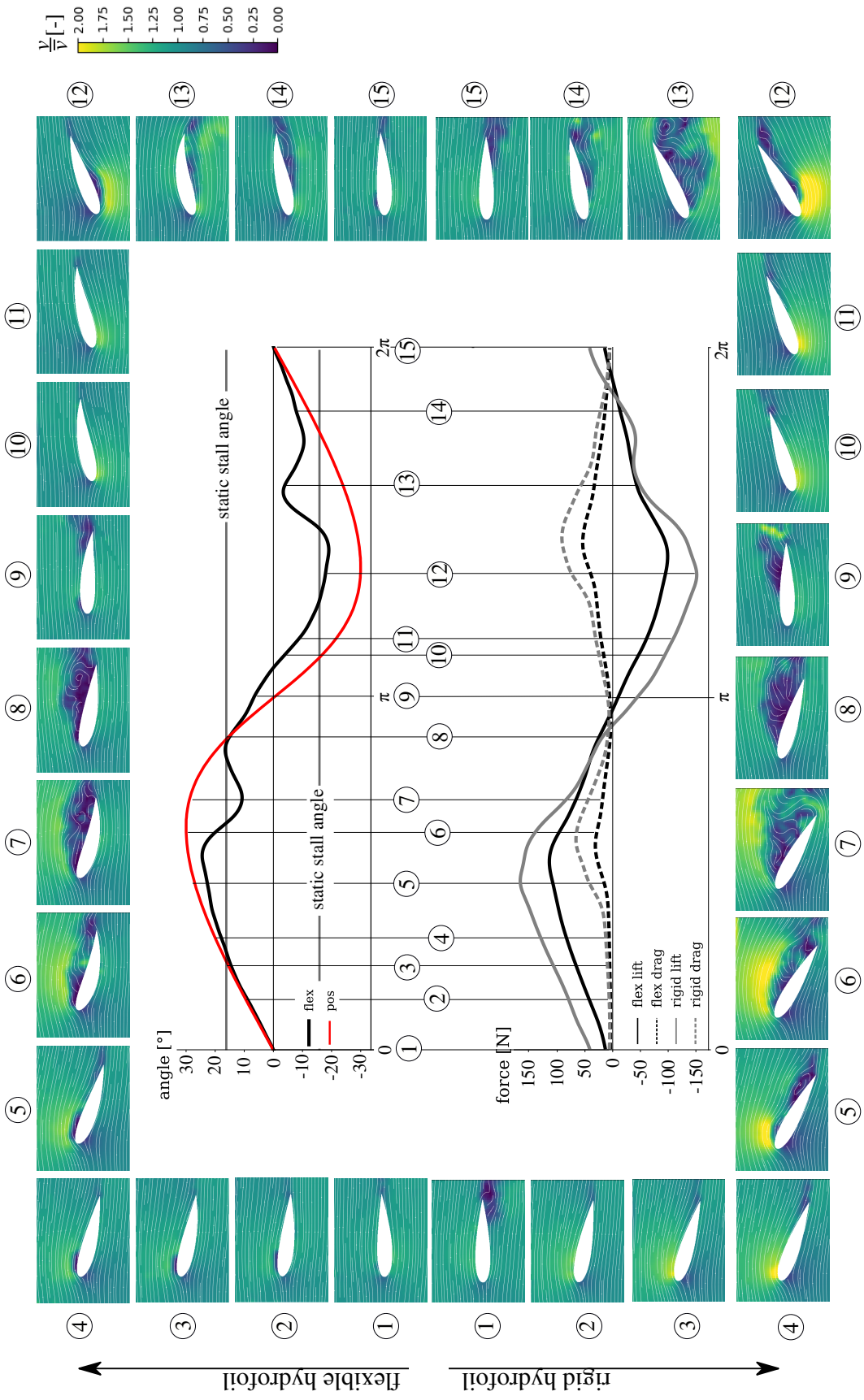

Figure 6.16: Fluid velocity fields (top half for the flex[03], bottom half for the rigid profile) for selected phase angles surrounding two diagrams, showing deformation angle and position feedback (top) and hydrodynamic forces (bottom): SFT and PIV at k_o=0.28

(0)-(4) 0° to 20° Same observations as in k_o=0.06 & k_o=0.14 (see fig. 6.14 & 6.15)

(5) 28° A separation bubble is visible for flex[03]. For the rigid hydrofoil, a trailing edge vortex is observed. The boundary layer is separated along around 50% of the upper surface. The rigid foil reaches its lift peak in the first half of the period. The drag remains moderate.

(6) 30° The flex[03] boundary layer is fully separated, and a strong foil deflection is observed. The rigid hydrofoil shows highly accelerated flow in the upper region. Flow over the upper surface fully detached. The drag reaches its maximum, while the lift decreases with moderate curve slope (this is by contrast to lower values of k_o where the lift breaks down more rapidly).

(7) 28° A deformation peak is found for the flex[03] profile, along with a large wake structure in the separated upper part of the surface. Lift and drag are decreasing constantly for both rigid and flex[03] hydrofoils. The rigid foil is fully stalled and features a large wake region.

(8) 16° Reaching the static stall angle, both hydrofoils are still fully separated and stall. However, the separated wake region diminishes. The flex[03] profile remains deformed.

(9) 0° At zero inclination angle, the flow of the flex[03] profile is still separated at the trailing edge, while the rest of the boundary layer reattaches. The rigid hydrofoil shows a large separated zone and wake.

(10)-(11) -16° to -20° The flow remains attached for both hydrofoils, the flex[03] profile deformation increases constantly, as well as the hydrodynamic forces acting on it.

(12) -30° A separation bubble is found for the flex[03].For the rigid hydrofoil separation occurs at both the trailing edge and leading edge. The rigid foil reaches the second lift peak.

(13) -25° The flex[03] profile just passed its deformation peak. The rigid foil shows post-stall hydrodynamic loads with high drag and low lift. The flow field is fully separated and the wake region size is maximal. The flex[03] profile features a separated boundary layer; however, no significant wake region is visible.

(14)-(15) -16° to 0° Reaching the static stall angle, both foils display remaining flow separation. The flow remains partly separated even at zero inclination.

In fig. 6.17 the results for a dynamic case at k_o=**0.38** are shown: The results are in general similar to the previous case. Differences mainly concern the phase angle. The stall inset is shifted further. Also, the deformation peaks are of high magnitude and occur at higher phase angles. The size of the wake region diminishes with rising k_o.

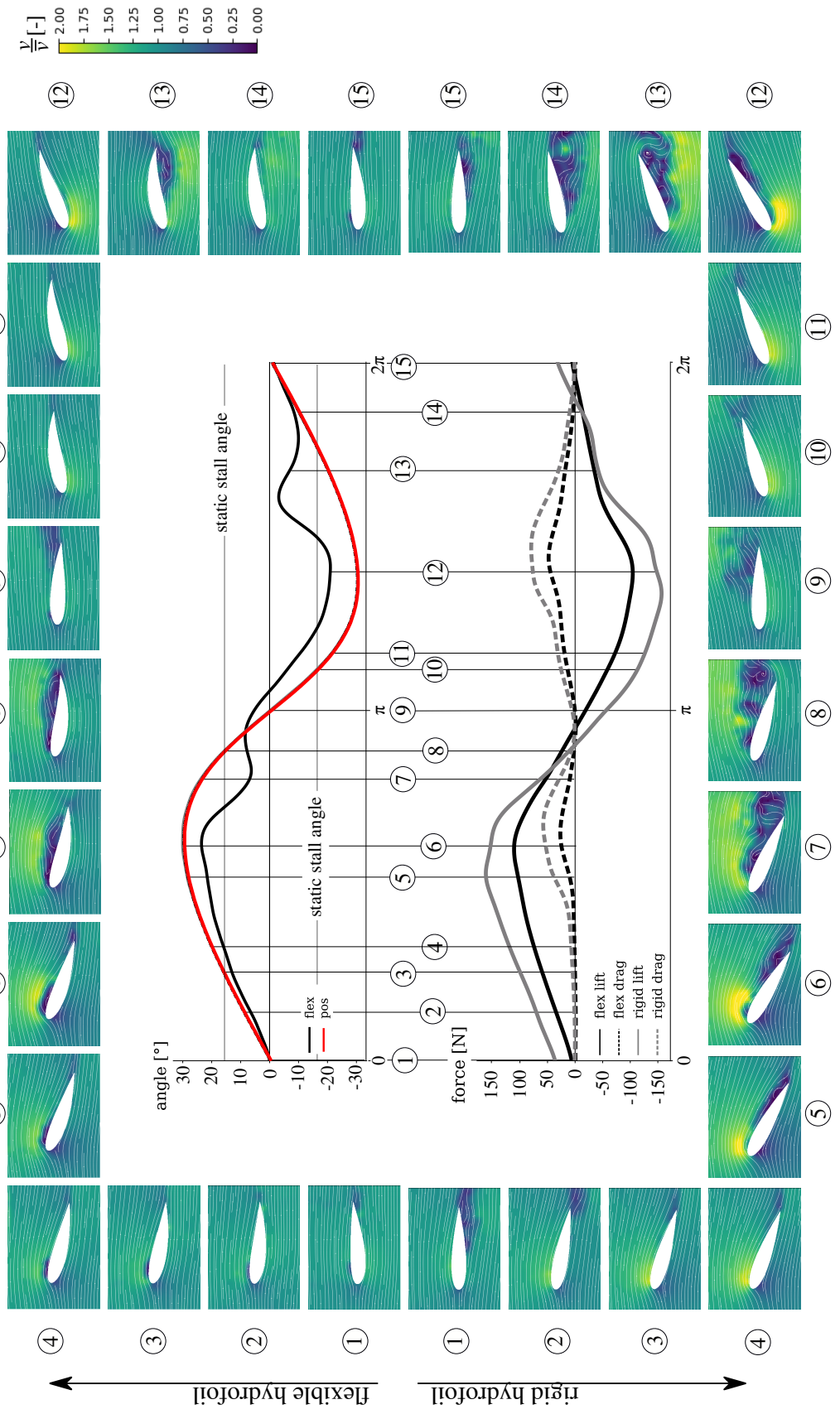

Figure 6.17: Fluid velocity fields (top half for the flex[03], bottom half for the rigid profile) for selected phase angles surrounding two diagrams, showing deformation angle and position feedback (top) and hydrodynamic forces (bottom): SFT at k_o=0.33, PIV at k_o=0.38

6.7 Conclusions of the postprocessing

This section had two objectives: the investigation of the mechanism of the oscillations in the force measurements, and the characteristics of the FSI on the blade.

Regarding the first objective, spectral analyses were performed on force signals, position and subsequently on the SFT data. The frequency of the base excitation (resulting from the forced oscillation) and its fist harmonics are too low to excite the natural frequencies of the hydrofoils. This remains true even when the natural frequencies are significantly reduced for the total system consisting of sensor, mounting structure and hydrofoils. An excitation can be observed in three frequency bands for both rigid and flex[03]. They differ in their frequency and are shifted to lower frequencies for the flex[03]. The excitation bands were found in a bandwidth of the natural frequencies, determined experimentally. In consequence, it can be assumed that self-excitation is the source of the vibrations observed.

The spectra for fluid velocity, solid height and hydrodynamic loads were presented in a unified plot with the position feedback angle from the drive system as base excitation. The differences in the spectra show the effect of the flexibility on the structural response and the deformation effects on the fluid dynamics, as well as the different characteristics of drag and lift forces in the interplay of fluid and structure.

The fluid-structure interaction was investigated with different methods, enabling observation of the fluid movement, the structural movement, as well as the hydrodynamic loads. In the last part of the section, these different methods were unified to provide the characteristics of the entire mechanism and the findings in the experiment. The presentation of the data from PIV, SFT and force measurements in one common plot allows to link the flow field to the deformation and the loads. The influence of the reduced frequency on the stall characteristics was elaborated, as well as the effects of flexibility.

Chapter 7

Summary and outlook

In future, hydrokinetic vertical-axis turbines may contribute to a sustainable, global energy strategy. This type of machine is particularly of interest for an application in marine environments, because of their very large unexploited resource potential. The simple construction of an H-rotor based turbine is a clear advantage over competing designs, but the vertical axis leads to highly complex flows at rotor level. The flow characteristics depend on the operating point. At low tip-speed ratios, they are governed by dynamic stall induced by high peaks of the angle of attack on the blades. At high tip-speed ratios, blade-blade interaction and other effects become dominant. Bioinspired, flexible rotor blades with adaptive characteristics increase the complexity of the flow even further.

Numerical experiments in the field of VAWT are challenging, and computationally expensive methods such DES or LES are required in order to reproduce flow separation and stall characteristics sufficiently well, even with a fully-rigid rotor. Numerical tools for strongly-coupled fluid-structure interaction were used in this thesis. In view of the complexity of the task, which requires dealing with orthotropic composite materials and unfavorable density ratios, those tools were not sufficient to deliver results with reasonable development and calculation costs.

In consequence, this study mainly focused on experiments in the water tunnel in the LEGI labs. The utilized experimental surrogate model consists of an oscillating hydrofoil performing a pitch trajectory. This trajectory is retrieved from the variation of the angle of incidence on a blade of a single blade rotor, as described in a rotating reference frame. The main benefit of this model is that it allows for testing of multiple hardware setups and operating points through the variation of the pitch trajectory and the oscillation frequency (see fig. 2.4). However, strong simplifications were made in the experimental setup. Neither the variation of the relative flow speed, nor any blade-blade interaction are reproduced. Furthermore, from a thermodynamic point of view, the electrical drive will add energy to the system with amounts increasing together with the oscillation frequency. In consequence, the simplifications made do not allow for a quantification of the improvements or a comparison of the effects reported in between different reduced frequencies.

For the purpose of the experiment, a custom control and data acquisition environment was developed in order to achieve a fully-automatized generation of position

control trajectories with high accuracy and a highly-dynamic control. The hydrodynamic forces were captured with a six-axis load cell positioned between the hydrofoil and the drive shaft. A custom amplifier was built in collaboration with the Magdeburg laboratory of electrical drive systems. The data was sampled with 1 kHz acquisition rate, allowing for a later consideration of the hydrodynamic loads in the spectral space with reasonable resolution.

Two independent methodologies were developed to measure the structural deformation of the flexible hydrofoil.

The first is based on a structured light projection. The advantage of this method is the measurement of the entire instantaneous surface, with high temporal (4 kHz) and spatial (600×275 points) resolution, combined with low hardware requirements (only a high-speed camera and a projector). The method was implemented in the *Python*-based *fluidimage* framework for parallel PIV postprocessing on HPC. The method was successfully validated with an analytical three-dimensional model of the rigid hydrofoil. The movements were linked with the position feedback of the drive system. The method showed an average measurement uncertainty of 0.66 mm in the given setup.

The second method is based on raw images acquired during PIV measurements, and searches for the cross section of the structure with a segmentation algorithm. A clear advantage of the method is that the existing data from PIV measurements can be used. However, it was not possible to evaluate the uncertainty of the method quantitatively. During the PIV measurements, no additional information except of the position feedback from the drive is available for the solid structure. A qualitative comparison was performed, based on SFT measurements which are not directly comparable, since the flow speed in both setups is different. Data from those two measurement campaigns were linked by use of similarity theory; with the reduced frequency being identified as the key non-dimensional parameter.

Finally, a 2D2C, time-resolved, high-speed PIV measurement campaign was carried out in order to investigate the instantaneous flow field around the hydrofoil. Two continuous laser sources installed below and above the hydrofoil generated a light sheet without significant hydrofoil shadow. This allowed for an investigation of the entire flow field around the hydrofoil. The high-speed camera recordings were of 4 kHz temporal resolution. For the purpose of postprocessing the images, an adaptive mask algorithm was developed and validated in order to mask the moving structure and reflections of particles stuck on the surface. The postprocessing software was again *fluidimage*.

In this study, two different approaches for performance and lifetime improvements of VAWT were studied. The first was the investigation of an optimized pitch trajectory for a VAWT with use of a hardware-in-the-loop method. The second, and the main focus of this study, was a the bioinspired approach with adaptive blades. Both approaches investigated, active blade pitch and flexible blades, show that drag reduction is the governing factor for any improvement in lifetime and performance (see figs. 5.7 & 5.10 left). Active pitch methods may show higher potential for performance improvements, but on the other hand, they require ambitious mechatronical setups. In both approaches, the adaptions led to a reduction of the peaks of the angle of in-

cidence. The pitch curve shapes differ significantly between the two approaches. The active blade pitch optimal trajectory shifts the zero-crossing of the angle of incidence to an earlier phase angle in the first half of the period (see fig. 5.5).
Peaks in lift and drag force are smoothed out by a flexible structure compared to a rigid one. A reduction of the size of the wake region, and a shorter duration of the stall phases is observed on such foils for high k_o. The onset of stall is phase lagged, but the phase shift for the reattachment of the flow is smaller. In consequence, a general reduction of the angle of incidence is observed because the structure deforms according to hydrodynamic loads.

The study aimed to investigate possible improvements in lifetime and efficiency when using adaptive blades. Improvements in lifetime are quantified based on lower amplitudes of the alternating structural loads, which have exponential influence on the lifetime. These are mainly achieved by a reduction of the lift forces. The largest share of the loads result from the lift force; however, reductions in lift affect the blade thrust negatively. In consequence, the largest performance improvements are obtained through a reduction of the drag forces. This is true in particular for operating points with low-λ and in consequence high angles of incidence. Then, the rigid profile stalls and the extreme overshooting of the drag forces counter effects the thrust of the turbine blade (see fig. 5.10).

The thrust efficiency for flexible profiles is higher for specific operating and design points (see figs. 5.14 & 5.20). From the force measurements, it can be concluded that flexible structures can provide significant improvements for vertical axis water turbines, at least in specific conditions. Results suggest that a drawback of the concept is that the blade design has to be adapted to the hydrodynamic loads. These depend on flow speed, operating point and turbine solidity. In consequence, this indicates that improvements can be achieved if the VAWT operates under constant conditions with an adapted design. Marine currents can feature such stable conditions, while applications in tidal currents as well as rivers, because of high fluctuations of their free stream velocity due to tide or seasonal volume flow rates, are less promising applications.

Future research should focus on the extension of the FSI toolkit in *foam-extend*. The surface-tracking method has high potential, in particular if the parallelization of the method could be improved in order to reduce computing time. Of particular interest is the cross-section tracking method with use of adaptive PIV masks. A better integration in *fluidimage* is needed. A quantitative validation of the error could be achieved by a synchronous measurement with a laser vibrometer.

Finally, the quantification of the benefits of adaptive blades requires further investigation. In future, experiments on a three-bladed VAWT with flexible blades, complemented by numerical investigations, could be carried out. The experiments could be performed in the open water channel built by the author of the thesis at the Magdeburg laboratory of fluid dynamics.

Bibliography

[1] S. Abbaszadeh, S. Hoerner, T. Maitre, and R. Leidhold. Experimental investigation of an optimized pitch control for a vertical axis turbine. *IET Renewable Power Generation*, online first. 2019. doi:10.1049/iet-rpg.2019.0309.

[2] S. Amaral, N. Perkins, D. Giza, and B. McMahon. Evaluation of fish injury and mortality associated with hydrokinetic turbines (1024569). Technical report, Electrical Power Research Institute Palo Alto, 2011.

[3] E. Amet, T. Maître, C. Pellone, and J.-L. Achard. 2D numerical simulations of blade-vortex interaction in a Darrieus turbine. *American Society of Mechanical Engineers*, 131:15, 2009. doi:10.1115/1.4000258.

[4] S. Antheaume, T. Maître, and J.-L. Achard. Hydraulic Darrieus turbine efficiency for free fluid flow conditions versus power farms conditions. *Renewable Energy*, 33:2186–2198, 10 2008. doi:10.1016/j.renene.2007.12.022.

[5] F. Arab, B. Augier, F. Deniset, P. Casari, and J.A. Astolfi. Morphing hydrofoil model driven by compliant composite structure and internal pressure. *Journal of Marine Science and Engineering*, 7:423, 11 2019. doi:10.3390/jmse7120423.

[6] I.M. Asher, M. Drela, and J. Peraire. A low order model for vertical axis wind turbines. In *28th AIAA Applied Aerodynamics Conference*, Chicago, USA, 06 2010. doi:10.2514/6.2010-4401.

[7] J.A. Astolfi, A. Lelong, P. Bot, and J.-B. Marchand. Experimental analysis of hydroelastic response of flexible hydrofoils. In *5th High Performance Yacht Design Conference, Auckland*, 03 2015.

[8] Q. Aubourg. *Experimental study of wave turbulence on the surface of a fluid. The theory of the weak turbulence against reality for capillary and gravity waves.* Thèse, Université Grenoble Alpes, October 2016. URL: https://tel.archives-ouvertes.fr/tel-01597576.

[9] P. Augier and C. Bonamy. Fluidimage, 2019. URL: https://bitbucket.org/fluiddyn/fluidimage.

[10] P. Augier, V. Mohanan, and C. Bonamy. Fluiddyn: a Python open-source framework for research and teaching in fluid dynamics by simulations, experiments and data processing. *Journal of Open Research Software*, 7, 2019. doi:10.5334/jors.237.

[11] V. Aumelas. *Bare and shrouded vertical axis water turbine modelling : development of an experimental device and a numerical facility for the study of cavitation.* Theses, Université de Grenoble, September 2011.

[12] V. Aumelas, Y. Lecoffre, G. Maj, and J.-P. Franc. Micro-bubbles seeding for flow characterization. *IOP Conference Series: Earth and Environmental Science*, 49:062005, nov 2016. doi:10.1088/1755-1315/49/6/062005.

[13] A. B. M. Baki, D. Z. Zhu, A. Harwood, A. Lewis, and K. Healey. Rock-weir fishway I: flow regimes and hydraulic characteristics. *Journal of Ecohydraulics*, 2(2):122–141, 2017. doi:0.1080/24705357.2017.1369182.

[14] A. B. M. Baki, D. Z. Zhu, A. Harwood, A. Lewis, and K. Healey. Rock-weir fishway II: design evaluation and considerations. *Journal of Ecohydraulics*, 2(2):142–152, 2017. doi:10.1080/24705357.2017.1369183.

[15] Y. Bazilevs, M.-C. Hsu, J. Kiendl, R. Wüchner, and K.-U. Bletzinger. 3d simulation of wind turbine rotors at full scale. part ii: Fluid-structure interaction modeling with composite blades. *International Journal for Numerical Methods in Fluids*, 65(1-3):236–253, 2011. doi:10.1002/fld.2454.

[16] G. Bedon, S. De Betta, and E. Benini. Performance-optimized airfoil for Darrieus wind turbines. *Renewable Energy*, 94:328 – 340, 2016. doi:doi.org/10.1016/j.renene.2016.03.071.

[17] G. Bedon, M. Raciti Castelli, and E. Benini. Optimization of a Darrieus vertical-axis wind turbine using blade element – momentum theory and evolutionary algorithm. *Renewable Energy*, 59:184 – 192, 2013. doi:doi.org/10.1016/j.renene.2013.03.023.

[18] S.I. Benton and M.R. Visbal. The onset of dynamic stall at a high, transitional Reynolds number. *Journal of Fluid Mechanics*, 861:860–885, 2019. doi:10.1017/jfm.2018.939.

[19] A. Bianchini, G. Ferrara, and L. Ferrari. Design guidelines for H-Darrieus wind turbines: Optimization of the annual energy yield. *Energy Conversion and Management*, 89:690 – 707, 2015. doi:10.1016/j.enconman.2014.10.038.

[20] C. Bonamy and S. Hoerner. Fluidimage surface-tracking software: development version, 2019. URL: https://bitbucket.org/CyrilleBonamy/fluidimage.

[21] I.D. Brownstein, M. Kinzel, and J.O. Dabiri. Performance enhancement of downstream vertical-axis wind turbines. *Journal of Renewable and Sustainable Energy*, 8:053306, 2016. doi:10.1063/1.4964311.

[22] A.-J. Buchner, D. Honnery, and J. Soria. Stability and three-dimensional evolution of a transitional dynamic stall vortex. *Journal of Fluid Mechanics*, 823:166–197, 07 2017. doi:10.1017/jfm.2017.305.

[23] A.-J. Buchner, J. Soria, D. Honnery, and A.J. Smits. Dynamic stall in vertical axis wind turbines: scaling and topological considerations. *Journal of Fluid Mechanics*, 841:746–766, 2018. doi:10.1017/jfm.2018.112.

[24] P. Cardiff, Z. Tuković, M. Clancy, P. De Jaeger H. Jasak, and A. Ivanković. Performance of lagrangian finite volume approaches for linear and nonlinear mechanics analyses. In *11th OpenFOAM Workshop Guimaraes, Portugal*, 2016.

[25] P. Cardiff, Z. Tuković, H. Jasak, and A. Ivanković. A block-coupled finite volume methodology for linear elasticity and unstructured meshes. *Computers & Structures*, 175:100 – 122, 2016. doi:https://doi.org/10.1016/j.compstruc.2016.07.004.

[26] J.-B. Carrat. *Experimental and numerical quantification of the cavitation aggressiveness*. Theses, Université Grenoble Alpes, June 2018. URL: https://tel.archives-ouvertes.fr/tel-01871731.

[27] E. Castillo and A. Fernandez-Canteli. *A Unified Statistical Methodology for Modeling Fatigue Damage*. Springer, 2009.

[28] O. Cleynen, S. Hoerner, and D. Thévenin. Characterization of hydraulic power in free-stream installations. *International Journal of Rotating Machinery*, 2017:10, 2017. doi:10.1155/2017/9806278.

[29] G. Combs. Wireshark the world's foremost network protocol analyzer, 2019. URL: https://www.wireshark.org.

[30] J.O. Dabiri. Potential order-of-magnitude enhancement of wind farm power density via counter-rotating vertical-axis wind turbine arrays. *Journal of Renewable and Sustainable Energy*, 3(4), 2011. doi:10.1063/1.3608170.

[31] G.J.M. Darrieus. Turbine having its rotating shaft transverse to the flow of the current, United States of America, Patent 1.835.018, 1931.

[32] L. Daróczy. *Practical issues in the optimization of CFD based engineering problems*. PhD thesis, Otto-von-Guericke-Universität Magdeburg, Fakultät für Verfahrens- und Systemtechnik, 2016.

[33] L. Daróczy, G. Janiga, K. Petrasch, M. Webner, and D. Thévenin. Comparative analysis of turbulence models for the aerodynamic simulation of H-Darrieus rotors. *Energy*, 90:680–690, 2015. doi:10.1016/j.energy.2015.07.102.

[34] L. Daróczy, G. Janiga, and D. Thévenin. Correlation of the power coefficients of H-Darrieus wind turbines obtained using different turbulence models in CFD computations. In *the 16th International Conference on Fluid Flow Technologies*, pages 1–8, 2015.

[35] L. Daróczy, G. Janiga, and D. Thévenin. Analysis of the performance of a H-Darrieus rotor under uncertainty using polynomial chaos expansion. *Energy*, 113:399–412, 2016.

[36] L. Daróczy, G. Janiga, and D. Thévenin. Computational fluid dynamics based shape optimization of airfoil geometry for an H-rotor using a genetic algorithm. *Engineering Optimization*, 50(9):1483–1499, 2018. doi:10.1080/0305215X.2017.1409350.

[37] P. Deglaire, S. Engblom, O. Ågren, and H. Bernhoff. Analytical solutions for a single blade in vertical axis turbine motion in two-dimensions. *European Journal of Mechanics - B/Fluids*, 28(4):506 – 520, 2009. doi:doi.org/10.1016/j.euromechflu.2008.11.004.

[38] J. Degroote, R. Haelterman, S. Annerel, P. Bruggeman, and J. Vierendeels. Performance of partitioned procedures in fluid–structure interaction. *Computers & Structures*, 88(7):446 – 457, 2010. doi:doi.org/10.1016/j.compstruc.2009.12.006.

[39] P.-L. Delafin. *Analyse de l'écoulement transitionnel sur un hydrofoil : application aux hydroliennes à axe transverse avec contrôle actif de l'angle de calage*. Thèse, Université de Bretagne occidentale - Brest, September 2014. URL: https://tel.archives-ouvertes.fr/tel-01147402.

[40] Z. Deng, T.J. Carlson, G.R. Ploskey, M.C. Richmond, and D.D. Dauble. Evaluation of blade-strike models for estimating the biological performance of Kaplan turbines. *Ecological Modelling*, 208(2):165 – 176, 2007. doi:doi.org/10.1016/j.ecolmodel.2007.05.019.

[41] E. Doujak and J. Unterluggauer. Fluid-structure interaction of Francis turbines at different load steps. In *Proceedings of 9th International Symposium on Fluid-Structure Interactions, Flow-Sound Interactions, Flow-Induced Vibration & Noise, Toronto, Ontario, Canada*, July 2018.

[42] M. Drela. Xfoil subsonic airfoil development system, 2013. URL: http://web.mit.edu/drela/Public/web/xfoil/.

[43] A. Ducoin, J. A. Astolfi, and J.-F. Sigrist. An experimental analysis of fluid structure interaction on a flexible hydrofoil in various flow regimes including cavitating flow. *European Journal of Mechanics - B/Fluids*, 36:63 – 74, 2012. doi:doi.org/10.1016/j.euromechflu.2012.03.009.

[44] Earth Science Communications Team. Nasa - global climate change, 2018. URL: climate.nasa.gov/vital-signs/.

[45] Enercon GmbH. Enercon e-44 technical details, 2018. URL: enercon.de/en/products/ep-1/e-44.

[46] Federal Ministry for the Environment, Nature Conservation and Nuclear Safety. Potentialermittlung für den Ausbau der Wasserkraftnutzung in Deutschland, 2010. URL: erneuerbare-energien.de.

[47] C. S. Ferreira, H. Bijl, G. van Bussel, and G. van Kuik. Simulating dynamic stall in a 2D VAWT: Modeling strategy, verification and validation with Particle Image Velocimetry data. *Journal of Physics: Conference Series*, 75(1):012023, 2007. doi:10.1088/1742-6596/75/1/012023.

[48] C. S. Ferreira, G. van Kuik, G. van Bussel, and F. Scarano. Visualization by PIV of dynamic stall on a vertical axis wind turbine. *Experiments in Fluids*, 46(1):97–108, Jan 2009. doi:10.1007/s00348-008-0543-z.

[49] C.S. Ferreira, A. Zanon, M. Barone, and P Giannattasio. Comparison of aerodynamic models for vertical axis wind turbines. *Journal of Physics Conference Series 524*, 2014. doi:10.1088/1742-6596/524/1/01212.

[50] B. Fischer, L. Beermann, C. Höfler, and H.-J. Bauer. Untersuchung eines Fluid-Struktur-Interaktion Referenzfalls mittels OpenFOAM Extend. In *Deutscher Luft und Raumfahrtkongress*, 2016. URL: https://www.dglr.de/publikationen/2016/420348.pdf.

[51] F.E. Fish. Power output and propulsive efficiency of swiming bottlenose dolphins (tursiops truncatus). *Journal of Experimental Biology*, 183(183):179–193, August 1993.

[52] T. Fu, Z.D. Deng, J.P. Duncan, D. Zhou, T.J. Carlson, G.E. Johnson, and H. Hou. Assessing hydraulic conditions through Francis turbines using an autonomous sensor device. *Renewable Energy*, 99:1244 – 1252, 2016. doi:doi.org/10.1016/j.renene.2016.08.029.

[53] N. Fujisawa and S. Shibuya. Observations of dynamic stall on Darrieus wind turbine blades. *Journal of Wind Engineering and Industrial Aerodynamics*, 89:201–214, 2001. doi:10.1016/s0167-6105(00)00062-3.

[54] German Federal Institute for Risk Assessment (BfR). AnimalTestInfo - Datenbank zu Tierversuchsvorhaben in Deutschland, 2018. URL: animaltestinfo.de.

[55] J.M.R. Gorle, S. Bardwell, L. Chatellier, F. Pons, M. Ba, and G. Pineau. PIV investigation of the flow across a Darrieus water turbine. In *17th International Symposium on Applications of Laser Techniques to Fluid Mechanics - Lisbon*, 2014.

[56] A.M. Gorlov. Unidirectional helical reactor turbine operable under reversible fluid flow for power systems, United States of America, Patent 5.451.137, 1995.

[57] B. Gschaider. Extend-bazaar/toolkits/fluid-structure interaction, 2019. URL: https://openfoamwiki.net/index.php/Extend-bazaar/Toolkits/Fluid-structure_interaction#Install_on_foam-extend-4.0.

[58] K.L. Hansen, N. Rostamzadeh, R.M. Kelso, and B.B. Dally. Evolution of the streamwise vortices generated between leading edge tubercles. *Journal of Fluid Mechanics*, 788:730–766, 2016. doi:10.1017/jfm.2015.611.

[59] I. Hashem and M.H. Mohamed. Aerodynamic performance enhancements of H-rotor Darrieus wind turbine. *Energy*, 142:531 – 545, 2018. doi:doi.org/10.1016/j.energy.2017.10.036.

[60] R. Hassaini and N. Mordant. Confinement effects on gravity-capillary wave turbulence. *Physical Review Fluids*, 3, 09 2018. doi:10.1103/PhysRevFluids.3.094805.

[61] N. Hassan, S.B. Elbaz, and A.D. Gat. Dynamics and instabilities of an arbitrarily clamped elastic sheet in potential flow with application to shape-morphing airfoils. *Journal of Fluid Mechanics (under review)*, 2019. URL: https://arxiv.org/abs/1805.02378v1.

[62] M. Hepperle. JavaFoil – Analysis of Airfoils, 2018. URL: `https://www.mh-aerotools.de/airfoils/javafoil.htm`.

[63] S. Hoerner. Sft utilities repository, 2019. URL: `https://bitbucket.org/sthoerner/sft_utilities`.

[64] S. Hoerner, S. Abbaszadeh, T. Maître, L. Vignal, C.-T. Weber, R. Leidhold, and D. Thévenin. Experimental Evaluation of the Behavior of Highly-Flexible Structures for Vertical Axis Water Turbines. In *Conference on Modelling Fluid Flow*, pages 1–8, Budapest, Hungary, September 2018.

[65] S. Hoerner, S. Abbaszadeh, T. Maître, O. Cleynen, and D. Thévenin. Characteristics of the fluid–structure interaction within darrieus water turbines with highly flexible blades. *Journal of Fluids and Structures*, 88C:13–30, 04 2019. `doi:10.1016/j.jfluidstructs.2019.04.011`.

[66] S. Hoerner and C. Bonamy. Structured-light-based surface measuring for application in fluid–structure interaction. *Experiments in Fluids*, 60(11):168, Oct 2019. `doi:10.1007/s00348-019-2821-3`.

[67] S. Hoerner, C. Bonamy, O. Cleynen, T. Maître, and D. Thévenin. Darrieus water turbines – deformation and force measurements on highly flexible blade profiles. *Experiments in Fluids (submitted)*, 2019.

[68] S. Hoerner, C. Bonamy, T. Maître, O. Cleynen, and D. Thévenin. Strongly-coupled fluid-structure-interation with large deformations on a flexible hydrofoil under forced oscillation. In *12th OpenFOAM Workshop Exeter, United Kingdom*, 2017. URL: `https://hal.archives-ouvertes.fr/hal-01685286v1`.

[69] Hydroquest. River and tidal turbines, 2018. URL: `hydroquest.net`.

[70] E. Jacobs, K. Ward, and R. Pinkerton. Report 460 - the characteristics of 78 related airfoil sections from tests in the variable-density wind tunnel. Technical report, NACA National Advisory Commitee for Aeronautics, 1933. URL: `ntrs.nasa.gov/archive/nasa/casi.ntrs.nasa.gov/19930091108.pdf`.

[71] E. Kerikous and D. Thévenin. Optimal shape of thick blades for a hydraulic Savonius turbine. *Renewable Energy*, 134:629 – 638, 2019. `doi:doi.org/10.1016/j.renene.2018.11.037`.

[72] I. Koesters, S. Hoerner, and D. Thévenin. Image-based cross-sectional deformation measurement on a flexible hydrofoil. In *20th International Symposium on Applications of Laser and Imaging Techniques to Fluid Mechanics 2020, Lisbon, Portugal, (under review)*, 2020.

[73] P. Krawczyk, A. Beyene, and D. MacPhee. Fluid structure interaction of a morphed wind turbine blade. *International Journal of Energy Research*, 37(14):1784–1793, 2013. `doi:10.1002/er.2991`.

[74] C. Laddey. Untersuchungen an einem oszillierenden hydrodynamischen Profil, 2019.

[75] C. Laddey. Report: Protokoll zum Zugversuch des Werkstoffs Wacker Elastosil M4600, University of Applied Science Magdeburg-Stendal, 2018.

[76] N. Lambert. Interaction fluide-structure pour des profils hydrodynamiques souples, 2017. URL: http://www.legi.grenoble-inp.fr/web/spip.php?article1323&lang=fr.

[77] A. Laneville and P. Vittecoq. Dynamic stall: The case of the vertical axis wind turbine. *Journal of Solar Energy Engineering, Transactions of ASME*, 108:140–145, May 1986. doi:10.1115/1.3268081.

[78] L. Lazauskas and B.K. Kirke. Modelling passive variable pitch cross flow hydrokinetic turbines to maximize performance and smooth operation. *Renewable Energy*, 45:41–50, 2012. doi:10.1016/j.renene.2012.02.005.

[79] M. Leblanc-Vickers. Turbine à l'axe de rotation transversal à la direction du courant, France, Patent 604.390, 1925.

[80] J.G. Leishman. Challenges in modelling the unsteady aerodynamics of wind turbines. *Wind Energy*, 5(2-3):85–132, 2002. doi:10.1002/we.62.

[81] A. Lelong, P. Guiffant, and J.A. Astolfi. An Experimental Analysis of the Structural Response of Flexible Lightweight Hydrofoils in Cavitating Flow. *Journal of Fluids Engineering*, 140(2), 11 2017. 021116. URL: https://doi.org/10.1115/1.4037990, arXiv:https://thermalscienceapplication.asmedigitalcollection.asme.org/fluidsengineering/article-pdf/140/2/021116/6201354/fe_140_02_021116.pdf, doi:10.1115/1.4037990.

[82] H. Li, K. Zhang, R.M. Waldman, and H. Hu. Quantification of dynamic droplet impact onto a solid surface by using a digital image projection technique. In *55th AIAA Aerospace Sciences Meeting*. American Institute of Aeronautics and Astronautics, 2017. doi:doi:10.2514/6.2017-0942.

[83] Y. Liang, L. Zhang, E. Li, and F. Zhang. Blade pitch control of straight-bladed vertical axis wind turbine. *Journal of Central South University: 23*, 23(5):1106–1114, 2016. doi:10.1007/s11771-016-0360-0.

[84] W. Liu and Q. Xiao. Investigation on Darrieus type straight blade vertical axis wind turbine with flexible blade. *Ocean Engineering*, 110:339 – 356, 2015. doi:doi.org/10.1016/j.oceaneng.2015.10.027.

[85] J.L. Loth and H. McCoy. Optimization of Darrieus turbines with an upwind and downwind momentum model. *Journal of Energy*, 7(4):313–318, 1983. doi:10.2514/3.62659.

[86] K.H. Ly and V.A.L Chasteau. Experiments on an oscillating aerofoil and applications to wind-energy converters. *Journal of Energy*, 5(2):116–121, 1981. doi:10.2514/3.62511.

[87] D.W. MacPhee and A. Beyene. Fluid-structure interaction analysis of a morphing vertical axis wind turbine. *Journal of Fluid and Structures*, 60:143–159, 2016. doi:10.1016/j.jfluidstructs.2015.10.010.

[88] D. Marten, J. Wendler, G. Pechlivanoglou, C.N. Nayeri, and C.O. Paschereit. Qblade: an open source tool for design and simulation of horizontal and vertical axis wind turbines. *International Journal of Emerging Technolology and Advanced Engineering*, 3:264–269, 2013.

[89] A. Maurel, P. Cobelli, V. Pagneux, and P. Petitjeans. Experimental and theoretical inspection of the phase-to-height relation in Fourier transform profilometry. *Applied optics*, 48:380–92, 02 2009. doi:10.1364/AO.48.000380.

[90] M. Mauri, I. Bayati, and M. Belloli. Design and realisation of a high-performance active pitch-controlled H-Darrieus VAWT for urban installations. In *3rd Renewable Power Generation Conference*, 2014. doi:10.1049/cp.2014.0930.

[91] T. Maître, E. Amet, and C. Pellone. Modelling of the flow in a Darrieus water turbine: Wall grid refinement analysis and comparison with experiments. *Renewable Energy*, 51:497–512, 2013. doi:10.1016/j.renene.2012.09.030.

[92] W.J. McCroskey. The phenomenon of dynamic stall. Technical report, NASA TM-81264, 1981.

[93] W.J. McCroskey. *Special Opportunities in Helicopter Aerodynamics*. Springer-Verlag New York, 1986. doi:10.1007/978-1-4612-4972-6_20.

[94] W.J. McCroskey, L.W. Carr, and K.W. McAlister. Dynamic stall experiments on oscillating airfoils. *AIAA Journal*, 14(1):57–63, January 1976. URL: https://doi.org/10.2514/3.61332, doi:10.2514/3.61332.

[95] W.J. McCroskey, L.W. Carr, and K.W. McAllister. Dynamic stall experiments on oscillating airfoils. *American Institute of Aeronautics and Astronautics Journal*, (1):57–63, 1976. doi:https://doi.org/10.2514/3.61332.

[96] M.A. Miller, S. Duvvuri, I. Brownstein, M. Lee, J.O. Dabiri, and M. Hultmark. Vertical-axis wind turbine experiments at full dynamic similarity. *Journal of Fluid Mechanics*, 844:707–720, 2018. doi:10.1017/jfm.2018.197.

[97] M. Mohamed. Performance investigation of H-rotor Darrieus turbine with new airfoil shapes. *Energy*, 47:522–530, 11 2012. doi:10.1016/j.energy.2012.08.044.

[98] H.F. Müller-Vahl, C.N. Nayeri, C.O. Paschereit, and D. Greenblatt. Dynamic stall control via adaptive blowing. *Renewable Energy*, 97:47–64, 2016.

[99] H.F. Müller-Vahl, C. Strangfeld, C.N. Nayeri, C.O. Paschereit, and D. Greenblatt. Control of thick airfoil, deep dynamic stall using steady blowing. *AIAA journal*, 53(2):277–295, 2014.

[100] S. Müller. Simulation der Fluid-Struktur-Interaktion an einem flexiblen oszillierenden aerodynamischen Profil mit der Opensource Toolbox OpenFOAM extend, Bachelor's Thesis LSS-B09/15, Lehrstuhl für Strömungsmechanik und Strömungstechnik, University Otto-von-Guericke Magdeburg, 2015.

[101] S. Müller, O. Cleynen, S. Hoerner, N. Lichtenberg, and D. Thévenin. Numerical analysis of the compromise between power output and fish-friendliness in a vortex power plant. *Journal of Ecohydraulics*, 3(2):86–98, 2018. doi:10.1080/24705357.2018.1521709.

[102] T. Naik, E.K. Longmire, and S. C. Mantell. Dynamic response of a cantilever in liquid near a solid wall. *Sensors and Actuators A: Physical*, 102(3):240 – 254, 2003. doi:doi.org/10.1016/S0924-4247(02)00398-9.

[103] B.G. Newman. Multiple actuator-disc theory for wind turbines. *Journal of Wind Engineering and Industrial Aerodynamics*, 24(3):215–225, 1986. doi:10.1016/0167-6105(86)90023-1.

[104] I. Paraschivoiu. *Wind Turbine Design: With Emphasis on Darrieus Concept*. Presses Internationales Polytechnique, 2 edition, 2002.

[105] T. Pärssinen, H. Eloranta, and P. Saarenrinne. Experimental investigation of material effects on free vibration of a splitter plate. *Experiments in Fluids*, 42(3):349–362, Mar 2007. doi:10.1007/s00348-006-0240-8.

[106] R. Patil, L. Daróczy, G. Janiga, and D. Thévenin. Large eddy simulation of an H-darrieus rotor. *Energy*, 160:388–398, 2018. doi:10.1016/j.energy.2018.06.203.

[107] N.C.K. Pawsey. *Development and evaluation of passive variable-pitch vertical axis wind turbines*. PhD thesis, School of Mechanical and Manufacturing Engineering, The University of New South Wales, 2002.

[108] K.M.M. Prabhu. *Window Functions and Their Applications in Signal Processing*. CRC Press, 1st edition edition, 2014. doi:10.1201/9781315216386.

[109] R. Pérez-Torró and J.W. Kim. A large-eddy simulation on a deep-stalled aerofoil with a wavy leading edge. *Journal of Fluid Mechanics*, 813:23–52, 2017. doi:10.1017/jfm.2016.841.

[110] V. Quaschning. Weltweit installierte regenerative Kraftwerksleistung, 2018. URL: volker-quaschning.de/datserv/ren-Leistung.

[111] P. Rojratsirikul, Z. Wang, and I. Gursul. Unsteady fluid–structure interactions of membrane airfoils at low Reynolds numbers. *Experiments in Fluids*, 46(5):859, Feb 2009. doi:10.1007/s00348-009-0623-8.

[112] D.M. Rosenberg, R.A. Bodaly, and P.J. Usher. Environmental and social impacts of large scale hydroelectric development: who is listening? *Global Environmental Change*, 5:127–148, 1995. doi:10.1016/0959-3780(95)00018-j.

[113] S. Roy, H. Branger, L. Christopher, D. Bourras, and B. Paillard. Design of an offshore three-bladed vertical axis wind turbine for wind tunnel experiments. In *ASME 2017 36th International Conference on Ocean, Offshore and Arctic Engineering OMAE 2017*, Trondheim, Norway, June 2017. URL: https://hal.archives-ouvertes.fr/hal-01629533, doi:10.1115/omae2017-61512.

[114] S. Khalid, Z. Liang, S. Qi-hu, and Z. Xue-Wei. Difference between fixed and variable pitch vertical axis tidal turbine-using CFD analysis in CFX. *Research Journal of Applied Sciences, Engineering and Technology 5(1)*, 2013.

[115] S. Shin and H. T. Kim. Numerical simulation of fluid-structure interaction of a moving flexible foil. *Journal of Mechanical Science and Technology*, 22(12):2542, Dec 2008. doi:10.1007/s12206-008-0816-8.

[116] M. Shiono, K. Suzuki, and S. Kiho. An experimental study of the characteristics of a Darrieus turbine for tidal power generation. *Electrical Engineering in Japan*, 132(3):38–47, 8 2000. doi:10.1002/1520-6416(200008)132:3<38::AID-EEJ6>3.0.CO;2-E.

[117] J.R. Stephenson, A.J. Gingerich, R.S. Brown, B.D. Pflugrath, Z. Deng, T.J. Carlson, M.J. Langeslay, M.L. Ahmann, R.L. Johnson, and A.G. Seaburg. Assessing barotrauma in neutrally and negatively buoyant juvenile salmonids exposed to simulated hydro-turbine passage using a mobile aquatic barotrauma laboratory. *Fisheries Research*, 106(3):271 – 278, 2010. doi:doi.org/10.1016/j.fishres.2010.08.006.

[118] M. Takeda, H. Ina, and S. Kobayashi. Fourier-transform method of fringe-pattern analysis for computer-based topography and interferometry. *J. Opt. Soc. Am.*, 72(1):156–160, Jan 1982. doi:10.1364/JOSA.72.000156.

[119] T.D. Ivanov, A.M. Simonović, J.S. Svorcan, O.M. Peković. VAWT optimization using genetic algorithm and CST airfoil parameterization. In *FME Transactions (2017) 45, 26-31*, 2017. doi:10.5937/fmet1701026I.

[120] F. Thönnißen, M. Marnett, B. Roidl, and W. Schröder. A numerical analysis to evaluate Betz's law for vertical axis wind turbines. *Journal of Physics: Conference Series*, 753(2):022056, 2016. doi:10.1088/1742-6596/753/2/022056.

[121] B. Tilt, Y. Braun, and D. He. Social impacts of large dam projects: A comparison of international case studies and implications for best practice. *Journal of Environmental Management*, 90:249–257, 2009. doi:10.1016/j.jenvman.2008.07.030.

[122] L. Tregidgo, Z. Wang, and I. Gursul. Unsteady fluid–structure interactions of a pitching membrane wing. *Aerospace Science and Technology*, 28(1):79 – 90, 2013. doi:https://doi.org/10.1016/j.ast.2012.10.006.

[123] Z. Tukovic, P. Cardiff, A. Karac, H. Jasak, and A. Ivankovic. OpenFOAM library for fluid structure interaction. In *9th OpenFOAM Workshop*, 2014.

[124] Z. Tuković and H. Jasak. Finite-volume method for fluid-structure interaction with large structural displacements. In *OpenFOAM Workshop*, 2007. URL: http://powerlab.fsb.hr/ped/kturbo/OpenFOAM/WorkshopZagrebJun2007/presentations/abstracts/abstractTukovicZagreb2007.pdf.

[125] S. Turek and J. Hron. *Proposal for a numerical benchmarking of fluid-structure interaction between an elastic object and laminar incompressible flow*, pages 371–385. Springer, Berlin, Heidelberg, 2006. doi:10.1007/3-540-34596-5_15.

[126] A. Turnpenny, S. Clough, K. Hanson, R. Ramsay, and D. McEwan. *Risk assessment for fish passage through small, low-head turbines.* Atomic Energy Research Establishment, Energy Technology Support Unit, New and Renewable Energy Programme, London, 2000. URL: `https://www.worldcat.org/title/risk-assessment-for-fish-passage-through-small-low-head-turbines/oclc/316564537`.

[127] S. van der Jeught and J.J.J. Dirckx. Real-time structured light profilometry: a review. *Optics and Lasers in Engineering*, 87:18 – 31, 2016. Digital optical & Imaging methods in structural mechanics. `doi:https://doi.org/10.1016/j.optlaseng.2016.01.011`.

[128] M. Viswanathan. *Simulation of Digital Communication Systems Using Matlab.* Viswanathan, second edition, 2014.

[129] G.S. West and C.J. Apelt. The effects of tunnel blockage and aspect ratio on the mean flow past a circular cylinder with Reynolds numbers between 10^4 and 10^5. *Journal of Fluid Mechanics*, pages 361–377, 1982. `doi:10.1017/s0022112082000202`.

[130] R.W. Whittlesey, S. Liska, and J.O. Dabiri. Fish schooling as a basis for vertical axis wind turbine farm design. *Bioinspiration & Biomimetics*, 5(3), aug 2010. `doi:10.1088/1748-3182/5/3/035005`.

[131] J. Zanette, D. Imbault, and A. Tourabi. A design methodology for cross flow water turbines. *Renewable Energy*, 35(5):997 – 1009, 2010. `doi:https://doi.org/10.1016/j.renene.2009.09.014`.

[132] A. Zanotti, R. Nilifard, G. Gibertini, A. Guardone, and G. Quaranta. Assessment of 2d/3d numerical modeling for deep dynamic stall experiments. *Journal of Fluids and Structures*, 51:97–115, 2014. `doi:doi.org/10.1016/j.jfluidstructs.2014.08.004`.

[133] D.H. Zeiner-Gundersen. A novel flexible foil vertical axis turbine for river, ocean and tidal applications. *Applied Energy*, 151:60–66, 2015. `doi:10.1016/j.apenergy.2015.04.005`.

[134] J. Zhang, D. Kitazawa, S. Taya, and Y. Mizukami. Impact assessment of marine current turbines on fish behavior using an experimental approach based on the similarity law. *Journal of Marine Science and Technology*, 22(2):219–230, Jun 2017. `doi:10.1007/s00773-016-0405-y`.

[135] L. Zhang, Y. Liang, X. Liu, and J. Guo. Effect of blade pitch angle on aerodynamic performance of straight-bladed vertical axis wind turbine. *Journal of Central South University*, 21:1417–1427, 2014. `doi:10.1007/s11771-014-2080-7`.

[136] S. Zhang. *High-resolution, High-speed 3-D Dynamically Deformable Shape Measurement Using Digital Fringe Projection Techniques*, chapter 2. IntechOpen, Rijeka, 2010. `doi:10.5772/8720`.